

Automatic Modeling and Localization for Object Recognition

Mark Damon Wheeler

October 25, 1996

CMU-CS-96-188

School of Computer Science
Carnegie Mellon University
Pittsburgh, PA 15213

*Submitted in partial fulfillment of the requirements
for the degree of Doctor of Philosophy.*

Thesis Committee:

Katsushi Ikeuchi, Chair
Martial Hebert
Steven Shafer, CMU/Microsoft
Eric Grimson, MIT

© 1996 Mark D. Wheeler

This research has been supported in part by the Advanced Research Projects Agency under the Department of the Army, Army Research Office grant number DAAH04-94-G-0006, and in part by the Department of the Navy, Office of Naval Research grant numbers N00014-95-1-0591 and N00014-93-1-1220. Views and conclusions contained in this document are those of the authors and should not be interpreted as necessarily representing official policies or endorsements, either expressed or implied, of the Department of the Army, the Department of the Navy or the United States Government.

Keywords: localization, pose refinement, automatic object modeling, recognition, tracking, robust statistics, consensus, M-estimation, surface merging

Abstract

Being able to accurately estimate an object's pose (location) in an image is important for practical implementations and applications of object recognition. Recognition algorithms often trade off accuracy of the pose estimate for efficiency—usually resulting in brittle and inaccurate recognition. One solution is object localization—a local search for the object's true pose given a rough initial estimate of the pose. Localization is made difficult by the unfavorable characteristics (for example, noise, clutter, occlusion and missing data) of real images.

In this thesis, we present novel algorithms for localizing 3D objects in 3D range-image data (3D-3D localization) and for localizing 3D objects in 2D intensity-image data (3D-2D localization). Our localization algorithms utilize robust statistical techniques to reduce the sensitivity of the algorithms to the noise, clutter, missing data, and occlusion which are common in real images. Our localization results demonstrate that our algorithms can accurately determine the pose in noisy, cluttered images despite significant errors in the initial pose estimate.

Acquiring accurate object models that facilitate localization is also of great practical importance for object recognition. In the past, models for recognition and localization were typically created by hand using computer-aided design (CAD) tools. Manual modeling suffers from expense and accuracy limitations. In this thesis, we present novel algorithms to automatically construct object-localization models from many images of the object. We present a consensus-search approach to determine which parts of the image justifiably constitute inclusion in the model. Using this approach, our modeling algorithms are relatively insensitive to the imperfections and noise typical of real image data. Our results demonstrate that our modeling algorithms can construct very accurate geometric models from rather noisy input data.

Our robust algorithms for modeling and localization in many ways unify the treatment of these problems in the range image and intensity image domains. The modeling and localization framework presented in this thesis provides a sound basis for building reliable object-recognition systems.

We have analyzed the performance of our modeling and localization algorithms on a wide variety of objects. Our results demonstrate that that our algorithms improve upon previous approaches in terms of accuracy and reduced sensitivity to the typical imperfections of real image data.

Acknowledgements

I would first like to thank Katsushi Ikeuchi, my advisor and friend for much of my 7 year stay at Carnegie Mellon. I thank him for giving me the freedom to explore a wide variety of ideas and for having an open door and open mind whenever I needed it. I also thank my thesis committee members Martial Hebert, Steve Shafer, and Eric Grimson for their careful reading of this thesis and their valuable feedback regarding this research.

Takeo Kanade deserves special thanks for creating such a wonderful group and environment for studying computer vision and robotics. The VASC facilities gurus Jim Moody, Bill Ross and Kate Fissell deserve much of the credit for keeping everything going in the VASC group; their frequent help and patience was greatly appreciated.

I thank the faculty at Tulane University, especially Johnette Hassell and Mark Benard, for providing me with a solid undergraduate education and encouraging me to pursue a research career.

I was fortunate to have many great people to work with during my stay at CMU. My fellow grad students contributed many ideas and insights which helped me to develop and implement the experimental systems in this thesis: thanks to Yoichi Sato, Harry Shum, Sing Bing Kang, Fredric Solomon, George Paul, Prem Janardhan, David Simon, and Andrew Johnson for their friendship and help over the years. I also benefited from the help of visiting scientists including Takeshi Shakunaga and Yunde Jiar. I have been fortunate to have a number of excellent officemates during my stay here including Kevin Lynch, Tammy Abel, Greg Morrisett, Andrzej Filinski, Lars Birkedal, Margaret Reid-Miller, and John Ockerbloom.

Grad school would have been much more difficult without the many of the friends I have made here. I am most grateful for having shared an office and house with Kevin Lynch. It was important to have a friend who shared so much in common and could always counted on. Kevin will always be like a brother to me. My friends in the CS PhD program were very special as well. I especially cherished our coop dinner group, including Rich Goodwin, Scott and LeAnn Neal Reilly, Dave Tarditi, Greg and Jack Morrisett, Susan Hinrichs, Alan Carroll, Mei Wang, Kevin Lynch, and Tammy Abel, which shared many fun times together. I also cherish the friendship of John Mount, Nina Zumel, Mark and Heather Leone and Bob Doorenbos (croquet anyone?).

Some of my favorite times were spent playing intramural sports at CMU, with teams such as the infamous Rude Dogs, NP Completions, Viking Death Rats, Base Registers and Bucket Brigade. I will greatly miss all these people, most especially “Super” Bill Niehaus, Will Marrero, John Cheng, John Greiner, Jerry Burch, Todd Jochem, Dave Kosbie, Fabio Cozman, Rich Voyles, David Steere,

Jay Kistler, John Pane, Mike Young, Bunsen Wong, Harry Shum and the many others too numerous to mention.

Lastly, I would like to thank the most important people in my life, my family, for always being there for me and supporting me unconditionally: my siblings Brandon, Douglas, and Dana who can crack me up at any time and make me proud to be related to them; my precious niece Aerial who makes me smile every time I think of her; and, most of all, my Mom and Dad for their love, advice, patience, and help for these many years and for the years to come.

Contents

1	Introduction	1
1.1	Notation, Terminology, and Assumptions	3
1.2	Philosophical Background	6
1.3	Thesis Overview	7
2	Object Modeling for 3D-3D Localization	13
2.1	Approach	13
2.2	Surface Acquisition	15
2.3	View Alignment	17
2.4	Data Merging	20
2.5	3D Object Modeling Results	34
2.6	3D Modeling: Summary	46
3	3D-3D Object Localization	53
3.1	Approach	53
3.2	Point Visibility	55
3.3	3D-3D Correspondence	65
3.4	3D-3D Pose Optimization	70
3.5	Putting It Together: 3D-3D Localization	84
3.6	3D-3D Localization: Experimental Results	87
3.7	3D-3D Object Localization: Summary	100
4	Object Modeling for 3D-2D Localization	102
4.1	Problems and Approach	102
4.2	View Acquisition	108
4.3	2D to 3D: View Alignment	110
4.4	View Merging: the Consensus-Edgel Algorithm	116
4.5	Modeling Occluding Contours for 3D-2D Localization	119
4.6	Object Modeling for 3D-2D Localization: Results	125
4.7	Object Modeling for 3D-2D Localization: Summary	127

5	3D-2D Object Localization	136
5.1	Problems and Approach	136
5.2	Edgel Visibility	139
5.3	Edgel Correspondence	145
5.4	Pose Optimization	150
5.5	Putting It Together: 3D-2D Localization	155
5.6	Multi-Image Localization	156
5.7	3D-2D Localization Results	157
5.8	3D-2D Localization: Summary	171
6	Related Work	175
6.1	3D Object Modeling	175
6.2	3D-3D Object Localization	181
6.3	Object Modeling for 3D-2D Localization	184
6.4	3D-2D Object Localization	190
6.5	Object Recognition	193
7	Conclusions	196
7.1	Contributions	198
7.2	Future Work and Discussion	198
A	Camera and Robot Calibration	203
Appendices		
B	Quaternions and Rotation	207
B.1	Why Quaternions?	207
B.2	Quaternions	208
B.3	The Jacobian of Rotation With Respect to Quaternions	209
C	Principal Curvatures from Triangulated Surfaces	213
	Bibliography	

List of Figures

1.1	An example of (a) 2D image edgels and (b) 3D edgels or edgel generators.	5
1.2	An example of the 3D object modeling process.	9
1.3	An example of 3D-3D localization for a simple sphere object.	10
1.4	An example of the 3D edgel modeling process.	11
1.5	An example of 3D-2D localization for a simple bulls-eye object.	12
2.1	Organization of this chapter.	15
2.2	Connecting range image points to form a surface.	16
2.3	Examples of triangulation errors.	17
2.4	An example of zero-crossing interpolation from the grid sampling of an implicit surface.	21
2.5	In practice, real surface samples are noisy and slightly misaligned and it is difficult to determine where the actual surface might lie.	24
2.6	Some effects of noise and misalignment on our naive algorithm.	24
2.7	Graphical illustration of the error in zero-crossing interpolation using Algorithm <i>ClosestSignedDistance</i> with two noisy observations.	26
2.8	An example of inferring the incorrect sign of a voxel's signed-distance function.	27
2.9	The extension of the implicit surface in unobserved regions of the grid.	30
2.10	A demonstration of gradient testing to eliminate false surfaces at zero crossings of the implicit surface.	31
2.11	A 2D slice of an octree representation of a simple surface illustrates the adaptive resolution which is high around the surface and low elsewhere.	33
2.12	The two degrees of freedom, θ_x and θ_y of the Puma used to vary of object position with respect to the camera's coordinate system.	35
2.13	Results from modeling the boxcar.	37
2.14	Three views of the resulting triangulated model of the boxcar.	38
2.15	Results from modeling the fruit.	39
2.16	Three views of the resulting triangulated model of the fruit.	40
2.17	Results from modeling the rubber duck.	41
2.18	Three views of the resulting triangulated model of the duck.	42

2.19	Results from modeling the ceramic mug.	43
2.20	Three views of the resulting triangulated model of the mug.	44
2.21	Results from modeling the toy car.	45
2.22	Three views of the resulting triangulated model of the car.	46
2.23	The result of the naive algorithm, Algorithm <i>ClosestSignedDistance</i> , on the duck image.	47
2.24	A cross section of the final model of the boxcar (thick black line) and the original range-image data (thin black lines) used to construct it.	48
2.25	A cross section of the final model of the fruit (thick black line) and the original range-image data (thin black lines) used to construct it.	49
2.26	A cross section of the final model of the rubber duck (thick black line) and the original range-image data (thin black lines) used to construct it.	50
2.27	A cross section of the final model of the ceramic mug (thick black line) and the original range-image data (thin black lines) used to construct it.	51
2.28	A cross section of the final model of the toy car (thick black line) and the original range-image data (thin black lines) used to construct it.	52
3.1	Organization of this chapter.	56
3.2	An example of the set of visible viewing directions (the unshaded portion of the hemisphere) for the point x on the L-shape.	58
3.3	Orthographic projection of viewing directions onto a simple LUT array.	60
3.4	Latitudinal/Longitudinal discretization of a hemisphere.	61
3.5	Stereographic projection of viewing directions onto a simple LUT array.	62
3.6	The mapping of viewing directions to visibility values via a two-level lookup table.	62
3.7	K-d tree subdivision of 2D points.	67
3.8	An example of nearest-neighbor correspondence (left) versus nearest neighbor+normal correspondence (right).	67
3.9	Plot of the 3D distance between two unit vectors with respect to the angle between the two vectors.	69
3.10	Examples of local versus global minima and basins of attraction.	74
3.11	Plots of $w(z)$ for each of the M-estimators listed in Table 3.1	78
3.12	Plots of $P(z)$ for each of the M-estimators listed in Table 3.1	78
3.13	Example of the fluctuation of E due to changes in the pose and the set of visible points.	82
3.14	The minimum distance function with respect to the dynamic correspondences.	82
3.15	Correspondences which compare normals can create discontinuities in the distance function.	83
3.16	Three views of the mug object generated using our surface point visibility approximation.	89

3.17	The variation of E along a line of translation in pose space.	91
3.18	The variation of E along a line of pure rotation in pose space.	91
3.19	The variation of E along a line of translation and rotation in pose space.	92
3.20	A close-up of a piece of the graphs of the function E for the Lorentzian, Gaussian and Threshold along a line of translation in pose space.	92
3.21	The Sharpei dog convergence test data.	95
3.22	The ceramic mug convergence test data.	96
3.23	The toy car convergence test data.	97
3.24	The rubber duck convergence test data.	98
3.25	Depiction of three iterations of the randomized localization search.	99
4.1	Organization of this chapter.	109
4.2	An example of raw and smooth edgel chains.	110
4.3	An example of mapping a 2D edgel onto a 3D triangulated surface.	111
4.4	A diagram representing the relationships between the various coordinate frames used in the analysis in this chapter.	112
4.5	An occluding boundary edgel which does not project onto the model surface.	114
4.6	The shortest distance between a ray and the surface triangles when they do not intersect.	114
4.7	An occluding contour mapped to the object.	115
4.8	The stages of a consensus-edgel search.	118
4.9	A circle and its occluding contour points.	121
4.10	Example of normal sections with (a) positive normal curvature and (b) negative normal curvature.	123
4.11	Classes of surfaces based on curvature.	125
4.12	Results from modeling the 3D edgel generators of the stop sign.	128
4.13	Results from modeling the 3D edgel generators of the T-sign.	129
4.14	Results from modeling the 3D edgel generators of the bulls-eye.	130
4.15	Results from modeling the 3D edgel generators of the boxcar.	131
4.16	Results from modeling the 3D edgel generators of the mug.	132
4.17	Results from modeling the 3D edgel generators of the car.	133
4.18	Results from modeling the 3D edgel generators of the duck	134
5.1	Organization of this chapter.	138
5.2	Examples of three types of edgel generators: (a) rigid surface marking, (b) convex edges, (c) occluding contours.	140
5.3	A normal section of a surface.	143
5.4	Using the tangent direction of an edgel to locate pixels to sample the left and right intensities, I_L and I_R , for computing the reflectance ratio.	148
5.5	Example of correspondence search using reflectance ratios.	149

5.6	Gradient-descent minimization path to align a 3d point x with the line of sight \hat{v} (a) infinitesimal steps, (b) discrete steps, (c) shortest path.	153
5.7	An example of the 3D error vector between the 3D point and the line of sight of edgel.	154
5.8	The stereo correspondence problem: several points are not visible in both views.	156
5.9	The variation of E along a line of translation in pose space for the Gaussian and Lorentzian weight functions.	159
5.10	The variation of E along a line of pure rotation in pose space for the Gaussian and Lorentzian weight functions.	159
5.11	The variation of E along a line of translation and rotation in pose space for the Gaussian and Lorentzian weight functions.	160
5.12	The bulls-eye convergence test data.	162
5.13	The stop sign convergence test data.	163
5.14	The T-sign convergence test data.	164
5.15	The boxcar convergence test data.	165
5.16	The duck convergence test data.	166
5.17	The car convergence test data.	167
5.18	The mug convergence test data.	168
5.19	Tracking the car through 5 images at 10 degree intervals.	170
5.20	Multi-image localization of the stop sign.	172
5.21	Multi-image localization of the paint can.	173
6.1	Illustration of the result of Curless and Levoy's signed distance integration in the neighborhood of thin object parts.	177
6.2	Illustration of estimating the distance to the surface along rays passing through a voxel.	178
6.3	Illustration of estimating the distance to the surface along rays passing through a voxel.	178
A.1	An image of the experimental setup including the CCD camera, light-striping projector, and Puma robot.	204
A.2	The calibration cube used for range sensor and camera calibration.	205

List of Tables

2.1	Statistics of the modeling experiments for each object.	40
3.1	Table of weight functions for M-estimation.	79
3.2	Results of the convergence experiments with variations of our 3D-3D localization algorithm and ICP.	95
3.3	Results of the convergence experiments with variations of ICP on the duck image.	98
3.4	Results of the randomization convergence experiments.	100
4.1	Statistics of the edgel modeling experiments for each object.	127
5.1	Results of the convergence experiments for our 3D-2D localization algorithm using the Lorentzian and Gaussian weight functions.	161
5.2	Results of the single versus multi-image convergence tests.	171

Chapter 1

Introduction

Object recognition remains one of the central problems in the fields of artificial intelligence and computer vision. The standard definition of the object-recognition problem is to *identify* and *locate* instances of known objects in an image [4, 23, 109]. That is, we do not simply desire to know that an object exists in the image, but that we also need to know where it is in the image. This location or positional information is commonly referred to as the object's *pose*.

Knowledge of an object's pose has many important applications; it enables us: to reason about the image scene, to interact with objects in the scene, to analyze geometric relationships between objects in the scene, and to describe the scene for later synthetic or physical reproduction.

Pose is also fundamental for practical object-recognition algorithms—impacting both the accuracy and efficiency of these algorithms. Pose allows us to improve recognition by enabling us: to accurately verify an object hypotheses using, for example, a project and test strategy; to efficiently recognize time-varying image sequences via object tracking; and to detect and reason about partial occlusion.

When we say that knowledge of the pose is important for applications in object recognition, we should qualify that by saying *accurate* knowledge of the pose is important. Object verification [50] is a very difficult problem for recognition algorithms when pose is perfectly known. If the pose is inaccurate, verification becomes a highly unreliable operation and recognition efficiency and accuracy will be affected. Likewise, applications that rely on knowing where the object is will also fail when the pose error is too large. Thus, we claim that determining accurate pose is a fundamental requirement for object recognition.

Accurate knowledge of pose is also crucial for object tracking. Tracking is a simplification of the object-recognition problem. In the case of tracking, we know roughly the position of the object in the image using a prediction from previous image observations. Thus, an efficient local search can be used to find the new object position and verify it. Tracking ability has great implications for practical recognition in the case of image sequences. If we can reliably track objects, we must perform full scale recognition only on parts of images that contain something new.

Unfortunately, much work on object recognition neglects the problem of accurately computing the object's pose. There are a wide variety of techniques for recognition that give identity of objects and their rough pose (see Chapter 6 for a discussion of these). Because of the highly unfavorable combinatorics of recognition, recognition algorithms must often sacrifice pose accuracy (and, hence, recognition accuracy) for efficiency. The best example of this is the alignment algorithm [70]. The alignment algorithm searches for minimal sets of matches between image and object features to align a 3D object to a 2D image. Grimson and Huttenlocher [50] have shown that the resulting uncertainty in the pose (when using a small number of matches) is enough to make verification prone to frequent failure. For example, under realistic uncertainty in the location of features in an image, an algorithm which estimates the position of the object using 3 or 4 point or line segment matches may be off by 20 or more degrees in rotation. Thus, the predicted positions of other features of the object will be significantly affected—resulting in a very low probability to correctly verify the presence of the object in the image. The solution is to search for more feature correspondences (create an over-determined system); however, this results in combinatorial explosion which is what we were trying to avoid in the first place.

The solution to this tradeoff problem is *localization*¹—a local search for the true pose given the rough pose of an object in an image. If localization can be done efficiently and reliably, recognition algorithms like the alignment algorithm and others will eventually become practical in terms of accuracy and efficiency. In addition, a solution to localization is immediately useful as a solution to the tracking problem. Localization is fundamentally equivalent to the object-tracking problem. In typical tracking systems, the object's estimated velocity and acceleration is used to better predict the object's current position. From that predicted position, a localization search is performed. Localization is a bit more general than object tracking in that no information other than the object's identity and pose is assumed to be known.

This thesis presents solutions to the localization problem in the two most prevalent sensor modalities in the field of computer vision: the range image (3D) and intensity image (2D) modalities. Specifically, we present novel techniques for localizing 3D objects in 3D range-image data (3D-3D localization) and for localizing 3D objects in 2D intensity-image data (3D-2D localization). The solutions presented here in many ways unify the treatment of the two domains.

This thesis also addresses another fundamental problem of recognition, tracking and localization: model acquisition. In the past, models for recognition and tracking have typically been manually created using computer-aided design (CAD) tools. Manual modeling suffers from expense and accuracy limitations. The modeling solutions presented in this thesis automatically construct object-localization models from real images of the object. These modeling solutions are insensitive to the noisy data typical of real image data (for both range and intensity images). Robust model acquisition is achieved by searching

¹The term localization has previously been used in [52] to denote the complete object-recognition task (from image to object identity and pose). Here we use the localization as a synonym for pose refinement and distinguish it from the task of object indexing and hypothesis generation.

for consensus information among the views to determine which image features justifiably constitute an element in the model. Together, the modeling and localization framework presented in this thesis provide a sound basis for building reliable recognition and tracking systems.

This thesis makes the following contributions:

- Robust 3D surface model construction with the consensus-surface algorithm.
- Robust 3D-3D and 3D-2D object localization by performing M-estimation using dynamic correspondences.
- Robust 3D edgel model construction with the consensus-edgel algorithm.
- Treatment of occluding contours in 3D-2D localization.
- 3D-2D localization performed in three dimensions, unifying the localization search for the 3D-3D and 3D-2D domains.

1.1 Notation, Terminology, and Assumptions

Before jumping into the technical portion of this thesis, it is prudent to specify the notation, terminology, and assumptions which will be used throughout this thesis. Much of this will be familiar to computer-vision and object-recognition researchers; however, some of the terminology may have slightly different meanings than used elsewhere.

1.1.1 Mathematical Notation

First, we list a few of our mathematical notations and notes:

- Vectors are in boldface type: \mathbf{x} is a vector, x is a scalar.
- Unit vectors have the hat symbol: $\hat{\mathbf{x}}$ is a unit vector, \mathbf{x} may not be.
- Matrices are capitalized and in boldface type: \mathbf{M} is a matrix, \mathbf{I} is the identity matrix.
- \mathbf{x} will be used to denote model points.
- \mathbf{u} will be used to denote 3D image coordinates (before projection to two dimensions).
- \mathbf{U} will be used to denote 2D image coordinates (note, this is the only vector that will be capitalized).
- \mathbf{y} will be used to denote image points.
- Vectors should be assumed to be three dimensional unless otherwise noted.

- Pairs or tuples will be denoted using the angle brackets $\langle \cdot \rangle$ (e.g., $\langle \mathbf{x}, \mathbf{y} \rangle$ denotes the pair of vectors \mathbf{x} and \mathbf{y}).
- \mathbf{p} will be used to denote the object's pose.
- The 3D rigid transformation defined by the pose \mathbf{p} may be specified by one of the following notations:
 - simply by \mathbf{p}
 - by a rotation and translation pair $\langle \mathbf{R}, \mathbf{t} \rangle$ where \mathbf{R} is a 3×3 rotation matrix and \mathbf{t} is a 3D translation vector.
 - by the equivalent homogeneous transformation \mathbf{R} where \mathbf{R} is the equivalent 4×4 homogeneous transform matrix and the point being transformed is assumed to be extended to 4D homogeneous coordinates (i.e., by placing a 1 at the end of the 3D vector)².

1.1.2 Terminology

We now define some of our terminology.

We will often refer to *range images* (sometimes known as depth images). Here, a range image is assumed to be a 2D view of a scene in which each image pixel contains the 3D coordinate of the scene in some world or camera coordinate system. The coordinate system should be assumed to be Euclidean.

We will often discuss intensity edges extracted from intensity images. An *edgel* is an individual point or edge element along an edge chain. Typically, an edgel will be represented by a pair $\langle \mathbf{U}, \hat{\mathbf{t}} \rangle$ where \mathbf{U} are image coordinates of the edgel and $\hat{\mathbf{t}}$ is its tangent direction, again in image coordinates. The edgel chain is usually extracted from intensity images using one of many edge operators (e.g., Canny [16] or Deriche [30]). For an example of an edgel, see Figure 1.1(a).

A *3D edgel* denotes the extension of a 2D edgel to an oriented point in 3D space. It is denoted $\langle \mathbf{x}, \hat{\mathbf{t}} \rangle$ where \mathbf{x} are the 3D coordinates of the edgel and $\hat{\mathbf{t}}$ is its (3D) tangent direction. Figure 1.1(b) shows an example of this. An *edgel generator* denotes the point on an object which produces the image of the (2D) edgel in the intensity image.

For intensity edge images, Breuel [14] used the terms *attached* and *non-attached* to distinguish between two types of edgels. *Attached* edgels refer to those detected edgels which are attached to the surface of an object (e.g., a surface marking or corner). *Non-attached* edgels refer to those detected edgels which belong to occluding contours of the object, and appear to float across the surface of the object as it is rotated.

As mentioned previously, the object's six location coordinates are collectively referred to as its *pose*. Again, *localization*—also known as *pose refinement*³—is a local search for

²The homogeneous notation will be used in place of $\langle \mathbf{R}, \mathbf{t} \rangle$ for brevity when discussing a transformation as a single entity.

³The terms *pose refinement* and *localization* will be used interchangeably throughout this thesis.

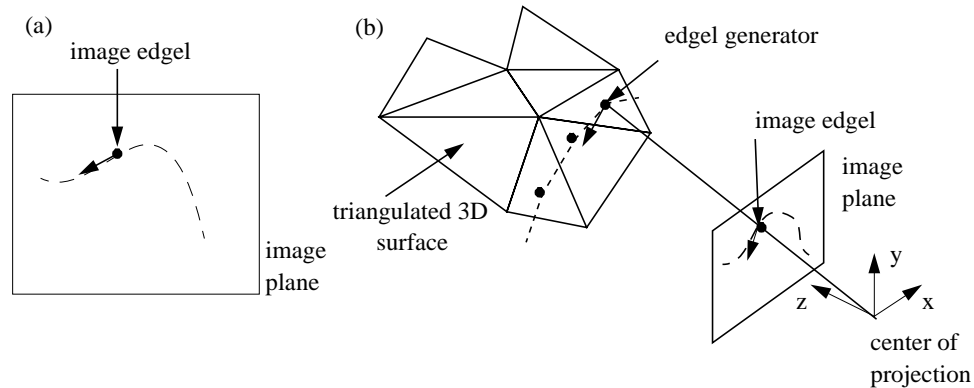


Figure 1.1: An example of (a) 2D image edgels and (b) 3D edgels or edgel generators.

the true pose given the rough pose of an object in an image. *3D-3D localization* refers to the process of localizing 3D objects in 3D range-image data. *3D-2D localization* refers to the process of localizing 3D objects in 2D intensity-image data.

1.1.3 Scope and Assumptions

We now briefly list some of the assumptions we make for the algorithms and experiments described in this work. Our main assumptions are practical limitations of the type of objects that may be used and a requirement for calibrated cameras and range sensors.

Our first assumption is that we only address the problems of modeling and localizing rigid, 3D objects. This means we consider objects with six degrees of freedom, three rotational and three translational. This thesis does not address issues related to deformable, non-rigid or generic objects. While not totally general, rigid objects do account for quite a large segment of everyday objects. Rigid object modeling and localization is still a very important area of current research with many applications. We view the rigid object case as an important first step which must be solved before considering completely general classes of objects. We also assume the objects are opaque and do not contain significantly large portions of high frequency texture with respect to our sensors.

Lastly, we assume that we are working with cameras and range sensors which are calibrated. The intrinsic sensor parameters must be known for us to be able to predict an object's appearance, using a 3D model of the object, in the sensor's images.

Our modeling work assumes that we have a calibrated object positioning system (details described in Chapter 2 and Appendix A), which limits the size of objects we may model to those that are mountable on a robot's end effector. We believe that this limitation will soon be obviated with more work on view alignment (as will be discussed in Chapter 7) and improvements in the area of structure from motion.

1.2 Philosophical Background

We take a few paragraphs to describe some of the high-level issues and ideas which drive this work.

1.2.1 Consensus

One of the key ideas which is embodied by our approach to object modeling and localization is the idea of *consensus*. For modeling from real data, consensus is the key to robustness. Because of the typical data from our sensors, no single measurement can be trusted. However, in sufficient numbers, several independent measurements of the same feature (e.g., a surface point or edgel) can be considered quite reliable.

Consensus is also subtly important for localization. The key for model based recognition and localization is the over-constrained nature of the problem (i.e., more constraints than free variables). Localization works because the consensus of the image data usually guides the local search to the true object pose.

1.2.2 3D vs View-Based Model Representations

An important decision is whether to use view-based (2D) models or full fledged 3D models. For recognition and localization in 3D image data, 3D models are obviously desirable. For recognition and localization in 2D images, there exists an ongoing debate between using many sample 2D views as the model or constructing a monolithic 3D model. One advantage of basic view-based methods is that model acquisition is trivial—take an image and add it to the collection. The problem is that an arbitrarily large number of images may be necessary to build a complete model of appearance. The model is only as good as the sampling resolution. For rigid, 3D objects, we will usually have six degrees of freedom over which to sample views. If we then consider lighting variations and camera model variations, the number of required samples can quickly become unmanageable.

Some view-based methods go a little further and try to alleviate the sampling problem by interpolating between views. This requires a complete set of correspondences between two views—this is not possible in general (see Chapter 6 for a discussion of this problem). Foreground/background separation becomes an important issue for modeling from real images; manual segmentation (i.e., selection of object features from the images) may be required.

3D models have the advantage that one model can be used to predict appearances with respect to all possible variations of pose, camera models, and illumination (if known a priori). Verification, localization and tracking can be accomplished with a 3D model as the change in appearance can be smoothly predicted with respect to changes in pose. The main detraction of monolithic 3D models is that they are difficult to construct. Automatically or semi-automatically constructing accurate 3D models from real images is a non-trivial problem. As we are already considering the problem of building 3D models for 3D-3D

localization, the acquisition of 3D models for localization in 2D images can be made practical as we shall show in this thesis.

1.2.3 Point-Based Models

Another philosophical issue is the type of models to use for these localization tasks. Our philosophy is to keep the model representation as simple as possible. Our choice of model representation is to consider each object as a collection of points.

For 3D-3D localization we represent an object as a set of points on the object's surface. This representation can be acquired from a densely triangulated surface model by sampling points from the triangles.

We also use points to represent the object for 3D-2D localization. Instead of simply using just any surface point, we use points on the model which generate edgels in intensity images. We refer to these points on the model as *3D edgels* or *edgel generators*. Such points comprise surface markings, occluding contours and convex/concave geometric edges of the object.

Not only are these representations simple, which makes them efficient to implement, but they are also very general. We can model a large subset of the possible rigid, 3D objects using these representations.

1.2.4 Data Driven Optimization

Our philosophy for localization derives much from the ideas of active contours introduced by Witkin, Terzopoulos and Kass [75, 134]. The active contour paradigm allowed the user to initialize the location of a contour and let the forces defined by image features act on the contour to find its optimal state. Besl and McKay's [6] iterative closest point (ICP) algorithm for 3D registration is based on this principle: correspondences are computed, a new estimate of the pose is computed and the process is repeated until the pose estimate converges. Our localization algorithm is designed in much the same way. We simply start it off in an initial position and find the local minimum of the energy function defined by the object model and the nearby image data. This is in contrast to other localization methods such as Lowe's [84], which performs a local interpretation-tree search that matches high level image tokens to the model. Our methods are data driven and rely on the lowest-level data available from our sensor (e.g., 3D points from range images and 2D edgels from intensity images).

1.3 Thesis Overview

There are four main technical contributions in this thesis which correspond to the breakdown of the following chapters:

- object modeling for 3D-3D localization

- 3D-3D object localization
- object modeling for 3D-2D localization
- 3D-2D object localization

We will now briefly discuss our approach to each of these problems and give a simple example to give the reader a hint of what follows.

1.3.1 Preview of Object Modeling For 3D-3D Localization

For the problem of object modeling for 3D-3D localization, we are interested in acquiring a 3D triangulated surface model of our object from real range data. From the triangulated surface model, we extract the points for the model for 3D-3D localization.

Our basic approach is to acquire several range-image views of the object, align the image data, merge the image data using the aid of a volumetric representation, and then extract a triangle mesh from the volumetric representation of the merged data. Our main contribution is a new algorithm for computing the volumetric representation from the sets of image data. Our algorithm, the consensus-surface algorithm, eliminates many of the troublesome effects of noise and extraneous surface observations in our data.

Figure 1.2 shows a simple example of the steps of the 3D object modeling process. We begin with by acquiring range images of the object from various views, the views are then aligned to the same coordinate system, and the views are merged into a volumetric implicit-surface representation which is then used to generate a triangulated model of the surface.

1.3.2 Preview of 3D-3D Object Localization

For the problem of 3D-3D object localization, we are interested in computing the precise pose of a 3D object in a (3D) range image given a rough estimate of the object's pose in the image.

Our localization algorithm iteratively refines the pose by optimizing an objective function defined over the image data, model data and the object's pose. The main contribution of our algorithm is the use of an objective function which is specified to reduce the effect of noise and outliers which are prevalent in real image data and a method for minimizing this function in practice. The objective function is effectively minimized by dynamically recomputing correspondences as the pose improves.

Figure 1.3 shows a simple example of our iterative 3D-3D localization algorithm. We begin with a range image of the object and an initial pose estimate. The correspondences between the model and image are a dynamic function of pose and allow the search to follow the proper path to the true pose of the object.

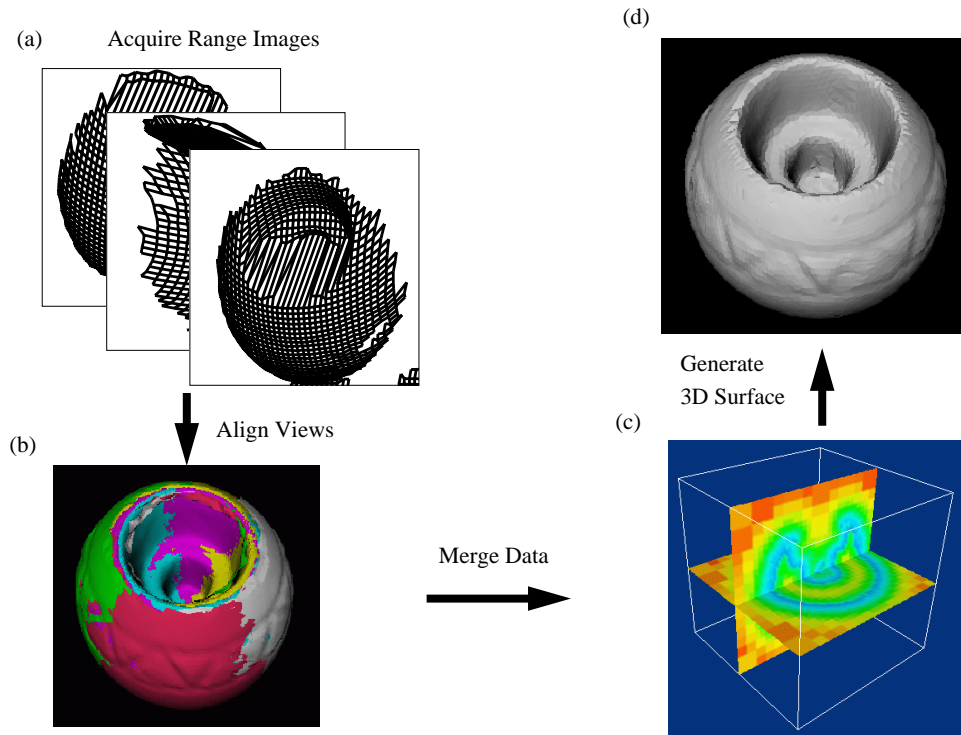


Figure 1.2: An example of the 3D object modeling process: (a) range-image acquisition, (b) view alignment, (c) the merged volumetric representation, (d) resulting triangulated model.

1.3.3 Preview of Object Modeling For 3D-2D Localization

For the problem of object modeling for 3D-2D localization, we are interested in acquiring a 3D model of the edgel generators of the object. Our approach is similar to our approach to 3D surface modeling

We also collect a set of intensity-image views of the object and extract the edgels from them using a standard edge operator. The edgels are then projected and aligned in the object's 3D coordinate system using a 3D surface model of the object (built using the 3D surface modeling approach alluded to previously). The aligned data is then merged to produce a set of rigid edgels. To account for occluding-contour edgels, we use curvature analysis of the points on our 3D surface model to predict which surface points are contour edgel generators. The main contributions of our 3D edgel modeling work is the consensus-edgel algorithm for extracting rigid edgel generators and the framework for representing occluding contours as edgel generator points. The consensus-edgel algorithm is able to reliably extract the significant edgel generators from large sets of rather noisy input data. Edgel generators can be used to efficiently and accurately predict the appearance of occluding contours in 2D

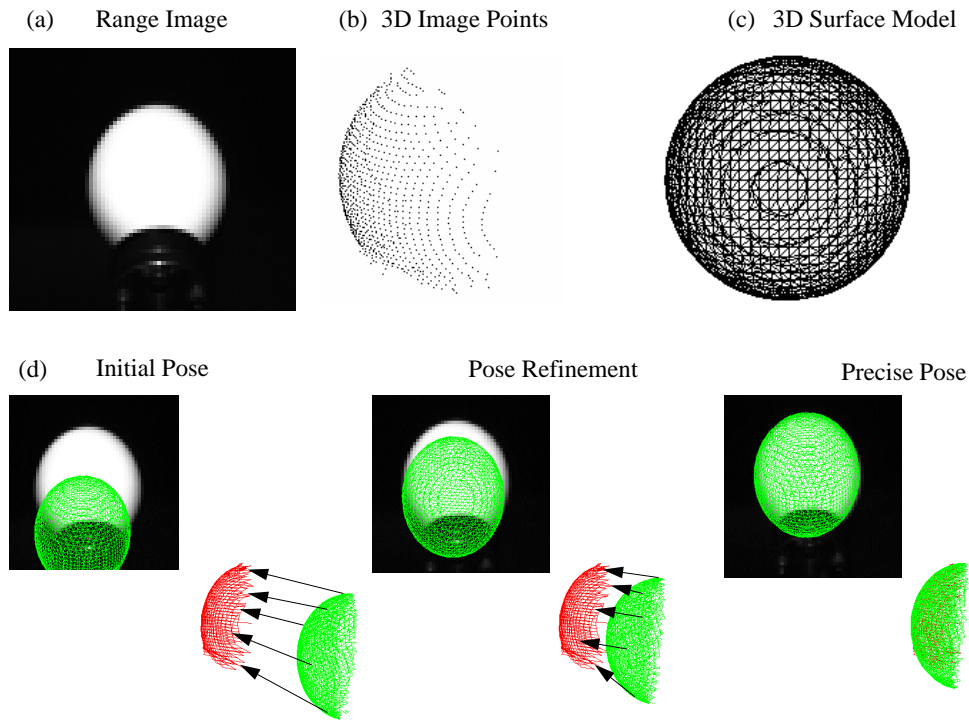


Figure 1.3: An example of 3D-3D localization for a simple sphere object: (a) range image of the sphere, (b) the 3D range data corresponding to the image, (c) the sphere object model, (d) three iterations of the localization search with arrows indicating the correspondences.

images.

Figure 1.4 shows a simple example of the steps of the 3D rigid edgel modeling process. We begin by acquiring intensity edges from various intensity-image views of our object, the edgels are then projected and aligned onto the object surface in the object's 3D coordinate system, and 3D edgel data is merged to form a 3D rigid edgel model.

1.3.4 Preview of 3D-2D Object Localization

For the problem of 3D-2D object localization, we are interested in computing the precise pose of a 3D object in a 2D intensity image given a rough estimate of the object's pose in the image.

Our localization algorithm iteratively refines the pose by optimizing an objective function defined over the image data, model data and the object's pose. The main contribution of our algorithm is the use of an objective function which is specified to reduce the effect of noise and outliers which are prevalent in real image data. The objective function is effectively minimized by dynamically recomputing correspondences as the pose improves.

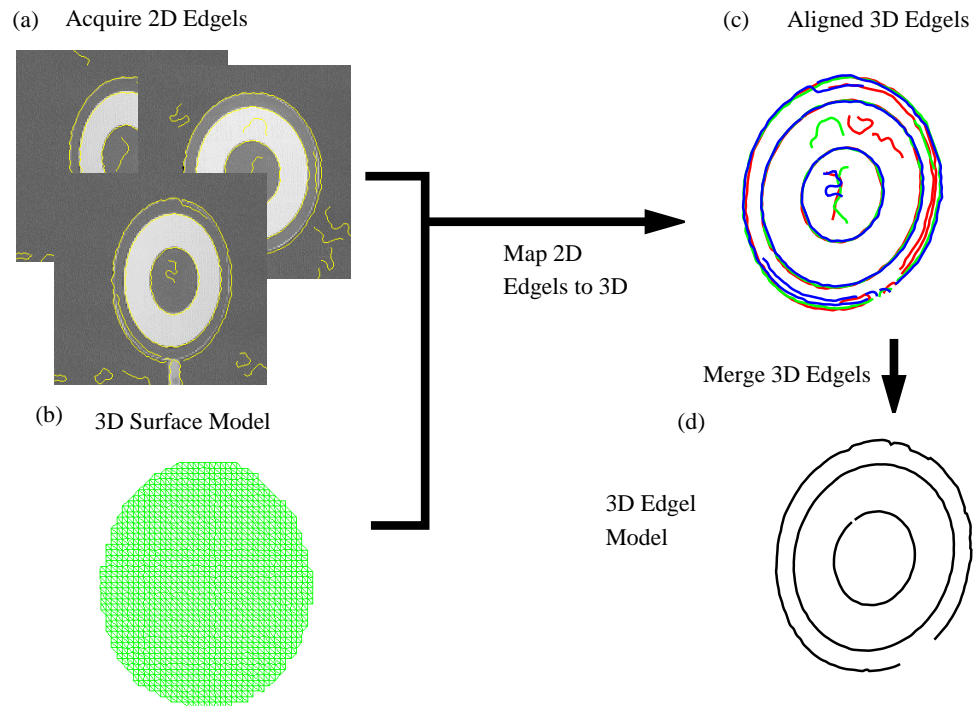


Figure 1.4: An example of the 3D edgel modeling process: (a) acquired intensity edgels (overlaid on the intensity images) (b) the object’s 3D surface model, (c) the edgels from various views mapped onto the object’s coordinate system, and (d) the rigid edgels extracted from the sets of mapped edgels.

Useful correspondences are efficiently found—despite significant pose errors and high densities of edgels in the intensity image—by extending the nearest-neighbor-search concept to include edgel attributes such as edgel normals and reflectance ratios. We show that the pose can be refined using much the same minimization algorithm as Algorithm 3D-3D Localization of Chapter 3.

Figure 1.5 shows a simple example of our iterative 3D-2D localization algorithm. We begin with an intensity image, its edge image, the 3D edgel model, and an initial pose estimate. The pose is refined iteratively as in the 3D-3D localization algorithm, the correspondences are computed dynamically as the pose search proceeds.

We now begin the technical discussion of object modeling for 3D-3D localization in Chapter 2, followed by discussion of 3D-3D object localization, object modeling for 3D-2D localization, and 3D-2D object localization in Chapters 3, 4 and 5, respectively. We then discuss the related research which influenced much of this thesis. We end by offering some conclusions, the contributions of this thesis, and a discussion of future research directions.

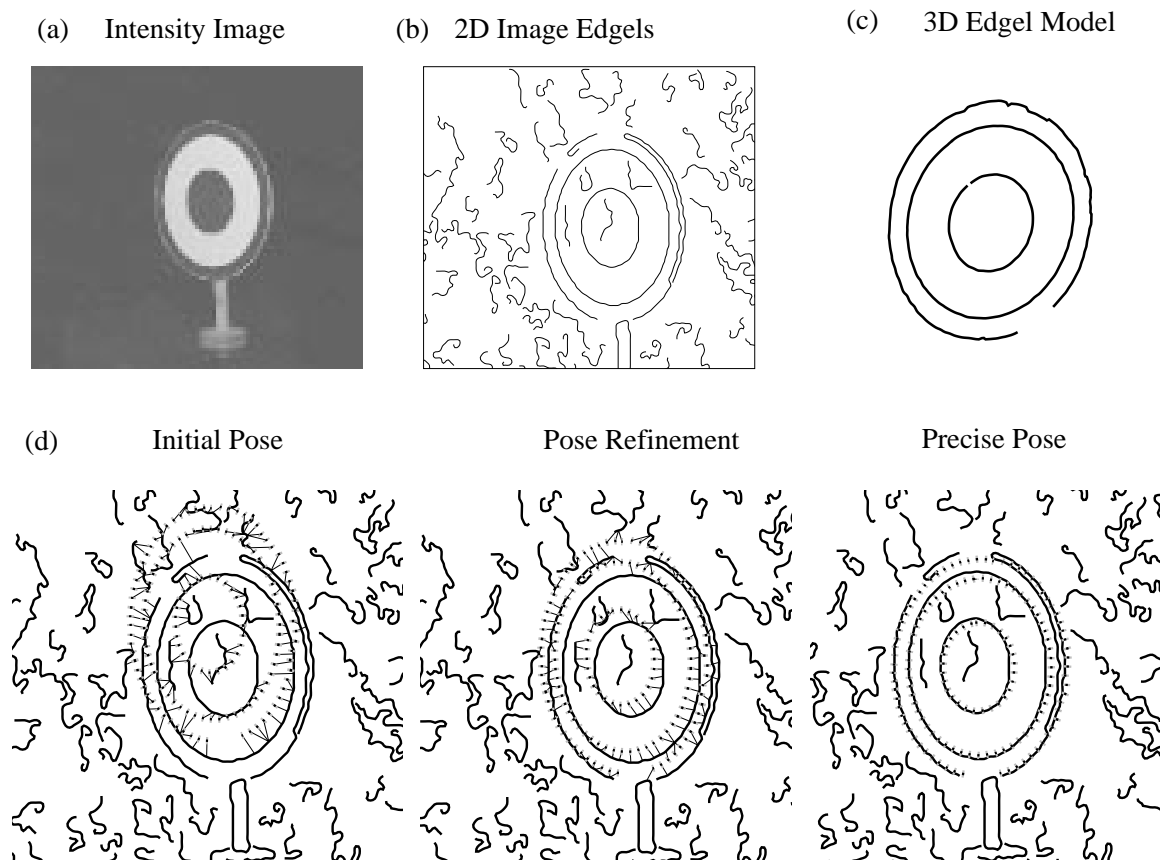


Figure 1.5: An example of 3D-2D localization for a simple bulls-eye object: (a) the input intensity image, (b) the intensity edges of the image, (c) the object model, and (d) three iterations of the localization search with lines drawn between the image to model edgel correspondences.

Chapter 2

Object Modeling for 3D-3D Localization

The goal of this thesis is to develop solutions for localizing known objects in images. The first localization problem that we will address is the 3D-3D localization problem—localizing 3D objects in 3D range-image data. This thesis also focuses on the problem of acquiring models for localization, in addition to the localization problems themselves. For 3D-3D localization, a good starting point for an object model is a 3D surface model.

In this chapter, we present a novel approach for building a 3D surface model from many range images of an object. The goal of this work is to use real images of an object to automatically create a model which is:

- Geometrically accurate: depicts the correct dimensions of the object and captures small details of the object geometry
- Clean: eliminates noise and errors in the views
- Complete: models the surface as much as is observable from the sample views

Efficiency is desirable, but is not a main concern, since model creation will be done off-line. The following section overviews the specific problems we face and our general approach for solving these problems.

2.1 Approach

The problem we are tackling in this chapter is to build a 3D model from a number of range images of an object. In other words, we will take N range images of an object from various views and use them to compute a unified surface representation of the object. We can simply stick all of the image data together; this sounds easy enough. Well, this is almost correct, but to do so, we must address several serious problems.

With a little bit of wishful thinking, let us assume that we can obtain 3D surfaces from various views and that we are able to align these views into a single object coordinate system. The first problem is how to combine the surfaces from all views into a single

surface representation—a data-merging problem. It is a problem of topology: how are all these surfaces connected?

Our solution makes use of a volumetric representation to avoid difficulties associated with topology. We will show how the volumetric representation simplifies our data-merging problem—virtually eliminating the topology issue. The volumetric representation can be conveniently converted into a triangulated mesh representation with little loss of geometric accuracy. The merging problem is then a matter of converting our input surface data to the volumetric representation.

Conversion from surfaces to the volumetric representation is simple if we are given perfect input surface data devoid of noise or extraneous data (image data which is nearby the object but not belonging to the object). The conversion problem is exacerbated by the fact that input surface data from real sensors (e.g., range sensors or stereo) is noisy and, in fact, will contain surfaces that are not part of the object we are interested in modeling. Our method for merging the surfaces into a volumetric representation takes full consideration of these facts to best take advantage of the multiple observations to smooth out the noise and eliminate undesired surfaces from the final model.

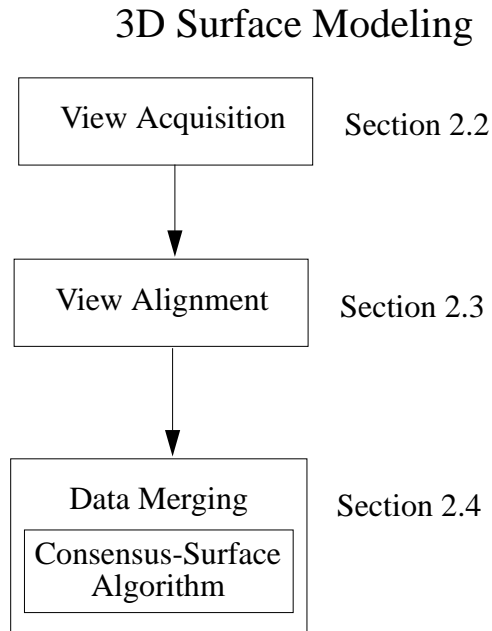
Unfortunately, the volumetric representation is not the answer to all that plagues us. We must now step back and determine how to get the image data aligned in the first place. Several strategies are possible, involving varying degrees of human interaction. Our approach is to make alignment fully automatic by taking the images using a calibrated robotic positioner.

Finally, we must consider the input from our sensor. Unfortunately, current sensors provide us with point samples of the surface—not the surface itself. Range-image sensors do not provide us with information on how the points in the image are connected. So even from a single view, we cannot guarantee that we know the topology of the viewed surface. This is a depressing state of affairs. Fortunately, we can make a good guess to get started. Also, we are fortunate that our data merging algorithm is designed to robustly handle errors such as the mistakes that we might make when converting our range data to surface data.

Another important issue which we do not address in this thesis is how to select views in order to best cover the surface. The sensor planning problem is very difficult and is the subject of ongoing research [128]. In this work, we do not try to optimize the number of views (i.e., taking the smallest number of views that cover the surface). Rather, we take a large set of views with the hope that they cover the surface. The human operator in fact determines the number of views and the object orientation for each view.

To summarize, to build a 3D surface model from multiple range images, we face the following problems:

- Input data: Surfaces are desired but the sensor provides points.
- View alignment: To merge the data, it must be in the same coordinate system.
- Data merging: We need to merge all the image data while eliminating or greatly reducing the effects of noise and extraneous data.



The rest of this chapter provides the details of our solutions to these problems which combine to form a practical method for building 3D surface models from range images of an object. Figure 2.1 shows a diagram of the technical sections of the thesis. We begin by discussing acquisition and alignment of surface views and then follow with a discussion of our surface merging algorithm, the consensus-surface algorithm, which is the main contribution of this chapter.

2.2 Surface Acquisition

Our first problem is that 3D sensors such as range finders produce images of 3D points; however, for many purposes including ours, it is necessary to sense surfaces. Unfortunately, such a sensor is not currently available. The missing information is whether the scene surface is well approximated by connecting two neighboring surface samples. With a little work, however, we can transform the 3D points from the range image into a set of triangular surfaces.

We can begin by joining pairs of neighboring range-image points based on our belief that the two points are connected by a locally smooth surface. When joining two points, there is very little basis for our decision. The limitations of the sensor prevents us from knowing the answer. However, we can make this decision based on our experience—understanding that

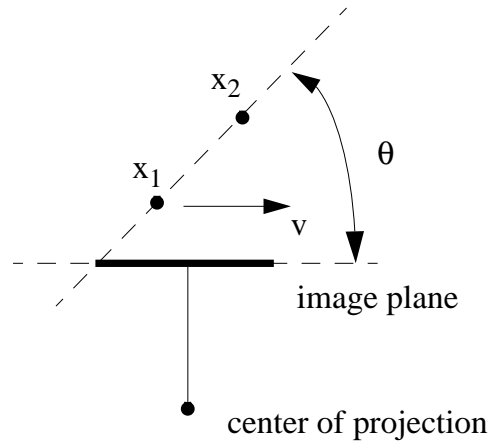


Figure 2.2: The orientation, θ , of the line connecting two 3D surface points x_1 and x_2 with respect to the image plane of the camera is used to determine whether the two points are connected.

we will often make mistakes. Our experience tells us that if two (pixel-wise) neighboring range-image points have similar 3D coordinates, then they are likely to be connected by a locally smooth surface; if 3D coordinates are far apart, it is very unlikely that they are connected. This is using accomplished by using a threshold to determine whether the two points are close enough in three dimensions according to our experience. We adopt a thresholding scheme used by [64]. Two range data points, x_1 and x_2 are labeled as connected if

$$\frac{(x_2 - x_1)}{\|x_2 - x_1\|} \cdot \hat{v} = \cos \theta \geq \cos \theta_0$$

where \hat{v} is the unit direction vector of the difference in image (pixel) coordinates¹ of the two points, θ is surface angle of the two connected points with respect to the camera, and θ_0 is the largest acceptable angle (typically 80 degrees or so). Figure 2.2 geometrically depicts the test performed here. This threshold scheme has the benefit that it does not depend on a specific scale of data or on specific camera parameters (e.g., aspect ratio). After all pairs of neighboring points are examined, we can create surface triangles by accumulating all triples of mutually connected points.

This, like most thresholds, is an *ad hoc* assumption and will often result in mistakes: surfaces will be created where there should be none, and some existing surfaces will be missed. Figure 2.3 which shows an example of such mistakes. These errors are not significantly different from other errors that our model building algorithm must confront. As will be shown in Section 2.5, our model building algorithm compensates for errors such

¹The direction vectors of pixel differences in the image plane can be converted to world coordinates using the camera parameters, which are acquired via calibration as described in Chapter 1.

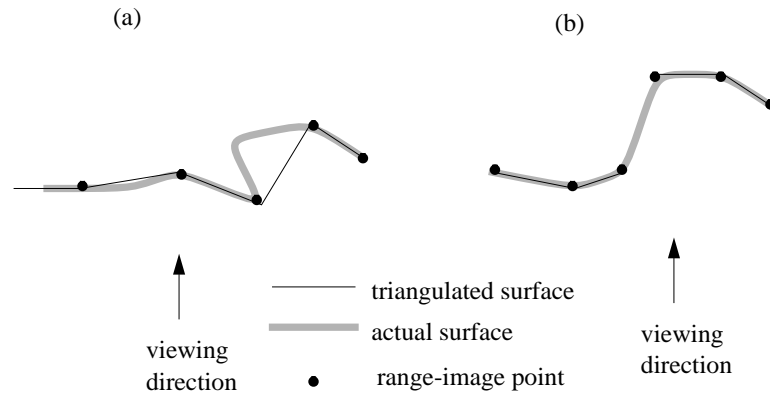


Figure 2.3: Examples of triangulation errors shown via 2D slices: (a) an incorrectly instantiated surface between two points and (b) a surface that is missed.

as these to produce correct surface models after merging.

2.3 View Alignment

After taking several range images of an object and converting them to surfaces, we need to eventually merge all these surfaces into a single model. The problem is that each view and, hence, the surface data is taken from a different coordinate system with respect to the object. In order to compare or match the data from different views, we have to be able to transform all the data into the same coordinate system with respect to the object.²

To do this implies that we need to determine the rigid body transformation (motion) between each view and some fixed object coordinate system. This rigid body motion comprises rotation and translation in 3D space—six degrees of freedom, three in translation and three in rotation. We can denote a rigid body motion by a linear transform

$$\mathbf{x}_1 = \mathbf{R}\mathbf{x}_0$$

where \mathbf{R} is a 4×4 homogeneous matrix³ denoting the rigid transform and the points \mathbf{x}_0 and \mathbf{x}_1 are in homogeneous coordinates. For clarity, let us denote \mathbf{R} by $\mathbf{R}_{1 \leftarrow 0}$ which indicates

²It is conceivable that we could merge all the data from different views without computing rigid motion but by determining correspondences among all the data between views [54]. If correct correspondences can be made, view alignment is certainly achievable [135, 106].

³We will sometimes find it useful to denote a rotation and translation using either homogeneous transformations (i.e., $\mathbf{R}\mathbf{x}$ where \mathbf{R} is a 4×4 matrix and \mathbf{x} is understood to be extended to 4 dimensions by appending a 1 to the 3D vector) or rotation followed by translation (i.e., $\mathbf{R}\mathbf{x} + \mathbf{t}$ where \mathbf{t} is a translation vector and \mathbf{R} is a 3×3 rotation matrix). Both are mathematically equivalent, however, the homogeneous form is used when we desire to be concise in our notation.

that the motion takes a point in coordinate system 0 and transforms it to coordinate system 1.

If we are given N views, we can start by making one of the views the *central* view. For convenience, the central view is chosen to be view 0. The goal is to compute the rigid motion $\mathbf{R}_{0 \leftarrow i}$ for all views $i \neq 0$. Once that is accomplished, the data in all views can be transformed to a single coordinate system (e.g., view 0), and we can then consider the problem of merging the data into a unified object model.

Notice the problem does not change if the camera is moving relative to the object or vice versa.⁴ Determining the motion between two views can be a difficult task and is the subject of a large body of previous and ongoing research [82, 135, 130, 124, 106]. There are several ways we can approach this alignment problem—each requiring varying levels of human interaction. We break these into three levels—manual alignment, semi-automatic alignment, and automatic alignment—which are briefly discussed in what follows.

2.3.1 Manual Alignment

The first option, and perhaps the least attractive, is manual alignment of the views. The user could choose a particular view as the object's coordinate system and manipulate each view separately using a graphical interface to align the data of each view to the data of the central view. This is tedious and is made difficult by the limits of visualizing 3D objects with 2D displays. For example, two points may be aligned as viewed from one direction, but when viewed from another direction, the two points may lie at different distances along the original line of sight.

A less painful and more precise option is the use of registration marks on the object. The registration marks are easily identified points on the object that can be seen in multiple views. These points may be painted (e.g., distinguishable white or black dots) onto the object for this purpose.

Another option is for the user to select them via a point-and-click interface. Care must be taken to ensure that the selected points are really the same point in different views.

Regardless of how marks are selected/detected, the user must manually denote the correspondence between marks in each view. Once this is accomplished, the motions between all views and the central view can be computed. For 3D data, three corresponding points between two views are sufficient to estimate the motion between the views. However, if there are any errors or noise in the 3D coordinates of any of these marks then the motion estimate will also be noisy. The accuracy of the motion estimate can be improved by using a larger number of points. The problem of rigid motion estimation, or pose estimation, from corresponding points in three dimensions is discussed further in Section 3.4.

Note that either of these methods will be painful and time consuming for the person doing the modeling; however, depending on the situation, it may be the only option.

⁴This is not completely true. The case where the camera is moving creates the problem that the object and background have the same motion which means manual editing will be necessary to separate the object from the background.

2.3.2 Semi-Automatic Alignment

With current motion estimation techniques [6, 135, 106], we may be able to automatically compute the motion between each pair of views. This may be possible if the images are taken in a single sequence with small motions between each view. What we would have is a list of transforms between neighboring views

$$\mathbf{R}_{0\leftarrow 1}, \mathbf{R}_{1\leftarrow 2}, \dots, \mathbf{R}_{N-2\leftarrow N-1}.$$

From this it is possible to compute the transform from each view to view 0 by composing transforms, for example,

$$\mathbf{R}_{0\leftarrow 2} = \mathbf{R}_{0\leftarrow 1}\mathbf{R}_{1\leftarrow 2}.$$

While this sounds easy enough, it suffers from a fatal flaw. The flaw is that each estimated transform will have some error associated with it, and that as we compose erroneous transforms, the error accumulates. What one will find is that $\mathbf{R}_{0\leftarrow N-1}$ will be too inaccurate for practical purposes for even moderate values of N .

The solution is to revert to manual alignment to finish the job by manually adjusting and improving the motion estimates to align the views and eliminate the accumulated errors. This is much easier than the previous fully manual alignment since the estimated transforms will actually be reasonably close and will only require small corrections.

2.3.3 Automatic Alignment

Finally, we can think about ways to achieve alignment without manual intervention. There are basically two ways that may allow us to achieve automatic view alignment: automatic motion estimation and controlled motion with calibration.

Fully automatic motion estimation [6, 135, 106] that is accurate enough for 3D modeling is still on the horizon. Currently, there are solutions to this problem which are becoming mature [135, 130, 124, 106] but are still not quite reliable enough for practical application which means some manual intervention may be required. The problem of error accumulation will still be an issue; however, recent work by Shum, Ikeuchi, and Reddy [127] using a technique called principal components analysis with missing data shows promise to solve this problem in the near future.

Because of the current state of the art, we use the second approach, controlled motion with calibration—the most practical option for an automatic solution. There are some arguments against such an approach:

1. Calibration is difficult.
2. Robots, turntables, and other positioning mechanisms are expensive.
3. Requiring controlled motion limits the applicability.

While arguments (2) and (3) are quite valid, argument (1) is not. Calibration is a mature area in photogrammetry and computer vision and many excellent algorithms exist [136, 121]. The process of acquiring calibration points can be made less tedious with the use of special calibration objects (specially painted boxes or boards) and simple techniques for detecting these points in the calibration images.

In our experimental setup, we calibrate two axes of a Unimation Puma robot with respect to a range-sensor coordinate frame. We can then mount the object on the robot's end effector and acquire images of an object at arbitrary orientations. The details of the camera and robot calibration process are described in Appendix A.

From this point we assume that the views are aligned. Next, we consider the problem of merging all the data from these views into a single model of the object's surface.

2.4 Data Merging

We are now faced with the task of taking many triangulated surfaces in 3D space and converting them to a triangle patch surface model. In this section, we assume that the various triangle sets are already aligned in the desired coordinate system.

As discussed in Section 2.1, even if we are given perfect sets of triangulated surfaces from each view which are more or less perfectly aligned, the merging problem is difficult. The problem is that it is difficult to determine how to connect triangles from different surfaces without knowing the surface beforehand. There are innumerable ways to connect two surfaces together, some acceptable and some not acceptable. This problem is exacerbated by noise in the data and errors in the alignment. Not only does the determination of connectedness become more difficult, but now the algorithm must also consider how to eliminate the noise and small alignment errors from the resulting model. Recently, however, several researchers have moved from trying to connect together surface patches from different views to using volumetric methods which hide the topological problems—making the surface-merging problem more tractable. In the next section we discuss the volumetric method which we use to solve the surface-merging problem.

2.4.1 Volumetric Modeling and Marching Cubes

When mentioning volumetric modeling, the first thought in most people's minds is the occupancy-grid representation. Occupancy grids are the earliest volumetric representation [95, 22] and, not coincidentally, the conceptually simplest. An occupancy grid is formed by discretizing a volume into many *voxels*⁵ and noting which voxels intersect the object. The result is usually a coarse model that appears to be created by sticking sugar cubes together to form the object shape. Of course, if we use small enough cubes, the shape will look fine, but this becomes a problem since the amount of memory required will be $O(n^3)$ where the volume is discretized into n slices along each dimension.

⁵*Voxel* is a common term for an individual element, rectangular box or cube, of the discretized volume. It is short for *volume element*.

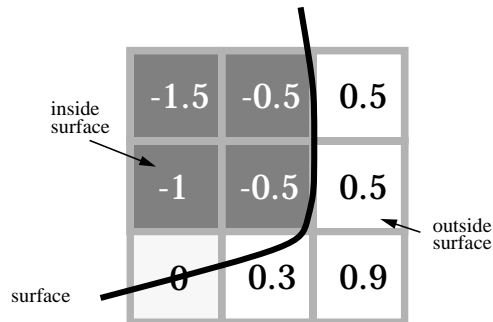


Figure 2.4: An example of zero-crossing interpolation from the grid sampling of an implicit surface.

Recently, however, an algorithm developed by Lorensen and Cline [83] for graphics modeling applications has made volumetric modeling a bit more useful by virtually eliminating the blocky nature of occupancy grids. This algorithm is called the marching-cubes algorithm [83]. The representation is slightly more complicated than the occupancy grid representation. Instead of storing a binary value in each voxel to indicate if the cube is empty or filled, the marching-cubes algorithm requires the data in the volume grid to be samples of an implicit surface. In each voxel, we store the value, $f(\mathbf{x})$, of the signed distance from the center point of the voxel, \mathbf{x} , to the closest point on the object’s surface. The sign indicates whether the point is outside, $f(\mathbf{x}) > 0$, or inside, $f(\mathbf{x}) < 0$, the object’s surface, while $f(\mathbf{x}) = 0$ indicates that \mathbf{x} lies on the surface of the object.

The marching-cubes algorithm constructs a surface mesh by “marching” around the cubes while following the zero crossings of the implicit surface $f(\mathbf{x}) = 0$. The signed distance allows the marching-cubes algorithm to interpolate the location of the surface with higher accuracy than the resolution of the volume grid. Figure 2.4 shows an example of the interpolation.

The marching-cubes algorithm and the volumetric implicit-surface representation provide an attractive alternative to other conceivable mesh-merging schemes (see Chapter 6 for more discussion on related 3D-modeling research). First, they eliminate the global topology problem—how are the various surfaces connected—for merging views. The representation can model objects of arbitrary topology as long as the grid sampling is fine enough to capture the topology. Most importantly, the whole problem of creating the volumetric representation can be reduced to a single, simple question:

What is the signed distance between a given point and the surface?

The given point is typically the center of a given voxel, but we don’t really care. If we can answer the question for an arbitrary point, then we can use that same question at each voxel in the volume.

Now we may focus on two more easily defined problems:

1. How do we compute $f(\mathbf{x})$?
2. How can we achieve desired resolutions and model accuracy knowing that the volumetric representation requires $O(n^3)$ storage and computation?

The real problem underlying our simple question is that we do not have a surface; we have many surfaces, and some elements of those surfaces do not belong to the object of interest but rather are artifacts of the image acquisition process or background surfaces. In the next subsection we present an algorithm that answers the question and does so reliably in spite of the existence of noisy and extraneous surfaces in our data.

2.4.2 Consensus-Surface Algorithm

In this section, we will answer the question of how to compute the signed distance function $f(\mathbf{x})$ for arbitrary points \mathbf{x} when given N triangulated surface patches from various views of the object surface. We call our algorithm the *consensus-surface algorithm*.

As described above, the positive value of $f(\mathbf{x})$ indicates the point \mathbf{x} is outside the object surface, a negative value indicates that \mathbf{x} is inside, and a value of zero indicates that \mathbf{x} lies on the surface of the object. We can break down the computation of $f(\mathbf{x})$ into two steps:

- Compute the magnitude: compute the distance, $|f(\mathbf{x})|$, to the nearest object surface from \mathbf{x}
- Compute the sign: determine whether the point is inside or outside of the object

We are given N triangle sets—one set for each range image of our object as described in Section 2.2—which are aligned in the same coordinate system. The triangle sets are denoted by T_i , where $i = 0, \dots, N - 1$. The union of all triangle sets is denoted by $T = \bigcup_i T_i$. Each triangle set, T_i , consists of some number n_i of triangles which are denoted by $\tau_{i,j}$, where $j = 0, \dots, n_i - 1$.

If the input data were perfect (i.e., free of any noise or alignment errors in the triangle sets from each view), then we could apply the following *naive algorithm*, Algorithm *ClosestSignedDistance*, to compute $f(\mathbf{x})$:

Algorithm *ClosestSignedDistance*

Input: point \mathbf{x}

Input: triangle set T

Output: the signed distance d

(* Naive algorithm for computing $f(\mathbf{x})$ by searching *)

(* for the closest surface from all triangles in T *)

1. $\langle \mathbf{p}, \hat{\mathbf{n}} \rangle \leftarrow \text{ClosestSurface}(\mathbf{x}, T)$
2. $d \leftarrow \| \mathbf{x} - \mathbf{p} \|$
3. **if** $(\hat{\mathbf{n}} \cdot (\mathbf{x} - \mathbf{p}) < 0)$

4. **then** $d \leftarrow -d$
5. **return** d

where Algorithm *ClosestSurface* returns the point, \mathbf{p} , and its normal, $\hat{\mathbf{n}}$, such that \mathbf{p} is the closest point to \mathbf{x} from all points on triangles in the triangle set T .

Algorithm *ClosestSurface*

Input: point \mathbf{x}

Input: triangle set T

Output: the point and normal vector pair $\langle \mathbf{p}, \hat{\mathbf{n}} \rangle$

(* Return the closest point to \mathbf{x} from all *)

(* points on triangles in the set T , and the normal *)

(* of the closest triangle. *)

1. $\tau \leftarrow \arg \min_{\tau \in T} \min_{\mathbf{p} \in \tau} \|\mathbf{x} - \mathbf{p}\|$
2. $\mathbf{p} \leftarrow \arg \min_{\mathbf{p} \in \tau} \|\mathbf{x} - \mathbf{p}\|$
3. $\hat{\mathbf{n}} \leftarrow$ outward pointing normal of triangle τ
4. **return** $\langle \mathbf{p}, \hat{\mathbf{n}} \rangle$

The naive algorithm for $f(\mathbf{x})$ finds the nearest triangle from all views and uses the distance to that triangle as the magnitude of $f(\mathbf{x})$. The normal of the triangle can be used to determine whether \mathbf{x} is inside or outside the surface. If the normal vector points towards \mathbf{x} , then \mathbf{x} must be outside the object surface. This fact can be verified by a simple proof. First, no other surface point lies within the circle of radius $|f(\mathbf{x})|$ around point \mathbf{x} . For \mathbf{x} to be inside the object, it is necessary that every line drawn between \mathbf{x} and any point outside the object will cross a surface first. If \mathbf{y} is the closest surface point to \mathbf{x} , the line from \mathbf{y} to \mathbf{x} must cross a surface if \mathbf{x} is inside the surface. The fact that no closer surface exists excludes the possibility that any such surface exists between \mathbf{x} and \mathbf{y} .

Again, the naive algorithm will work for perfect data. However, we must consider what happens when we try this idea on real data. The first artifact of real sensing and small alignment errors is that we no longer have a single surface, but several noisy samples of a surface (see Figure 2.5). We are now faced with choices on how to proceed. Clearly, choosing the nearest triangle (as in Algorithm *ClosestSignedDistance*) will give a result as noisy as the constituent surface data. For example, a single noisy bump from one view can result in a bump on the final model, as shown in Figure 2.6 (a). Inconsistent values for the implicit distances will appear when a voxel center is on or near a surface, since the samples will be randomly scattered about the real surface location. For example, we could see three surfaces form if noise or alignment error produces an inside-outside-inside-outside (+/-/+/-) transition when, in fact, only one real surface was observed (see Figure 2.6 (b)). This is especially a problem if the noise is of similar scale to the voxel size.

With many views, the computed implicit distances from the surface will be biased towards the closest side of the surface and result in inaccurate zero-crossing interpolation during surface-mesh generation. This is a very subtle problem best explained by considering noisy samples of a surface as it crosses a line between two adjacent voxel points (see Figure 2.7). We can show mathematically that the zero-crossing interpolation will generate

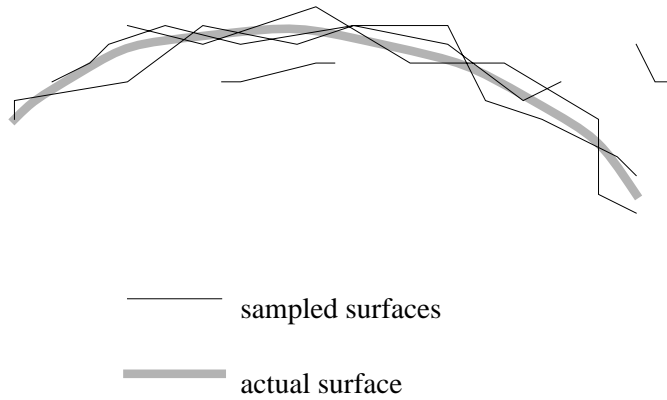


Figure 2.5: In practice, real surface samples are noisy and slightly misaligned and it is difficult to determine where the actual surface might lie.

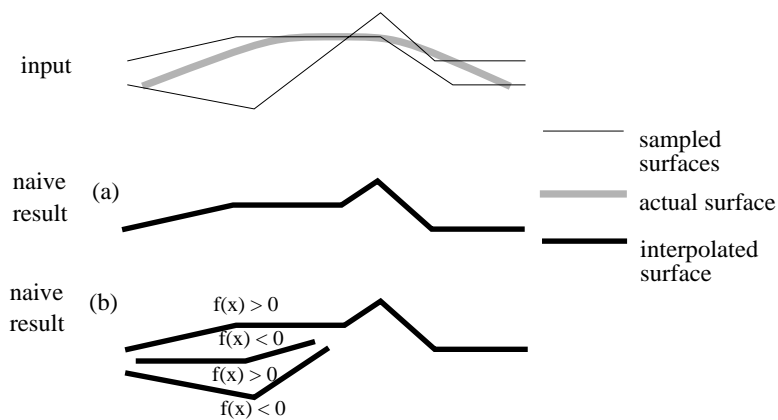


Figure 2.6: Some effects of noise and misalignment on our naive algorithm, Algorithm *ClosestSignedDistance*. In each case two observations of the same surface (actual surface is denoted by the shaded line) are shown, the resulting surface is : (a) the resulting surface is as noisy as the data, (b) three surfaces are detected when only one exists created by an inside-outside-inside-outside transition of $f(x)$.

significant errors. Suppose that we are evaluating $f(x)$ (along the line $y = z = 0$) at points $x_0 = 0$ and $x_1 = 1$, and there is a real surface in between the two points at $x \in [0, 1]$. Also, let us assume that two observations are available at $x + \epsilon$ and $x - \epsilon$. Assuming x_0 is outside the surface (i.e., $f(x_0) > 0$), the signed distances will be

$$f(x_0) = x - \epsilon \quad (2.1)$$

$$f(x_1) = -(1 - (x + \epsilon)). \quad (2.2)$$

Using these values of f , the zero crossing will be interpolated to give an estimate, \hat{x} , of x :

$$\hat{x} = \frac{x - \epsilon}{1 - 2\epsilon}$$

The error of the estimate is

$$e_x = x - \hat{x} \quad (2.3)$$

$$= x - \frac{x - \epsilon}{1 - 2\epsilon} \quad (2.4)$$

$$= \frac{\epsilon(1 - 2x)}{1 - 2\epsilon}. \quad (2.5)$$

Thus, the error, e_x , will only be zero when $x = 0.5$ (i.e., the real surface is exactly between points x_0 and x_1). The magnitude of the interpolation error will increase as the real surface approaches either of the points. This illustration points out the fragility of zero-crossing estimates based on inaccurate values of $f(x)$. If a discrete implicit surface is to be used, the estimates of $f(x)$ must be as accurate as possible and the values must be locally consistent across surfaces. In the above scenario, a simple estimate of the average of the observations when computing $f(x_0)$ and $f(x_1)$ would yield the correct zero-crossing estimate.

A more sinister problem for the naive algorithm applied to real images is the existence of noise and extraneous data. For example, it is not uncommon to see triangles sticking out of a surface or other triangles that do not belong to the object. This can occur due to sensor noise, quantization, specularities and other possibly systematic problems of range imaging. Also, we must consider the fact that other incorrect triangles may be introduced by the range image triangulation process as described in Section 2.2. This makes it very easy to infer the incorrect distance and more critically the incorrect sign, which will result in very undesirable artifacts in the final surface. For example, Figure 2.8 shows how one badly oriented triangle can create an implicit distance with the incorrect sign. This results in a hole rising out of the surface as shown.

Our solution to these problems is to estimate the surface locally by averaging the observations of the same surface. The trick is to specify a method for identifying and collecting all observations of the same surface.

Nearby observations are compared using their location and surface normal. If the location and normal are within a predefined error tolerance (determined empirically), we can consider them to be observations of the same surface. Given a point on one of the observed triangle surfaces, we can search that region of 3D space for other nearby observations from

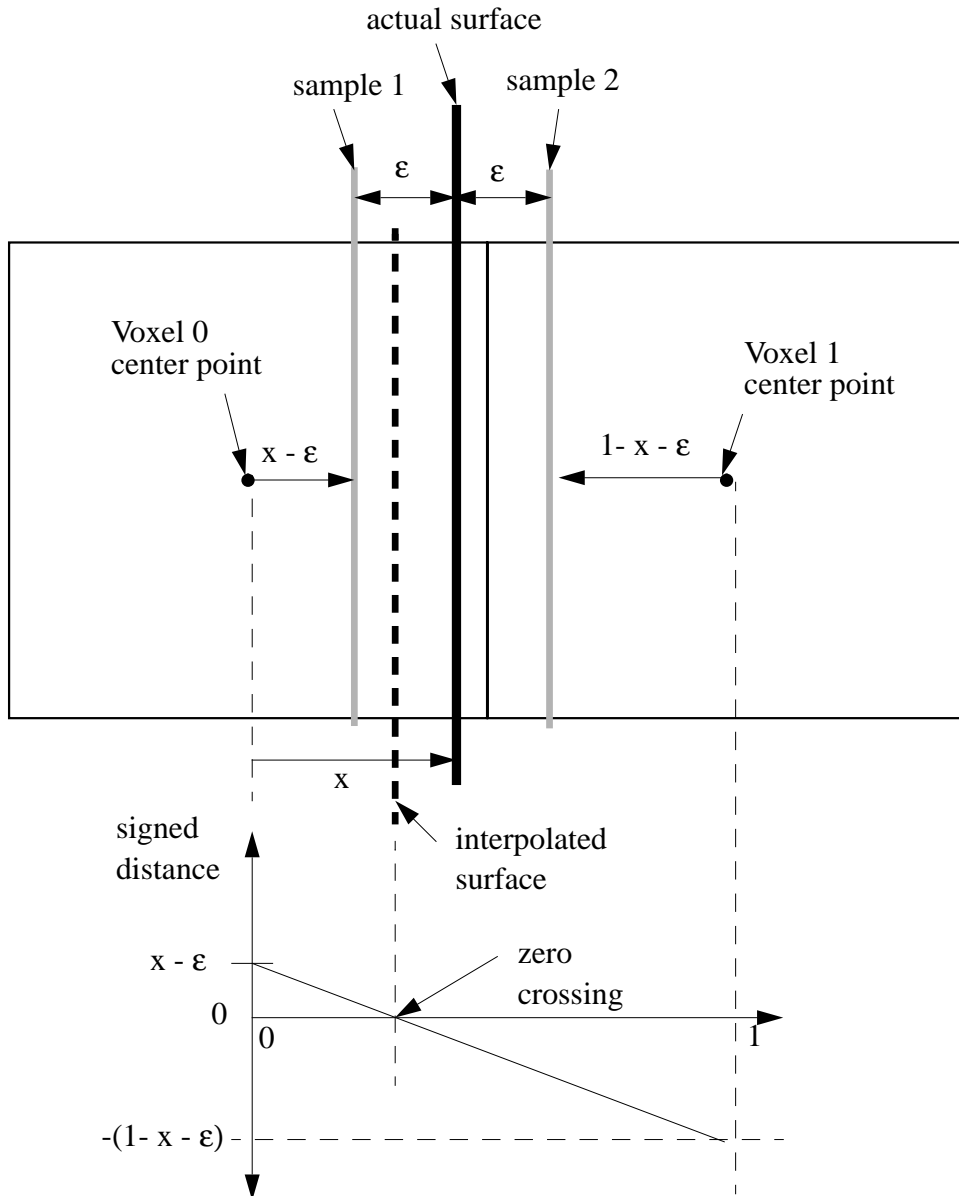


Figure 2.7: Graphical illustration of the error in zero-crossing interpolation using Algorithm *ClosestSignedDistance* with two noisy observations.

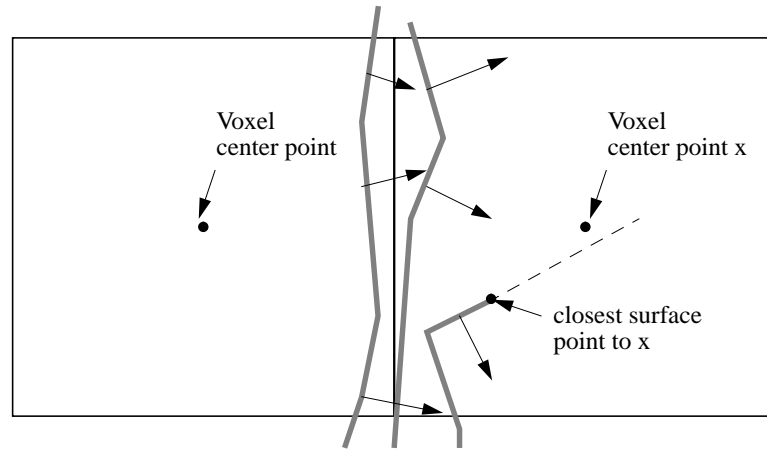


Figure 2.8: An example of inferring the incorrect sign of a voxel’s value, $f(x)$, due to a single noisy triangle. The algorithm incorrectly thinks point x is inside the surface based on the normal information from the closest point. The result will be a hole at that point in the surface since additional zero-crossings will result around the error at x .

other views which are potentially observations of the same surface. This search for nearby observations can be done efficiently using k-d trees [41] which is a structure for storing data of arbitrary dimensions for optimal nearest neighbors search. Here, a k-d tree is created for each view, and contains the 3D coordinates of all the triangle vertices in the view’s triangle surface set. Given a point in 3D space, we can quickly locate the nearest vertex in a given view by searching that view’s k-d tree much like a binary search [41].

If an insufficient number of observations are found, then the observation can be discarded as isolated/untrusted and the search can continue. Thus, we are requiring a quorum of observations before using them to build our model. The quorum of observations can then be averaged to produce a *consensus surface*. This process virtually eliminates the problems described previously (with respect to the naive algorithm).

As an improvement over using an equally weighted voting scheme, we can assign a confidence value ω to each input surface triangle. A common technique is to weight the surface points/triangles from a range image by the cosine of the angle between the viewing direction and the surface normal [72]. This is simply computed by

$$\omega = \hat{v} \cdot \hat{n}$$

where \hat{v} and \hat{n} are the viewing direction and normal, respectively, of the given triangle. The consensus can now be measured as a sum of confident measures and the quorum is over this weighted sum. The rationale is that two low-confidence observations should not have the same impact on the result as two high-confidence observations. We can now

specify the consensus-surface algorithm. Instead of searching for the closest surface using Algorithm *ClosestSurface*, we can search for the closest *consensus surface*:

Algorithm *ConsensusSignedDistance*

Input: point \mathbf{x}

Input: triangle set T

Output: the signed distance d

(* Compute the signed, implicit distance $f(\mathbf{x})$ *)

1. $\langle \mathbf{p}, \hat{\mathbf{n}} \rangle \leftarrow \text{ClosestConsensusSurface}(\mathbf{x}, T)$
2. $d \leftarrow \| \mathbf{x} - \mathbf{p} \|$
3. **if** $(\hat{\mathbf{n}} \cdot (\mathbf{x} - \mathbf{p})) < 0$
4. **then** $d \leftarrow -d$
5. **return** d

The only change from Algorithm *ClosestSignedDistance* is that Algorithm *ConsensusSignedDistance* computes the closest consensus-surface point and its normal in line 1. The algorithm for computing the closest consensus-surface point and its normal is as follows:

Algorithm *ClosestConsensusSurface*

Input: point \mathbf{x}

Input: triangle sets $T_i, i = 1..N$

Output: the point and normal vector pair $\langle \mathbf{p}, \hat{\mathbf{n}} \rangle$

1. $O_{set} \leftarrow \emptyset$
- (* O_{set} is the set of non-consensus neighbors *)
2. $C_{set} \leftarrow \emptyset$
- (* C_{set} is the set of consensus neighbors *)
3. **for** each triangulated set T_i
4. **do** $\langle \mathbf{p}, \hat{\mathbf{n}} \rangle \leftarrow \text{ClosestSurface}(\mathbf{x}, T_i)$
5. $\langle \mathbf{p}, \hat{\mathbf{n}}, \omega \rangle \leftarrow \text{ConsensusSurface}(\mathbf{p}, \hat{\mathbf{n}}, T)$
6. **if** $\omega \geq \theta_{quorum}$
7. **then** $C_{set} \leftarrow C_{set} \cup \langle \mathbf{p}, \hat{\mathbf{n}}, \omega \rangle$
8. **else** $O_{set} \leftarrow O_{set} \cup \langle \mathbf{p}, \hat{\mathbf{n}}, \omega \rangle$
9. **if** $C_{set} \neq \emptyset$
10. **then** $\langle \mathbf{p}, \hat{\mathbf{n}}, \omega \rangle \leftarrow \arg \min_{\langle \mathbf{p}, \hat{\mathbf{n}}, \omega \rangle \in C_{set}} \| \mathbf{x} - \mathbf{p} \|$
11. **else** $\langle \mathbf{p}, \hat{\mathbf{n}}, \omega \rangle \leftarrow \arg \max_{\langle \mathbf{p}, \hat{\mathbf{n}}, \omega \rangle \in O_{set}} \omega$
12. **return** $\langle \mathbf{p}, \hat{\mathbf{n}}, \omega \rangle$

Algorithm *ClosestConsensusSurface* examines the closest point in each view and searches for its consensus surface if one exists. After computing the closest consensus surfaces for each view, it chooses the closest of those from the consensus set C_{set} . C_{set} contains those locally averaged surfaces whose observations' confidence values sum to at least θ_{quorum} . Note that two consensus surfaces are not differentiated based on their confidence sum ω but rather on their proximity to \mathbf{x} . If none of the consensus surfaces exist, the algorithm selects the average surface which has the highest summed confidence out of set O_{set} .

For completeness, we outline Algorithm *ConsensusSurface* which is required by line 5 of Algorithm *ClosestConsensusSurface*. Algorithm *ConsensusSurface* basically finds all surface observations that are sufficiently similar to the given point and normal. These observations are then averaged to generate a consensus surface for the input surface. This algorithm relies on the predicate

$$\text{SameSurface}(\langle \mathbf{p}_0, \hat{\mathbf{n}}_0 \rangle, \langle \mathbf{p}_1, \hat{\mathbf{n}}_1 \rangle) = \begin{cases} \text{True} & (\| \mathbf{p}_0 - \mathbf{p}_1 \| \leq \delta_d) \wedge (\hat{\mathbf{n}}_0 \cdot \hat{\mathbf{n}}_1 \geq \cos \theta_n) \\ \text{False} & \text{otherwise} \end{cases} \quad (2.6)$$

which determines whether two surface observations are sufficiently close in terms of location and normal direction, where δ_d is the maximum allowed distance and θ_n is the maximum allowed difference in normal directions. Now we present the pseudo code for Algorithm *ConsensusSurface*:

Algorithm *ConsensusSurface*

Input: point \mathbf{x}

Input: normal $\hat{\mathbf{v}}$

Input: triangle set $T = \bigcup_i T_i$

Output: the point, normal vector, and the sum of the observations confidences $\langle \mathbf{p}, \hat{\mathbf{n}}, \omega \rangle$

1. $\mathbf{p} \leftarrow \mathbf{n} \leftarrow \omega \leftarrow 0$
2. **for** $T_i \subset T$
3. **do** $\langle \mathbf{p}', \hat{\mathbf{n}}', \omega' \rangle \leftarrow \text{ClosestSurface}(\mathbf{x}, T_i)$
4. **if** $\text{SameSurface}(\langle \mathbf{x}, \hat{\mathbf{v}} \rangle, \langle \mathbf{p}', \hat{\mathbf{n}}' \rangle)$
5. **then** $\mathbf{p} \leftarrow \mathbf{p} + \omega' \mathbf{p}'$
6. $\mathbf{n} \leftarrow \mathbf{n} + \omega' \hat{\mathbf{n}}'$
7. $\omega \leftarrow \omega + \omega'$
8. $\mathbf{p} \leftarrow \frac{1}{\omega} \mathbf{p}$
9. $\hat{\mathbf{n}} \leftarrow \frac{\mathbf{n}}{\|\mathbf{n}\|}$
10. **return** $\langle \mathbf{p}, \hat{\mathbf{n}}, \omega \rangle$

Note that in Algorithm *ConsensusSurface*, the definition of Algorithm *ClosestSurface* was slightly modified to also return the confidence ω' of the closest surface triangle.

We refer to this algorithm as a whole as the consensus-surface algorithm. The following conditions are assumed:

1. Each part of the surface is covered by a number of observations whose confidences add up to more than θ_{quorum} .
2. No set of false surfaces with a sufficient summed confidence will coincidentally be found to be similar (following the definition of Equation 2.6) or this occurrence is sufficiently unlikely.
3. Given N surface views, the real surface is closest to \mathbf{x} in at least one view.

If these assumptions are violated, mistakes in the surface mesh will result. From our experiments, a quorum requirement, θ_{quorum} , of 1.5 to 3.0 is usually sufficient given a reasonable number of views.

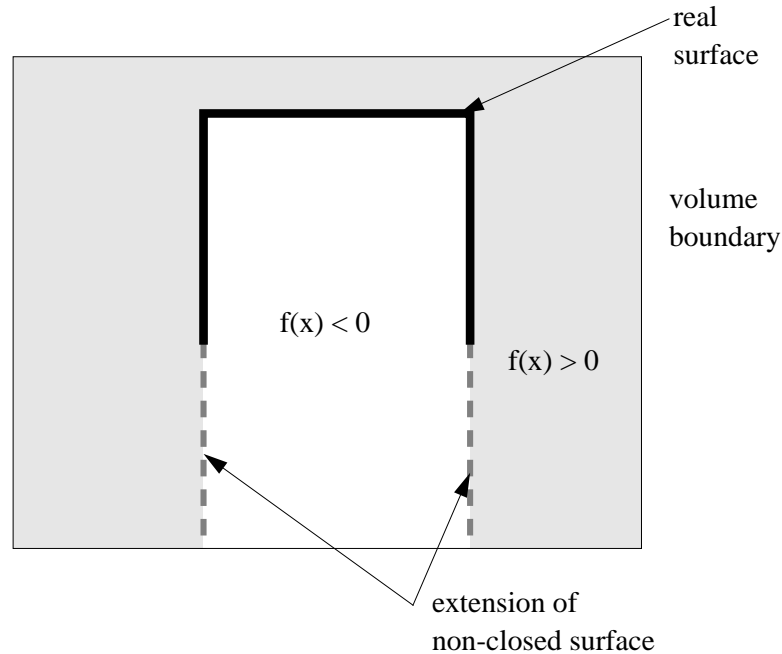


Figure 2.9: The extension of the implicit surface in unobserved regions of the grid.

2.4.3 Holes in the Marching-Cubes Algorithm

Using the standard marching-cubes algorithm [83] and consensus-surface algorithm as outlined above, there is a problem if there are holes or missing data. The marching-cubes algorithm works on the assumption that the surface is defined by zero crossings of the implicit surface function. It is almost always the case that parts of the object's surface are unobservable. For the regions of the volume where the surface is unobservable, the implicit surface we compute will be rather poorly justified and perhaps ill-defined.

For example, consider what happens when we sample the surfaces for all but the bottom of a cube. If we use the consensus-surface or naive algorithm described above, we will set the voxels directly underneath the cube to have a negative value and the rest positive. As shown in Figure 2.9, the effect is to literally extend the sides down to the bottom of the voxel grid. This is the best we can do using a local computation for $f(x)$. Essentially any non-closed boundaries of the observed surface will be extended until the side of the volume grid or another observed surface is reached.

Previous methods go to great lengths to prevent the difficulties presented by incomplete data. These workarounds involve creating special cases for dealing with regions near holes, greatly complicating implementation of the voxel filling as well as requiring a modification of the marching-cubes algorithm. For example, Curless and Levoy [28] try to detect this situation and label those voxels near holes as undefined or not on the surface. However, if

	inside surface	outside surface	Gradient
Voxels	-0.5	0.5	1.0
	-0.5	0.5	1.0
	-0.7	0.7	1.4
	-1.6	1.6	3.2

gradient > 1
cutoff

Figure 2.10: The use of gradient testing to eliminate false surfaces at zero crossings of the implicit surface, from the previous example. The gradient is labeled next to each zero crossing. Gradients greater than 1 can be ignored by the marching-cubes algorithm.

one examines the values of the distances around holes, there is one significant difference between the values around the real surface and those around holes. Around a surface, the gradient of the signed-distance function is at or near unity. However, when at a zero contour near a hole, the gradient at x , $\frac{\partial f}{\partial x}$, is necessarily larger than one since the distances from points in the neighborhood of a hole must be greater than one voxel length. This fact provides a simple mechanism for eliminating holes without complicating the signed-distance function. Figure 2.10 shows our previous example of the bottomless cube with gradient values labeled over each zero-crossing—demonstrating how non-surfaces can be easily detected by the marching-cubes algorithm. We can simply test the gradient at each voxel before adding it to the surface. The gradient must be computed to find zeros already, so it is a simple matter to modify the marching-cubes algorithm to check the magnitude of the gradient.

2.4.4 Accuracy and Efficiency

First, to achieve desired accuracy we must use a dense sampling of the volume. Since the memory requirements of a volume grid is cubic with respect to the density of the sampling for volumetric modeling, the first thing that gets sacrificed is accuracy. With our problem,

the standard volume-grid approach is also deficient in terms of computation time.

The straightforward use of volume grids presents several problems. One obvious problem with a voxel grid representation is that the number of voxels is n^3 where each axis of the volume is discretized into n elements. This affects the achievable accuracy since we must choose the dimension to be small enough that the grid can fit in memory: we quickly reach the memory limits of our computers. In addition to storage cost, we must remember that for each voxel we must compute the signed distance; thus, the number of computations of our signed distance function $f(\mathbf{x})$ will be cubic as well. Specifically, computation resources are wasted by computing signed distances in parts of the volume that are distant from the surface. For our purposes, the only voxels that we need to examine are those near the surface, a small fraction of the entire volume grid.

Curless and Levoy [28] alleviate this problem by run length encoding each 2D slice of the volume. This approach depends upon a complicated procedure which carves out voxels that are determined to be well outside of the surface. The procedure is tailored to their scheme for averaging the voxel values iteratively, view by view; it is not well suited to an algorithm such as ours which uses all the data simultaneously to compute each value. Their algorithm is discussed in more detail in Chapter 6.

Fortunately, there is a data structure, called an octree, that is perfect for our merging algorithm and requirements. Octrees [95] were developed as an efficient way for representing 3D occupancy grids for computer graphics and CAD modeling. An octree is a hierarchical representation of the volume in which we divide a given volume into eight octants and then we can subdivide each octant individually if necessary and so on to any level of subdivision desired.

For our purposes, we are only interested in the surface of our object, which octrees can efficiently represent. Octrees are designed just for this purpose: the sampling resolution can be adjusted to the level of detail necessary at each region of the volume. It is efficient in that respect—sampling finely near the surface and sampling coarsely away from the surface. Figure 2.11 shows a 2D slice of an octree representation of a simple surface.

The octree representation [95, 22] solves both the accuracy and the efficiency problems while keeping the algorithm implementation simple. Instead of iterating over all elements of the voxel grid, we can apply a recursive algorithm on an octree that samples more finely in octants only when necessary. To interpolate the zero crossings properly, we will need the implicit distance for the voxel containing the surface (the zero crossing) and all voxels neighboring this voxel: these voxels must all be represented at the finest level of precision. This constraint means that if we have a surface at one corner of an octant, the longest possible distance to the center of a neighboring octant is one and one-half diagonals of the voxel cube, which is a distance of $\frac{3\sqrt{3}}{2}$ cube units.

Given the current octant, we can compute the signed distance. If the magnitude of the signed distance, $|f(\mathbf{x})|$, is larger than $\frac{3\sqrt{3}}{2}$ of the octant width, then it is not possible for the surface to lie in the current or neighboring octant. If the surface is not in the current or neighboring octant, we do not care to further subdivide the current octant. The algorithm is as follows:

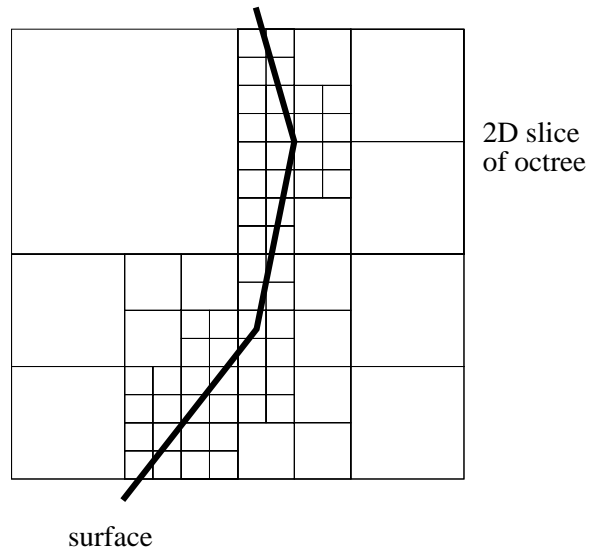


Figure 2.11: A 2D slice of an octree representation of a simple surface illustrates the adaptive resolution which is high around the surface and low elsewhere.

Algorithm *FillOctant*

Input: octant $\langle v, \mathbf{x}, w, c \rangle$ with value v , center \mathbf{x} , width w , and children c

(* Fill the value and recursively subdivide the octant *)

(* to the finest required resolution. *)

1. $v \leftarrow \text{ConsensusSignedDistance}(\mathbf{x}, T)$
2. **if** $(|v| < \frac{3\sqrt{3}}{2}w) \wedge (w > w_{\text{finest}})$
3. **then** create sub-octants $\langle v_i, \mathbf{x}_i, \frac{w}{2}, c_i \rangle$ for $i = 0, \dots, 7$ by subdividing the current octant
4. **for** $i \leftarrow 0$ **to** 7
5. $\text{FillOctant}(\langle v_i, \mathbf{x}_i, \frac{w}{2}, c_i \rangle)$
6. **else** $c \leftarrow \emptyset$

The octree in practice reduces the $O(n^3)$ storage and computation requirement to $O(n^2)$. This is because the surfaces of 3D objects are, in general, 2D manifolds in a 3D space.⁶

Thus, the octree allows us to efficiently compute the implicit surface representation and uses memory efficiently—allowing us to achieve desirable levels of accuracy. The marching-cubes algorithm must be converted to manipulate octrees rather than voxels. This is handled by simply replacing the indexing of volume elements with macros that traverse the octree.

⁶Unless it behaves as a volume-filling surface or a porcupine—surfaces that seem to fill occupy 3D space—the surface of a 3D object will tend to sparsely occupy the 3D volume enclosing it.

2.4.5 Cost of the Consensus-Surface Algorithm

We can get rough estimate of the cost of our model-building algorithm by first considering the cost of the basic operation: computing a consensus surface. To simplify analysis, we assume that there are N views being merged and that for each view the triangle set T_i has n triangles.

Algorithm *ConsensusSurface* computes the closest surface for each view which on average will be an $O(N \log n)$ operation assuming k-d trees [41] are used. Algorithm *ClosestConsensusSurface* computes the closest surface and then the respective consensus surface for each view, which adds up to a cost of $O(N^2 \log n)$. Since N will usually be much smaller than n , this operation is relatively cheap. Algorithm *ClosestConsensusSurface* is performed for each voxel or octree element.

Assuming that an $M \times M \times M$ voxel grid is used, the modeling algorithm will cost $O(M^3 N^2 \log n)$. However, if octrees are used we may loosely assume that the number of voxels or octree elements which are evaluated will be proportional to the surface area of the object. For sake of approximation, we may assume that the area is $O(M^2)$ where M is the number of elements in the equivalent voxel grid. This reduces the complexity of our modeling algorithm to $O(M^2 N^2 \log n)$ which is a significant reduction since M will be relatively large in practice to enable accurate modeling.

2.5 3D Object Modeling Results

Here we present some experimental results of our implementation of the 3D object modeling algorithm described in this chapter.

The major limitation of our modeling system is the requirement for calibrated object positioning. Our calibrated image acquisition system—a Unimation Puma robot, and our range sensor, an Ogis light-stripe range finder—limits the objects which we are able to model. Due to this, the objects must be small enough to be imaged by the range finder and to be mountable on the Puma. As described in Chapter 1, we assume that the objects are rigid and opaque (lucent surfaces are not usually detectable by the range finder). However, despite these limitations there remains a large class of objects which we can use to test our model-building algorithm.

Since the object must be physically attached to the Puma, we are further limited by the surface area of the object which we can effectively observe. For this work, we do not attempt to model the undersides of the objects. A process of reattaching the object and aligning the new views would be required. Though it is feasible, reattaching the object to model its underside was not fundamental for testing our ideas.

For our experiments, we selected 5 objects to model using our system: a toy boxcar, a rubber duck, a piece of fruit, a ceramic mug, and a toy car. For each object, we manually determined the number of range images of the object to 1) maximally cover the viewable surface of the object, and 2) provide a sufficient amount of overlap between views for the

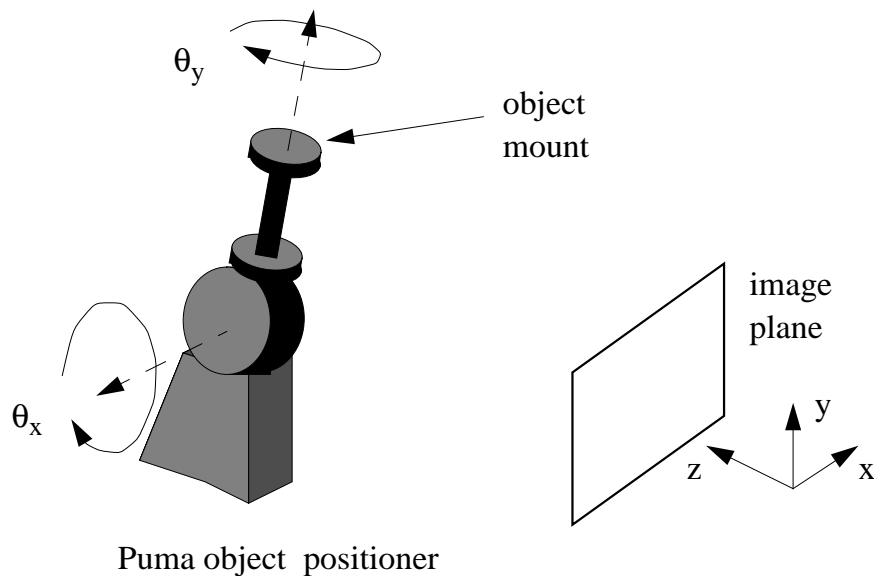


Figure 2.12: The two degrees of freedom, θ_x and θ_y of the Puma used to vary of object position with respect to the camera's coordinate system.

consensus-surface algorithm. The number of views required is related to the geometric complexity of the object: varying from 18 for the boxcar to 54 for the toy car.

The views were acquired by varying the angles of two rotation axes on the Puma's end effector: rotating around the camera's y-axis direction and rotating around the camera's x-axis direction. The Puma robot is capable of 6 degrees of freedom but for this work using only two was sufficient to detect the visible surfaces of our objects. We refer to these rotations as θ_y and θ_x respectively. Figure 2.12 shows a diagram of the rotational degrees of freedom used in our experiments. Generally, we would vary θ_y from -180 degrees to 160 in increments of 20 degrees and would vary θ_x from anywhere from -30 degrees to +30 degrees in 20 degree increments as well. For objects like the mug, we would have to add some views to observe difficult to view surfaces such as the bottom of the inside of the mug.

Each range image contained 256×240 pixels with each pixel containing a 3D coordinate. The resolution of data is approximately 1 mm (i.e., the distance between two pixels on a flat surface at the nominal distance from the camera is roughly 1 mm). The accuracy of data is on the order of roughly 0.5 mm.

The results of our modeling algorithm for each object are shown in Figures 2.13- 2.22. Each of these figures show:

- an intensity image of the object

- a close-up of some of the triangulated range images used as input to the consensus-surface algorithm (shaded to better indicate the roughness of the original data)
- a slice of the volume grid where the grey-scale indicates the proximity to a surface point (black closest, white furthest)
- three views of the resulting triangulated model

The relevant statistics of the modeling experiments for each object are presented in Table 2.1. These statistics include the number of input images and triangles, the number of triangles in the resulting model, the resolution of the voxel/octree grid, the percentage of voxels in the volume grid which were actually represented in the octree structure, the execution time on an SGI Indy 5 (a 124 MIPS/49.0 MFLOPS machine), and the parameters for our consensus-surface algorithm (the quorum requirement θ_{quorum} , the maximum distance, δ_d , between similar points and the maximum angle, θ_n between normal vectors of similar points). The volume grid was divided into at most 128 cubes along each dimension. Of the parameters used by the modeling algorithm, the quorum requirement parameter is the most difficult to determine. Proper choice of the quorum parameter depends on the number of views, the geometry of the object (i.e., how many views in which a given patch of the surface is visible), and the noise in the data. Setting this parameter automatically would be a difficult problem. It is very similar to the view-selection problem: how to choose an appropriate set of views to cover an object when the geometry is unknown.

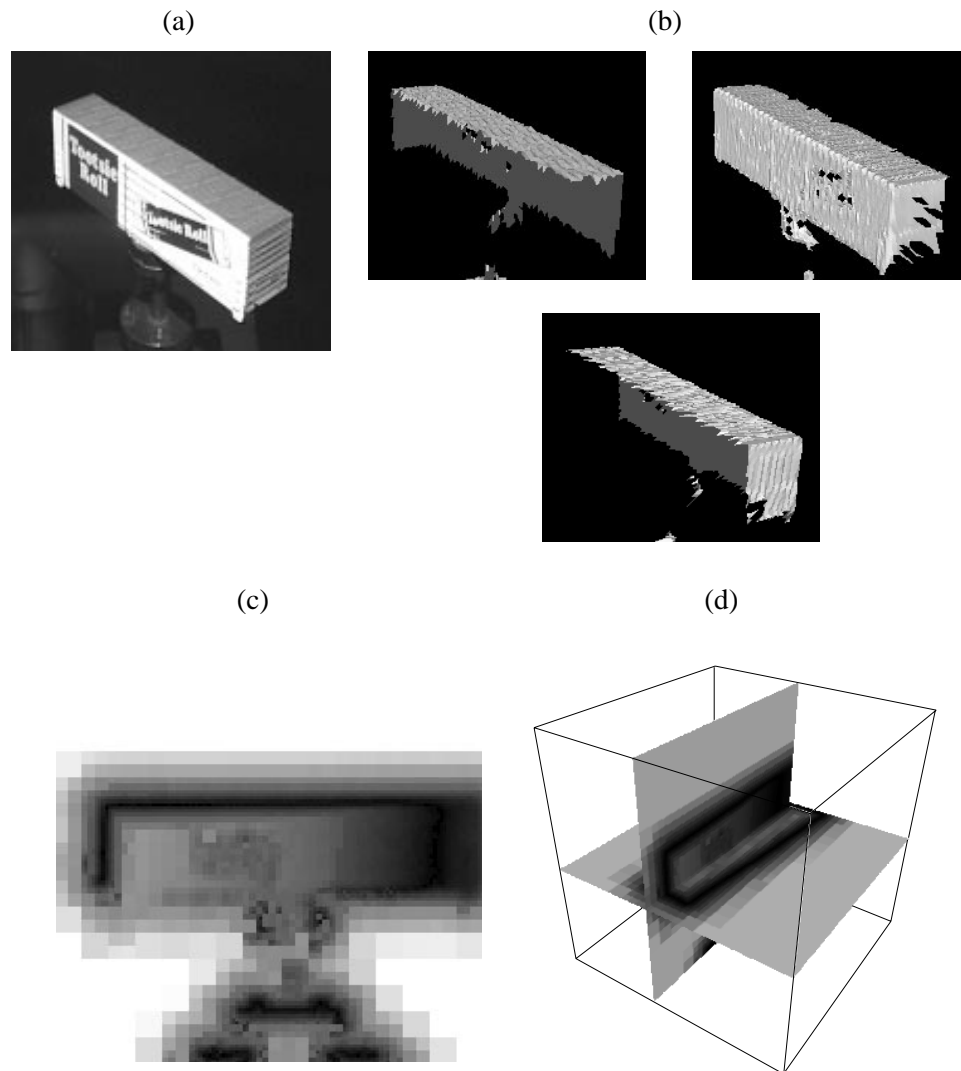


Figure 2.13: Results from modeling the boxcar. (a) An intensity image of the boxcar, (b) a close-up of some of the triangulated range images used as input to the consensus-surface algorithm, (c) a slice of the implicit-surface octree volume where the grey-scale indicates the proximity to a surface point (black closest, white furthest), and (d) a 3D view of two cross sections of the implicit-surface octree volume.

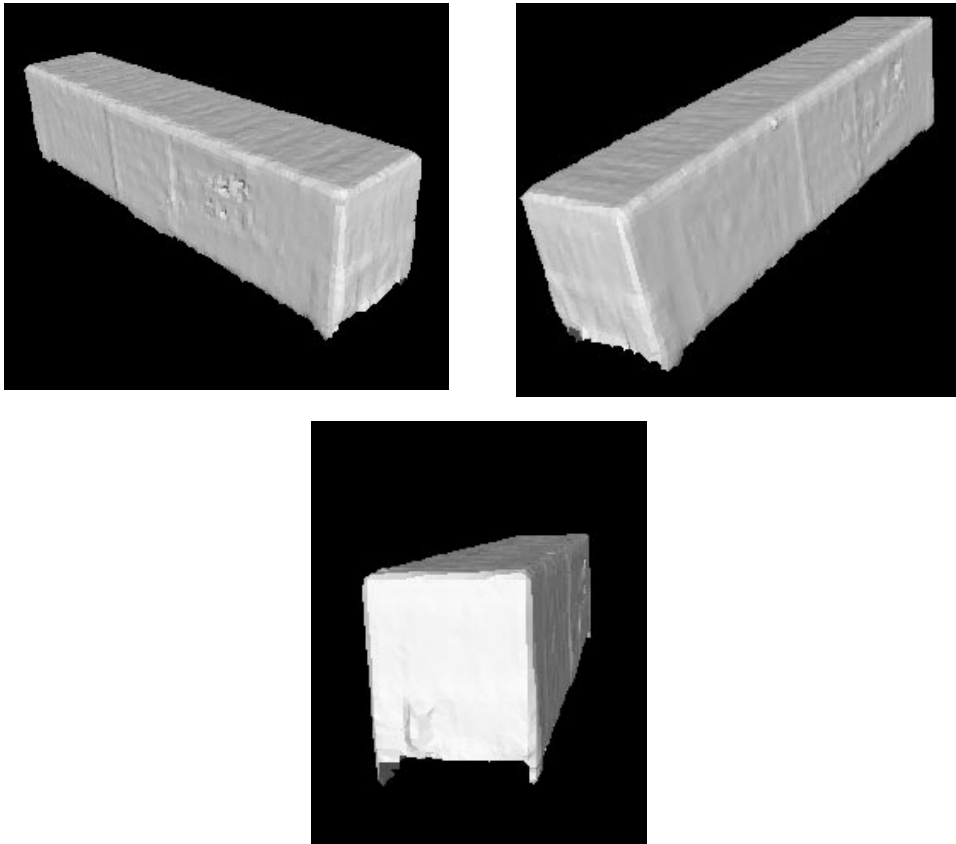


Figure 2.14: Three views of the resulting triangulated model of the boxcar.

The resulting triangulated models had to be cleaned to remove data corresponding to the Puma mounting device, which, despite the fact that its surface is black, was rather cleanly reproduced in the resulting models. If another object has the same rigid motion as the object being modeled, our algorithm considers this other object to be part of the object being modeled; it is unable to distinguish between objects with identical motion with respect to the camera.⁷ Holes on the undersides of the objects were also filled during the cleaning process.

As an example of what the naive algorithm, Algorithm *ClosestSignedDistance* of Section 2.4.2, would produce we show the example of the the result of the naive algorithm on the duck data set in Figure 2.23. Notice how many extraneous surfaces exist near the duck

⁷Distinguishing two objects that have the same rigid motion is a fundamental limitation of algorithms that build models from sequences of data. This is the fundamental advantage of modeling by moving the object rather than modeling by moving the camera around the object. When the object is moved with respect to the camera, the rest of the background is unlikely to follow the same motion and thus will not be consistently detected by the data merging algorithm.

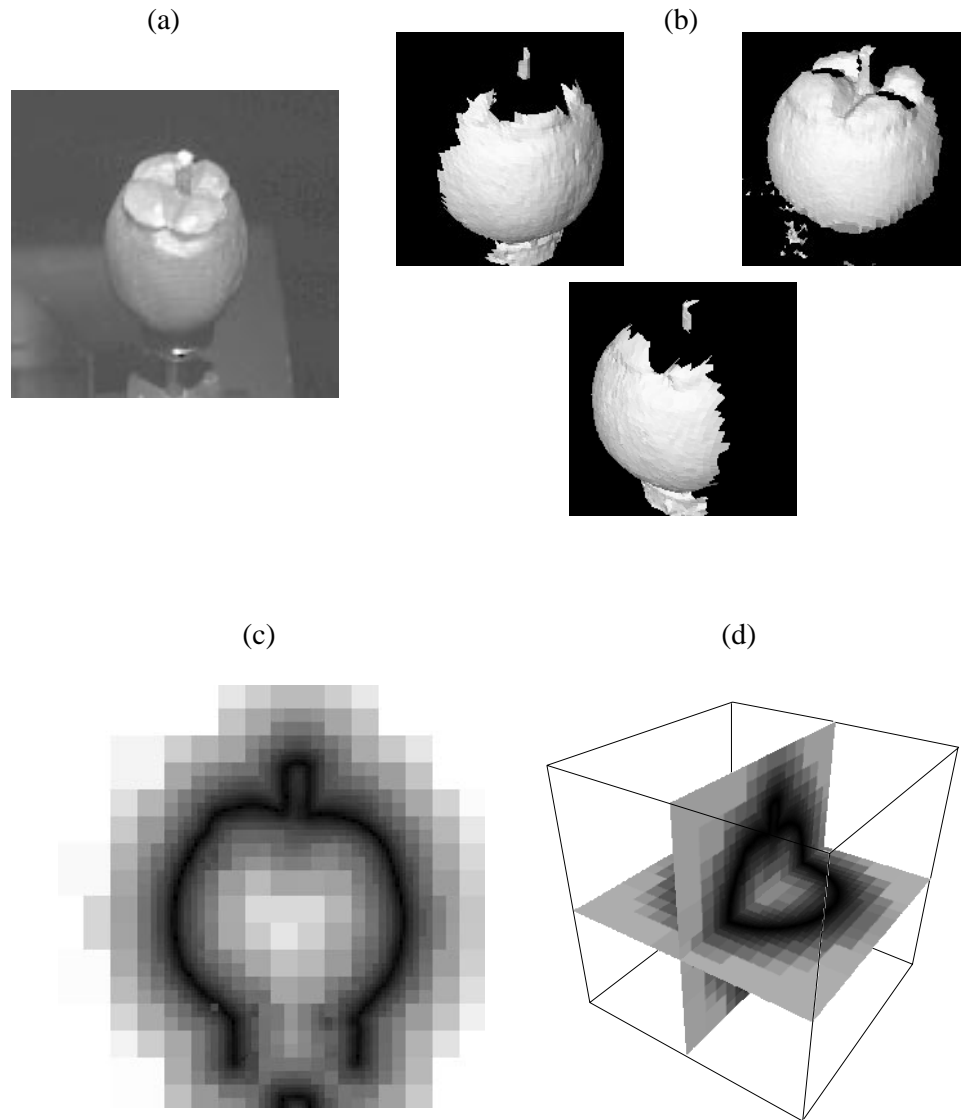


Figure 2.15: Results from modeling the fruit. (a) An intensity image of the fruit, (b) a close-up of some of the triangulated range images used as input to the consensus-surface algorithm, (c) a slice of the implicit-surface octree volume where the grey-scale indicates the proximity to a surface point (black closest, white furthest), and (d) a 3D view of two cross sections of the implicit-surface octree volume.

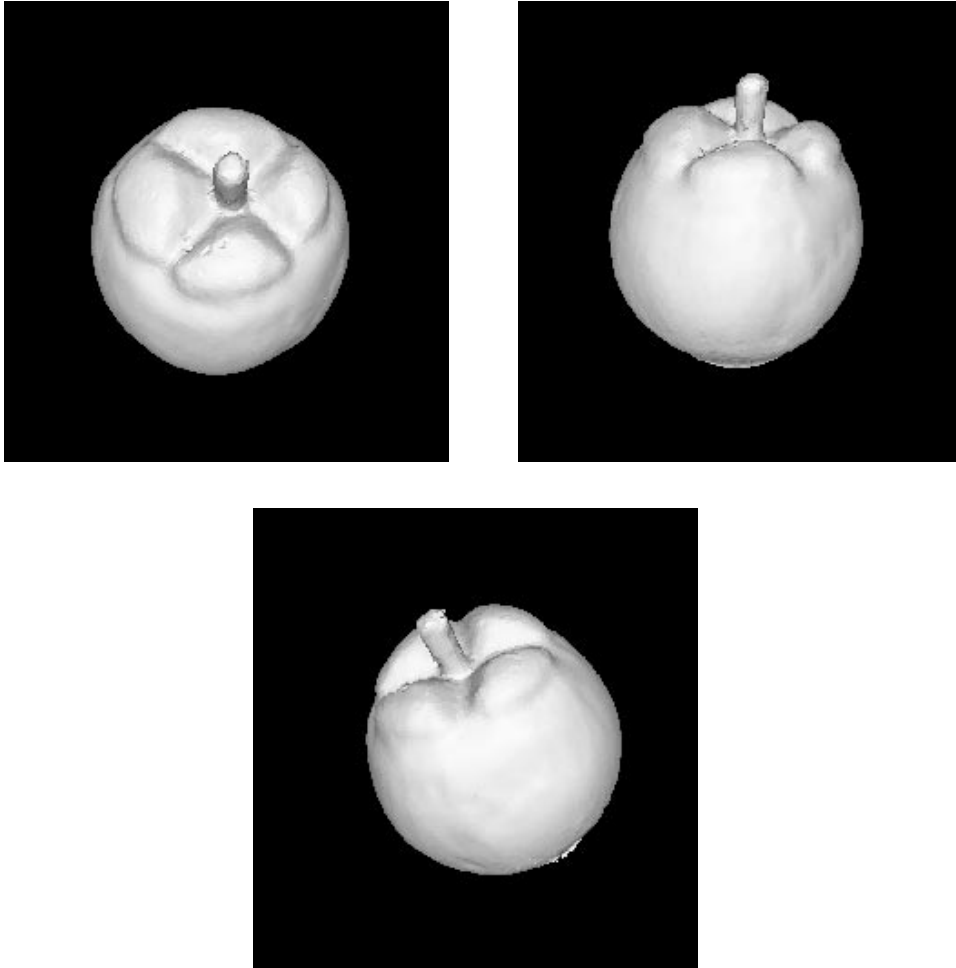


Figure 2.16: Three views of the resulting triangulated model of the fruit.

Object	Images	Tris In	Tris Out	Voxel Res.	Octree Usage	Time (minutes)	θ_{quorum}	δ_d (mm)	θ_n (degrees)
boxcar	18	300k	23k	1.6mm	6%	17	1.5	2	45
fruit	36	370k	49k	1mm	6.8%	39	1.5	2	53
duck	48	555k	27k	1.8mm	4%	52	2.25	3	45
mug	50	680k	24k	2.5mm	23%	48	2.5	3	45
car	54	747k	26k	2mm	5.5%	86	1.5	2	53

Table 2.1: Statistics of the modeling experiments for each object.

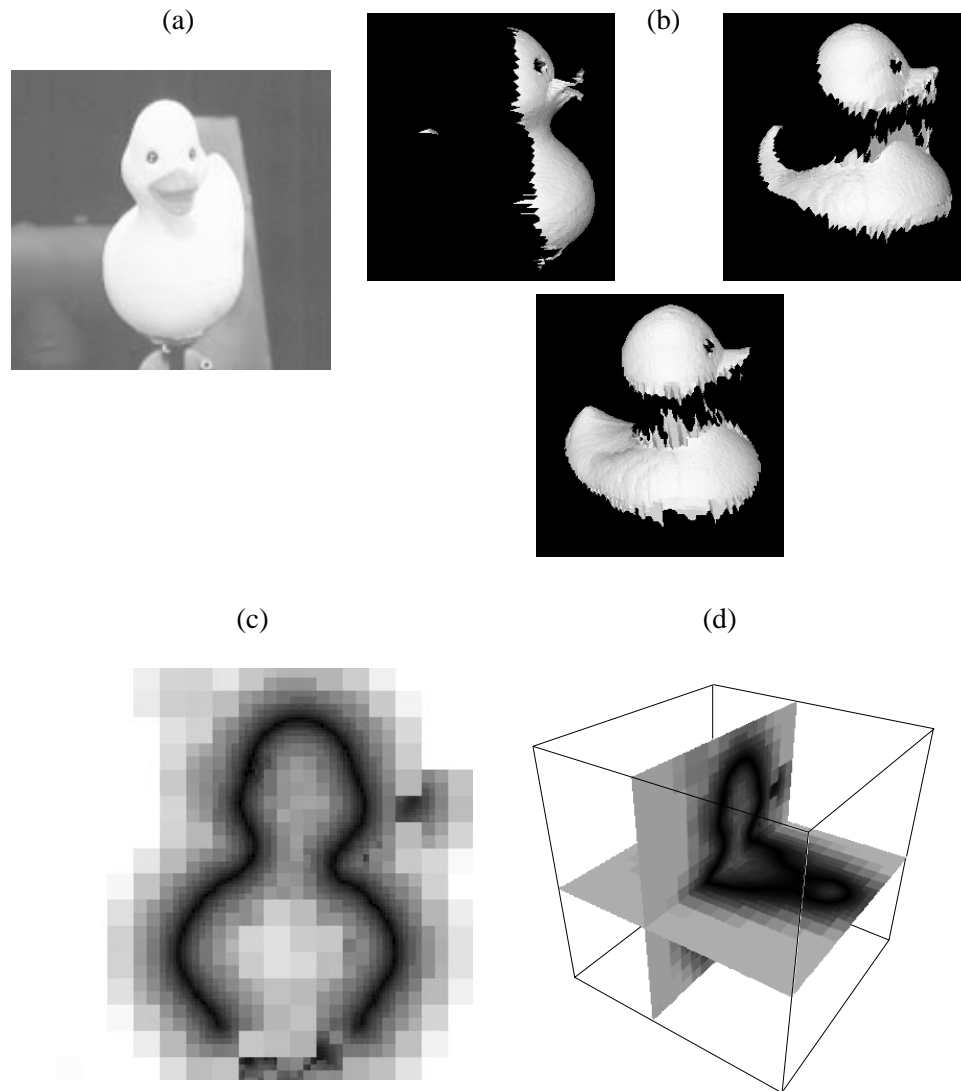


Figure 2.17: Results from modeling the rubber duck. (a) An intensity image of the duck, (b) a close-up of some of the triangulated range images used as input to the consensus-surface algorithm, (c) a slice of the implicit-surface octree volume where the grey-scale indicates the proximity to a surface point (black closest, white furthest), and (d) a 3D view of two cross sections of the implicit-surface octree volume.

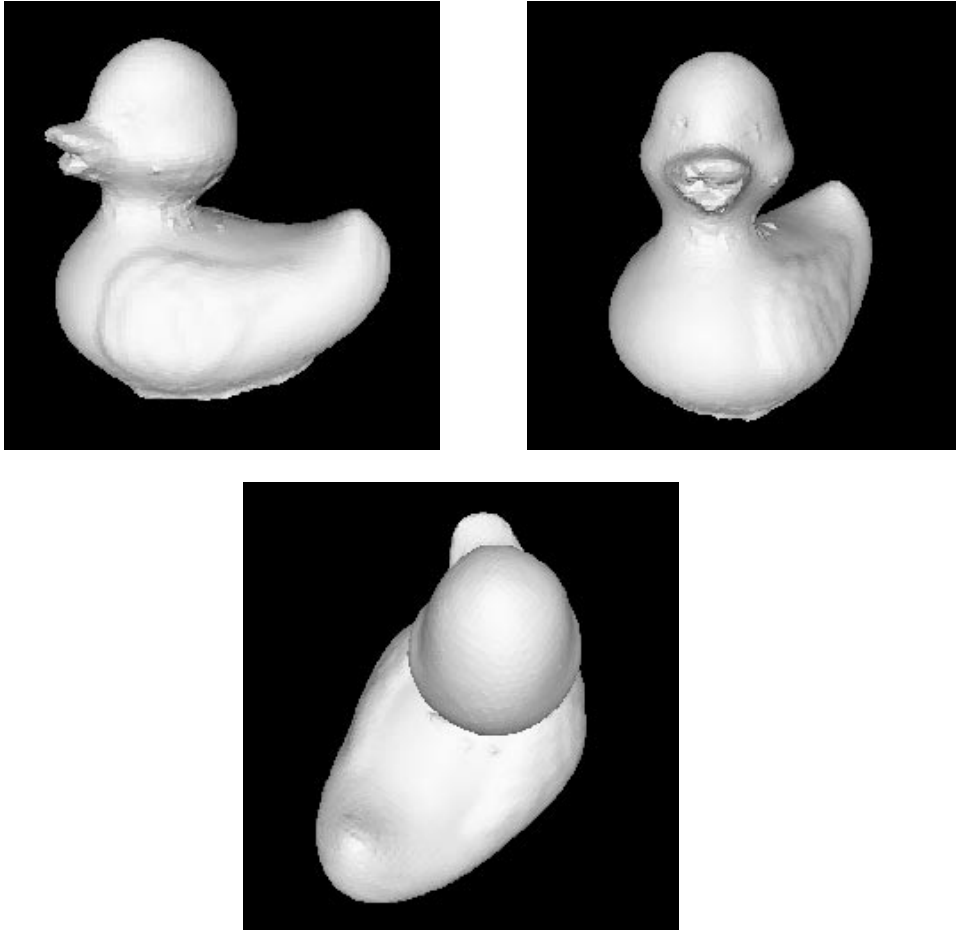


Figure 2.18: Three views of the resulting triangulated model of the duck.

from the input range-image data. Also notice the large number of holes and bumps over the resulting surface. The naive algorithm fails because it trusts that every surface observation is an accurate observation of the object surface. As can be seen from the sample range data of the duck in Figure 2.17, this is not the case.

To more clearly illustrate the accuracy of our modeling algorithm, Figures 2.24- 2.28 show cross sections of our final models and the original input range-image data. These examples demonstrate the ability of our consensus-surface algorithm to accurately locate the surface in very noisy data.

The range-image data was most noisy in dark regions of an object and regions of specular reflection and interreflection. For the most part, the consensus-surface algorithm was able to make sense of the data in spite of these significant errors. Small bumps sometimes resulted in those regions (e.g., on the boxcar and the duck) but that is to be expected when

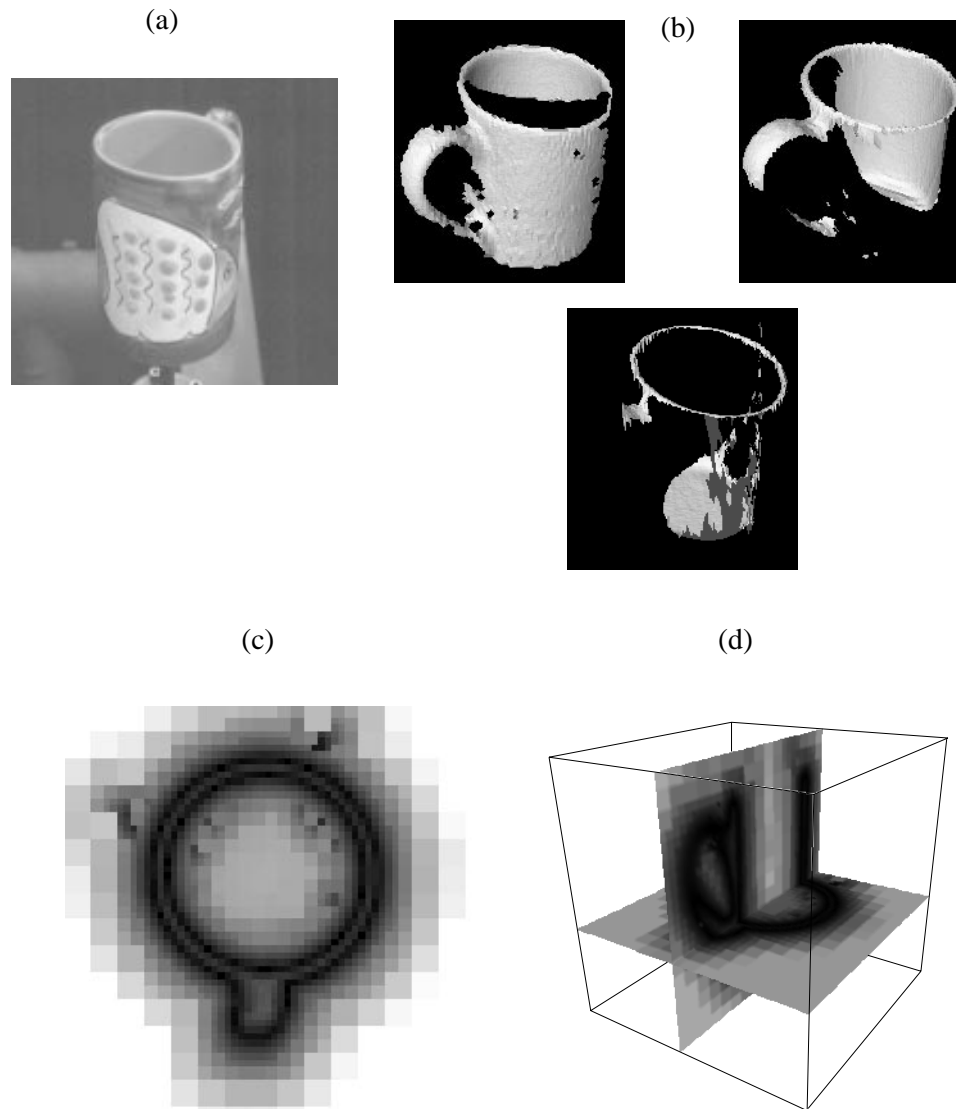


Figure 2.19: Results from modeling the ceramic mug. (a) An intensity image of the mug, (b) a close-up of some of the triangulated range images used as input to the consensus-surface algorithm, (c) a slice of the implicit-surface octree volume where the grey-scale indicates the proximity to a surface point (black closest, white furthest), and (d) a 3D view of two cross sections of the implicit-surface octree volume

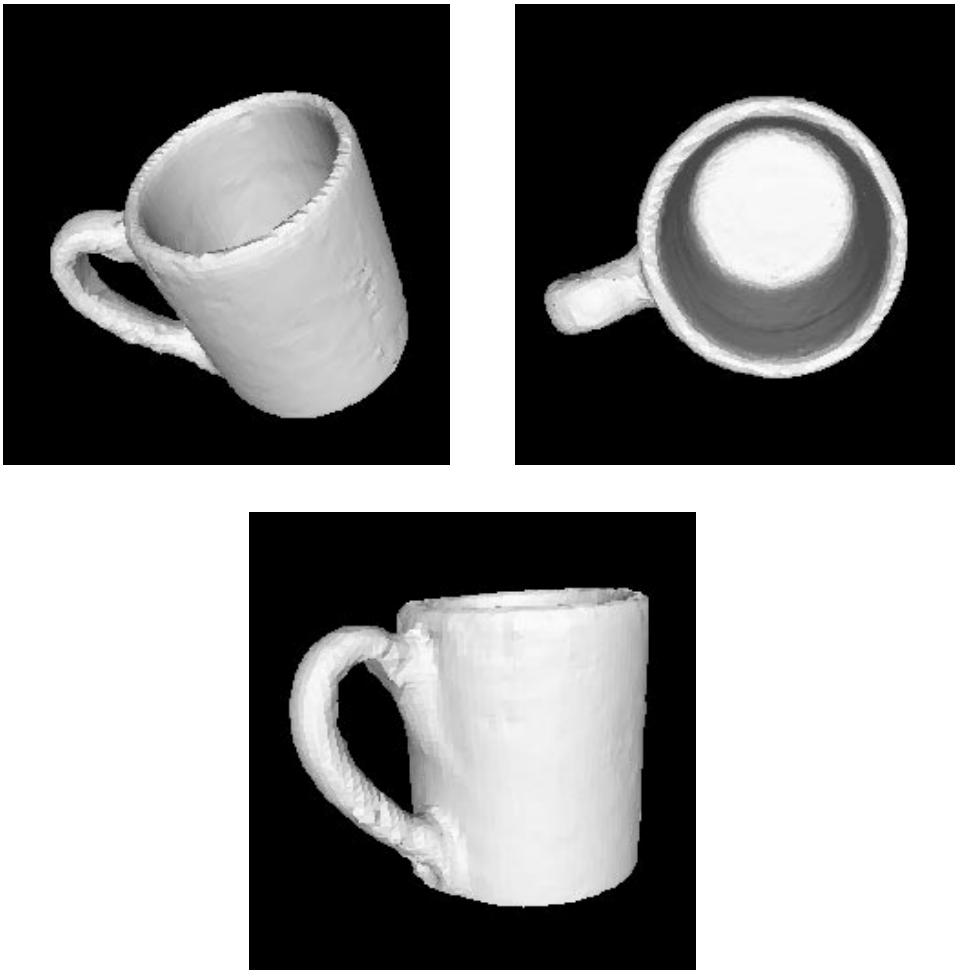


Figure 2.20: Three views of the resulting triangulated model of the mug.

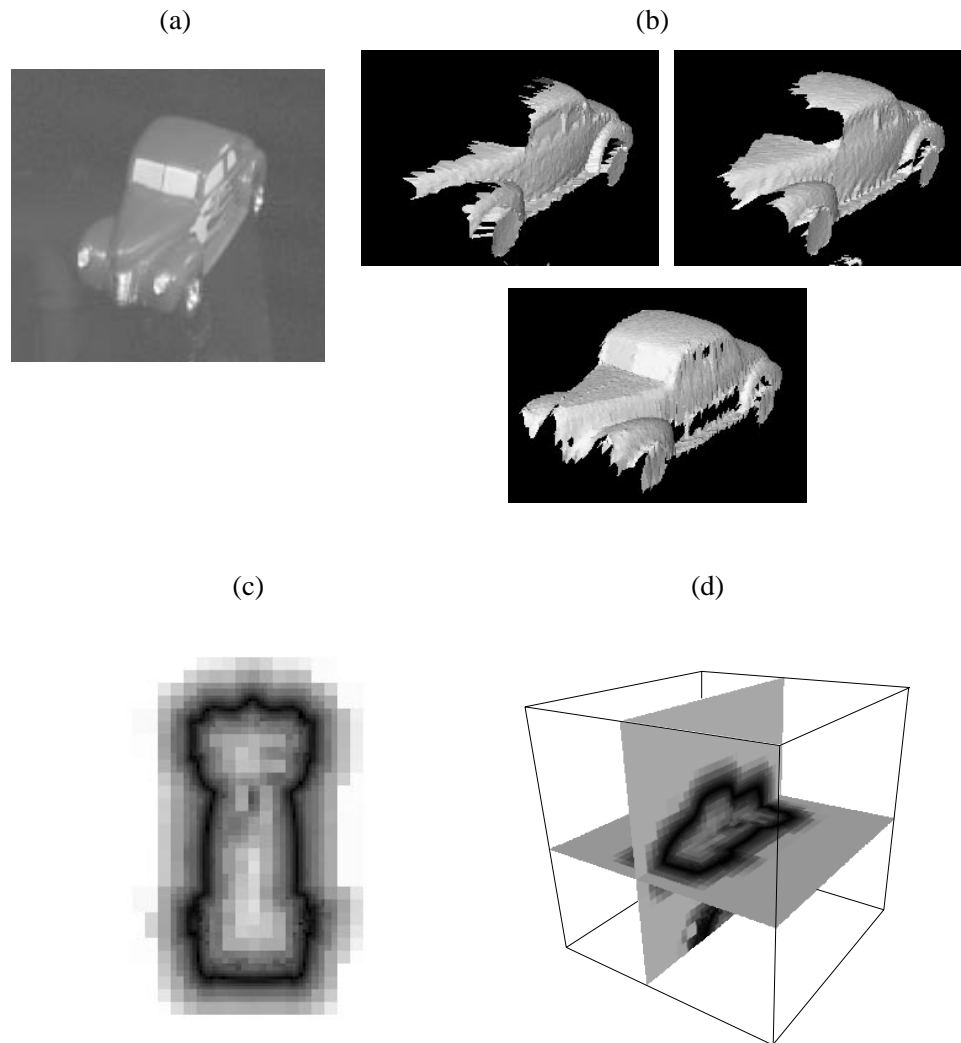


Figure 2.21: Results from modeling the toy car. (a) An intensity image of the toy car, (b) a close-up of some of the triangulated range images used as input to the consensus-surface algorithm, (c) a slice of the implicit-surface octree volume where the grey-scale indicates the proximity to a surface point (black closest, white furthest), and (d) a 3D view of two cross sections of the implicit-surface octree volume.

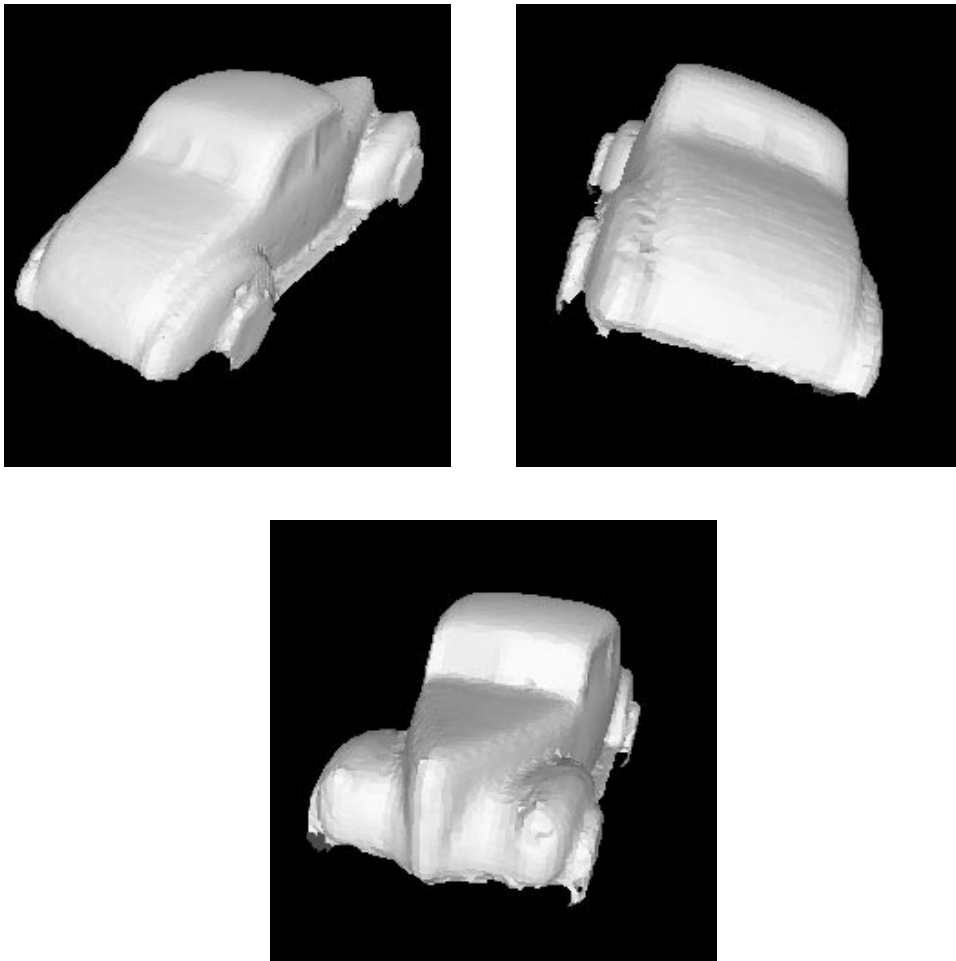


Figure 2.22: Three views of the resulting triangulated model of the car.

the data is consistently bad in a region. However, for the quality of the data, the model surfaces in those regions are still very good. One problem we were unable to solve was modeling the wheels on the toy car. The chrome wheel hubs refused to be imaged by our light-stripe range finder. This is due to the highly specular nature and interreflections on the wheel hub which gave no image data resembling a wheel surface from any views. To work around this, we placed white tape over the wheels of the car.

2.6 3D Modeling: Summary

We have described a method to create a triangulated surface mesh from N range images. Robotic calibration is used to acquire images of the object under known transformations,

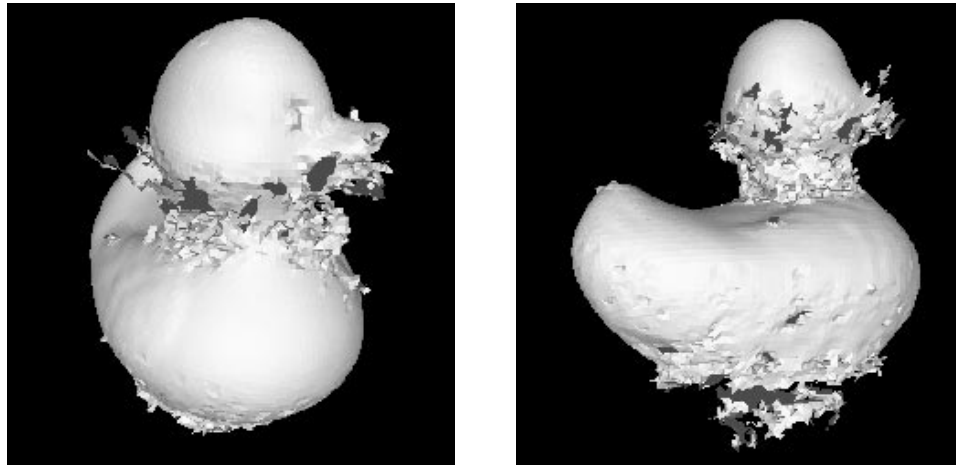


Figure 2.23: The result of the naive algorithm, Algorithm *ClosestSignedDistance*, on the duck image.

allowing us to align the images into one coordinate frame reliably. Our method for data merging takes advantage of the volumetric implicit-surface representation and the marching-cubes algorithm to eliminate topological problems.

The main contribution of this chapter is our algorithm for merging data from multiple views: the consensus-surface algorithm which attempts to answer the question

What is the closest surface to a given point?

With the answer to this question, we can easily compute the signed distance $f(\mathbf{x})$ correctly. While other known methods (described in detail in Chapter 6) also implicitly address this question, their algorithms do not capture the essence of the problem and produce answers by taking averages of possibly unrelated observations. In contrast, our algorithm attempts to justify the selection of observations used to produce the average by finding a quorum or consensus of locally coherent observations. This process eliminates many of the troublesome effects of noise and extraneous surface observations in our data.

Consensus surfaces can be computed independently for any point in the volume. This feature makes it very easy to parallelize and allows us to straightforwardly use the octree representation. The octree representation enables us to model objects with high accuracy with greatly reduced computation and memory requirements. By modifying the marching-cubes algorithm to do a simple gradient test at zero crossings, we also are able to avoid special cases in our algorithm.

We have presented the results of our modeling algorithm on a number of example problems. These results demonstrate that our consensus-surface algorithm can construct

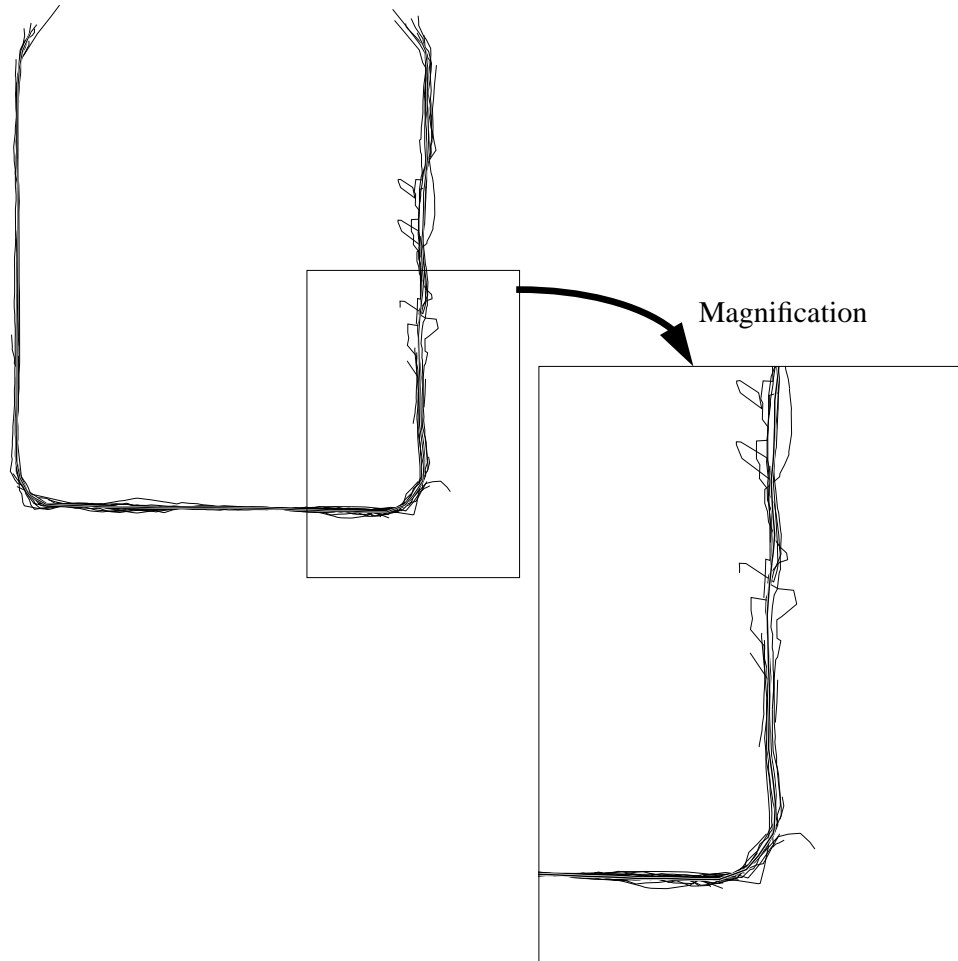


Figure 2.24: A cross section of the final model of the boxcar (thick black line) and the original range-image data (thin black lines) used to construct it.

accurate geometric models from rather noisy input range data and somewhat imperfect alignment.

We now discuss our algorithm for 3D-3D object localization.

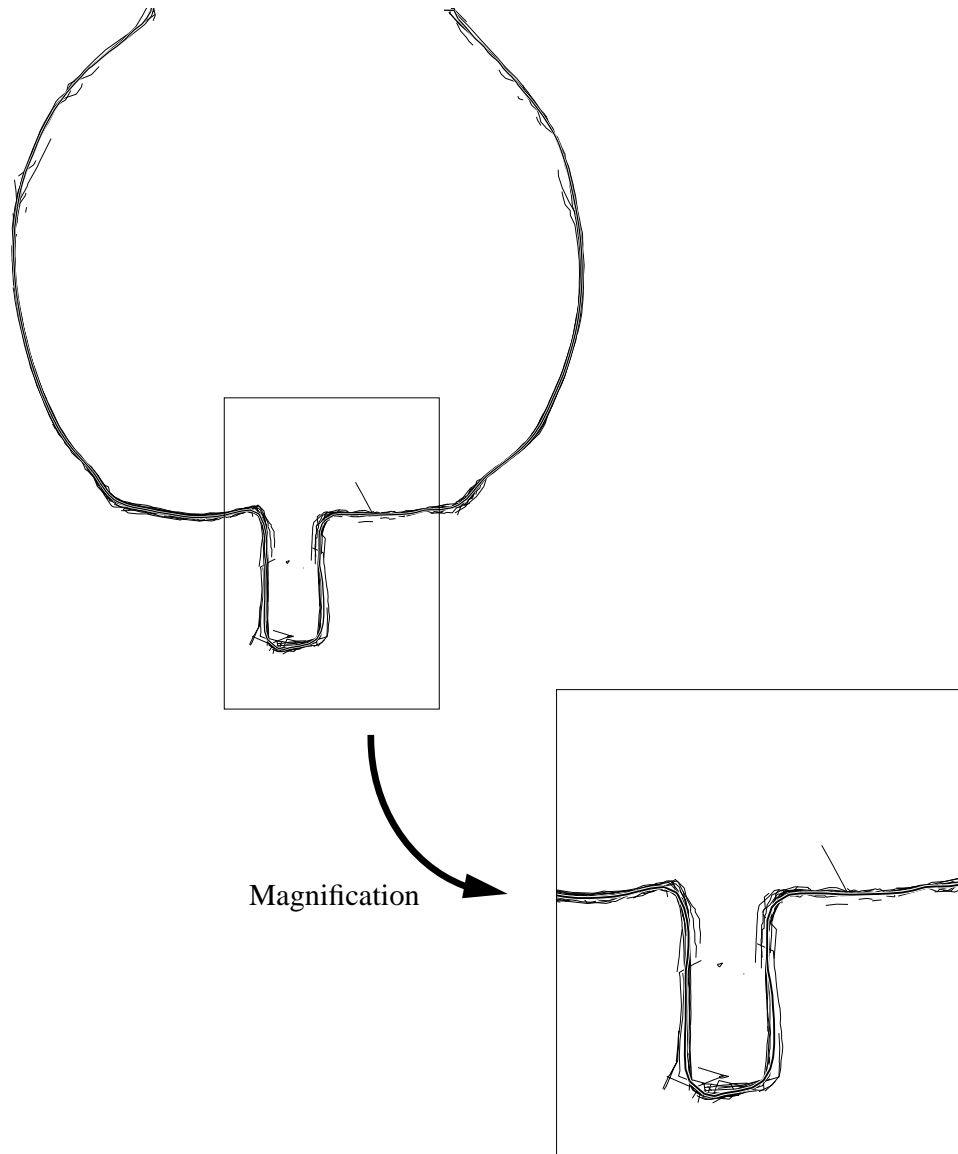


Figure 2.25: A cross section of the final model of the fruit (thick black line) and the original range-image data (thin black lines) used to construct it.

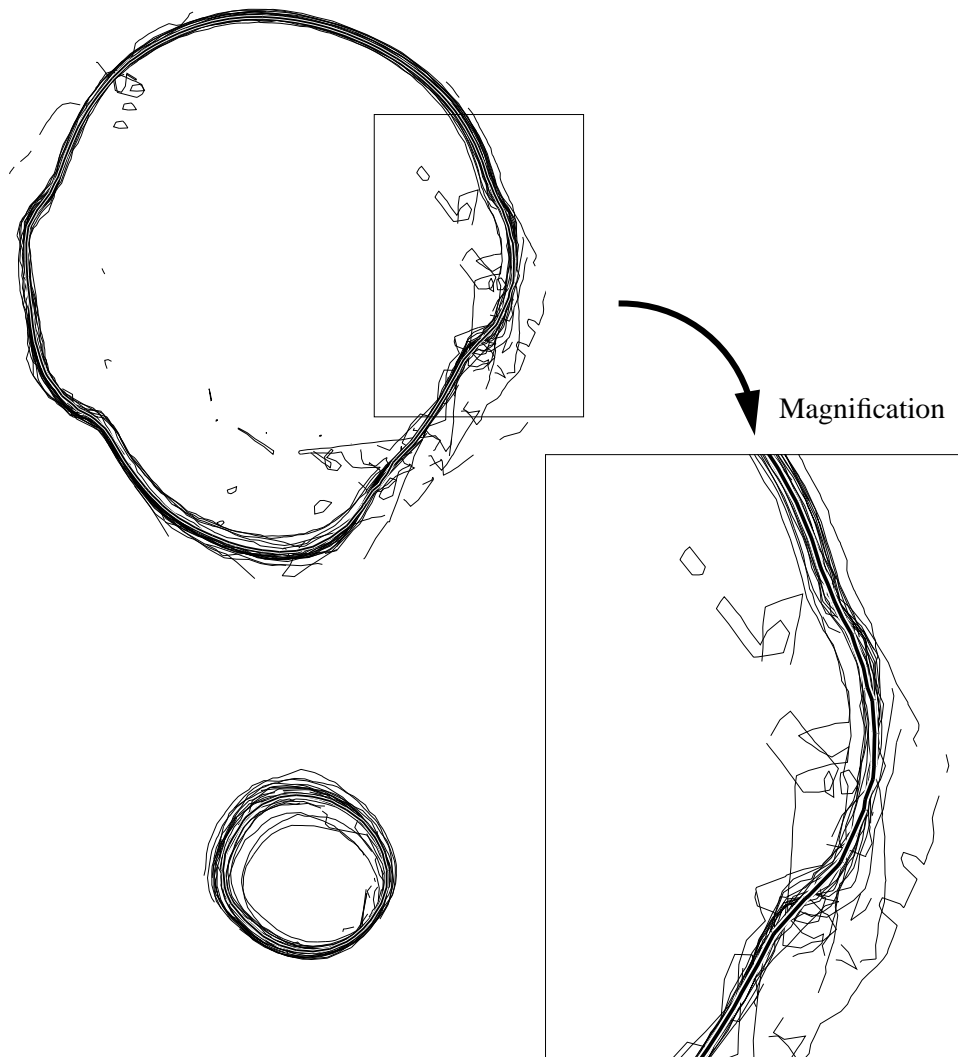


Figure 2.26: A cross section of the final model of the rubber duck (thick black line) and the original range-image data (thin black lines) used to construct it.

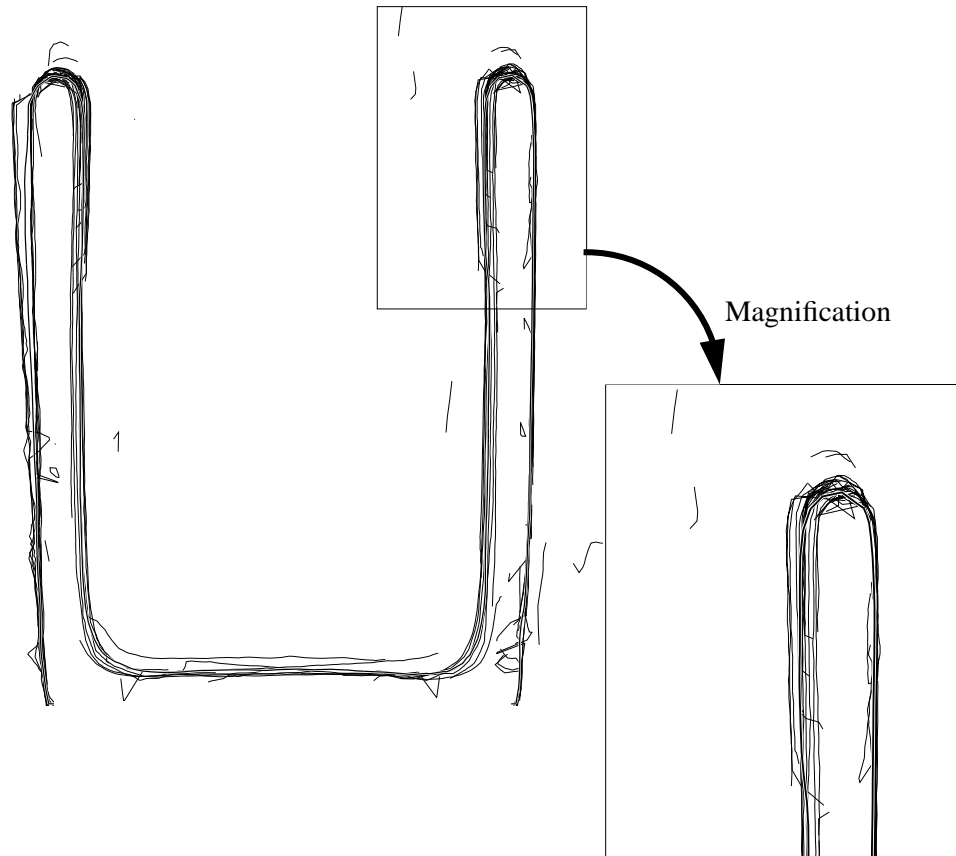


Figure 2.27: A cross section of the final model of the ceramic mug (thick black line) and the original range-image data (thin black lines) used to construct it.

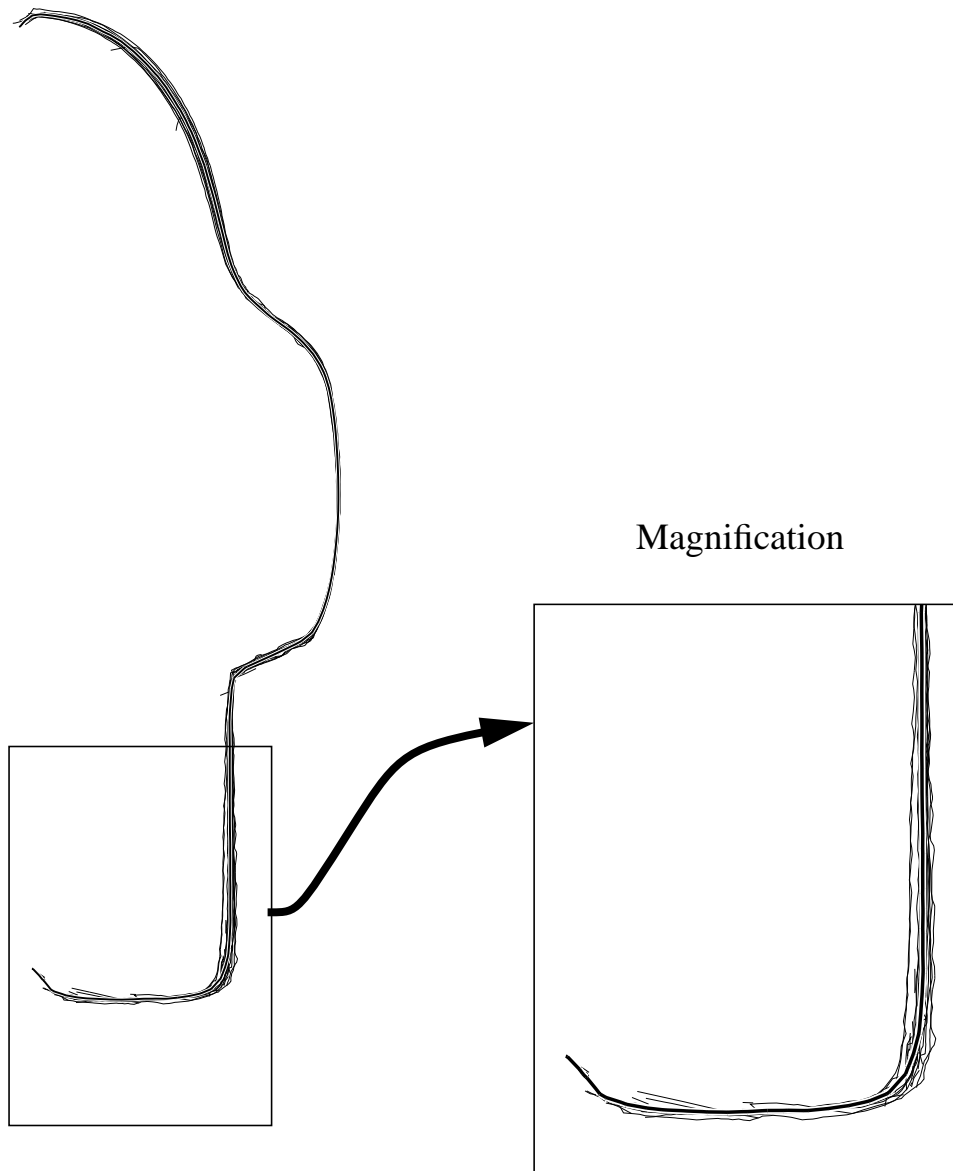


Figure 2.28: A cross section of the final model of the toy car (thick black line) and the original range-image data (thin black lines) used to construct it.

Chapter 3

3D-3D Object Localization

The main goal of this thesis is to localize a known object in an image given a rough estimate of the object’s pose. In the previous chapter, we described a method for automatically building a 3D triangulated surface model from multiple range-image views. In this chapter, we will detail our approach to using such models for the task of localizing 3D objects in 3D range-image data—3D-3D object localization¹.

For localization to be useful for recognition and tracking applications, it must be an efficient, robust operation and should be applicable to a wide variety of object shapes. There are many subtle problems to be solved to achieve robust and efficient localization in practice. We begin this chapter by briefly overviewing the problems involved and our approach to solving them.

3.1 Approach

Here, we assume that we are given an accurate, triangulated model of our 3D object’s surface (using the techniques presented in Chapter 2 or an appropriately triangulated CAD model), a range image, and a rough estimate of the object’s pose in the image. The localization task is to estimate the precise pose of the object in the range image. In approaching this task, we regard as axiomatic that localization is an optimization problem: we can evaluate any pose estimate, and the true pose has the optimal value. The primary problem is how to evaluate a pose candidate. Once pose candidates can be evaluated the next problem is how to efficiently and effectively search for the best pose candidate.

Our first decision is to evaluate the pose by measuring the distance between points on the model and points in the image. The rationale is that the range image provides us with samples of visible surface points in three dimensions. Thus, it makes sense to match points on the model surface with their samples in the image and measure the distance between them. In general, we use one point per triangle in the model though we could easily sample

¹Earlier versions of this worked appeared in [144, 145, 146, 148].

more or fewer points.²

We prefer to rely on low-level data available from the sensor rather than higher-level features inferred from the data. 3D points (available directly from range images) are the simplest possible feature and points suit our purposes nicely: they are efficient to process and manipulate and relatively easy to match with one another. Points are also a very general representation of shape. If higher-level features are used, the shapes that could be modeled would most certainly be restricted (e.g., using algebraic surfaces).

At the highest level, our approach to localization comprises the following steps:

- Predict the appearance of model points in the image
- Match the model points to image points
- Refine the pose estimate using the point matches

The first problem we face is how to efficiently compute the visibility of the points of the model with respect to the range-image view. We present a local approximation method for efficiently predicting the visibility of points given the pose of the object and camera parameters. This method is general for all standard camera projection models and obviates the need for expensive ray-casting or z-buffering.

The second issue is how to compute correspondences between model and image points. We describe the use of k-d trees [41] to perform nearest-neighbor searches for efficiently computing these correspondences. We also describe a method for extending the nearest-neighbor search to consider attributes other than 3D location to improve the accuracy of correspondences when the error in the initial pose estimate is high.

The third problem is dealing with incorrect correspondences and noise. Our reason for computing the correspondences is to use them to refine our estimate of the pose. This closely resembles the classic pose estimation problem—computing the optimal pose from a set of correspondences. In pose estimation, the correspondences are usually assumed to be correct but that the data is possibly corrupted by noise (e.g., Gaussian noise). Here we are faced with a more difficult task—dealing with incorrect correspondences as well as noise, and no fixed/precomputed correspondences. Knowing that many of our correspondences will be incorrect, we draw upon the field of robust statistics [67, 96] to create a solution that is relatively insensitive to noise and outliers. The solution is more complicated than least-squares estimation—the standard solution for 3D-3D pose-estimation problems. The solution to localization requires non-linear optimization. In general, closed-form solutions do not exist for non-linear optimization problems—implying that an iterative solution scheme is necessary, as is the case here.

Our approach to optimization borrows much philosophically from Kass, Witkin and Terzopoulos's [75, 134] work on active contour models and energy minimizing snakes and

²The models built using the methods of Chapter 2 can be composed of triangles of arbitrary size. If the tessellation is too coarse, we can straightforwardly increase the density of triangles by interpolation using many schemes. If the tessellation is too fine, we can use decimation techniques (e.g., Johnson [73]) to reduce the triangle density.

from Besl and McKay’s [6] iterative closest point (ICP) algorithm for 3D registration. Instead of assigning correspondences and statically solving for the pose, our method achieves robustness by allowing the model to dynamically settle on the optimal pose with respect to the constraints of the image. We accomplish this by making the correspondences a dynamic function of pose during optimization. The objective function that we minimize is specifically chosen to make the estimation robust to outliers and is based on solid statistical principles. As will be described later, this approach is intuitively and mathematically well justified.

The rest of this chapter will provide the details of our solutions to the problems described above:

- Point visibility
- Point-to-point correspondence
- Pose optimization

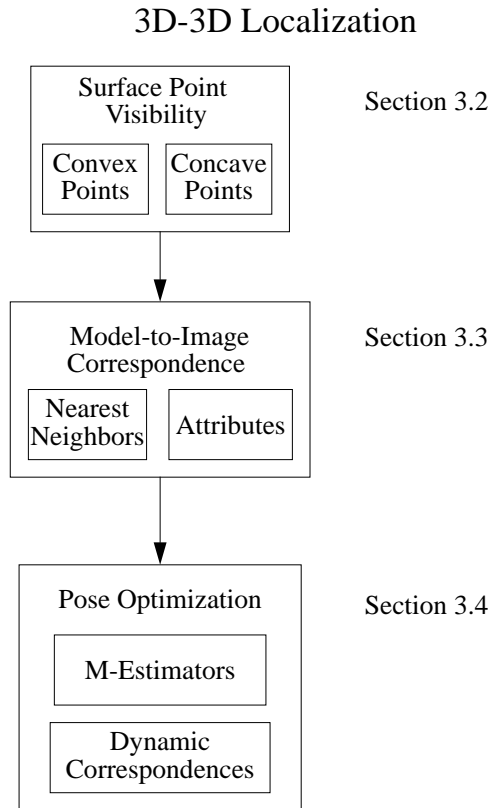
Figure 3.1 shows a diagram of the technical sections of the thesis. We begin by discussing an efficient approximation for surface point visibility computation. This is followed by a discussion of an efficient search technique for nearest neighbor correspondences and an extension to include attributes other than spatial coordinates. We then discuss the pose optimization problem and the main contribution of this chapter, our method for minimizing a robust M-estimator via dynamic correspondences with standard non-linear optimization techniques.

The chapter will conclude by summarizing the localization algorithm. The methods and algorithms described here are of a very practical nature. We will attempt to describe the steps with great attention to detail as there are many traps to catch the unsuspecting practitioner.

3.2 Point Visibility

Before matching a surface point of a model with a point in a range image, it is prudent to first determine if the model point is geometrically visible from the given pose. We need to answer the question of visibility for every point of the model. Since the visibility computation will be performed many times, the computation must be as efficient as possible. For an exact computation of the visible portions of an object model, there are two standard algorithms from the field of computer graphics: ray-casting and z-buffering.

Ray-casting [40, 141] works by casting a ray from the camera’s center of projection through a given point on the model. The model point is visible if the ray does not first pass through any other point on the model surface. A ray is thus traced for each point of the model. Ray-casting is a rather complicated operation. For every triangle of the object, it is possible that we must test every other triangle on the object surface to determine if the triangle is the first surface that intersects the ray—resulting in $O(n^2)$ ray-triangle



intersection tests for a surface model composed of n triangles. This is much too expensive to consider for localization in practice.

Z-buffering [40, 141] works by creating a depth image of the object. The object surface is projected into the image, triangle by triangle. If a surface point projects to the same image coordinate as a previous point, the point that is closest to the camera is placed in the depth image. Finally, only visible surface points are present in the depth image. Z-buffering is less expensive than ray-casting, $O(n)$ operations³ for a surface model composed of n triangles. Despite the existence of fast hardware implementations, z-buffering is still too time-consuming for our purposes. Z-buffering only works if the entire surface is projected triangle by triangle onto the depth image. Thus, there is no speedup benefit to be gained by using sparse collections of points. As a practical matter for efficiency, we must limit our localization search to use only a sparse set of points on surface of our object model.⁴

³Assuming a triangle fill is a constant time operation.

⁴For example, a reasonable coverage of a small object could have 40,000 triangles. Using that many triangles is inefficient and unnecessary to solve the task. Our experience is that using several hundred to a few thousand triangles is sufficient for localization of most objects.

Z-buffering necessarily solves for the visibility of *all* points on the surface (at the specified depth-image resolution); thus, z-buffering is not a desirable solution.

Since we are using a large set of points for localization, having a perfect visibility computation is not critical. Our localization algorithm should be resilient to a few mistakes out of a hundred. Thus, exact solutions such as z-buffering or ray tracing are not necessary for our purposes.

For 3D surfaces, we can reduce the problem to two cases: convex surface visibility and concave surface visibility. The convex case covers all points which lie on the convex hull of the surface: wherever the surface normal points towards the camera center, the point is visible (assuming outward pointing normals on every surface). The concave case covers all surface points which are not on the convex hull of the object. The solution for the concave case subsumes the convex case but has an added complication that the concave point will be occluded by other parts of the object surface from some viewpoints. In the following, we present an efficient approximation to solve for convex and concave surface visibility.

3.2.1 Convex Surface Visibility

We discuss the simplest case, the convex case, first. For this discussion, let us assume that the object is completely convex (e.g., a sphere or ellipsoid). As in Chapter 2, the surface is represented as a set of triangles. For any point x on a triangle, we can straightforwardly compute its visibility given the current viewing direction, \hat{v} —the vector from the camera’s center of projection to x .⁵ Wherever the surface normal points towards the camera center, the point is visible. Without loss of generality, we focus our interest on the center points of each triangle. In the following, τ_i denotes the i th triangle of the model, \hat{n}_i denotes τ_i ’s outward pointing normal and c_i denotes τ_i ’s center point. The visibility of point c_i is computed by the test

$$\text{visible}_{\text{convex}}(c_i) = \begin{cases} \text{true} & \hat{n}_i \cdot \hat{v} > 0 \\ \text{false} & \text{otherwise} \end{cases}$$

where \hat{v} is the viewing direction vector from the camera center of projection to c_i . This visibility test only requires a dot product and a comparison and, since it is local, can be computed independently for each triangle. Note that the definition of \hat{v} in this equation means that this test will work correctly regardless of camera parameterization. \hat{v} is the only information that we need to know about the camera projection to make the visibility determination.

In practice, a point on the surface will only be visible when the surface orientation is just less than 90 degrees from the viewing direction. Thus, we generally use a small threshold instead of 0 for the comparison in the above test. The slightly modified test is:

$$\text{visible}_{\text{convex}}(\tau_i) = \begin{cases} \text{true} & \hat{n}_i \cdot \hat{v} > \cos \theta \\ \text{false} & \text{otherwise} \end{cases} \quad (3.1)$$

⁵The camera’s center of projection is readily available from the camera calibration parameters as described in Chapter 1.

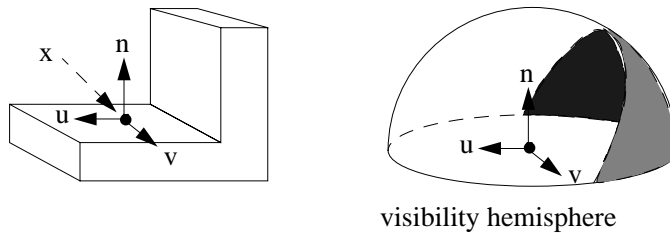


Figure 3.2: An example of the set of visible viewing directions (the unshaded portion of the hemisphere) for the point x on the L-shape.

where θ is an angle close to 90 degrees which is the maximum orientation angle of the surface that will be detected by the range sensor. θ is chosen empirically. This visibility test for the convex case nicely satisfies our requirements of efficiency and locality; however, we are not simply interested in localizing ovoids. The concave surface case is discussed next.

3.2.2 Concave Surface Visibility

In general, we must be prepared to compute point visibility for arbitrary shapes which will include concavities and self-occlusions where our simple convex visibility test (Equation 3.1) would be grossly insufficient.

As in the convex case, we prefer a local visibility test for the concave points. We can still make good use of our previous test for convex points. Since it is inexpensive, it makes sense to first check to see if the surface point in question is even oriented toward the camera. Once that is determined, we can then perform more expensive tests to determine whether the point is occluded by another part of the object or not. As stated previously, we cannot afford to perform ray-casting or z-buffering each time that we need to compute point visibility.

For each point, the visibility function is a binary function over the set of viewing directions. In practice, by assuming that the point lies on the planar center of the triangle, only the viewing directions lying in the unit hemisphere above the surface point (triangle) need to be tested for visibility. Figure 3.2 illustrates this for a simple L-shaped object. Thus, we can reduce the visibility problem to representing the set of viewing directions from which the point is visible. For the convex case, the visibility set is trivial—the hemisphere above the point's surface. Our main problem is how to represent the visibility set such that:

- the membership test is efficient, and
- the memory requirements are tolerable.

If it were necessary to represent the visibility set exactly, we would be in a lot of trouble. First, as one can imagine, the visibility set could take on arbitrarily complicated subsets of the viewing hemisphere—making the representation arbitrarily large. Secondly, it could become very expensive to evaluate membership in such a set. Fortunately, we can tolerate small errors: as described in Section 3.1 our localization algorithm must be robust to small numbers of errors. Thus, an approximation of the visibility set is sufficient.

We will use a discrete representation of the viewing hemisphere: a *lookup table* (LUT). We can tessellate the viewing hemisphere into discrete bins representing sets of similar viewing directions—all viewing directions in a particular bin are considered equivalent for the visibility computation. Such a scheme involves a time versus space trade-off. In general, we are always looking to reduce the time requirements of localization algorithms, thus, we will usually choose time savings over space savings. In practice, the more important trade-off is space versus accuracy. Do we prefer an LUT approximation which is accurate to 0.1 degrees or an approximation which is accurate to 3 degrees but can be efficiently stored and loaded.

One common LUT scheme [47, 81, 148] is to store in each bin a list of all object features (e.g., points, surfaces, lines) which are visible from the viewing directions corresponding to the bin. The problem with this approach is that it assumes that all points on the object are viewed from the same direction. This is adequate for an orthographic-projection camera model; however, under perspective projection the viewing direction depends on the projected image coordinates of the scene point. For example, the LUT scheme described above does not account for changes in the visibility set as an object translates along the central viewing direction.

Since we do not wish to restrict ourselves to a specific camera model, we must devise another approach. Instead of listing all visible entities in each bin, we allocate a separate LUT for each surface point used in the model (for example, the center points of each triangle). We refer to these LUTs as *visibility LUTs*. Each bin in a visibility LUT contains a binary value indicating whether the point is visible or not from viewing directions which map to the given bin. Since we have a visibility LUT for each point, each point's visibility can be independently computed using the viewing direction to *that* particular point, thus, allowing for arbitrary camera models.

The next issue is how to tessellate up the viewing hemisphere into discrete bins. We have two criteria for carving up the hemisphere:

1. The mapping from viewing directions to bins must be efficient.
2. The bins should cover approximately uniform areas of the hemisphere.

The first criteria is obvious: it is very important that the membership test is efficient as it will be evaluated frequently (once for every point of the model). The second criteria is a practical detail: if some bins are much larger than others, the error of the visibility approximation will vary with respect to viewing direction.

The simplest and most efficient mapping between viewing directions of a hemisphere and the bins of a 2D LUT is orthographic projection. Consider the 2D LUT as a grid lying

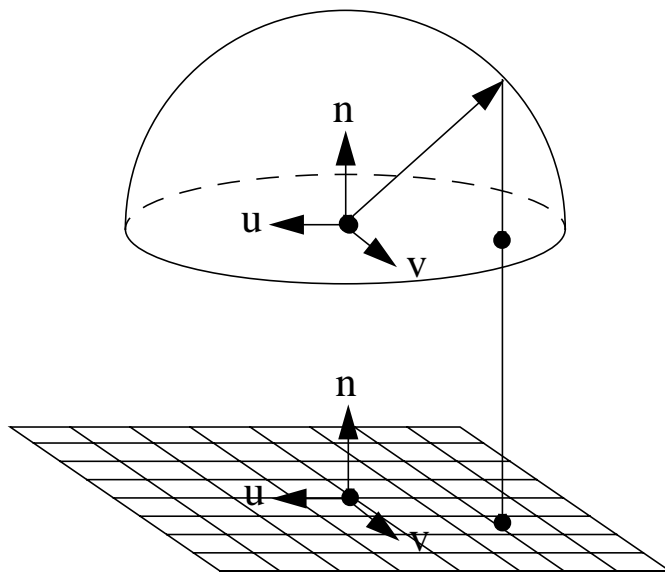


Figure 3.3: Orthographic projection of viewing directions onto a simple LUT array.

on the equatorial plane of the hemisphere. The 2D orthographic coordinates, $[f \ g]^T$, of a viewing direction projected onto the grids are simply the x and y components of the viewing direction \hat{v} (i.e., $f = x$ and $g = y$). This is a bit unsatisfactory, however, because the result is that two different grid elements may cover vastly different areas on the viewing sphere (see Figure 3.3).

We would prefer a more uniform tessellation of the hemisphere. No perfectly uniform tessellation exists; however, there are several other options. One such improvement over orthographic projection is stereographic projection: each point on the sphere projects onto a grid lying on the equatorial plane by intersecting this plane with a ray passing through the point and the south pole (i.e., lowest point) of the sphere. Figure 3.5 shows the stereographic projection of a 2D LUT array. Stereographic projection is slightly more complicated than orthographic, but not beyond reason. The stereographic projection of $\hat{v} = [x \ y \ z]^T$ to 2D stereographic coordinates, $[f \ g]^T$, is accomplished by

$$f = \frac{x}{z + 1} \quad (3.2)$$

$$g = \frac{y}{z + 1} \quad (3.3)$$

assuming that the radius of the sphere is 1, the sphere is centered at $[0 \ 0 \ 0]^T$, and the 2D grid $[f \ g]^T$ lies on the $z = 0$ plane. Using more advanced tessellations than orthographic and stereographic projection would require much more elaborate (and computationally expensive) mappings between viewing directions and LUT bins. One such tessellation is

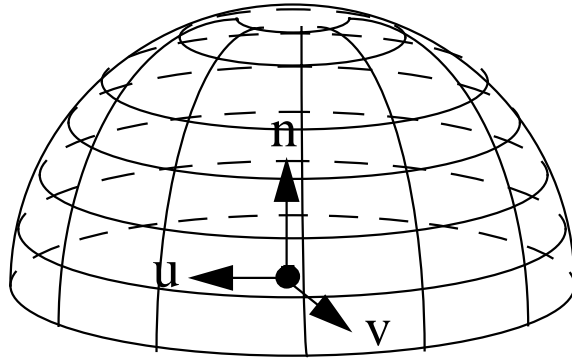


Figure 3.4: Latitudinal/Longitudinal discretization of a hemisphere.

based on latitude and longitude (see Figure 3.4). The problem with a latitudinal-longitudinal tessellation is the cost of indexing the LUT by viewing direction. Computing the latitude and longitude of the viewing direction requires the (relatively) expensive evaluation of trigonometric functions which we would like to avoid. What we can do, however, is essentially to use LUT methods again to compute the latitudinal-longitudinal coordinates. Since we are only really interested in mapping the viewing direction to a bin in the visibility LUT, the latitudinal-longitudinal coordinates can be ignored altogether. LUT methods can be used to index the indices of our visibility LUT. Thus, we have two levels of lookup tables:

- Visibility LUT: unique for each point, each bin contains the binary value indicating the visibility of the point from the set of viewing directions that map to the bin.
- Index LUT: identical structure for all points and models, each bin contains the indices of the Visibility LUT which correspond to the set of viewing directions that map to the bin.

It appears that we have the same problem as before: how do we tessellate the index LUT? The problem is a bit different for the index LUT than for the visibility LUTs.

Since one visibility LUT is required for each point of the localization model, the number of bins must necessarily be small; however, only one index LUT is necessary since the mapping from viewing directions to bin indices is the same for all points. Thus, it is feasible to use a much higher resolution table. The previous problem of uniform tessellation can be ignored as long as the resolution of the index LUT is substantially higher than resolution of the visibility LUTs (i.e., many index LUT bins correspond to each visibility LUT bin). The index LUT can be indexed by the f and g components of stereographic projection to provide the corresponding indices of the visibility LUT (implicitly providing the latitude and longitude, or any other mapping for an arbitrary tessellation of the hemisphere). Figure 3.6 demonstrates how the two-level indexing of viewing directions to visibility works.

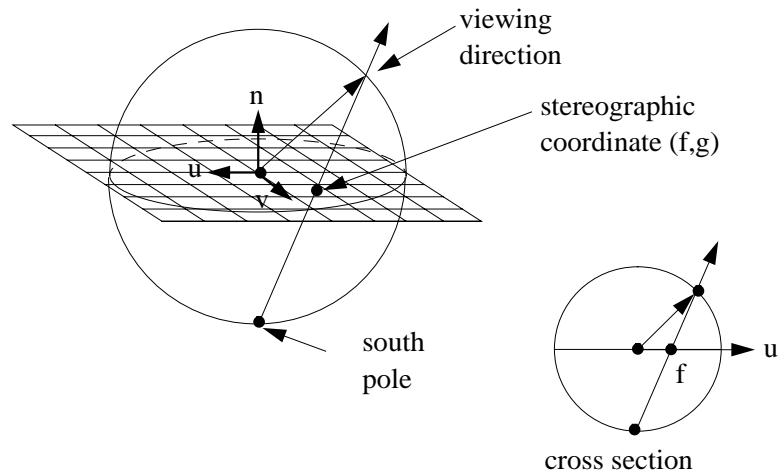


Figure 3.5: Stereographic projection of viewing directions onto a simple LUT array.

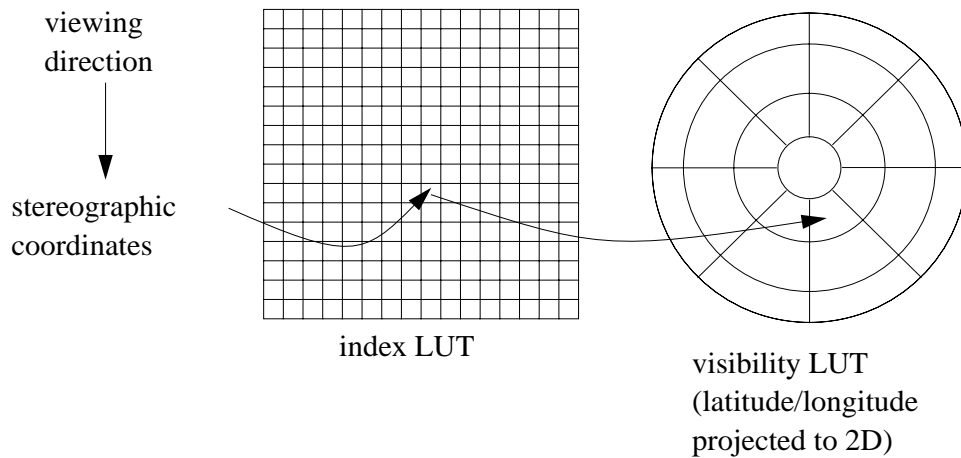


Figure 3.6: The viewing direction is mapped to the index LUT using stereographic projection (note, in practice the resolution of the index LUT would be extremely fine as opposed to the coarse LUT pictured here). The bin of the index LUT provides the index into the visibility LUT which may have an arbitrarily complex tessellation (latitude and longitude in this case).

This two-level indexing technique will work for any discretization of the viewing sphere. We can enumerate an endless list of possibilities, such as tessellations of pentagons or hexagons (as in a soccer ball), an icosahedron, or semi-regular triangulation of the sphere. The latitudinal-longitudinal tessellation allows us more control over the size of the bins than some of these other practical tessellations. Any tessellation can be used; the only requirement is that there is some (arbitrarily complicated/expensive) function that maps viewing directions to the index of the corresponding discrete chunk. This function can be used to generate the index LUT off-line, and then we have a simple and efficient way to map viewing directions to the bins of our viewing hemisphere tessellation.

One subtle point that was omitted from the preceding discussion was the coordinate system of the viewing direction vector $\hat{\mathbf{v}}$. Each point must have its own coordinate system since the viewing hemisphere is oriented in the direction of the point's normal; there is no single coordinate system which will work for all points on the model. The viewing direction must be in the point's local coordinate frame in order to index the correct element of the point's visibility LUT. We can define local coordinate system of triangle τ_i 's center, \mathbf{c}_i , as follows. We require the z direction, $\hat{\mathbf{z}}_i$, to correspond with the τ_i 's normal:

$$\hat{\mathbf{z}}_i = \hat{\mathbf{n}}_i.$$

The x and y directions can be arbitrarily chosen to be orthogonal to $\hat{\mathbf{z}}_i$. We choose the x direction, $\hat{\mathbf{x}}_i$, to be the direction from the center point, \mathbf{c}_i , to τ_i 's first vertex \mathbf{p}_0 :

$$\hat{\mathbf{x}}_i = \frac{\mathbf{p}_0 - \hat{\mathbf{c}}_i}{\|\mathbf{p}_0 - \hat{\mathbf{c}}_i\|}.$$

The y direction, $\hat{\mathbf{y}}_i$, follows directly from $\hat{\mathbf{z}}_i$ and $\hat{\mathbf{x}}_i$:

$$\hat{\mathbf{y}}_i = \hat{\mathbf{z}}_i \times \hat{\mathbf{x}}_i.$$

To index our LUT all we need to do is convert $\hat{\mathbf{v}}$ to local coordinates, which can be accomplished by the following matrix multiplication:

$$\hat{\mathbf{v}}_i = [\hat{\mathbf{x}}_i \ \hat{\mathbf{y}}_i \ \hat{\mathbf{z}}_i]^T \hat{\mathbf{v}} \quad (3.4)$$

$$\hat{\mathbf{v}}_i = \mathbf{R}_i \hat{\mathbf{v}} \quad (3.5)$$

The stereographic coordinates of $\hat{\mathbf{v}}_i$ index a bin in the index LUT which gives us the index into the visibility LUT. The computation cost of this visibility test is also reasonable: one matrix-vector multiplication and two table lookups. The index LUT can be computed off-line and loaded at run-time, and for each concave point we must precompute and store its visibility LUT. The visibility LUT is most efficiently implemented as a bit vector. The resolution of the visibility LUT can be chosen based on memory limitations, required accuracy or efficiency requirements. For example, we can carve up the viewing hemisphere into 256 chunks and store this in eight, 32-bit words.

3.2.3 Off-line Lookup Table Creation

Now that we have chosen a representation for the visibility set, we must compute the LUT for each point of the model. Though this computation is relatively expensive, it can be computed in reasonable time (several minutes) off-line and stored with the model.

For each triangle τ_i , the algorithm for filling the visibility LUT is as follows

Algorithm *CreateVisibilityLUT*

Input: point c_i of triangle τ_i

Input: triangle set T

Output: the visibility LUT for point c_i of triangle τ_i

1. create the index LUT of dimension $N \times N$
2. create bitmap LUT of dimension $N \times N$, initialize all bins to true
3. **for** $\tau_j \in T$ s.t. $\tau_j \neq \tau_i$
4. **if** τ_j occludes τ_i
5. **then** project τ_j into τ_i 's local stereographic coordinates
6. fill in the bitmap LUT bins corresponding to the projected triangle with false to denote occlusion
7. **if** all bitmap LUT bins are true
8. **then** declare τ_i convex
9. **return**
10. **else** create and clear the visibility LUT
11. **for** all bitmap LUT bins, initialize all bins to true
12. **if** bin is false
13. **then** set the corresponding visibility LUT bin to false
14. **return** visibility LUT

The index LUT is created and a bitmap of the same dimensions is created to record the visibility at each of these bins. The visibility of the bitmap's bins is computed by projecting all occluding triangles onto the bitmap and marking those bits which overlap the triangle as occluded (i.e., painting the triangle onto the bitmap). After doing this for all triangles of T , we can convert the bitmap to the (coarser) visibility LUT bitmap. If the bitmap indicates that all bins are visible, the point c_i is convex and no visibility LUT is necessary.

3.2.4 On-line Visibility Testing

When performing localization, we need to test the visibility of a point before using it for refining the pose. If we're dealing with orthographic projection, then we can use the same viewing direction for all points (and previous aspect LUT methods become an option). For perspective projection, the viewing direction depends on the point's location in the image. Thus, for perspective, we must first compute the image projection of the point and compute \hat{v} using the image coordinates and the known camera parameters. \hat{v} must then be rotated into the model's coordinate system and then the point's coordinate system. These transformations can be composed for efficiency. Once \hat{v} is transformed to the point's local

coordinate system, we first perform the convex visibility test from Equation 3.1. If the test returns true and the point is concave, then the visibility LUT is checked as described in Section 3.2.2.

The visibility tests described in this section are very efficient. Practical requirements force us to make approximations; however, the approximations as discussed here typically err on the safe side: points may be declared invisible when in fact they are visible, however, it is not possible that a point is declared visible when it is geometrically invisible. Since our localization algorithm will have to cope with a significant number of errors, declaring a few visible points to be invisible will not have a big effect on the result. On the other hand, declaring a few invisible points to be visible is pointless as they will never be detected.

3.3 3D-3D Correspondence

Once the set of visible model points has been computed, we need to compute the correspondences between these model points and points in the range image. The correspondences will be used to evaluate the current estimate of the pose.

The correspondence problem is circular. One cannot easily find the correct correspondences without first knowing the pose of the object (i.e., knowing where to look), but our interest in finding correspondences is to aid our search for the correct pose of the object.

One of the points of this thesis is that the exact correspondences are not necessary to refine the pose. What is necessary are correspondences which lead to improvements in the pose estimate. When starting with a small pose error, local search can often provide a set of correspondences that are close enough to the correct correspondences to guide the search to the correct pose. What we desire is a quick local search which will usually produce matches to points which are nearby the correct match. As the pose estimation is improved, these matches will approach the correct matches.

Given a point on the model and a current pose estimate, we must select a corresponding point from our range image. The obvious approach is to find the nearest point in 3D (Cartesian) space (nearest neighbor or closest point). Mathematically, the closest image point y to a given point x can be defined as

$$y = \arg \min_{y \in D} \|x - y\|$$

where D is the set of three-dimensional data points in the image. The theoretical complexity of the nearest-neighbor search is $O(|D|)$. However, geometry is on our side. 3D objects occupy a volume in 3D space and their surfaces occupy 2D manifolds in 3D space. The surface tends to sparsely occupy the 3D volume. Thus, it is possible to partition the surface points in the 3D space to more efficiently search for the nearest points in practice. We now describe a technique which utilizes this characteristic distribution of surface points in 3D space to make the search efficient.

3.3.1 K-D Trees for Efficient Correspondence Search

The key to efficient search in two or more dimensions is a generalization of binary-search trees called *k-d trees* [42] (“kd” is an abbreviation for *k-dimensional* where k is an arbitrary integer greater than zero).⁶ The k-d tree is created by recursively splitting a data set down the middle of its dimension of greatest variance. The splitting continues until the leaf nodes contain a small enough number of data points. The result is a tree of depth $O(\log n)$ where n is the number of points stored in the k-d tree. Figure 3.7 shows an example of how 2D points would be separated into leaf nodes using this technique.

The k-d tree can be searched efficiently by following the appropriate branches of the tree until a leaf node is reached (as in binary-tree search). The distance to all points in the leaf node is computed. A hyper-sphere centered at the key point (with radius of the distance to the current closest point) can be used to determine which, if any, neighboring leaf nodes in the k-d tree must be checked for closer points. This test can be performed very efficiently. Once we tested all the data in leaf nodes which could possibly be closer, we are guaranteed to have found the closest point in the tree.

To use k-d trees and nearest-neighbor search for point sets in a particular coordinate system, we need a measure of *dissimilarity* between a pair of points. The dissimilarity, Δ , between k-d points \mathbf{x} and \mathbf{y} must have the form

$$\Delta(\mathbf{x}, \mathbf{y}) = F \left(\sum_{i=1}^k f_i(\mathbf{x}_i, \mathbf{y}_i) \right) \quad (3.6)$$

where the functions f_i are symmetric functions over a single dimension and functions f_i and F are monotonic. Most notable of these restrictions is that Δ must be composed by a sum of dissimilarities along each individual coordinate. All metric distances satisfy these conditions—most importantly, the Euclidean distance

$$\Delta(\mathbf{x}, \mathbf{y}) = \|\mathbf{x} - \mathbf{y}\|. \quad (3.7)$$

Such a dissimilarity allows us to partition the k-d tree for optimal expected time of the nearest-neighbor search.

Though its worst case complexity is still $O(n)$, the expected number of operations is $O(\log n)$, which will be the case if the data is evenly distributed—as is the case for surfaces in 3D space. The overhead involved is that the k-d tree of range-image points must be built prior to the search. This is a one-time cost per image of $O(n \log n)$ time since the points in the range image are static. For most cases of 3D localization, using closest points is sufficient. This is because surfaces sparsely occupy 3D space and points are not often found immediately above the surface of a visible object. As long as the majority of correspondences are to the correct surface in the image, localization will often succeed. The next section discusses an extension of this nearest-neighbor search to make the correspondence search a little more robust to initial position errors.

⁶The k-d tree [42] representation and nearest-neighbors search are extremely useful tools for many problems in computer vision, computer graphics, as well as computer science and artificial intelligence. K-d trees are used for many applications throughout this thesis, notably in Sections: 2.4, 4.3, 4.4, and 5.3.

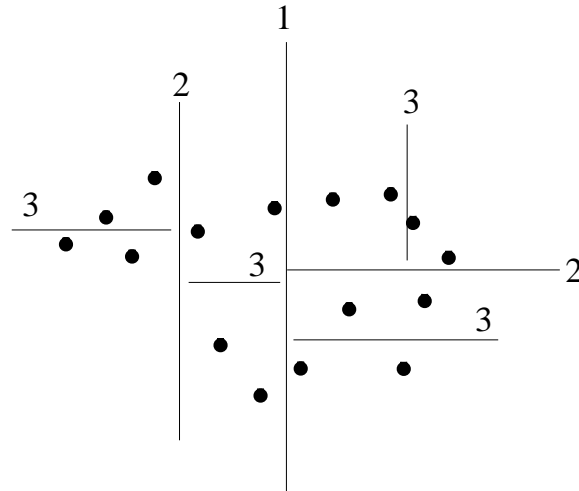


Figure 3.7: K-d tree subdivision of 2D points. Each line splits the data in half across the dimension of greatest spread. The number indicates which level of the tree at which the split occurs.



Figure 3.8: An example of nearest-neighbor correspondence (left) versus nearest neighbor+normal correspondence (right).

3.3.2 Attributes for Improving 3D-3D Correspondences

Besides proximity there are other possible constraints which we may want to consider when searching for correspondences. One such example is surface normal similarity—the surface normal of the model point should be similar to the normal of its matching image point. Figure 3.8 shows an example where, because of the error in the pose estimate, the simple nearest-neighbor search results in non-useful correspondences, while the addition of normal constraints on the local search improves the utility of the matching.

The ideal dissimilarity measure for comparing two unit vectors (normals) is the angle

between the two vectors

$$\Delta_\theta(\hat{\mathbf{n}}_1, \hat{\mathbf{n}}_2) = \cos^{-1}(\hat{\mathbf{n}}_1 \cdot \hat{\mathbf{n}}_2).$$

This metric is non-linear in terms of the two normals, n_1 and n_2 , that we are comparing and can not be decomposed into a dissimilarity function as specified in Equation 3.6.

As a matter of efficiency, we would prefer a linear metric that is of the form of Equation 3.7, such as the metric

$$\Delta_n(\hat{\mathbf{n}}_1, \hat{\mathbf{n}}_2) = \|\hat{\mathbf{n}}_1 - \hat{\mathbf{n}}_2\|. \quad (3.8)$$

We need to characterize Δ_n to determine if it is suitable for our purposes: whether Δ_n bears any relationship to our desired dissimilarity measure Δ_θ . Without loss of generality, we can rotate $\hat{\mathbf{n}}_1$ and $\hat{\mathbf{n}}_2$ such that

$$\hat{\mathbf{n}}'_1 = \mathbf{R} \hat{\mathbf{n}}_1 = [1 \ 0 \ 0]^T \quad (3.9)$$

$$\hat{\mathbf{n}}'_2 = \mathbf{R} \hat{\mathbf{n}}_2 = [\cos \theta \ \sin \theta \ 0]^T \quad (3.10)$$

where θ is the angle between $\hat{\mathbf{n}}_1$ and $\hat{\mathbf{n}}_2$. This step uses the facts that the normals are unit vectors and that 3D and angular distances are invariant to rigid rotation. Now we can simplify $\Delta_n(\hat{\mathbf{n}}_1, \hat{\mathbf{n}}_2)$ to

$$\Delta_n(\hat{\mathbf{n}}'_1, \hat{\mathbf{n}}'_2) = \|\hat{\mathbf{n}}'_1 - \hat{\mathbf{n}}'_2\| \quad (3.11)$$

$$= \sqrt{(\cos \theta - 1)^2 + \sin^2 \theta} \quad (3.12)$$

$$= \sqrt{\cos^2 \theta - 2 \cos \theta + 1 + \sin^2 \theta} \quad (3.13)$$

$$= \sqrt{2(1 - \cos \theta)} \quad (3.14)$$

$$= \sqrt{4 \sin^2 \frac{\theta}{2}} \quad (3.15)$$

$$= 2 \sin \frac{\theta}{2}. \quad (3.16)$$

Using the small-angle approximation for θ , $2 \sin \frac{\theta}{2} \approx \theta$ for small values of θ . If we plot this function (see Figure 3.9) over the valid range of θ , which is between 0 and 180 degrees, then we see that though this metric is not linear, it is close to linear and monotonic in θ —only diverging near 100 degrees. This is qualitatively sufficient for our purposes.

Our immediate goal is to efficiently compute correspondences. Proximity is our first criteria, normal similarity is another. Comparing both of these quantities at the same time is a difficult proposition with no absolute solution. For example, assume we have three points $\mathbf{x} = [0 \ 0 \ 0]^T$ with normal $\hat{\mathbf{n}} = [1 \ 0 \ 0]^T$, $\mathbf{x}_1 = [0 \ 0 \ 1]^T$ with normal $\hat{\mathbf{n}}_1 = [1 \ 0 \ 0]^T$, and $\mathbf{x}_2 = [0 \ 0 \ 0]^T$ with normal $\hat{\mathbf{n}}_2 = [0 \ 0 \ 1]^T$. How do we decide which of \mathbf{x}_1 and \mathbf{x}_2 is closer to \mathbf{x} ? \mathbf{x}_1 has a closer normal to point \mathbf{x} , while \mathbf{x}_2 is closer to \mathbf{x} in position; the choice is not clear.

The answer depends on what the application's requirements are. Returning to the previous example, is it more important to have a point which is closer or a point which has a closer normal vector? We have to decide which constraint is more important and how

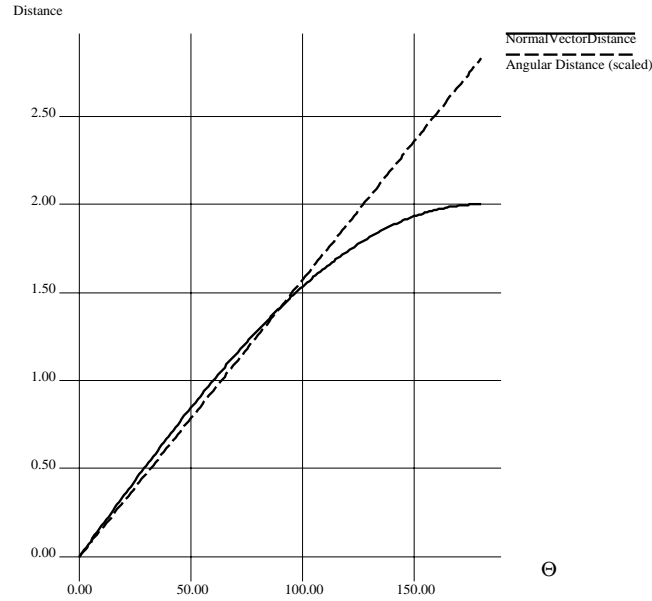


Figure 3.9: Plot of $\Delta(\hat{\mathbf{n}}_1, \hat{\mathbf{n}}_2)$ (the 3D distance between two unit vectors) with respect to θ (the angle between the two vectors). The (desired) angular distance is plotted for comparison.

much more important it is. We can do this easily by weighting either the point or normal and combining the vectors to form a higher-dimensional vector (e.g., six dimensions in the previous example).

Each data point is then stored in the k-d tree as the 6D vector

$$\mathbf{p} = [\mathbf{x}^T \ w \mathbf{n}^T]^T \quad (3.17)$$

$$= [x \ y \ z \ w n_x \ w n_y \ w n_z]^T \quad (3.18)$$

where w is the scaling factor for the normals. Applying the Euclidean distance metric to these points gives

$$\Delta(\mathbf{p}_1, \mathbf{p}_2) = \|\mathbf{p}_1 - \mathbf{p}_2\| \quad (3.19)$$

$$= \sqrt{\|\mathbf{x}_1 - \mathbf{x}_2\|^2 + \|w\hat{\mathbf{n}}_1 - w\hat{\mathbf{n}}_2\|^2} \quad (3.20)$$

$$= \sqrt{\|\mathbf{x}_1 - \mathbf{x}_2\|^2 + w^2 \|\hat{\mathbf{n}}_1 - \hat{\mathbf{n}}_2\|^2} \quad (3.21)$$

which is the desired effect. For example, if we decide that an error of one unit in distance is just as undesirable as an error of .25 units between normals, then we can scale the normals by setting $w = 4$ in the previous equation.

Thus, no modification of the k-d tree and nearest-neighbor search technique is required to add the additional orientation attribute for correspondence search. The weighting factor w is used to effect the desired constraint on the correspondences.

Depending upon other constraints of the system, other attributes can be added in a similar manner. Curvature is another possible attribute for improving the correspondence search in 3D-3D localization. The main drawback of curvature is that computing curvature from range images is a particularly noise-sensitive operation. Another potential source for attributes is color information. The key is to select attributes that can be reliably measured and are invariant to object pose and other possible scene variations such as lighting.

3.3.3 3D-3D Correspondence Summary

Given an estimate of the pose, we have shown how to efficiently compute nearest neighbor correspondences between visible model points and points in the range image. We have also shown how the nearest-neighbor search can be extended to consider attributes other than 3D positional information.

One must be reminded that for 3D-3D localization, the use of additional attributes for correspondence search will only be necessary in extreme situations. In general, if the pose is reasonably accurate, correspondences based on proximity will yield useful results (i.e., model point is matched to a point near the correct point of the object surface). This is due to the nature of range-image data. The points in the image sparsely occupy 3D space. Thus, as a point moves away from a surface, the space between the point and the surface is usually empty. If the initial position estimate is too far or, perhaps, the current pose estimate is closer to an object other than the desired object, then proximity may not be sufficient for effective localization. Using additional attributes for the correspondence search may alleviate the problem, but there are limits. If the pose estimate is nearly correct, proximity will almost always be sufficient for 3D-3D localization to converge to the true pose.

Now that we have a method for efficiently generating local correspondences, our goal is to use these correspondences to improve our estimate of the pose; this is the topic of the next section.

3.4 3D-3D Pose Optimization

This section discusses a variety of techniques dealing with the computation of pose of a 3D object (point set) with respect to observed 3D points. We refer to this general area as *3D-3D pose optimization* which includes the problems of 3D-3D pose estimation and 3D-3D pose refinement.

The desired results of pose estimation and pose refinement are much the same: find the pose of the object in the image. The assumptions are quite different; pose estimation is *given a set of correspondences* while pose refinement is *given an image and a rough initial pose estimate*. For pose estimation, the given correspondences are assumed to be correct and are fixed. Pose estimation is very much a static problem. Because of this, the pose-estimation

problem is well suited to abstract formulations and theoretical analysis. In contrast, the problem of primary interest here, localization, is a dynamic operation involving possibly all information available from the image.

It must be noted that there is a medium ground between pose estimation and pose refinement—hybrids of pose estimation and pose refinement. Some examples include the work of Grimson [52, 49] and Lowe [85, 84, 89, 90] in which the pose is iteratively computed by a sequence consisting of pose estimation and correspondence search. During each iteration a new correspondence (found using local search) is added to the previously accumulated set of correspondences and pose estimation is performed on the whole set. The goal is to gradually increase the accuracy of the pose estimate by adding constraints (correspondences).

Instead of jumping straight to our solution for 3D-3D localization, we will build up to it by first discussing a simpler version of the problem—pose estimation. The form of the pose-estimation problem of interest here is 3D-3D pose estimation—to compute the pose of an object given a number of correspondences between a set of measured 3D (image) points and a set of 3D points of our prior model. The 3D-3D localization techniques presented in this thesis borrow much from the theory and practice of 3D-3D pose estimation.

We begin by considering the problem of 3D-3D pose estimation—a problem which has a long history [36, 1, 66, 58] and is generally considered to be solved.

3.4.1 3D-3D Pose Estimation

The 3D-3D pose-estimation problem is to compute the pose (a rigid transformation) which aligns the 3D model points \mathbf{x}_i with their corresponding image points \mathbf{y}_i where $i = 1, \dots, n$. The rigid transformation is specified by the matrix-vector pair $\langle \mathbf{R}, \mathbf{t} \rangle$ where \mathbf{R} is a 3×3 rotation matrix and \mathbf{t} is a 3D translation vector.

Each correspondence provides three linear constraints on our unknown pose variables via the rigid transformation equation

$$\mathbf{y}_i = \mathbf{R}\mathbf{x}_i + \mathbf{t}.$$

In general, the sensed points \mathbf{y}_i will be contaminated by noise:

$$\mathbf{y}_i = \mathbf{y}_i^{actual} + \beta$$

where β is a random 3D variable. Assuming that β is unbiased (i.e., β 's mean is $[0 \ 0 \ 0]^T$) and follows a normal distribution (i.e., $P(\beta) \propto e^{-\frac{\beta^T \beta}{2\sigma^2}}$), then the optimal transformation is the least-squared error solution—the values $\langle \mathbf{R}, \mathbf{t} \rangle$ that minimize

$$f(\mathbf{R}, \mathbf{t}) = \sum_i \|\mathbf{R}\mathbf{x}_i + \mathbf{t} - \mathbf{y}_i\|^2. \quad (3.22)$$

This seems like an easy enough problem to solve— f is quadratic in its input parameters—until we consider rotation. A rotation in 3D space has only three degrees of freedom, yet

is represented in our linear formula by a 3×3 matrix \mathbf{R} . The three degrees of freedom restrict the values of \mathbf{R} in a non-linear way. \mathbf{R} must satisfy the constraints

$$\mathbf{R}\mathbf{R}^T = \mathbf{I} \quad (3.23)$$

$$|\mathbf{R}| = 1 \quad (3.24)$$

where \mathbf{I} is the 3×3 identity matrix. The first constraint requires the rows of \mathbf{R} to be orthonormal. The second constraint ensures that the rotation is rigid and not a reflection. Capturing all these constraints while taking advantage of the linear matrix form of rotation is difficult.

The generally accepted solution to the rotation problem is to represent the rotation using a unit 4-vector called a quaternion. A quaternion is composed of a 3-vector $[u \ v \ w]^T$ and a scalar s . We will use the 4-vector

$$\mathbf{q} = [u \ v \ w \ s]^T$$

to denote the rotation. The rotation matrix, \mathbf{R} , corresponding to \mathbf{q} is denoted by $\mathbf{R}(\mathbf{q})$ (refer to Appendix B for the derivation).

The 7-vector

$$\mathbf{p} = [\mathbf{q}^T \ \mathbf{t}^T]^T$$

denotes the complete set of pose parameters/rigid transformation. Now we have three equivalent notations for the pose which will be used interchangeably: $\langle \mathbf{R}, \mathbf{t} \rangle$, \mathbf{p} , and $\langle \mathbf{R}(\mathbf{q}), \mathbf{t} \rangle$.

The best intuitive description of a quaternion is that the 3-vector of the quaternion represents the axis of rotation and the scalar represents the angle of rotation. This is not entirely accurate, as the quaternion is not simply an axis and angle representation. Quaternions have many nice mathematical properties which have proven useful for deriving several solutions as will be described below. For the reader's convenience, an overview of quaternions is provided in Appendix B.

The importance of the quaternion representation for the 3D-3D pose-estimation problem was first demonstrated by Sanso [116] in the field of photogrammetry and then later introduced to the field of computer vision by the work of Hebert and Faugeras [36] and Horn [66]. They independently showed that a closed form solution for $\langle \mathbf{R}, \mathbf{t} \rangle$ existed by formulating the minimization of Equation 3.22 using quaternions to represent rotation. Their methods are slightly different, but we will describe the general idea central to both. First, both sets of points \mathbf{x}_i and \mathbf{y}_i are translated so that the centers of gravity of both translated sets are located at the origin. The centered points are denoted by \mathbf{x}_i^c and \mathbf{y}_i^c respectively. Using the centered points we can solve for the rotation quaternion \mathbf{q} independent of the translation \mathbf{t} . The optimal quaternion can be computed as the eigenvector corresponding to the maximum eigenvalue of a matrix composed from the points \mathbf{x}_i^c and \mathbf{y}_i^c . The reader should consult [116, 36, 66] for the derivation of this matrix. With \mathbf{q} and, hence, \mathbf{R} determined, \mathbf{t} is easily determined to be the difference between the centroid of the point set \mathbf{y}_i and the centroid of the rotated point set $\mathbf{R}\mathbf{x}_i$.

Horn also showed that the closed-form solution generalizes to weighted least squares as well. Haralick [58] and Arun [1] presented a closed-form solution for 3D-3D pose estimation which compute \mathbf{R} directly using singular value decomposition of a matrix composed from the points \mathbf{x}_i^c and \mathbf{y}_i^c . The quaternion formulation is favored over the SVD formulation which is not as robust, numerically speaking.

If the errors in the observed data are not normally distributed, least-squares estimation may be inappropriate as the resulting estimate is optimal only for normally distributed errors. It may be necessary to consider a different objective function which is the optimal estimator with respect to the error distribution of the data. Also, if we have statistically significant errors or outliers, then the closed-form solutions for $\langle \mathbf{R}, \mathbf{t} \rangle$ are no longer useful. In fact, least-squares estimation will usually fail when outliers are present as the estimation is very sensitive to large errors.

Unfortunately, the existence of outliers is the rule for computer vision applications rather than the exception. When viewing objects, it is often true that parts of the object surfaces are occluded by other objects in the scene or shadows. When points on an object are occluded or go undetected, the errors for the corresponding point of the model will be much larger than the errors for visible points of the object. This is because these unobserved points violate the assumption that the observation actually corresponds to a point in our model.

Since the closed form solution is no longer valid, an iterative approach is probably necessary to solve this problem. The best known method for iterative search is gradient-descent search. The basic algorithm is to follow the path of best improvement (the gradient direction) until no local move improves the estimate (i.e., until the minimum of our objective function is reached).

There are a couple of well known problems with gradient-descent techniques. First, they assume a starting position is available. This is not a problem for pose-refinement since a starting point is already assumed. Second, gradient descent is a slave to local minima. Depending on the starting point, the desired minima may or may not be reachable. For example, Figure 3.10 shows an example search of a one dimensional function with two starting positions, s_1 and s_2 that lead to different local minima r_1 and r_2 . In this example, r_2 is the desired result. The range $[x_{min}, x_{max}]$ denotes the set of starting points that will lead to the solution r_2 ; this range is referred to as r_2 's basin of attraction. To ensure a high probability of success, we would like a good initial starting guess (i.e., $|s - r|$ is small) and a wide basin of attraction (i.e., $|x_{min} - x_{max}|$ is large). In general, the size of the basin of attraction and the initial error will depend on the complex interaction of the model and data points that are matched as well as the number and size of any outlier correspondences.

We can now step back and examine how our localization problem relates to the pose estimation problem. The main similarity is that local minima will be a problem, since we will in general have some number of incorrect correspondences to deal with. However, the localization problem is still more difficult. First, we are not given absolute correspondences, only a rough pose as a starting point of the search. Correspondences are acquired using the efficient local search described in Section 3.3; however, it is unlikely that any significant portion of these correspondences will be correct unless the pose estimate is also correct.

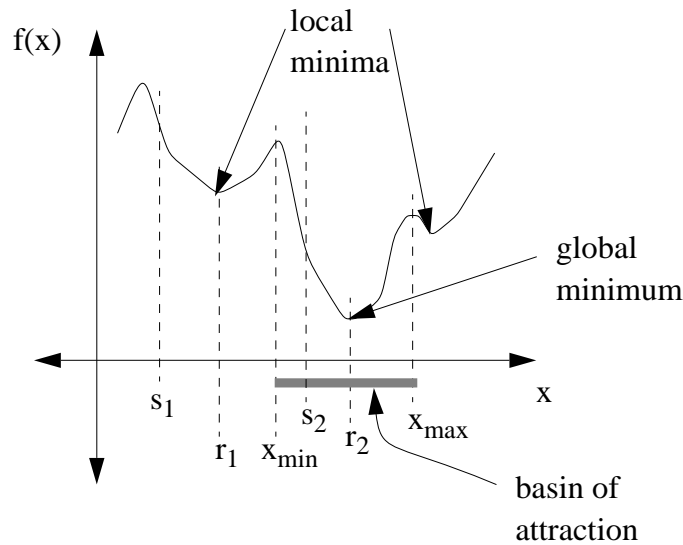


Figure 3.10: Examples of local versus global minima and basins of attraction.

We must deal with two problems:

- Poor initial correspondences: we must assume that at the start of the search most of the correspondences will not be correct.
- Outliers: even when most of the correspondences are correct, we must be able to handle outliers gracefully.

The next section will describe methods from the field of robust statistics to handle outliers. The methods described there will lead to an approach that also overcomes the problem of poor initial correspondences.

3.4.2 Robust Estimation

We return to the pose estimation problem described in the previous section. We are given a set of n observed points y_i and corresponding model points x_i , and we want to compute the pose $\langle \mathbf{R}, \mathbf{t} \rangle$ which will align the two sets. The additional complication is that some percentage of the n correspondences will be incorrect, and we do not know which ones are incorrect *a priori*. The errors for these incorrect correspondences will not fit a normal distribution that describes the expected errors when comparing a point with its observation.

We look to the field of robust statistics [67, 96] for a solution to this problem. Robust statistics provides solutions to the problem of estimating statistics reliably despite data contaminated by outliers—data which do not belong to the desired sample population.

There are three classes of robust-estimation techniques that we will consider here: outlier thresholding, median/rank estimation, and M-estimation.

Outlier Thresholding

The first class of solutions, outlier thresholding, is the simplest and, hence, the most prominent robust-estimation technique used in computer-vision applications such as localization. Outlier thresholding is also the most efficient of the three methods, but, unfortunately, the most unreliable. The basic idea is to estimate the standard deviation, σ , of the errors in the data and eliminate data points which have errors outside the range $[-k\sigma, k\sigma]$ where k is typically greater than or equal to 3. One problem with this is that an estimate of σ may be grossly incorrect if there are many outliers. Another problem is that outliers with errors less than $k\sigma$ are possible. If a large number of these outliers exist, then least-squares estimation will still be inaccurate. Another popular (and somewhat similar technique) is to find the first mode of the distribution of data and throw out the data past that point [151]. This assumes that the number of outliers is much smaller than the correct data and that the outliers do not harmfully alter the shape of the mode.

The essential problem with these methods is that a hard threshold must be used to eliminate the outliers. This is an unfortunate situation since regardless of where the threshold is chosen, some number of valid data points will be classified as outliers and some number of outliers will be classified as valid. In this sense, it is unlikely that a perfect method for selecting the threshold exists unless the outliers (or perhaps their distribution) are known *a priori*. As will be discussed in Sections 3.4.2 and 3.6, a hard threshold also creates a highly non-linear (non-smooth) objective function which causes difficulties for numerical optimization techniques.

The above methods may not always be useful for the localization problem since the initial correspondences and pose are likely to be incorrect anyway. Initially, these errors may not have any unimodal distribution and the valid correspondences and outliers may have indistinguishable error values.

Median/Rank Estimation

The second class of robust estimators that we will discuss is the median/rank estimation methods. The basic idea is to select the median or k th value (for some percentile k) with respect to the errors for each observation and use that value as our error estimate. The logic behind this is that the median is almost guaranteed not to be an outlier as long as half of the data is valid. In fact, median estimation has the optimal breakdown point of any estimator (smallest percentage of outliers that are capable of forcing the estimate outside some finite range).

An example of median estimators is the least-median-of-squares method (LMedS) [96, 79]. LMedS computes the parameters \mathbf{p} which minimizes the median of the squared error:

$$\mathbf{p} = \arg \min_{\mathbf{p}} \left(\text{med}_i z_i(\mathbf{p})^2 \right)$$

where $z_i(\mathbf{p})$ is the error in the i th observation and med_i returns the median value of its argument over all values of i . Generally, to solve this problem, we must perform exhaustive search of possible values \mathbf{p} by testing least-squares estimates of \mathbf{p} for all possible combinations of matches from model to observed data. Techniques like randomization and Monte Carlo methods are necessary to make searches such as LMedS feasible. The need to exhaustively try all combinations of estimates \mathbf{p} underscores a major limitation of median methods for localization. Localization is based on the idea that local search can solve the task efficiently. As will become clear later in this section, the efficiency is gained via local optimization of a smooth objective function. LMedS and other median methods are not well suited to this type of search, since the objective is the error from a single data point.

LMedS bears a striking resemblance to a couple of classic methods in pose optimization and object recognition: random sample consensus (better known as RANSAC) by Fischler and Bolles [38], the alignment method of Huttenlocher and Ullman [70], and the interpretation-tree (IT) search of Grimson and Lozano-Perez [52]. The common idea is that combinations of subsets of the data are used to estimate the (pose) parameters, after which the evaluation of the parameters can be performed. In the case of RANSAC, alignment, and IT search, the evaluation involves checking the correspondence of other model points with the observed data set, while in LMedS it involves measuring the median of the errors for all the model points. These methods solve a slightly more difficult problem than localization, however, since no set of correspondences or initial pose estimate is assumed.

While median/rank techniques can be very robust, they are also extremely computationally expensive.

M-estimation

The third and final class of robust-estimation techniques which we will discuss is M-estimation. M-estimation is a generalization of least squares. The “M” refers to maximum-likelihood estimation.

The general form of M-estimators allows us to define a probability distribution which can be maximized by minimizing a function of the form

$$E(z) = \sum_i \rho(z_i) \quad (3.25)$$

where $\rho(z)$ is an arbitrary function of the errors, z_i , in the observations. The equivalent probability distribution to $E(z)$ is

$$P(z) = e^{-E(z)}$$

which, not coincidentally, is maximized by minimizing $E(z)$. Thus, the M-estimate is the maximum-likelihood estimate of $P(z)$. Our choice of $\rho(z)$ determines $P(z)$ which is our prior model of the distribution of errors in our observations. It also determines whether our estimate will be sensitive to unusually large numbers of outliers.

As described previously, least-squares estimation is very sensitive to outliers. Least-squares estimation corresponds to M-estimation with $\rho(z) = z^2$ —equivalent to performing maximum likelihood estimation of

$$P(z) = e^{-\sum_i z_i^2}$$

which is readily identifiable as the probability of n independent observations of a normally distributed variable.

We can find the parameters \mathbf{p} that minimize E by taking the derivative of E with respect to \mathbf{p} and setting it to 0:

$$\frac{\partial E}{\partial \mathbf{p}} = \sum_i \frac{\partial \rho}{\partial z_i} \cdot \frac{\partial z_i}{\partial \mathbf{p}} = 0$$

By substituting

$$w(z) = \frac{1}{z} \frac{\partial \rho}{\partial z}$$

we get

$$\frac{\partial E}{\partial \mathbf{p}} = \sum_i w(z_i) z_i \frac{\partial z_i}{\partial \mathbf{p}}. \quad (3.26)$$

which, if we momentarily forget that w is a function of z , has the same form as if $\rho(z) = wz^2$ —readily recognized as weighted-least squares. In this interpretation, the term $w(z)$ measures the weight of the contribution of errors of magnitude z towards a WLS estimate.

The weight term can also be interpreted as confidence in a given observation. For pure least squares, we have $w(z) = 1$ —indicating that each error has equal confidence, regardless of how large the error. A weight function, $w(z)$, can be defined that has the effect as outlier thresholding:

$$w(z) = \begin{cases} 1 & |z| \leq \theta \\ 0 & |z| > \theta \end{cases}. \quad (3.27)$$

In words, observations which have errors above the threshold θ are ignored. Thus, we have another way of specifying an M-estimator, as a weight function.

There are many other possible choices of $\rho(z)$ to reduce the sensitivity to outliers on the estimation. Table 3.1 lists several possible functions that can be used for M-estimation. Plots of the respective weight functions are shown in Figure 3.11 for comparison. All except the Gaussian function (least squares) can be considered for robust estimation.

The five robust M-estimators—the threshold function, Sigmoid function and functions by Tukey, Huber, and Lorentz—described in Table 3.1 strongly weight observations with small errors while discounting observations with large errors. Looking at the plots of the equivalent probability distributions in Figure 3.12, we see that the distributions are all similar to a normal distribution near the center of the distribution, but have noticeably larger tails (i.e., a higher prior likelihood for large errors).

In what follows, when we refer to robust M-estimation, we will be referring to the minimization of a function of the form of Equation 3.25 where $\rho(z)$ is derived from one

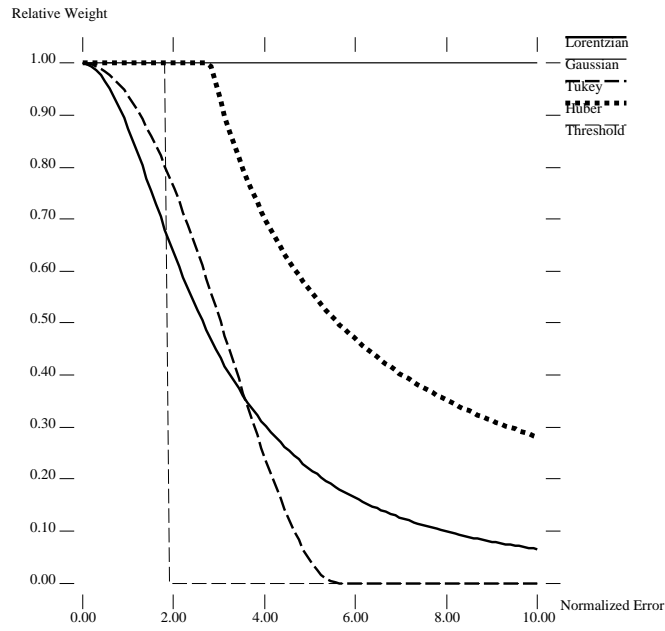


Figure 3.11: Plots of $w(z)$ for each of the M-estimators listed in Table 3.1 .

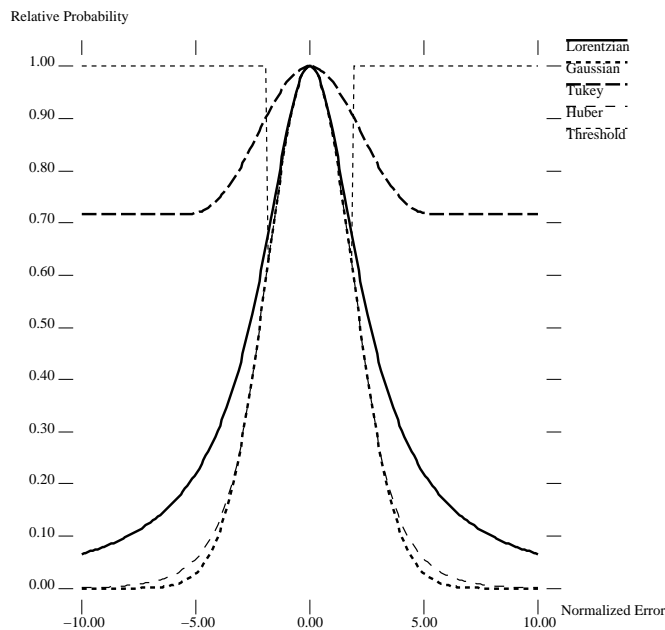


Figure 3.12: Plots of $P(z)$ for each of the M-estimators listed in Table 3.1 .

Function Name	$w(z)$	Comments
Gaussian	1	least-squares estimation
Threshold	$w(z) = \begin{cases} 1 & z \leq \sigma \\ 0 & z > \sigma \end{cases}$	outlier thresholding, σ is the threshold
Lorentz's function	$w(z) = \frac{1}{(1+\frac{1}{2}(\frac{z}{\sigma})^2)}$	σ controls width of distribution [111]
Tukey's function	$w(z) = \begin{cases} (1 - (\frac{z}{\sigma})^2)^2 & z \leq \sigma \\ 0 & z > \sigma \end{cases}$	σ controls width of distribution [137, 58]
Huber's function	$w(z) = \begin{cases} 1 & z \leq \sigma \\ \frac{\sigma}{ z } & z > \sigma \end{cases}$	σ controls width of distribution [67]
Sigmoid function	$w(z) = \frac{1}{1+e^{\beta(z-c)}}$	β controls falloff and c is the center of the falloff, related to mixture of Gaussian and uniform background [62, 143]

Table 3.1: Table of weight functions for M-estimation.

of the five robust weight functions described above or a function with similar weighting characteristics to one of the above five functions in Table 3.1.

M-estimators are often loosely mixed with weighted least-squares (WLS) estimation. Haralick et al. [58] use an iterative reweighting technique based on WLS for the optimal pose with respect to a robust M-estimator. In our experience, weighted least squares is only appropriate when the correspondences are fixed as is standard for pose-estimation problems.

As one can see, the weight term in M-estimation is a function of the pose p . If we attempt to solve the M-estimation as a WLS problem, the function being minimized is different from the objective function, and the computed step may take the pose into a different minima. Thus the closed form (WLS) solution is no longer valid. The problem is that if the magnitude of the derivative of the weight function is great, small changes in the pose will have large changes on the function being minimized. A proper implementation of M-estimation is likely more computationally intensive than outlier thresholding, but it is likely to be better behaved.

3.4.3 Robust Pose Refinement

Our original problem is to solve for the pose, \mathbf{p} , of an object given a set of correspondences between visible object points \mathbf{x}_i and image points \mathbf{y}_i . Since we know that we will have many outliers in our set of correspondences, we will use a robust M-estimator to solve for \mathbf{p} . We will minimize

$$E(\mathbf{p}) = \frac{1}{|V(\mathbf{p})|} \sum_{i \in V(\mathbf{p})} \rho(z_i(\mathbf{p})) \quad (3.28)$$

where $V(\mathbf{p})$ is the set of visible model points for the model pose parameters \mathbf{p} (computed using the methods of Section 3.2), $z_i(\mathbf{p})$ is the 3D distance between the i th pair of correspondences. We define

$$z_i(\mathbf{p}) = \|\mathbf{R}(\mathbf{q})\mathbf{x}_i + \mathbf{t} - \mathbf{y}_i\|$$

where $\mathbf{R}(\mathbf{q})$ is the 3x3 rotation matrix for the rotation component of \mathbf{p} and \mathbf{t} is the translation component. Since there is no closed form solution for this problem, an iterative optimization technique such as gradient descent is necessary.

Unfortunately, minimizing E is not so straightforward. The corresponding image points, \mathbf{y}_i , are a function of \mathbf{p} as well⁷:

$$\mathbf{y}_i = \mathbf{y}(\mathbf{x}_i, \mathbf{p}) = \arg \min_{\mathbf{y} \in D} \|\mathbf{R}(\mathbf{q})\mathbf{x}_i + \mathbf{t} - \mathbf{y}\|$$

Ignoring this fact can result in inefficiency and possibly incorrect results. This complicates the minimization algorithm in practice.

The whole idea of localization is that we can start with a crude set of correspondences and gradually converge to the correct correspondences and at the same time find the true pose of the object in the image—much like active contour approach of Witkin, Kass and Terzopoulos [75, 134] and the ICP algorithm of Besl and McKay [6]. Thus, as we search the pose space, an improvement in E should correspond to an improvement in \mathbf{p} as well as an improvement in the correspondences. If we hold the correspondences fixed for any search, we are minimizing a different function.

Fortunately, with a little work, we can perform the gradient-descent search to correctly minimize the desired function E . The basic algorithm for gradient descent search of a function $f(x)$ with initial guess x_0 is

Algorithm *GradientDescent*

Input: starting point \mathbf{x}

Input: function $f(\mathbf{x})$

Input: gradient of f , $\nabla f(\mathbf{x})$

Output: the location, \mathbf{x}_f of the local minimum of $f(\mathbf{x})$

1. **repeat**

⁷If attributes are used to find correspondences as described in Section 3.3.2, then this function would have to include the additional error term in this equation.

2. $f \leftarrow f(\mathbf{x})$
3. $\mathbf{dx} \leftarrow -\nabla f(\mathbf{x})$
4. $\lambda \leftarrow \arg \min_{\lambda} f(\mathbf{x} + \lambda \mathbf{dx})$
5. $\mathbf{x} \leftarrow \mathbf{x} + \lambda \mathbf{dx}$
6. **until** $f - f(\mathbf{x}) < \epsilon$
7. **return** \mathbf{x}

The crucial step of Algorithm *GradientDescent* is the computation of λ in Line 4—generally referred to as a line minimization [111]. If we take a step λ in the gradient direction, a proper evaluation of E requires that we reevaluate the correspondences at that step to determine if E decreases with respect to the correspondences at that point. By doing so, the correspondences become *dynamic*, and the search begins to simulate the effect of model points floating in a potential field [75, 134, 29, 104, 133] in which the only force felt by each point is from the attraction of the nearest point—its correspondence.

Another complication is that the set of points that are visible in the model is also a function of \mathbf{p} . With a slight change of \mathbf{p} , we could see a large change in the set of visible points. This can cause great problems for a line-minimization routine since changes in visibility will cause discontinuous jumps in E as λ varies. Even though E (Equation 3.28) is normalized, adding and removing many observations will often have large changes on the value of E . For example, consider a cube rotating in front of a camera. As the cube rotates, different sides become visible. The equivalent to this in localization is when the localization search rotates the model to improve the pose estimate. As the estimate of the model's orientation changes, surfaces of the model may make the transition from occluded to visible and vice versa. This will cause the value of E to abruptly change. Figure 3.13 shows an example of this effect with a cross section of a cube and the value of E as the orientation changes.

To implement line minimization efficiently and reliably, $E(\mathbf{p})$ must be smooth along the line (at least within the current basin of attraction). If we allow $V(\mathbf{p})$ to vary, then we cannot achieve smoothness during line-minimization: this is an unfortunate fact which we must accept. Our solution is to compute the visibility set, $V(\mathbf{p})$, before the line minimization and keep this set fixed during the line minimization.

One may wonder what the effect of changing correspondences will have on the smoothness of $E(\mathbf{p})$. The answer is that $E(\mathbf{p})$ is *usually* smooth when a change of correspondence occurs. This is because the changes of correspondences usually occur continuously with respect to z_i . For example, consider the minimum distance z between point \mathbf{x} and two other points \mathbf{x}_0 and \mathbf{x}_1 . If point \mathbf{x} is in between \mathbf{x}_0 and \mathbf{x}_1 , the distance function, $z(\mathbf{x})$, is maximum when the point is halfway between the two points and linearly decreases as it approaches either of the points (see Figure 3.14). The important fact is that the function is continuous as the point moves. It is not C^1 as there are first derivative discontinuities at each point and the midpoint between them as can be seen in the graph of z in Figure 3.14.

When using correspondences with attributes (e.g., points and normals as described in Section 3.3.2), it is indeed possible that the minimum distance function will have discontinuities. For example, we can modify the previous example to give each point a normal as

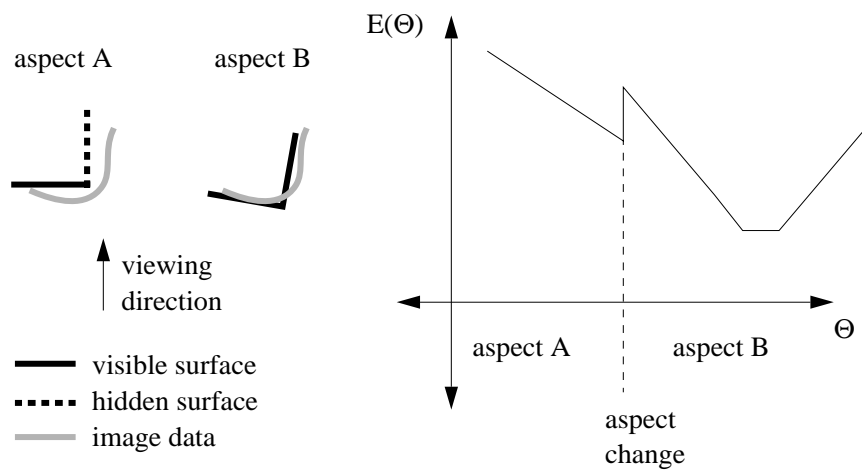


Figure 3.13: Example of the fluctuation of E due to changes in the pose and the set of visible points. The graph shows the value of E as the object rotates from one aspect to another with respect to the camera.

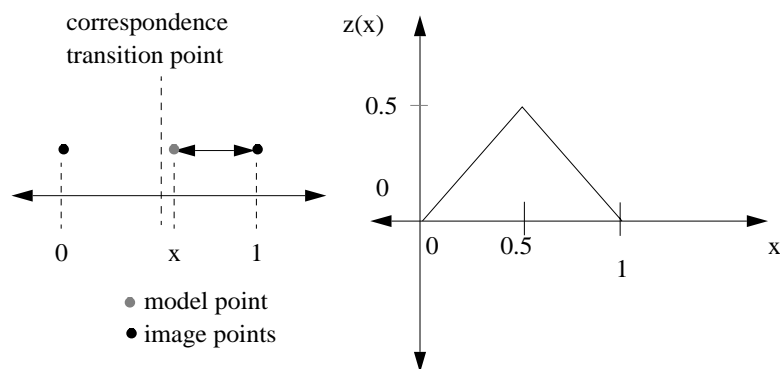


Figure 3.14: The minimum distance function with respect to the dynamic correspondences.

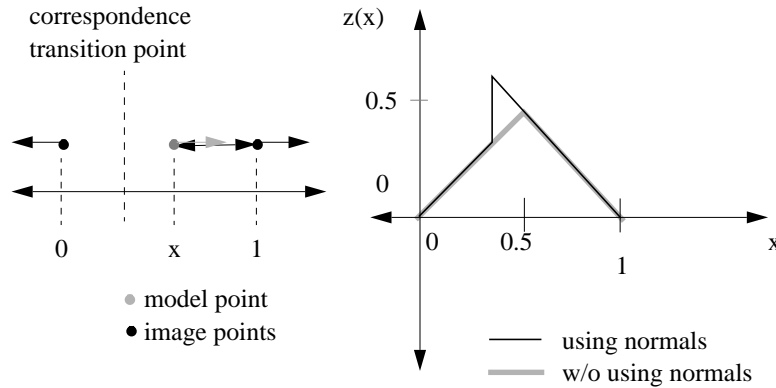


Figure 3.15: Correspondences which compare normals can create discontinuities in the distance function z . Note how the transition point (where the correspondences switch) has moved due to the influence of the normal constraint.

an attribute. If the two points have different normals, then the point at which the correspondence shifts is no longer the midpoint (depending on the weight of the normal constraint). Figure 3.15 shows this effect. Point x has a left facing normal and is, thus, more strongly attracted to x_0 , whose normal is also facing left. Thus, as x approaches x_1 , the transition point—the point where x becomes closer to x_1 than x_0 in the 6D point and normal space—is closer to x_1 than x_0 since the correspondence prefers x_0 because of its similar normal. At some point, the proximity to x_1 will overwhelm the difference in surface normal directions. As can be seen in Figure 3.15, the minimum distance function has a noticeable discontinuity at the transition point. However, such discontinuities are relatively small compared to the discontinuities caused by changes in the set of visible points.

To complete our minimization algorithm, the only thing remaining to discuss is the computation of the gradient of $E(\mathbf{p})$. The presence of dynamic correspondences does not cause any problems since the gradient is an instantaneous measure and the likelihood of a model point lying exactly on a discontinuity is small enough to ignore.

When computing the gradient of $E(\mathbf{p})$ (Equation 3.28), we have from Equation 3.26

$$\frac{\partial E}{\partial \mathbf{p}} = \sum_i w(z_i) z_i \frac{\partial z_i}{\partial \mathbf{p}}.$$

It turns out that we can greatly simplify the following derivations with a few algebraic manipulations. First, instead of using

$$z_i(\mathbf{p}) = \|\mathbf{R}(\mathbf{q})\mathbf{x}_i + \mathbf{t} - \mathbf{y}_i\|$$

we redefine z_i to be

$$z_i(\mathbf{p}) = \|\mathbf{R}(\mathbf{q})\mathbf{x}_i + \mathbf{t} - \mathbf{y}_i\|^2.$$

This only requires a slight change in $w(z)$ to compensate for having arguments that are the square of the distance rather than the distance itself. We will also assume that the model points have been pre-rotated so that the current quaternion is $\mathbf{q}_I = [0 \ 0 \ 0 \ 1]^T$ which has the property that $\mathbf{R}(\mathbf{q}_I) = \mathbf{I}$. This allows us to take advantage of the fact that the gradient of $\mathbf{R}(\mathbf{q})\mathbf{x}$ has a very simple form when evaluated at $\mathbf{q} = \mathbf{q}_I$:

$$\left. \frac{\partial(\mathbf{R}\mathbf{x})}{\partial\mathbf{q}} \right|_{\mathbf{q}_I} \mathbf{x} = 2\mathbf{C}(\mathbf{x})^T. \quad (3.29)$$

where $\mathbf{C}(\mathbf{x})$ is the 3×3 , skew-symmetric matrix (i.e., $\mathbf{C}(\mathbf{x}) = -\mathbf{C}(\mathbf{x})^T$) of the vector \mathbf{x} (the derivation of Equation 3.29 is presented in Appendix B). Multiplying by this matrix and a vector is equivalent to taking the cross product of \mathbf{x} and that vector, i.e.,

$$\mathbf{C}(\mathbf{x})\mathbf{v} = \mathbf{x} \times \mathbf{v}.$$

Using these facts, $\frac{\partial z}{\partial \mathbf{p}}$ can easily be derived:

$$\frac{\partial z}{\partial \mathbf{p}} = 2(\mathbf{R}(\mathbf{q})\mathbf{x}_i + \mathbf{t} - \mathbf{y}_i) \frac{\partial(\mathbf{R}(\mathbf{q})\mathbf{x}_i + \mathbf{t} - \mathbf{y}_i)}{\partial \mathbf{p}} \quad (3.30)$$

$$= \begin{bmatrix} 2(\mathbf{x}_i + \mathbf{t} - \mathbf{y}_i) \\ 4\mathbf{C}(\mathbf{x})^T(\mathbf{x}_i + \mathbf{t} - \mathbf{y}_i) \end{bmatrix} \quad (3.31)$$

$$= \begin{bmatrix} 2(\mathbf{x}_i + \mathbf{t} - \mathbf{y}_i) \\ -4\mathbf{x}_i \times (\mathbf{t} - \mathbf{y}_i) \end{bmatrix}. \quad (3.32)$$

Thus, very simple formulas define the gradient with respect to the rotation quaternion and translation vector.

We now have covered the point visibility problem, the correspondence problem and pose optimization as they relate to the 3D-3D localization problem. In this section, we described an optimization method, gradient descent with dynamic correspondences, that solves the localization problem using a robust M-estimator. We can now put together the methods discussed so far into a complete algorithm for performing robust 3D-3D localization.

3.5 Putting It Together: 3D-3D Localization

We have described the principal components of our 3D-3D localization algorithm: point visibility, point-to-point correspondence, and robust pose optimization.

Here, we put everything together to present a pseudocode description of our complete 3D-3D localization algorithm:

Algorithm *3D-3D Localization*

Input: initial pose \mathbf{p}

Input: range image point set D

Input: object localization model

Output: final pose \mathbf{p}

1. create k-d tree for the points D
2. **repeat**
3. compute the set of visible model points: $V(\mathbf{p})$
4. $E_0 \leftarrow E(\mathbf{p})$
5. $\mathbf{dp} \leftarrow -\nabla E(\mathbf{p})$
6. $\lambda \leftarrow \arg \min_{\lambda} E(\mathbf{p} + \lambda \mathbf{dp})$
7. $\mathbf{p} \leftarrow \mathbf{p} + \lambda \mathbf{dp}$
8. **until** $E_0 - E(\mathbf{p}) < \epsilon$
9. **return** \mathbf{p}

The above algorithm is more or less a complete description of the localization as we have implemented it. There are however a few practical details which were omitted for clarity and are discussed below.

3.5.1 Scale's Effect on Gradient Directions

A problem affecting gradient-based search methods is that the amount of change due to rotation and translation is related to the scale of the data. The problem is that a unit change of rotation results in a change in the error that is dependent on the scale of the vector being rotated. At the same time, a unit change in translation is independent of the scale of the data. Roughly, as the scale increases, the sensitivity of the rotation parameters increases at a rate that is much faster than that of the translation parameters. This is not a good situation for a gradient-based search. The implication is that if we have a given problem and simply scale the data, the algorithm which uses gradients will follow two different solution paths when rescaled.

From the derivation of the rotational Jacobian in Equation 3.29, one can quickly derive the gradient of the following example, a typical squared error between a point \mathbf{x} at pose $\langle \mathbf{q}, \mathbf{t} \rangle$ and an observation \mathbf{y}

$$f = (\mathbf{R}(\mathbf{q}_c) \mathbf{x} + \mathbf{t} - \mathbf{y})^2.$$

Assuming that $\mathbf{q} = \mathbf{q}_I$ (i.e., the point \mathbf{x} has already absorbed the current rotation), the rotational gradient is of the form

$$\frac{\partial f}{\partial \mathbf{p}} = 4\mathbf{C}(\mathbf{x})^T(\mathbf{x} + \mathbf{t} - \mathbf{y}) \quad (3.33)$$

$$= -4\mathbf{x} \times (\mathbf{t} - \mathbf{y}) \quad (3.34)$$

and the translational gradient is of the form

$$\frac{\partial f}{\partial \mathbf{t}} = 2(\mathbf{x} + \mathbf{t} - \mathbf{y}). \quad (3.35)$$

If the scale of our data, \mathbf{x} and \mathbf{y} , (assume \mathbf{t} is zero, or equivalently that it is already subtracted from \mathbf{y}), is roughly Σ , then

$$\left| \frac{\partial f}{\partial \mathbf{p}} \right| \approx \sin \theta |\mathbf{x}| |\mathbf{y}| \propto \Sigma^2$$

using the relation between the angle, θ , between two vectors and the magnitude of their cross product, while

$$\left| \frac{\partial f}{\partial t} \right| \approx |\mathbf{x} - \mathbf{y}| \approx \frac{\sin \theta}{\sin(90 - \frac{\theta}{2})} |\mathbf{x}| \propto \Sigma$$

using the law of sines and assuming that \mathbf{x} and \mathbf{y} approximately form an isosceles triangle. Thus, as the scale of our data increases, the gradient direction shifts towards a pure rotation, and vice versa as the scale decreases.

When the gradient is a pure translation or pure rotation, gradient-based searches will have poor convergence characteristics. Imagine that the desired pose is a pure translation. The gradient with respect to rotation will dominate, and infinitesimal steps will have to be taken during each line minimization to ensure that progress is made⁸. What would be desirable for most applications is that the solution to a problem at a scale where rotation and translation have roughly the same influence would be the same (modulo scaling of t) regardless if the data were rescaled or not. To affect this is not difficult, it simply involves normalizing the data to some canonical frame (say a unit cube). It is a good idea to include the normalization in any algorithm that will deal with objects of different sizes, otherwise algorithm performance may unexplainedly get worse when applying it to a new domain.

This is related to numerical conditioning of matrices for solving linear systems [61]. For purely quadratic functions, a standard technique for rescaling the variables to form spherical objective functions is called preconditioning. Preconditioning involves computing an approximation of the inverse of the quadratic coefficient matrix of the objective function. The system is premultiplied with this approximation and if the inverse approximation is accurate the condition number of the linear system can be improved (the objective is transformed to be more spherical than elongated). Preconditioning and scaling the data will generally improve the performance of gradient-based searches.

Hartley [61] recently showed that the scale of the data can cause numerical problems for Longuet-Higgins' 8-point algorithm for computing the fundamental matrix of two uncalibrated cameras. He showed that by simply normalizing the data before applying the algorithm, the condition number of the solution matrix is greatly improved resulting in reduced error. The same logic applies to evaluation and use of the gradient in our case.

3.5.2 Efficient Gradient Search

Gradient-descent search (as described in Section 3.4.3) is notoriously inefficient in practice [7, 111]. While gradient descent solves the minimization problem, it does so inefficiently since each gradient step requires the evaluation of the objective function's gradient—Equation 3.26, which is relatively expensive to compute—and a line minimization. Ideally, the gradient would point directly to the local minimum of the objective function, and the

⁸A seemingly straightforward solution is to iteratively move in pure translations or pure rotations. This may be effective in some cases, but it suffers from the same problems of pure gradient-descent search. For example, if the error is pure translation, a step in rotation that reduces the error will later have to be undone to reach the desired result.

solution would be found in one line-minimization step. In practice, this is usually not the case.

By definition, each successive gradient step direction is perpendicular to the previous step direction (otherwise the directional derivative in the current search direction would still be non-zero). This means the search must travel between two points by making a sequence of 90 degree turns. Unless pointed directly toward the minimum, the search will be accomplished by a potentially large number of 90 degree steps which zig-zag back and forth towards the local minimum.

The problem is that each gradient step undoes some of the work of the previous step unless the *change* in the gradient direction along the new step direction is perpendicular to the previous step (i.e., the change in gradient is in the same direction as the current gradient). Such a direction is referred to as a conjugate direction. As the search moves away from the current point along the conjugate direction, the gradient direction of the point on the line of search continues to be perpendicular to the previous step.

For efficiency, a variation of gradient descent that follows conjugate directions, the conjugate-gradient algorithm [7, 111], is used. Conjugate gradient search avoids much of the zig-zagging that pure gradient descent will often suffer from. For purely quadratic functions, conjugate-gradient search can be shown to converge to the local minima in n line minimization steps, where n is the number of free parameters of the objective function. The modification of Algorithms *GradientDescent* and *3D-3D Localization* to utilize conjugate-gradient search is trivial [7, 111].

Line Minimization

Line minimization (Line 4 of Algorithm *GradientDescent*) is a critical step for any localization method using gradient-based optimization. The critical issue is that the choice of line-minimization method will determine the number of evaluations of the objective function being minimized. In our case, the objective function, $E(\mathbf{p})$ (Equation 3.28), is very expensive to evaluate—computing correspondences and summing up the weighted errors between model and image points. It is, thus, important to minimize the number of evaluations of $E(\mathbf{p})$ to compute the minimum point, λ , along the search direction. For the line minimization, there are many techniques to choose from [7, 111]. We use a combination of golden-ratio bracketing and parabolic fits [111] to quickly isolate the minima in the gradient direction with as few evaluations of $E(\mathbf{p})$ and $\frac{\delta E}{\delta \mathbf{p}}$ as possible. If the bracket cannot be found quickly, we stop the search and return the best value of λ so far.

3.6 3D-3D Localization: Experimental Results

In this section, we present the results of our experimental evaluation of our 3D-3D localization algorithm.

We first present examples of the performance of the surface-point visibility approximation (described in Section 3.2) used by our algorithm. This gives us a qualitative feel for the accuracy and errors in the approximation.

Next, we present a qualitative evaluation of the smoothness of our objective function E (Equation 3.28) with respect to the various M-estimator functions $\rho(z)$ described in Section 3.4.2.

We then present quantitative results demonstrating the convergence of our algorithm with respect to the various M-estimators.

To provide a baseline for comparing our algorithm with the state of the art, the convergence experiments were also performed using Besl and McKay's iterative closest point algorithm [6]—the most widely used algorithm for 3D-3D alignment and localization.

Finally, we present convergence results for a randomized version of our 3D-3D localization algorithm which shows that there is a potential for improving both accuracy *and* efficiency of our algorithm.

Note, the models used in this section (with one exception⁹) were created using the method of Chapter 2. The models created using this method generally contain on the order of 30,000 triangles in the mesh. Currently it is not practical to perform localization on surface meshes this dense. For the purposes of localization, we must decimate (reduce the density of triangles) the triangle mesh.

There are several algorithms developed for triangle-mesh decimation including [119]. However, most of these algorithms are designed with graphics applications in mind—all that is desired is an accurate geometric approximation. For localization it is important that the triangulation is relatively uniform across the object surface. Otherwise, the pose estimate will be biased by the dense regions of the surface—the objective function will weight dense regions more than sparse regions and the dense regions will thus be closer aligned to the image data than the sparse regions. Fortunately, there is a decimation algorithm designed with object recognition and localization tasks in mind. Johnson's decimation algorithm [73] optimizes the decimated mesh to keep the lengths of triangles nearly uniform, the result is that the surface is triangulated by nearly uniform area triangles—no long, thin or extremely large triangles are generated as is the case with other algorithms. Johnson's algorithm was used to produce lower resolution surface meshes for each object using approximately two to three-thousand triangles per object. This number of triangles is reasonable for testing our 3D-3D algorithm on the SPARC 20 workstations (resulting localization time approximately 20 to 30 seconds for large initial errors). The geometric accuracy of the decimated model is preserved in all but the high curvature regions of the surface. The decimated surface meshes are sufficiently accurate for 3D-3D localization in range images with relatively coarse resolution as used in this work— 256×240 pixels with a resolution of approximately 1 mm.

⁹The model of the Sharpei dog is courtesy of Heung-Yeung Shum [127]

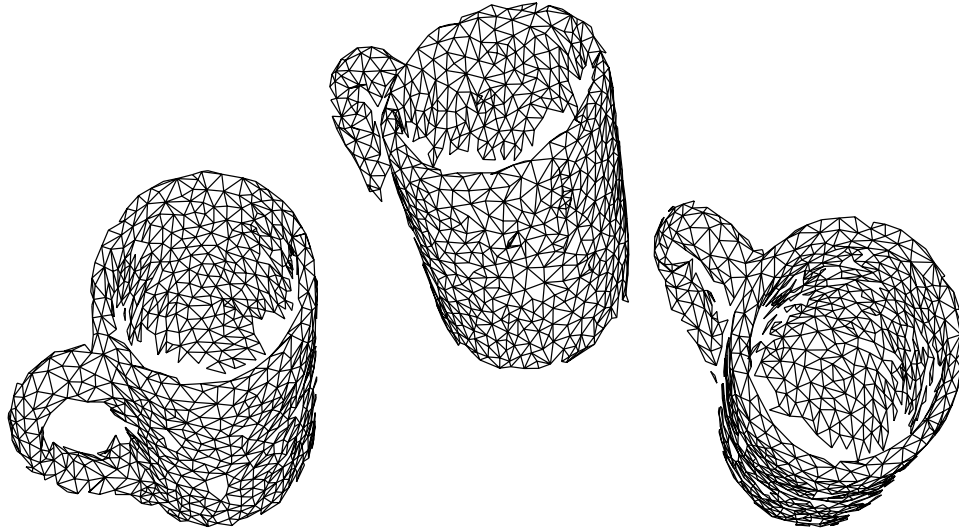


Figure 3.16: Three views of the mug object generated using our surface point visibility approximation.

3.6.1 Qualitative Analysis of the Surface-Point Visibility Approximation

We first briefly demonstrate the accuracy (or rather inaccuracy) of our surface-point visibility approximation as described in Section 3.2. Presenting a few simple examples will give us a qualitative feel for the accuracy and errors in our visibility approximation.

The case of interest is the approximation of hidden surface point removal. As described in Section 3.2, the visibility function for a given surface point is efficiently approximated by a lookup-table (LUT) approach. The discrete sampling of the visibility LUT results in errors since there will invariably be a bin in the point's visibility LUT which contains both occluded and unoccluded viewing directions.

The best example of these approximation errors is the ceramic mug model from Chapter 2. Figure 3.16 shows several views of the mug in which the visible surface triangles are drawn using our approximation for visibility. For our purposes of localization, we only use the center point of each triangle. A visibility LUT is defined for each center point and the triangle is drawn if the center point is determined to be visible. Note that, in all views, several triangles are missing along the border between visible and occluded surface points on the mug. Also note that no triangles are drawn if their center point is occluded by other surface triangles. This is true because our algorithm for LUT generation errs on the safe side with respect to our localization task. Generally, the number of such incorrectly classified points will be very small in relation to the total number of visible surface points.

3.6.2 Qualitative Analysis of the Objective Function

We now consider the smoothness¹⁰ and shape of our objective function E (see Equation 3.28) with respect to the various M-estimators, $\rho(z)$, that we may use for robust localization. For 3D-3D localization to be successful, it is necessary that E is smooth and has a wide basin of attraction. That is, we would prefer E to be easily and reliably minimized using standard non-linear optimization techniques¹¹ over wide ranges of initial pose estimates.

Smoothness is not an obvious property of $E(\mathbf{p})$. We have changes in the set of visible points ($V(\mathbf{p})$) as \mathbf{p} changes. The correspondences vary with respect to \mathbf{p} as well. Add to that the non-linear effect of the robust M-estimators (described in Section 3.4.2) and it is not obvious how smooth $E(\mathbf{p})$ might be.

To inspect the shape of $E(\mathbf{p})$, we computed the values of $E(\mathbf{q})$ over several range images containing known objects in known positions. Here, we show some plots of $E(\mathbf{q})$ for a range image of a ceramic dog¹². The intensity image corresponding to the range image used for this analysis is shown in Figure 3.21 (a), an off-center view of the range data is shown in Figure 3.21 (b), and the alignment of the dog model in the image is shown in Figure 3.21 (c). The correct pose of the dog was manually estimated.

Barring large amounts of noise, partial occlusion, or shadows, we would expect the correct pose estimate to be a local minima of any of the robust estimator functions described previously and this is indeed the case.

For each of the M-estimator functions $\rho(z)$ from Section 3.4.2, we plotted the value of E along various lines in pose space which cross the desired pose. The plot in Figure 3.17 shows the values of E for each function $\rho(z)$ along a pure translation through the correct pose (at point $x = 0$). The axis dimensions of the plot is in millimeters and the range of the plot is 120 mm. The dog is approximately 120 mm high. Figure 3.18 shows the value of E for each function $\rho(z)$ along a pure rotation through the correct pose (at point 0). The axis dimensions of the plot is in degrees and the range of the plot is 80 degrees. Finally, Figure 3.19 shows the value of E for each function $\rho(z)$ along a rotation and translation through the correct pose (at point 0). The axis dimensions of the plot is in combined degrees and millimeters and the range of the plot is 80 degrees and 120 mm.

One can see that the E is relatively smooth for all M-estimator functions except the threshold function. Once the pose is close enough to the desired pose, the threshold version of E begins to become smoother but still has many bumps and local minima created by the differential nature of the threshold. On a closer look (see Figure 3.20), we see that E is smoother for the smooth down-weighting M-estimators such as the Lorentzian than it is for the Gaussian. In practice, this difference in relative smoothness results in poorer performance by the Gaussian.

¹⁰By smoothness of a function, we refer to lack of bumps and local minima along the function's landscape. Optimally, we prefer a purely quadratic function which has a single global minimum and no other local minima.

¹¹Randomized optimization techniques such as simulated annealing [43, 62, 111, 140] are not considered here but are discussed in the future work in Chapter 7.

¹²The model of the Sharpei dog is courtesy of Heung-Yeung Shum [127].

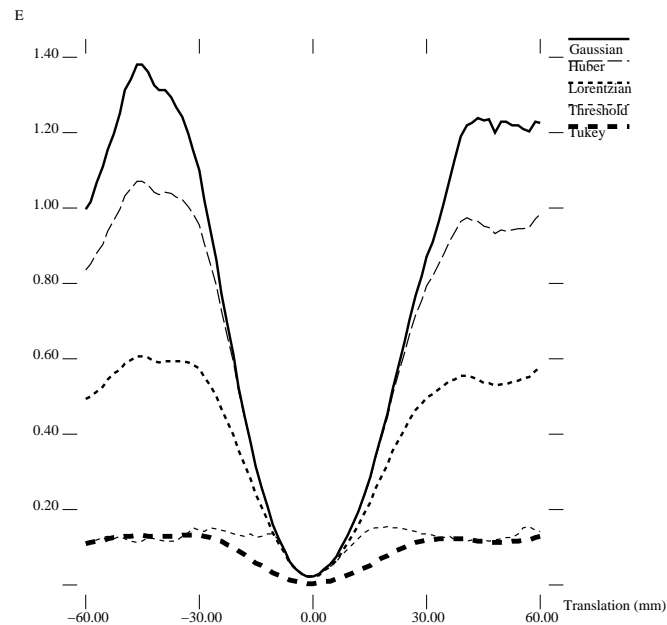


Figure 3.17: The variation of E along a line of translation in pose space for five M-estimators. The true pose is at $x = 0$. The x -axis represents translation in millimeters. The rough range of the graph is $[-60, 60]$ millimeters (about half the length of the dog).

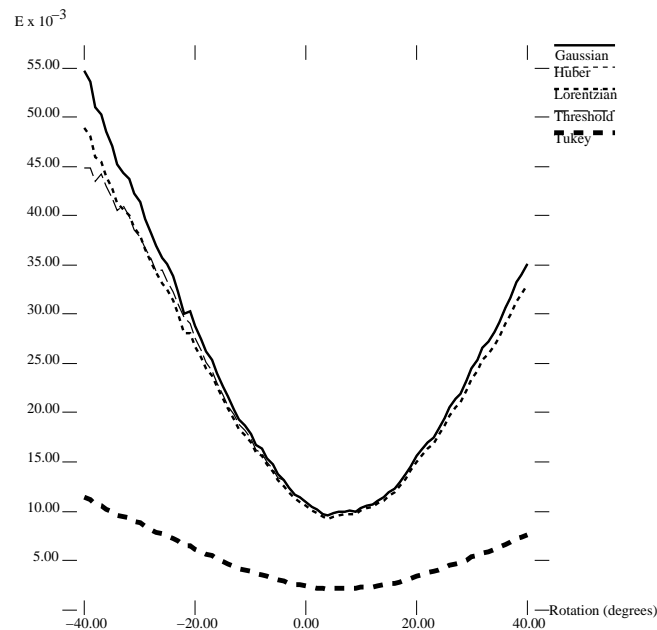


Figure 3.18: The variation of E along a line of pure rotation in pose space for five M-estimators. The true pose is at $x = 0$. The x -axis represents rotation in degrees. The rough range of the graph is $[-40, 40]$ degrees.

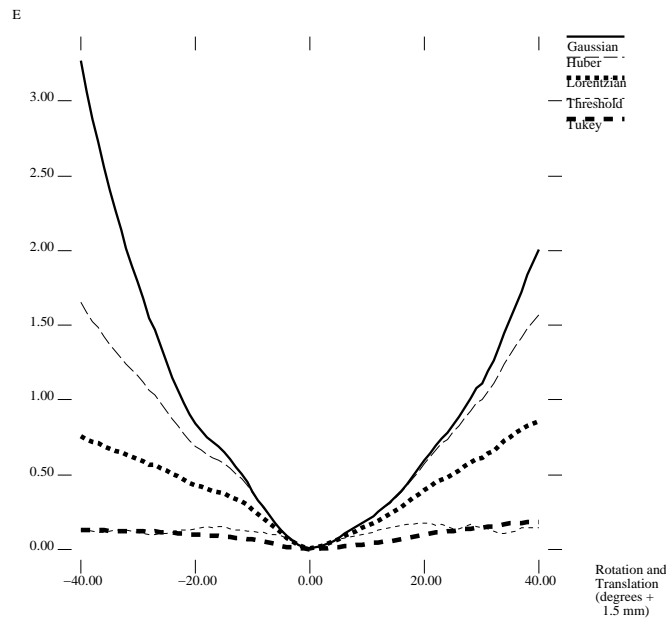


Figure 3.19: The variation of E along a line of translation and rotation in pose space for five M-estimators. The true pose is at $x = 0$. The x -axis represents simultaneous rotation and translation. The rough range of the graph is $[-60, 60]$ millimeters and $[-40, 40]$ degrees.

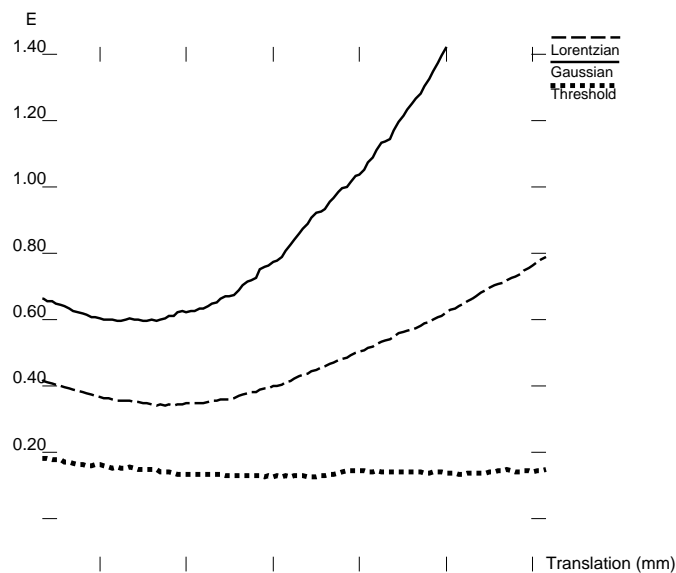


Figure 3.20: A close-up of a piece of the graphs of the function E for the Lorentzian, Gaussian and Threshold along a line of translation in pose space. The Threshold and Gaussian versions of E have many small local minima which causes problems for optimization algorithms in practice.

3.6.3 3D-3D Localization Convergence Results

We now present quantitative results demonstrating the convergence of our algorithm using the various M-estimators described in Section 3.4.2. To provide some basis for comparison with the state of the art, we also repeated each experiment using Besl and McKay’s iterative closest point algorithm [6]—which is currently the most widely used algorithm for 3D-3D alignment and localization.

We performed experiments on images of 4 objects: the dog, the mug, the car, and the duck. For each experiment, we took a range image of our object in a known position—using the robotic positioner or by manually estimating the object’s precise position. Each image contains 256×240 pixels, each pixel containing a 3D point. The test images are shown in Figures 3.21, 3.22, 3.23, and 3.24. These figures show the intensity image view corresponding to the range finder’s view, an off-center view of the range-image points, an overlay example of an initial (incorrect) pose estimate as used in the experiments and an overlay of the object model on the intensity image at the estimated position.

Each experiment consists of 100 trials of the 3D-3D localization algorithm from a randomly generated initial pose estimate. The initial pose estimates were generated by perturbing each pose by a random translation vector and a random rotation. Each trial was performed with the same magnitude of initial pose error: 20 millimeters in translation and 30 degrees of rotation. We wish to emphasize that the initial errors are not uniformly distributed between 0 and 20 millimeters of translation, and 0 and 30 degrees of rotation, but are exactly 20 millimeters and 30 degrees, respectively. Thus, there are no easy (i.e., close to the actual pose) initial estimates in our set of trials. Our algorithm is capable of convergence from larger errors but characterizing the convergence range in general is difficult since convergence will vary greatly with respect to the input data. The objects presented here have dimensions of at most 200 millimeters, thus 20 mm translation errors are significant. Combining this with 30-degree rotation errors makes for a difficult localization task in general.

For each image, we performed the convergence experiment on four versions of our 3D-3D localization algorithm. The versions differ only by the M-estimator weight function which is used. The following weight functions were used: Gaussian (constant weight), Lorentzian, Tukey, and Huber. See Section 3.4.2 and Figure 3.11 for a review of these functions. To account for large initial pose errors it is important that the errors z are normalized accordingly so that the robust estimators do not immediately discount correct correspondences. The errors are normalized by a progressively decreasing normalization factor σ (i.e., use $z' = \frac{z}{\sigma}$). This is effectively the standard deviation which controls the width of the M-estimator weight-functions (e.g., a 3σ threshold). In these experiments, we begin with $\sigma = 12$ mm and reduce it to 6 mm and then to 3 mm as the algorithm progresses.

In addition to the four versions of our algorithm, we also executed the same experiment using Besl and McKay’s iterative closest point algorithm [6]. ICP iteratively solves for the closed-form pose estimate (using techniques such as those by Sanso [116], Faugeras and Hebert [36], Horn [66], or Arun [1] as described in Section 3.4.1) given correspondences between model points and the closest points in the 3D image data. As described previously,

these closed-form techniques are very sensitive to incorrect correspondences and outliers. Our implementation of ICP follows the typical approach and uses a hard threshold for removing outliers. The threshold is progressively decreased from $\sigma = 12$ mm to $\sigma = 3$ mm as in the implementation of our algorithm as described above.

We manually verified the results of each trial and determined the number of correct trials—those that correctly align the model with the image—for each experiment. The results are listed in Table 3.2.

From these results we see that the robust weight functions have much better convergence properties than a pure least-squared error objective function (corresponding to the Gaussian). The Tukey and Lorentzian weight functions perform slightly better than Huber's weight function. We speculate that this may be due the first-order discontinuity in the Huber weight function which may create more local minima than the smooth Lorentzian and Tukey weight functions. ICP is not successful with such large initial pose errors. For each convergence trial, our localization algorithm typically performed 40 conjugate-gradient steps and 180 function evaluations for each trial (approximately 25 seconds on a SPARC 20 workstation). The ICP algorithm typically performed 30 iterations per trial.

There is nothing special about the images used for these tests (i.e., they weren't hand chosen, but rather randomly selected from a large set of sample images). They were taken with a plain black background which would suggest that the localization task would be trivial. This is a bit deceptive since they do contain a considerable amount of background noise (random points floating in space), much of which is near the object. The range data of the dog image (Figure 3.21) is the cleanest of the four which partly explains the better convergence results for that image. This noise is typical of the light-stripe range finder when imaging black points in the scene. The duck and car images are made difficult by the fact that they are nearly singular views. A slight twist of the duck will reveal many previously hidden surface points. The mug image is a tough problem for any localization algorithm because other than the handle the object is symmetric. Thus, a localization search could settle on any rotation that matches the body of the mug to the image while down-weighting or ignoring the large errors for the handle. Surprisingly the robust M-estimators were very adept at locating the precise pose of the mug, though the above problem was the main source for the trial failures. The dog object is also very tricky, the problem is that it has a lot of low curvature surface area which leaves two degrees of freedom. The localization task is also more difficult when one considers the large change in point visibility from the initial to final pose. So though these localization tasks may appear simple or trivial to most readers, there are many subtleties to beware of.

Seeing the poor convergence results for ICP in the experiments, we performed two more experiments with variations of ICP. We repeated the duck image experiments using a weighted-least squares version of ICP and using the Gaussian and Lorentzian weight functions. This was done to determine if the use of hard thresholds (and their known susceptibility to local minima as demonstrated in Section 3.6.2) were the reason for ICP's failure and whether smoothly weighting the errors (as done by the other robust M-estimators) would offer an improvement. The results of these experiments are shown in Table 3.3. The results showed that by changing to a smooth down-weighting function (the ICP w/

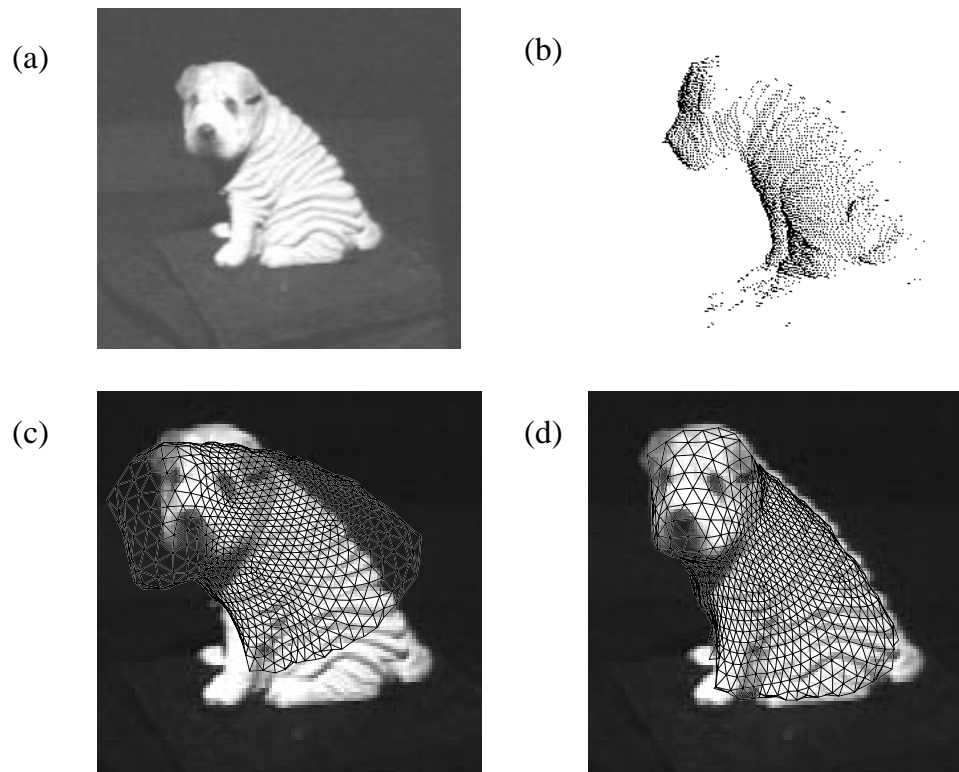


Figure 3.21: The Sharpei dog convergence test data: (a) the intensity image view, (b) an off-center view of the 3D range data points, (c) a typical initial starting point for the convergence tests (20 mm translation error and 30 degrees rotation error) (d) an overlay of the dog model at its estimated actual location.

Object	% Correct				
	Gaussian	Lorentzian	Tukey	Huber	ICP
dog	65	98	100	85	24
mug	52	70	67	67	2
car	37	54	61	57	4
duck	50	60	58	58	9

Table 3.2: Results of the convergence experiments with variations of our 3D-3D localization algorithm and ICP. The initial errors were of uniform magnitudes: 30 degrees of rotation and 20 mm of translation.

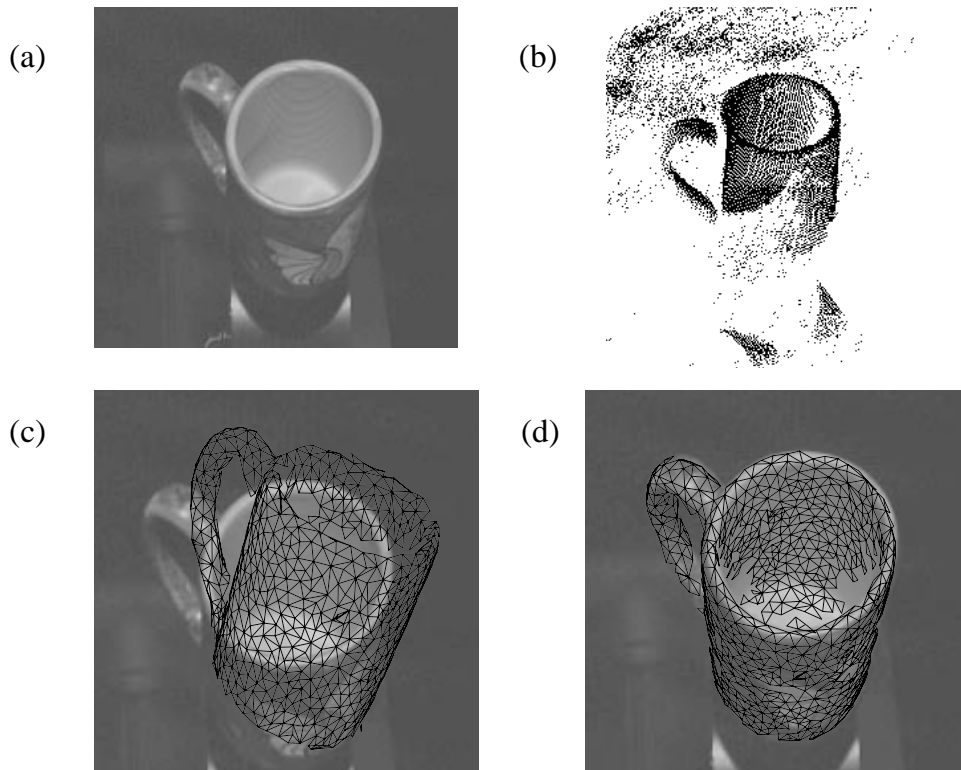


Figure 3.22: The ceramic mug convergence test data: (a) the intensity image view, (b) an off-center view of the 3D range data points, (c) a typical initial starting point for the convergence tests (20 mm translation error and 30 degrees rotation error), and (d) an overlay of the mug model at the estimated location.

Lorentzian case) the convergence is improved. It also showed that using a hard threshold is slightly better than none at all (the ICP w/ Gaussian case). However, neither attempts managed to improve the convergence to approach that of any of the versions of our 3D-3D localization algorithm.

We offer a few hypotheses about ICP's relative inability to converge to the desired location for the above images:

1. ICP does not anticipate changes in visibility sets when taking a step in pose space. It often inadvertently forces itself out of the local basin of attraction by stepping to a view with a significantly different set of visible points. For example, in the duck example (see Figure 3.24), the view is singular. A slight rotation introduces many newly visible surface points on the duck. Thus, creating a situation where ICP has jumped to a position of a function which it has little information about. ICP was originally designed to register two (true) 3D data sets. Range images are incomplete

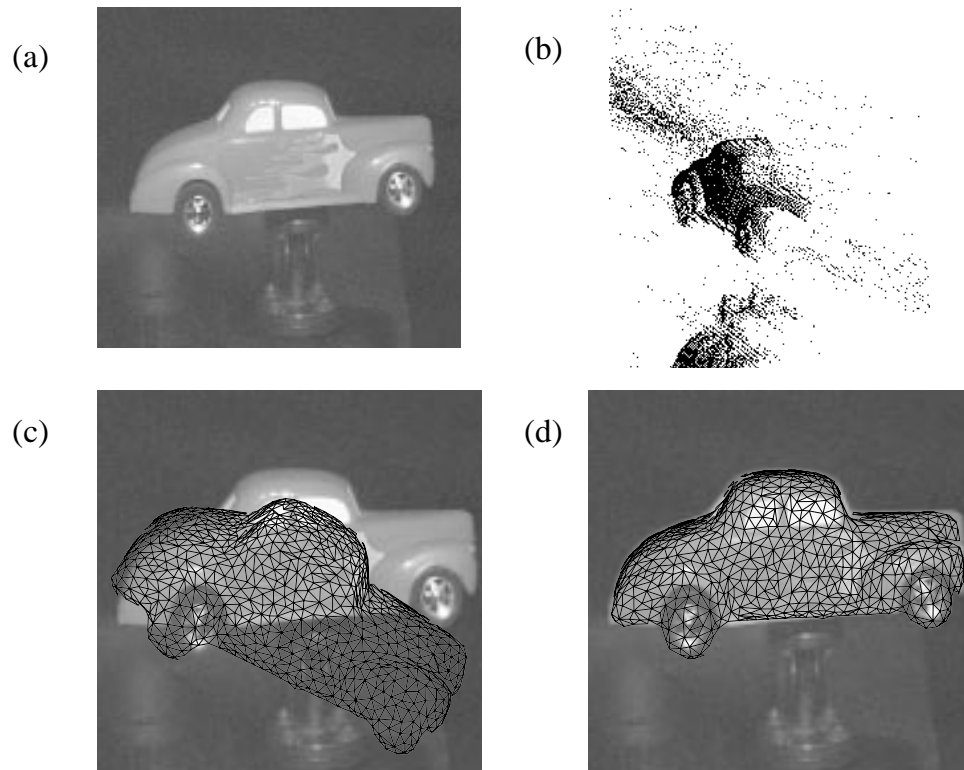


Figure 3.23: The toy car convergence test data: (a) the intensity image view, (b) an off-center view of the 3D range data points, (c) a typical initial starting point for the convergence tests (20 mm translation error and 30 degrees rotation error), and (d) an overlay of the car model at the estimated location.

3D data sets with respect to an object. The overlap between model and image data will necessarily be limited and ICP was not designed with this in mind.

2. ICP does not cope well with inaccurate correspondences. In our experience, it does well if all or most of the image data belongs to the object or if the initial pose error is small. The images (a) through (c) have a substantial amount of noise. Range data points are randomly scattered about in the background (see Figure 3.24) and are often found to be correspondences. The closed-form pose estimation methods do not deal gracefully with such inconsistent correspondences.
3. ICP attempts to make a global decision using information (correspondences) which is often only valid locally.

These results demonstrate that using dynamic correspondences within a gradient-descent search of a robust objective function is a key component to achieve a wide degree of

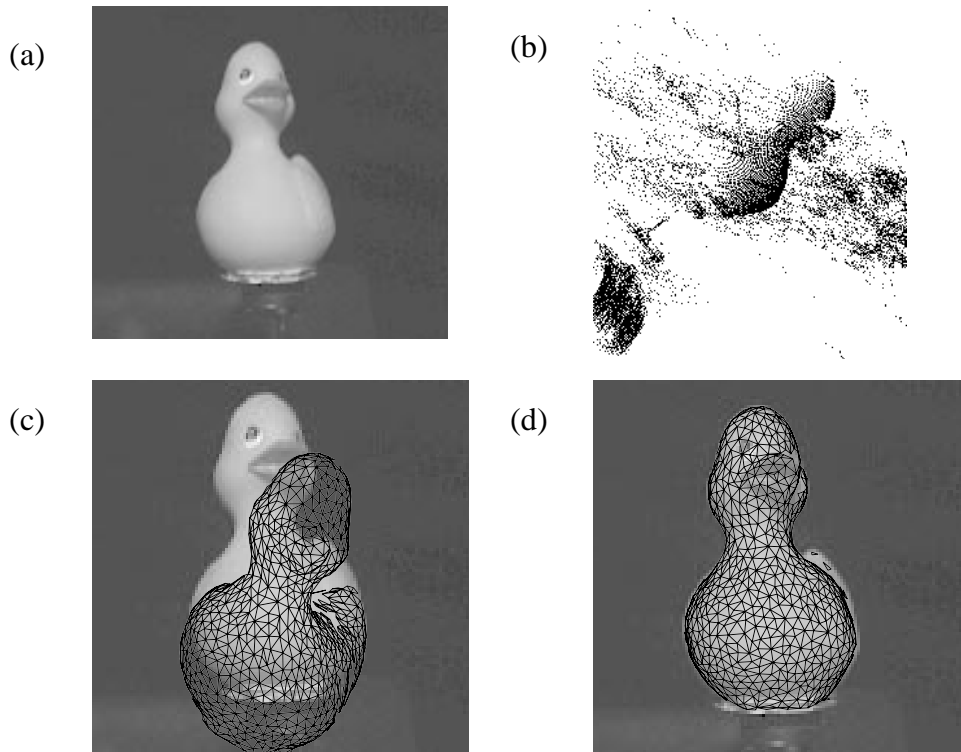


Figure 3.24: The rubber duck convergence test data: (a) the intensity image view, (b) an off-center view of the 3D range data points, (c) a typical initial starting point for the convergence tests (20 mm translation error and 30 degrees rotation error), and (d) an overlay of the duck model at the estimated location.

Object	% Correct			
	Lorentzian	ICP w/ Lorentzian	ICP w/ Threshold	ICP w/ Gaussian
duck	60	17	9	7

Table 3.3: Results of the convergence experiments with variations of ICP on the duck image. The leftmost entry is the result of our 3D-3D localization algorithm using the Lorentzian weight function and is intended as a point of reference.

convergence for object localization in noisy image data.

3.6.4 Randomization Experiments

Viola [140] demonstrated a method for aligning shapes by maximizing the entropy between two functions. A key result of his work was the demonstration of a randomized gradient-

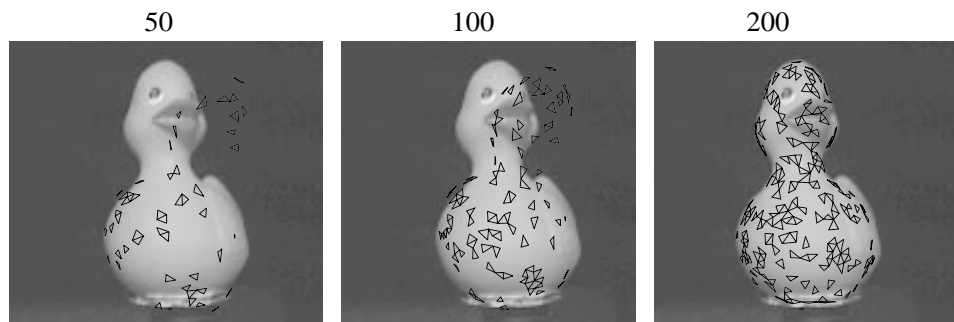


Figure 3.25: Depiction of three iterations of the randomized localization search. Each image shows an overlay of the randomly selected points from the model surface which were used for localization during the iteration.

descent algorithm which increased the speed of the algorithm and reduced the susceptibility of his algorithm to local minima (the randomness helps the algorithm to get “unstuck”). While local minima is also a problem for almost every localization algorithm, including ours, the opportunity for algorithm speedups via randomization may be critical for practical applications.

In this section, we present the result of an experiment to test the convergence of a modification of our 3D-3D localization algorithm to use a simple randomization strategy. The modification is to perform each gradient computation and line minimization (Lines 6 and 7 of Algorithm *3D-3D Localization*) of our search using only a small randomly sampled subset of our model data to measure the objective function. Since the accuracy of the localization result will increase with the number of samples of the error, we progressively increase the number of random samples just as we decrease the standard deviation σ in the above convergence trials. In these randomization experiments, we doubled the number of surface point samples as we halved the value of σ . The rationale is similar to the simulated-annealing search algorithm [111, 43, 62, 24] which starts out with a high degree of randomness in the search and gradually settles to non-random search. With a small number of point samples we may not be able to accurately estimate the pose, but we may be able to quickly find a better estimate. As we get closer to the true pose, the convergence rate improves thus we can afford to add more points as we get closer to get the desired accuracy of the pose estimate. Figure 3.25 shows a snapshot of three iterations of the randomized localization algorithm. Each overlay shows the randomly selected points from the model surface which were used for localization during the iteration. The number of sampled points is gradually increased as the pose estimate converges to the true pose.

We performed three experiments with the following randomization schedules: 200 to 400 to 800, 100 to 200 to 400, and 50 to 100 to 200. The results of these experiments (again performed using the duck image of Figure 3.24) are presented in Table 3.4.

Object	% Correct			
	Non-Random (3000)	200,400,800	100,200,400	50,100,200
duck	60	57	52	34
speed (seconds)	27.5	8.5	6	4.5

Table 3.4: Results of the randomization convergence experiments. Each column lists the number of surface point samples used in the randomization schedule, the number of percentage of correct results and the execution time in seconds. All these experiments used the randomization modification of our 3D-3D localization algorithm with the Lorentzian weight function. The initial errors were of uniform magnitudes: 30 degrees of rotation and 20 mm of translation.

As these results show, the convergence accuracy gradually decreases as the random set size decreases. The speedup is significant, however, thus the potential exists for applying randomization techniques to capitalize on the relationship between speedup and convergence and produce an algorithm that is faster and has wider convergence on average. For example, running the randomized algorithm multiple times from slightly different starting points may be more efficient *and* more likely to converge to the desired global minima. This work is beyond the scope of the current thesis.

3.7 3D-3D Object Localization: Summary

We have described the principal components of our 3D-3D localization algorithm: point visibility, point-to-point correspondence, and robust pose optimization. Our algorithm iteratively optimizes an objective function which is specified to reduce the effect of noise and outliers which are prevalent in real image data.

Since an iterative algorithm is required, the computation of the objective function must be as efficient as possible. Our solution utilizes an efficient and accurate approximation to compute point visibility with respect to the pose and camera parameters. Point correspondences are efficiently computed using k-d trees and nearest-neighbor search. We showed how to extend the point correspondence search to include attributes, such as surface normals, in the nearest-neighbor search.

The most significant contribution of this chapter is our method for minimizing a robust M-estimator via dynamic correspondences with standard non-linear optimization techniques. We described the use of robust M-estimators to define an objective function over which to optimize the pose such that the effect of noise and outliers is greatly reduced. We showed that optimizing such objective functions requires the use of dynamic correspondences to properly evaluate the objective function. The optimization was implemented using standard techniques such as conjugate-gradient minimization.

Our results demonstrate that our 3D-3D localization algorithm using a smooth down-weighting M-estimator, such as the Lorentzian, can consistently and efficiently converge from rather large initial pose errors despite the presence of large number of extraneous range-image points around the object. The convergence results showed that our algorithm has much wider convergence ranges than Besl and McKay's ICP algorithm [6]. We also showed that through randomization, the potential exists for a substantial speedup and convergence improvement.

This ends our description of our 3D-3D localization algorithm. Experiments presented in Section 3.6 show that this algorithm has a acceptable convergence time and produces accurate results. We will now describe our extensions of this work to 3D-2D localization. Our discussion begins with building object models for the 3D-2D localization task and is followed by a description of our algorithm for 3D-2D localization.

Chapter 4

Object Modeling for 3D-2D Localization

The previous two chapters have described our approach for 3D object modeling and 3D-3D localization. This chapter focuses on the problem of building models for the purpose of localizing 3D objects in 2D intensity images—from here on referred to as 3D-2D localization.

In many ways, model building for 3D-2D localization is similar to the problem of building 3D models, which was addressed in Chapter 2. As in that work, here we seek to build a model—for the task of localization—from several real images of the object while automating the process as much as possible. 3D-2D localization is an inherently more difficult problem than 3D-3D localization because the appearance of an object in an intensity image is dependent on a combination of geometric and photometric properties of the object rather than geometry alone as in the 3D-3D case.¹ The choice of model representation is also not immediately obvious as the intensity images are 2D projections of 3D phenomena.

4.1 Problems and Approach

In this section, we overview the issues, problems, and our approach to building the models for 3D-2D localization.

Before we can begin to build our object models for 3D-2D localization, we need to know what information about the object will be required to solve this task. In order to localize an object in an intensity image, we must establish some correspondence between a localizable feature of the object and its 2D projection in the image. What features should be used? Once we have decided on a certain set of features, we need to decide upon a model representation that allows us to predict the appearance of those features in various images of the object. After the features and model representation are decided upon, we

¹Photometric properties and effects do play a role in range-image acquisition (e.g., effects such as interreflectance and specular reflection can cause problems for light-stripe range finders and stereo vision). In general, these effects are ignored except during image processing. The range sensor effectively abstracts away these effects.

then face the problem of building such models from real images of the object. We break the following discussion into three sections:

1. What features should we use for 3D-2D localization?
2. How should we model the features?
3. How do we build such a model from a set of images of the object?

The focus of this chapter is on Question 3, but before jumping in we will answer the first two questions—thus motivating our approach to 3D-2D localization (Chapter 5).

4.1.1 Features for 3D-2D Localization

If we are to align a 3D object in a 2D intensity image, we need to correlate the model to its the image. There are several types of features which have been used to correlate/matching an object with its intensity image:

- Pixels/Regions: intensity/color/texture
- Interest points: corners, junctions, inflection points, distinguished points
- Edge curves: lines/arcs/ellipses fit to edgel chains
- Edgels: edge points extracted by the edge operator.

We will discuss the use of each of these features for model-to-image correlation.

One possibility is to correlate regions of constant surface properties on the model with intensity, color or texture of pixels/regions in the image. This is difficult because the image intensity of an object region may vary greatly because of changes in surface orientation, lighting, shadows and reflections. Predicting pixel intensity or color requires detailed knowledge of scene geometry, surface reflectance properties, light source properties and positions, and the camera's geometric and photometric parameters. Without being able to predict sensed intensities or colors, matching prediction with observation for localization will be very error prone.

There have been several recent findings and results which may make pixel/region correlation feasible in the near future. Nayar and Bolle [100] discovered a photometric invariant involving the ratios of intensities between two neighboring points on a smooth surface. Maxwell [93] has developed techniques to analyze and segment color images into connected regions of similar material properties. Texture information may vary because of the factors which influence intensities. However, texture the spatial properties of certain textures may be reliably detectable—using methods such as Krumm's [78] local spatial frequency—over a wide range of lighting and scene variations. Changes in texture appearance caused by changes in orientation and scale can be predicted since the rough object location is known during the localization process. A drawback is that while many objects have distinctive texture, most objects do not. Thus, texture alone will not be sufficient to

localize most objects. Viola [140] presented an approach that minimizes the entropy of the correlation of the model shape with the intensity image rather than simple pixel intensity correlation. This approach avoids some of the above problems for some simple object shapes and reflectance properties. His approach is discussed further in Chapter 6.

A popular class of features used for structure from motion [135, 130, 124, 106] and robot navigation [98, 91, 92, 135] are interest points and corners. Definitions of these interest points may differ but most follow the same principal: small image windows with distinct intensity profiles. Some definitions include image windows with high standard deviations in intensity, zero crossings of the Laplacian of the intensity, or corners. Tomasi [135] defines a criterion for interest points based on the likelihood that the point can be tracked from image to image. A similar feature is found by analyzing edge curves extracted from the image and selecting junctions of multiple curves and high curvature (corner) points. These kind of features are useful for motion estimation because they are distinct and can reliably be tracked from image to image. Such interest points are usually too sparse for localization and verification applications; however, they may be good candidates for recognition indexing schemes where sparseness is more of an asset.

Another possibility is intensity edges—discontinuities in the image’s intensity profile. Using present day techniques, intensity edges are the most reliable, well-understood, practical, and, not coincidentally, the most popular feature for object recognition and localization in intensity images. Intensity edges occur at points in the scene where there are geometric discontinuities (e.g., occluding contours of objects), surface orientation discontinuities (e.g., peak edges or corners) or surface reflectance discontinuities (i.e., transitions of surface color or reflectance). These intensity edges have a direct correlation with points on the object surface; however, there are other sources of intensity edges which may appear on an object but are not intrinsic to the object—examples include cast shadows on the object, specular reflections, or digitization noise. The intensity edges that are intrinsic to the object are themselves subject to external sources of variation. For example, occluding contours will only be apparent in the image if the background reflects a sufficiently different intensity than the object, or surface markings may only be visible when viewed from certain directions or under certain light source conditions. However, in general, the intrinsic discontinuity sources of an object are detectable over wide changes in illumination and can be accurately predicted without precise knowledge of the light source.

There are several types of intensity edge features. Curves (e.g., line segments, arcs, ellipses, etc.) fit to a collection of edgel data is the most common [47, 85, 110, 48, 49, 122, 54, 3, 15, 113]. Junctions and corners of the fitted curves are also a popular choice of feature [81, 15, 110, 54]. Junctions and corners of edge curves are most similar to the interest points described previously. Models consisting of a collection of curves and junctions can be localized by matching them to the image curves and junctions. These features are simple to specify and the process of curve fitting greatly reduces the combinatorics of matching since the number of curves and junctions will invariably be much smaller than the number of edgels in the image. However, using edge curves immediately constrains the type of objects for which localization/recognition systems will be applicable.

Another option is to dispense with relying on a high-level feature extractor and use the raw edgels themselves. This is the approach taken by [14, 143, 124]. Other than the pixel intensities, edgels are likely the lowest-level information available from the image that we can use for localization. This approach has been used recently by quite a few researchers [143, 17, 14, 124] developing methods following the alignment paradigm of Basri and Ullman [139]. Using the lowest-level edge data to perform localization makes some sense since localization is not necessarily concerned with the same combinatoric matching problem as in the general object-recognition problem. Thus, more data is not necessarily a bad thing. This reduces the number of assumptions made by the algorithm and restrictions placed on our system. The algorithm will also be more robust to the small variations in edgel data which have significant effects on curve fitting or higher level features extracted from the edgel data. Also, collections of edgels can represent a wide variety of shapes.

For the reasons discussed above, we will use intensity edgels as our basis for localizing 3D objects in intensity images. Of course, using combinations of color, intensity, texture, and intensity-edge information would be preferable if practical, but for this thesis, we focus on using intensity edgels for 3D-2D localization.

4.1.2 Edgel Models for 3D-2D Localization

Now that we have decided on the type of feature to use for localization, we must choose an appropriate representation. The key requirement for our representation is the ability to efficiently predict the appearance of the object edgels from any given viewing direction or arbitrary camera parameters. We must also keep in mind the difficulty of automatically building the model from real images. In the following we consider two general approaches: 2D representations and 3D representations.

2D Edgel Models

By 2D representation, we refer to representing an object by a set of representative 2D images (views). In our case, each view would be an edge image.

Each view is a discrete sample from the space of object locations and orientations, as well as lighting conditions and camera parameters. To model an object using this approach, we must sample a sufficient number of views to cover the expected variations for the given task or application. The number of required views can be quite large for even a few degrees of freedom since the number of required views is roughly exponential with respect to the number of degrees of freedom which will be modeled. For example, for each degree of freedom, if we take n samples along each degree of freedom, we will have n^d samples in total where d is the degrees of freedom. In addition to sampling the view space of the object, for the task of localization, this space must be made continuous, this is done by connecting edges in neighboring views so that intermediate views can be interpolated. Computing these correspondences between two views is nearly an impossible task in general, since given any two neighboring views, the set of visible points is almost never the same.

Shashua [124] proposed an approach for modeling reflectance and geometry by computing correspondences using optical flow. Gros [54] described a framework for matching line segments and points by approximating the motion between views as an affine transformation and searching for an affine transformation using a clustering technique similar to the Hough transform [2].

Much work has been done using 2D representations dating back to Basri and Ullman [139]; this and other work using 2D representations is discussed in Chapter 6. This representation is most popular for ease of building models, however, the price that is paid is accuracy and applicability. The motivation for most of the 2D representations is for the problem of object identification or indexing. Only the alignment method of Basri and Ullman [139] is suited and intended to localize and verify an hypothesized pose; however, their method is only applicable to orthography or scaled orthography.

Other basic types of 2D representation include efficient methods for image correlation and pattern recognition. Murase and Nayar [99] introduced the eigenspace representation for image sets. Using their method, the object is represented by a large number of intensity images. Eigenspace analysis is used to reduce the images to points in a low-dimensional subspace (the principal components of the eigenspace). Image matching can then be efficiently performed in the subspace. Huttenlocher, Lilien and Olson [69] used this method to represent binary edgel images of the object, which is more robust to changes in lighting. They cleverly showed that the correlation between vectors in the subspace is approximately the same as a Hausdorff distance between the binary edgel images. The Hausdorff relationship makes their formulation somewhat insensitive to partial occlusion as well. The eigenspace techniques are essentially an efficient form of image correlation and suffer from all the same problems as correlation. Another related technique is the use of artificial neural networks to solve pattern matching problems [107, 33, 114, 97]. Implicitly, the networks learn a functional mapping between images and object/view identification—equivalent to image correlation and pattern recognition. Localization and verification is not possible in this framework, though these methods show promise for solving the indexing problem.

3D Edgel Models

The other choice for representation is a 3D representation. Here each edgel is represented as an edgel in three dimensions in, preferably, the coordinate system of the object. The advantage of this representation is that we only need one model for all possible object poses and camera parameters. The main drawbacks of such a representation are how to acquire such a model from 2D data and how to efficiently predict the appearance from a given view.

Much of the previous work [47, 85, 122, 3, 15] on 3D representations of edges for 2D recognition and localization tasks have been based on CAD modeling and acquiring the 3D edge model from CAD geometry; however, most of this work has been limited to simple features such as straight edge segments, arcs, and junctions [81, 15, 110, 54]. In general, CAD modeling is labor intensive and often results in crude models.

Our approach is to treat edgels just like surface points in the 3D-3D case. That is, the model is a collection of edgels (oriented points) on the object where each edgel has a computationally efficient, local visibility criteria associated with it. Given such a model, we can easily and accurately predict appearances of the object's edges continuously with respect to pose for any given camera model. The rest of this chapter describes our approach to build an object centered, 3D edge model.

4.1.3 Building 3D Edgel Models from Real Images

We have decided to build an object-centered, 3D edgel model from a set of intensity images of the object. Many of the problems involved with this task are very similar to the problems of Chapter 2. The steps of view acquisition, view alignment, and data merging seem relevant for the 3D edgel modeling problem as well. The basic problems involved in building 3D edgel models from real images are:

1. Distinguishing background from foreground edgels
2. Converting 2D data to 3D data
3. Aligning all of the data into the same coordinate system
4. Merging all the edgel data to form a single 3D edgel model
5. Dealing with occluding contours

We now will briefly overview our method for building 3D edgel models for 2D localization, while addressing these problems along the way.

We begin by acquiring a set of intensity images of the object that adequately samples the range of viewing directions and, if desired, lighting conditions that are expected when applying 3D-2D localization. The intensity images are then processed to provide sets of 2D edgels. We must then deal with a non-trivial complication—creating a 3D model from a set of 2D projections of the 3D object. There are possible ways to get 3D information from sets of 2D information such as structure from motion [82, 135, 130, 124, 106] or epipolar/stereo analysis [45, 131]. None of these are currently practical, however.

Fortunately, we have a trick up our sleeve, namely, the 3D modeling techniques described in Chapter 2. That is, we are able to build a 3D model of an object's surface geometry. Using the 3D surface model solves the first three problems: the foreground/background problem, 2D-to-3D conversion, and alignment of the 3D data. In fact, a common theme of our work on 3D-2D localization is to use 3D information, whenever possible, to solve the 2D problems.

Once all the 2D edgel data is mapped and aligned in 3D model coordinates, the 3D edgel data must be merged into a single, unified edgel model. Our algorithm for merging edgels is closely related to the consensus-surface algorithm of Chapter 2 and is appropriately called the *consensus-edgel* algorithm. The idea is to find clusters of similar edgels from multiple views. Much like the surfaces from range images, the edgels that are extracted

from intensity images are often noisy, and spurious edgels are frequently detected due to reflections, specularities and image noise. Thus, we do not want every observed edgel as part of the final model. Only stable edges—edges that are consistently detected over many views—are desired. By searching for a consensus of edges from the observed edgel data, we can guarantee that only stable edgel generators are part of the edgel model.

The consensus edgel algorithm is not sufficient for our purposes however; it is only applicable for building models of rigid edgel generators. That is, edgels whose position with respect to the 3D model is fixed (e.g., surface markings or corners). The other class of edgels, non-attached edgels, are those resulting from occluding contours of an object such as the side of a cylinder. Occluding contours appear to be detectable over many views. For example, as a cylinder rotates about its axis, the projection of the side contours remains stationary in the 2D image. However, the object coordinates of the apparent contour generator is constantly changing as the cylinder rotates. This is because the contour generator is changing between views (i.e., a different point is generating the perceived contour). To model the edgels generated by occluding contours, we can do no better than modeling the geometry of the object surface. Since we already have an accurate surface model, we utilize the surface geometry to predict the appearance of occluding-contour edgels for localization.

Figure 4.1 shows a diagram of the technical sections of the thesis. This chapter has two principal components dealing with the modeling of rigid edgels and occluding-contour edgels. Rigid edgels (including surface markings and corner edgels) are modeled from a large set of sample images of the object. We first describing in detail each step of our rigid-edgel-modeling algorithm: view acquisition, view alignment via 2D to 3D mapping, and edgel merging using the consensus-edgel algorithm. We then discuss the geometric curvature analysis required to model occluding contour edgels of an object.

4.2 View Acquisition

The first step of the edgel-modeling process is view acquisition—sampling intensity images of the object from various views and processing them to produce 2D edgel sets representing each view. As in Chapter 2, we do not explicitly deal with the problem of view selection. We simply assume that we are given a set of views that provides adequate coverage for our purposes.

To compute edgels from an intensity image, the usual process involves convolving the image with an edge operator and linking the maxima of this operator into edgel chains. The choice of edge operator is rather arbitrary, and there are a number of them to choose from. The Canny operator [16] and Deriche operator [30] are the two most popular edge operators for computer-vision applications.

We use the Canny operator, although other operators would give similar results. The Canny operator is the most common edge operator and implementations are found in nearly every computer-vision software package. It is implemented as a first derivative of a Gaussian convolution operator, which Canny [16] showed to be a very close approximation of the optimal convolution operator for detecting step edges. The Canny operator measures

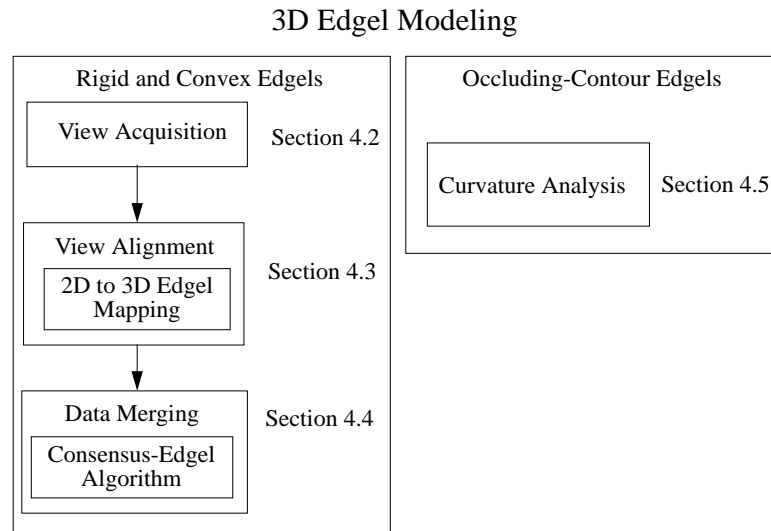


Figure 4.1: Organization of this chapter.

the edge strength at each point in the image. All pixels that are not local maxima of the edge measure are suppressed. The remaining pixels are local maxima of the Canny operator and are linked to form edgel chains. The linker uses hysteresis thresholding [16] to connect adjacent edgels that may not be as strong as other edgels on the chain. This prevents edges from being broken into smaller pieces randomly due to fluctuations in the measured edge strength along the chain. Linking also eliminates many spurious points from the immediate neighborhoods of strong intensity edges.

The result of the Canny detector and edgel linking is a set of raw edgel chains. Figure 4.2 (a) shows an example of typical raw edgel chains from a Canny operator. As can be seen in that figure, these chains are jagged—much like a staircase—due to the discrete nature of the image pixels. For the purposes of modeling and localization, smooth edge data is very desirable (this will be made clear later in this and the next chapter).

Edge smoothness can be achieved by applying a smoothing operator over each edge chain [88, 147]. Figure 4.2 (b) shows an overlay of the edgel chains resulting from such a smoothing operation. As can be seen, the smoothing removes much of the noise and aliasing effects (kinks) from the edgel chains while maintaining accuracy of the edgel positions (an important aspect for localization). In fact the edgel positions for most edgels are improved to sub-pixel accuracy after the smoothing removes the discrete kinks in the chains. For details of the smoothing operation, the reader is referred to the paper by Wheeler and Ikeuchi [147]. Smoothing also makes the computation of edgel normals much more reliable. After smoothing the edgel chains, it is possible to subsample the edgel chains if desired to get a denser set of edgels than pixel resolution.

The result after image acquisition, edge detection, and smoothing is a set of edgel chains

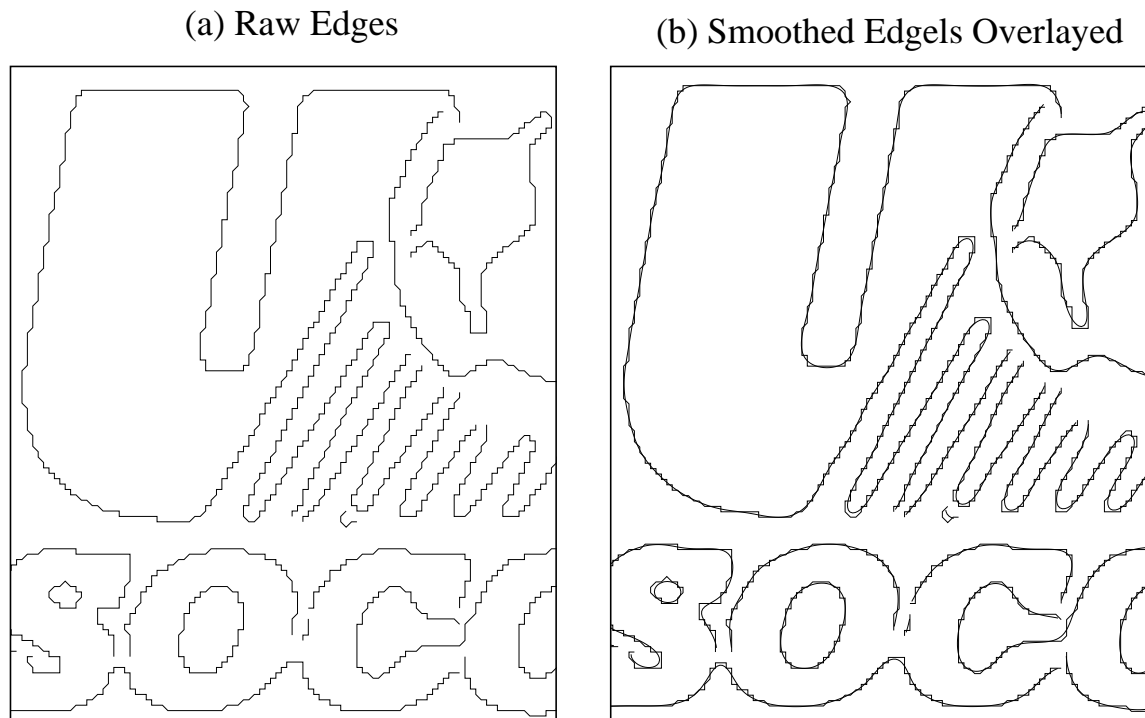


Figure 4.2: An example of (a) raw and (b) smoothed edgel chains (overlaid over the raw chains).

for each image. $E_i = \cup_j e_{i,j}$ denotes the set of edgel chains for view i . $e_{i,j} = \{\mathbf{U}_0, \dots, \mathbf{U}_n\}$ denotes the j th edgel chain of view i . Each edgel chain is an ordered list of 2D edgel points where \mathbf{U}_k denotes the (continuous) 2D coordinate of the k th edgel point in the chain.

After acquiring 2D edgel sets from various views of the object, these edgels must somehow be mapped into a common 3D coordinate system. Next, we describe our method for mapping and aligning the acquired 2D edgels in 3D model coordinates.

4.3 2D to 3D: View Alignment

The goal of this section is to map all the 2D edgels into a 3D coordinate system so that the data from all views can be merged to form the localization model. The problems (repeated from Section 4.1) that we face include:

- Distinguishing background from foreground edgels
- Converting 2D data to 3D data

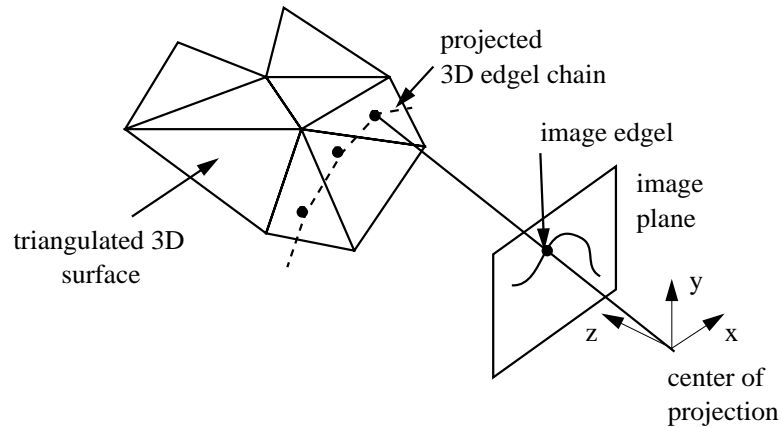


Figure 4.3: An example of mapping a 2D edgel onto a 3D triangulated surface.

- Aligning all the data into the same coordinate system

We can use the 3D modeling technique and calibrated-positioning system of Chapter 2 to virtually eliminate the above problems while enabling us to align all of the edgel data in the object's 3D coordinate system.

To begin, a triangulated surface model of the object is built using the techniques of Chapter 2. We assume that the pose of the object in each intensity image is known—for example, using the calibrated object positioner as described in Section 2.3. The position is denoted by the rigid transform $\mathbf{R}_{0 \leftarrow i}$, which represents the motion between view 0 and the view i .² We can use view 0 as the object coordinate system. All the 2D edgel data will be transformed to this central view.

Given the 3D surface model and its pose $\mathbf{R}_{0 \leftarrow i}$ in the image with respect to the object's coordinate system, we can project the 2D edgels onto the 3D model—in a sense, texture mapping the edges onto the model's surface. This is accomplished much like ray tracing; for each edge point in the image, we follow the ray from the camera's center of projection, through the edgel in the image plane, and into the scene. We then determine which surface triangles intersect with the ray and select the closest of these triangles. Figure 4.3 shows an example of the edgel mapping process.

Though this operation is intuitively simple, in practice there are several changes of coordinate system involved in mapping the 2D edgel to the model's coordinate system. In particular, we have 3 coordinate systems to deal with: image, camera, and object. The image coordinate system is in terms of pixels while the others are defined as 3D Cartesian frames in metric units. The transformations between coordinate systems are:

$$\mathbf{x}_c = \mathbf{R}_{c \leftarrow m} \mathbf{x}_m \quad (4.1)$$

²As in Section 2.3, $\mathbf{R}_{0 \leftarrow i}$ is a 4×4 homogeneous transformation matrix.

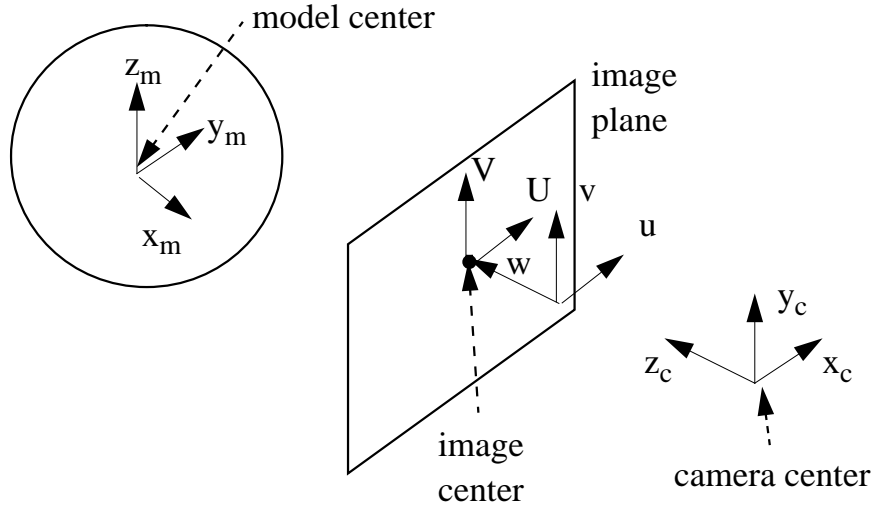


Figure 4.4: A diagram representing the relationships between the various coordinate frames used in the analysis in this chapter.

$$\mathbf{u} = \mathbf{R}_{u \leftarrow c} \mathbf{x}_c \quad (4.2)$$

$$\mathbf{U} = \begin{bmatrix} \frac{u}{w} \\ \frac{v}{w} \end{bmatrix} \quad (4.3)$$

where \mathbf{x}_m and \mathbf{x}_c are the positions in model and camera coordinates respectively, $\mathbf{u} = [u \ v \ w]^T$ are the image projection coordinates, and $\mathbf{U} = [U \ V]^T$ are the 2D image pixel coordinates. $\mathbf{R}_{c \leftarrow m}$ is a rigid transformation that transforms model coordinates to an orthographic camera-centered frame. The camera-centered frame is defined such that $[0 \ 0 \ 0]^T$ is the center of projection and $[0 \ 0 \ 1]^T$ is the camera's focal axis. $\mathbf{R}_{u \leftarrow c}$ transforms the Euclidean camera coordinates to (possibly non-Euclidean) 3D projection coordinates. This transform accounts for scaling factors (such as aspect ratio) and translation of the image center to non-zero image coordinates. The image projection coordinates are specified so that the final transformation is purely a perspective projection. Figure 4.4 shows the relationship between these coordinate frames.

The 2D edgel observations are defined in the image coordinate system, but to build 3D edgel models of an object, it is necessary to have these measurements in a 3D coordinate system, preferably the model coordinate system. There are several ways that one could go about mapping these edges. We begin by projecting the triangles of the 3D surface model into the image (much like z-buffering) using the equations presented above. Then, given the 2D edgel coordinates, \mathbf{U} , we can quickly determine which triangle intersects the ray corresponding to the edgel. First, we convert the edgel \mathbf{U} to a viewing direction \mathbf{v} in camera

coordinates by inverting the projection transform

$$\mathbf{v} = \mathbf{R}_{u \leftarrow c}^{-1} \begin{bmatrix} U \\ V \\ 1 \end{bmatrix}. \quad (4.4)$$

We then compute the precise intersection of ray $\hat{\mathbf{v}}$ with triangle τ_i

$$\mathbf{x}_c = \frac{\mathbf{n}_i^c \cdot \mathbf{c}_i^c}{\mathbf{n}_i^c \cdot \hat{\mathbf{v}}} \hat{\mathbf{v}} \quad (4.5)$$

where \mathbf{n}_i^c and \mathbf{c}_i^c are the normal and center point, respectively, of triangle τ_i in camera-centered coordinates. Once the intersection point is computed, we can then transform the point to the model coordinates by inverting the model-to-camera transform:

$$\mathbf{x}_m = \mathbf{R}_{c \leftarrow m}^{-1} \mathbf{x}_c.$$

We have now shown one way to map 2D edgels to 3D model coordinates. There are many other possible strategies to perform this mapping; however, none will be significantly more efficient than the one above. In any case, since model building will be done off-line, efficiency is not a real concern, thus, there is no need to discuss other possible methods.

As each 2D edgel in a chain is mapped to 3D model coordinates, the ordering of the edgels in the chain is maintained so that the 3D tangent direction for each edgel may be estimated. For example, the tangent vector, $\hat{\mathbf{t}}_i$, of the i th edgel in a chain is

$$\hat{\mathbf{t}}_i = \frac{\mathbf{x}_{i+1} - \mathbf{x}_i}{\|\mathbf{x}_{i+1} - \mathbf{x}_i\|}$$

where each \mathbf{x}_i is the mapped point corresponding to 2D edgel \mathbf{U}_i . The i th 3D edgel in a chain is then represented as the point and tangent vector pair $\langle \mathbf{x}_i, \hat{\mathbf{t}}_i \rangle$. This mapping solves the foreground/background problem. Only the edgels originating from the surface of the object are mapped to three dimensions; the other edgels may be ignored for purposes of modeling the object.

The basic approach that we have presented is not fool-proof however. It will often fail for edgels on or near occluding boundaries when the edgel rays do not intersect with our surface model. Figure 4.5 shows an example of this problem. Several factors contribute to the misalignment of occluding contour edgels with the surface model. Some degree of variability in 2D edgel location is due to edge detection, image discretization, and image noise. These errors will be propagated to the 3D mapping. Also, we can expect some errors to be introduced by the 3D mapping because of alignment/calibration error (in our calibrated image acquisition system) and 3D surface model error. Due to all of these factors an edgel corresponding to an occluding contour will randomly fall on either the object side or non-object side of the actual edge position. Thus, there will always be many instances of edgel rays that are generated by occluding contours of our object but do not intersect the object. We can rectify this problem by testing not only for intersection but also for near misses—edgel rays passing near triangles on the occluding boundary of the surface model.

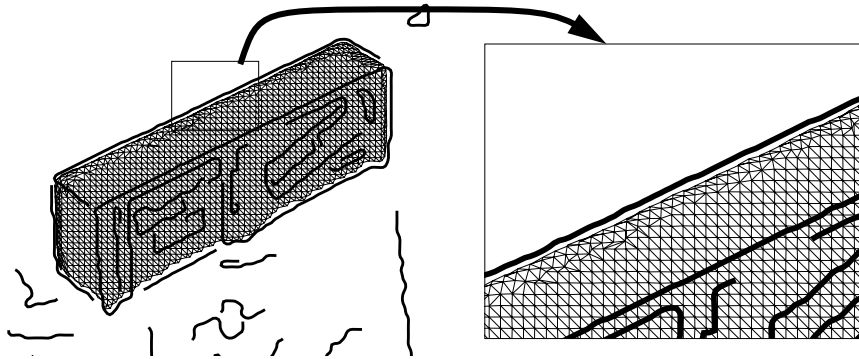


Figure 4.5: An occluding boundary edge which does not project onto the model surface.

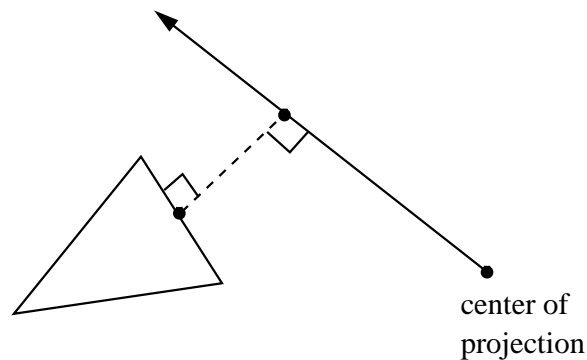


Figure 4.6: The shortest distance between a ray and the surface triangles when they do not intersect.

Occluding boundary triangles are easily detected when the model is projected into the image. These triangles will be adjacent to a triangle which is not visible (using the visibility tests of Section 3.2) from the given pose—thus creating an occluding boundary. The occluding boundary triangles can be checked separately for the near miss condition. We calculate the shortest distance between the edgel ray and any triangle on the model surface (see Figure 4.6). If this distance is within some threshold (for example, say 2 mm), then we can accept it as a potential 3D edgel in the model. The 3D coordinate of this edgel is the point on the edgel ray that is closest to the model (again see Figure 4.6).

This strategy seems like a reasonable solution. The result, however, is still unsatisfactory. The problem is that while the 2D projection of the surface model's occluding contour may appear smooth, the contour is not smooth in three dimensions. Figure 4.7 (b)

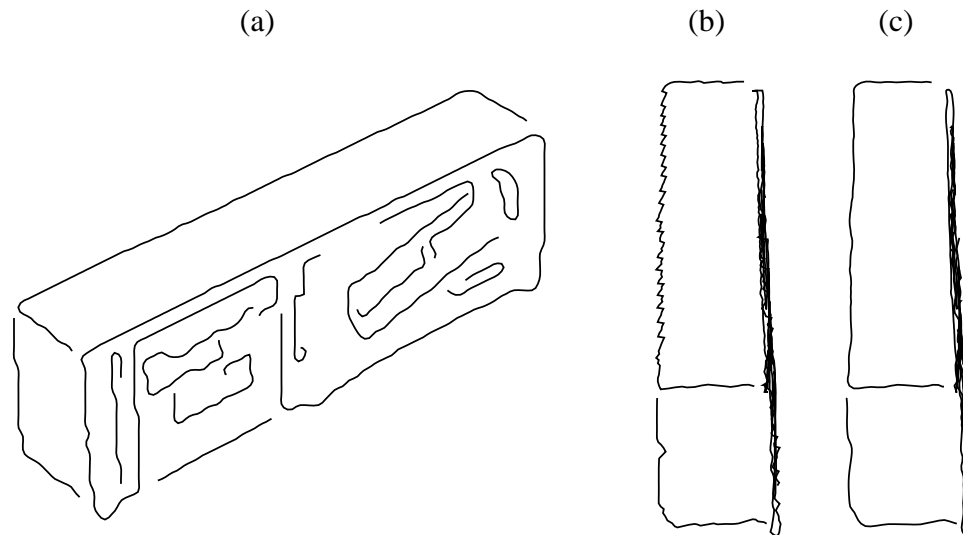


Figure 4.7: An occluding contour mapped to the object. (a) original 2D view, (b) another view of the mapped contour in three dimensions shows that it is not smooth in three dimensions, (c) the same contour after smoothing.

shows this phenomenon. The cause of the jagged 3D edgel is the triangulation along the occluding contour of the model surface. Much like the problem with jagged edges after edge detection in Section 4.2, we can use a smoothing operator to remove the kinks in the edge while retaining most of the original edge shape. In this case, we are smoothing a 3D edge chain. The smoothing operator of Wheeler and Ikeuchi [147] is as easily applied to 3D edgel chains as it is to 2D edgel chains. The smoothed result is suitable for our purposes. Figure 4.7 shows an example of such a 3D edgel before and after smoothing.

As one may imagine, the use of a threshold to attach edgels to occluding boundaries may be prone to errors. Often there will be edgels from the background that are near occluding boundaries of our object. Such mistakes are not critical as they are indistinguishable from spurious edgels that will invariably appear on the object. A successful algorithm for merging the 3D edgel data must account for the presence of extraneous and spurious edgels in the set of observations. The algorithm must minimize the possibility of including such edgels in the final model.

We have described how 2D edgels are acquired from a view of our object and how these edgels are mapped onto the surface of our object. In this section, we have shown how to align all of our edgel data into an object-centered coordinate system via an edgel-mapping process using a surface model. This process nicely eliminates two difficult problems: first, it directly solves the foreground/background problem—a problem that is likely unsolvable automatically using any other method; second, the correspondence problem is now tractable as all of the edgels are transformed to the same coordinate system which allows a natural

and reliable way to match and compare edgels.

The next problem is how to convert a large set of edgel observations to a single model representation of these observations. Our solution, the consensus-edgel algorithm, is the subject of the next section.

4.4 View Merging: the Consensus-Edgel Algorithm

In this section, we will describe an algorithm for merging the 3D edgel sets acquired by using the methods of the previous two sections. Given multiple aligned edgel sets, the question is how to combine the edgels from all the views to produce a unified representation of the edgel generators of the object. The main problem here is distinguishing random and extraneous edgels from those which will be visible over a wide variety of scenes. We must also be prepared for a significant amount of uncertainty in the edgel positions due to:

- Edge detection and discretization
- Image noise
- View alignment/calibration error
- 3D surface model error

This problem bears much similarity to the merging problem for 3D surface model building described in Section 2.4.

One difference between the surface and edgel case is that the topological problem is much simpler with edgels. In fact, topology is not necessary at all as we only need to build a model of edgels (points and tangent directions). Modeling the connectivity of the edgels may be useful for other tasks but is not necessary for the current localization task. We do not have the equivalent of the implicit surface representation to simplify the data merging process, nor do we need such a device. The main reason for using the implicit surface representation in Chapter 2 was to obviate a difficult problem of topology. If edgel connectivity is desired, this information would be easily obtainable as the topology of edgel chains is quite simple.

As in the 3D surface-merging problem, our edgel-merging algorithm must compensate for noisy/spurious edgel observations. Again, in the presence of such observations, there is little or no basis to trust that a single observation should be part of the object model. Our goal is to build models of edgel generators which are stable over many views of the object. We wish to take advantage of multiple observations to get a better estimate of the true source of the edgels with respect to the object's coordinate system. Simultaneously, we wish to exclude spurious and random edgels from the final model. Again, we are drawn to the concept of *consensus* as the basis for merging the observed data.

The basis of the merging algorithm is to find consensus sets of similar edgels from various views and compute an average of these edgels to add to the model. As in the surface-merging problem of Chapter 2, the concepts of consensus and similarity are relevant for

edgel merging. For the edgel-merging case, similar edgels are defined to be observations of the same edgel generator on the object. In the surface-merging case, similarity was defined in terms of surface location and normal direction. In the edgel-merging case, it is much the same; we define edgel similarity in terms of edgel location and tangent direction. Two edgels are grouped as similar if the distance between the two is below a threshold and the angle between their tangent directions is smaller than a threshold. We define the predicate

$$\text{SameEdgel}(\langle \mathbf{x}_0, \hat{\mathbf{t}}_0 \rangle, \langle \mathbf{x}_1, \hat{\mathbf{t}}_1 \rangle) = \begin{cases} \text{true} & (\| \mathbf{x}_0 - \mathbf{x}_1 \| \leq \delta_d) \wedge (|\hat{\mathbf{t}}_0 \cdot \hat{\mathbf{t}}_1| \geq \cos \theta_n) \\ \text{false} & \text{otherwise} \end{cases} \quad (4.6)$$

which determines whether two surface observations are sufficiently close in terms of location and tangent direction, where δ_d is the maximum allowed distance and θ_n is the maximum allowed difference in tangent directions. Much like the consensus-surface algorithm, consensus is defined as the minimum number of similar observed edgels required to instantiate an edgel generator in the model.

Our problem now is where to begin the search for consensus edgels. In the surface-merging case, we only needed to fill all the voxels in the volume grid; the order in which we proceed is irrelevant as each voxel is independent of the other voxels. In the current problem, all we have is an unorganized set of edgels with no obvious way to proceed.

Having no other information than the edge sets themselves and without the benefit of a representational aid like the volumetric representation for surfaces, it makes sense to begin the search for consensus edgels at one of the observed edgels. A good edgel to start with is one which is likely to be a consensus edgel (i.e., an observation of a stable edgel generator). One possibility is to begin with large edgel chains first. It is unlikely that noise or random external events will result in the detection of very long edgel chains. Also, long edgel chains are often indicative of significant geometric or photometric features of the object which are often detectable over many views.

Our strategy will be to take each 3D edgel chain—longest first—and check each edgel of the chain to see if it belongs to a consensus edgel. We perform a local search of the edgels from all other views to find the nearest edgel in each view. These edgels are tested for similarity to the current edgel and if a consensus is found, we add the averaged, consensus edgel to our final model.

Figure 4.8 shows an example of the local search for a case where we have four views. The edgels found to be in the consensus can be eliminated from further consideration. Thus, we are able to identify all consensus edgels from our set of 3D edgel observations.

As in the consensus-surface search, the local search for nearest edgels can be implemented efficiently using k-d trees [42]. A k-d tree of 3D edgels is built for each different view of the object. A nearest-neighbor search of the respective k-d trees can be computed in $O(\log n)$ expected time where n is the number of edgels in the given tree.

The consensus-edgel algorithm can now be specified more precisely. In the algorithm below $e_{i,j}$ denotes the j th edgel chain of view i . Again, an edgel chain comprises a list of 3D edgels—3D points and tangent direction pairs $\langle \mathbf{x}_i, \mathbf{t}_i \rangle$.

Algorithm *BuildConsensusEdgelModel*

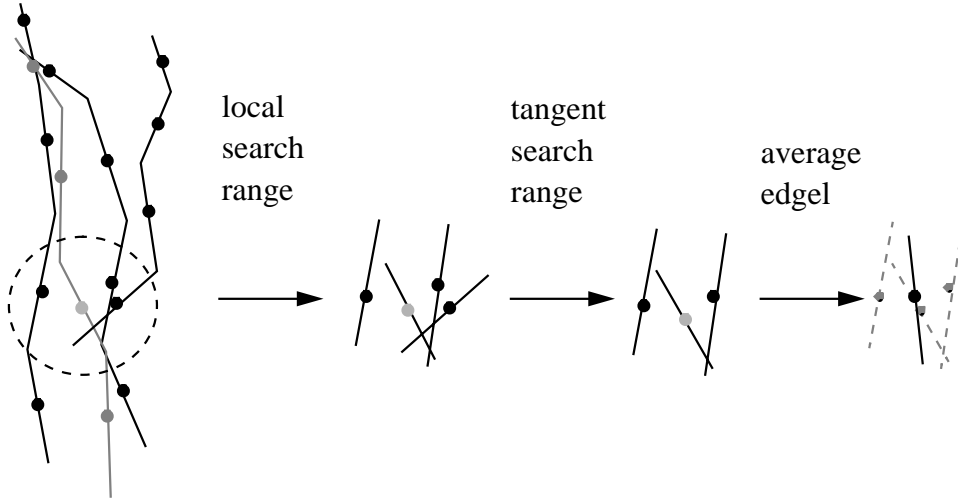


Figure 4.8: The stages of a consensus-edgel search for the grey edgel (center left). Eliminate candidates first using proximity, then the tangent direction constraint, then average the remaining edgels to form a consensus edgel.

Input: 3D edgel sets $E_i, i = 1, \dots, N$

Output: consensus edgel model E_f

1. $E_f \leftarrow \emptyset$
2. **for each** E_i
3. **do** *Build K-D Tree*(E_i)
4. **for each** edgel chain $e_{i,j} \in \cup_i E_i$, largest $|e_{i,j}|$ first
5. **do for all** $\langle \mathbf{x}, \hat{\mathbf{t}} \rangle \in e_{i,j}$
6. **do** $\langle \mathbf{x}_c, \hat{\mathbf{t}}_c, count \rangle \leftarrow \text{ConsensusEdgel}(\langle \mathbf{x}, \hat{\mathbf{t}} \rangle, E_k)$
7. **if** $count \geq \theta_{quorum}$
8. **then** $E_f \leftarrow E_f \cup \langle \mathbf{x}_c, \hat{\mathbf{t}}_c \rangle$
9. **return** E_f

Algorithm *BuildConsensusEdgelModel* makes use of an important subroutine: *ConsensusEdgel*. Algorithm *ConsensusEdgel* performs the local search around the neighborhood of the given edgel to estimate the average of the edgels that are determined to correspond to the same edgel generator on the object. Algorithm *BuildConsensusEdgelModel* uses a threshold θ_{quorum} to determine if the support for a given edgel is sufficient to add it to the final edgel model.

Algorithm *ConsensusEdgel*

Input: edgel $\langle \mathbf{x}, \hat{\mathbf{t}} \rangle$ of chain e_j in edgel set E_i

Input: 3D edgel sets $E_k, k = 1, \dots, N$

Output: average consensus edgel and count: $\langle \mathbf{x}_{avg}, \hat{\mathbf{t}}_{avg}, count \rangle$

1. $\mathbf{x}_{avg} \leftarrow \mathbf{x}$
2. $\hat{\mathbf{t}}_{avg} \leftarrow \hat{\mathbf{t}}$
3. $count \leftarrow 1$
4. **for** each edgel set $E_j \neq E_i$
5. **do** $\langle \mathbf{x}_c, \hat{\mathbf{t}}_c \rangle \leftarrow \text{NearestEdgel}(E_j, \mathbf{x})$
6. **if** $\text{SameEdgel}(\langle \mathbf{x}, \hat{\mathbf{t}} \rangle, \langle \mathbf{x}_c, \hat{\mathbf{t}}_c \rangle)$
7. **then** $\mathbf{x}_{avg} \leftarrow \mathbf{x}_{avg} + \mathbf{x}_c$
8. $\hat{\mathbf{t}}_{avg} \leftarrow \hat{\mathbf{t}}_{avg} + \hat{\mathbf{t}}_c$
9. $count \leftarrow count + 1$
10. $\mathbf{x}_{avg} \leftarrow \frac{1}{n} \mathbf{x}_{avg}$
11. $\hat{\mathbf{t}}_{avg} \leftarrow \frac{\hat{\mathbf{t}}_{avg}}{\|\hat{\mathbf{t}}_{avg}\|}$
12. **return** $\langle \mathbf{x}_{avg}, \hat{\mathbf{t}}_{avg}, count \rangle$

Algorithm *NearestEdgel* returns the closest edgel (in terms of position) from a set of edgels to the given edgel. Three thresholds are required and are almost identical to those required for the consensus surface algorithm (see Section 2.4). δ_d and θ_n are required for the predicate *SameEdgel*, which is defined in Equation 4.6, to determine how close the edgel points and tangent directions must be to consider them as similar. These can be estimated based on the variations expected from the observed data. θ_{quorum} is the consensus threshold which determines the required number of similar edgels for consensus. This threshold must be chosen while considering the number of total views and the number of views from which the edgel sources may be visible. θ_{quorum} will determine how stable the edgels must be for inclusion in the model.

The result of Algorithm *BuildConsensusEdgelModel* will be the set of consensus edgels over the edgel sets from all views. The above description omits one bookkeeping detail for clarity. We must keep track of which edgels have been used to add a consensus edgel to the final model and eliminate these edgels from further consideration.

We now have a method to merge rigidly attached object edgels (i.e., edgel sources whose position is fixed on the object). This method overlooks a large source of edgels, namely occluding contours. Occluding contours are quite different from rigid edgels and thus require slightly different representation and treatment for localization. It is unlikely that the same point on the contour generator would be observable from a sufficient number of views for consensus to be applicable. Since the appearance of occluding contours is based purely on local geometry of the generator's surface, we can utilize our 3D surface model to predict the appearance of the surface's occluding contours. This is the topic of the next section.

4.5 Modeling Occluding Contours for 3D-2D Localization

Occluding contours are the boundaries observed at points on a smooth surface where there is a transition from visible surface points to occluded surface points from a particular

viewing direction. Occluding contours are often detected as edges in images since the object surface and background are often of distinctly different shades, colors or intensities. Thus, occluding contours are prominent features for object recognition and localization. For smooth convex surfaces, every point on the surface can generate an occluding contour from many viewing directions. For example, each point on a sphere generates an occluding contour in the image for all viewing directions \hat{v} such that

$$\hat{v} \cdot \hat{n} = 0$$

where \hat{n} is the surface normal at the given point. This set of \hat{v} 's spans the tangent plane of the surface at that point.

For localization, we need to be able to predict the appearance of occluding contours from a given viewing direction. Appearance prediction needs to be an efficient operation as well. Another consideration is that our representation must be derived from our 3D surface model.

One possible solution would be to represent the surface of the object using an algebraic polynomial, and then analytically solve for occluding contours. This is the approach taken by Ponce and Kriegman [77]. The problem is that these algebraic equations can become very large even for simple shapes. Another complication for algebraic representations of occluding contours is how to build models of algebraic surfaces. In practice, objects will have to be modelled using a collection of algebraic surfaces. Inferring the algebraic representation from a triangulated surface is an extremely difficult problem—fundamentally the same as range-image segmentation [5], for which no completely satisfactory solution exists. Even if segmentation were solved, the boundaries between surfaces greatly complicates the solution of the algebraic surfaces.

Another possibility, and the approach that we use in this thesis, is to use a piecewise planar approximation of the surface. It is a reasonable option for several reasons:

- Our surface is already approximated by a piecewise planar model (triangular patches).
- The approximation error of the contour projection can be made arbitrarily small (but is limited by the original surface-model resolution).
- We can use a point-based representation consistent with our rigid edgel representation and 3D surface representation.

The piecewise-planar approximation idea is made clear by considering the piecewise-linear approximation of a 2D circle (cross section of a sphere). Figure 4.9 (a) shows a circle and a set of viewing directions (equivalent to tangent directions) at the corresponding contour generators. As the viewing direction changes, the contour generator traverses the circle. If the circle is represented by a set of connected line segments (see Figure 4.9 (b)), the contour generator still changes as the viewing direction changes, but now it changes in discrete intervals corresponding to the endpoints of the line segments.

For the localization task, the most important aspect of the approximation is the accuracy of the projected contour. The worst-case error is the distance between the piecewise-linear

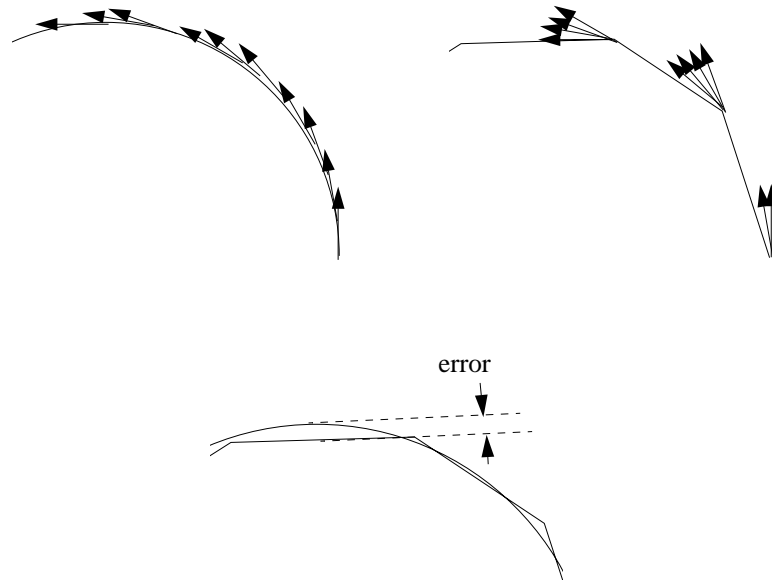


Figure 4.9: A circle and its occluding contour points (a) continuous circle, (b) piecewise-linear circle, (c) the error of approximation

circle and the true circle and is maximum at the midpoint of each approximating line segment (see Figure 4.9 (c)). We can represent a curve's occluding contours to a desired accuracy using piecewise-linear approximation. This naturally extends to 3D using piecewise-planar models (such as our triangulated surface models).

Applying z-buffering [40, 141] to our triangulated surface model is one possibility for computing the occluding-contour edges. Basically, the occluding-contour points can be identified by finding points which lie on edges which border a visible triangle on one side and an invisible triangle on the other side. However, as noted in Section 3.2, z-buffering is too expensive for our localization application. Using the same idea with our surface-point visibility approximation produces very poor results since the mistakes of the approximation will always imply occluding-contours where none should exist.

Instead we concentrate on defining a local computation over points on the object surface to determine whether they generate a contour or not from a given viewing direction. Our triangulated surface model consists of vertices which are connected to form triangles that cover the surface. Each vertex or surface point is a potential contour generator. We are interested in finding a quick local computation to determine if the vertex is on the occluding contour generated by the surface model from a certain viewing direction. The curvature at a point provides the information necessary to predict the appearance of contour points.

4.5.1 Curvature

Curvature is, technically, a property of a curve, not a surface [102]. The curvature of a surface usually refers to the curvature of a specific curve that lies on the surface. For a length-parameterized curve in three dimensions, $\beta(t) = [x(t) \ y(t) \ z(t)]^T$, the curvature is the magnitude of the change in the tangent vector, $\beta'(t)$. Curvature is also described as the magnitude of the bending of the curve where the direction of the bending is $\beta''(t)$. Thus, the curvature of $\beta(t)$ is defined as

$$\kappa(t) = \|\beta''(t)\| = \sqrt{x''(t)^2 + y''(t)^2 + z''(t)^2}$$

For a circle of radius r , $\kappa = \frac{1}{r}$. A rough characterization of curvature is the inverse of the local radius of the curve.

For curves, the Frenet frame [102] defines a coordinate system at each point. The coordinate system is defined such that the normal $\hat{n} = \frac{\beta''}{\|\beta''\|}$. Thus, with the normal direction already specified, the magnitude of bending is sufficient to describe the curvature at a point on a curve.

Getting back to smooth surfaces, we are interested in whether a surface point generates a contour from a given viewing direction. The first requirement is that the viewing direction \hat{v} is perpendicular to the surface normal \hat{n} at the point (i.e., $\hat{n} \cdot \hat{v} = 0$). Given \hat{v} and \hat{n} , we can extract a particular curve from the surface—the intersection of the surface with the plane spanned by \hat{v} and \hat{n} . This curve is called a *normal section* [102] since the surface normal lies in the plane of the curve. For example, the normal section of a point on a sphere of radius r is a circle of radius r (see Figure 4.10). The curvature of the normal section at the given point is appropriately called the *normal curvature*.

The curvature of a normal section is not simply a magnitude (as in the 2D case) but also indicates the direction of bending by its sign. Surfaces have a unique normal \hat{n} at each point while a normal section at a point may bend in either the \hat{n} or $-\hat{n}$ directions (see Figure 4.10). Thus, the sign of curvature of a 3D point differentiates between normal-section curves that bend away from the surface normal and those that bend in the direction of the surface normal.

To generate an occluding contour for a surface with an outward pointing normal, we require that the normal section has negative normal curvature (see Figure 4.10 (b)). Negative normal curvature implies that the point is a transition from visible to invisible points—thus generating the contour.

For a 3D surface point, the curvature depends on the specific normal section. Fortunately, Euler's formula gives us a simple characterization of the curvatures of all normal sections given an arbitrary viewing direction \hat{v} such that $\hat{n} \cdot \hat{v} = 0$. Euler's formula is

$$\kappa(\hat{v}) = \kappa_1(\hat{e}_1 \cdot \hat{v})^2 + \kappa_2(\hat{e}_2 \cdot \hat{v})^2 \quad (4.7)$$

where κ_1 and κ_2 are the maximum and minimum curvatures, respectively, and are referred to collectively as the principal curvatures. \hat{e}_1 and \hat{e}_2 are the tangent directions corresponding to the maximum and minimum curvatures, respectively, and are referred to as the principal

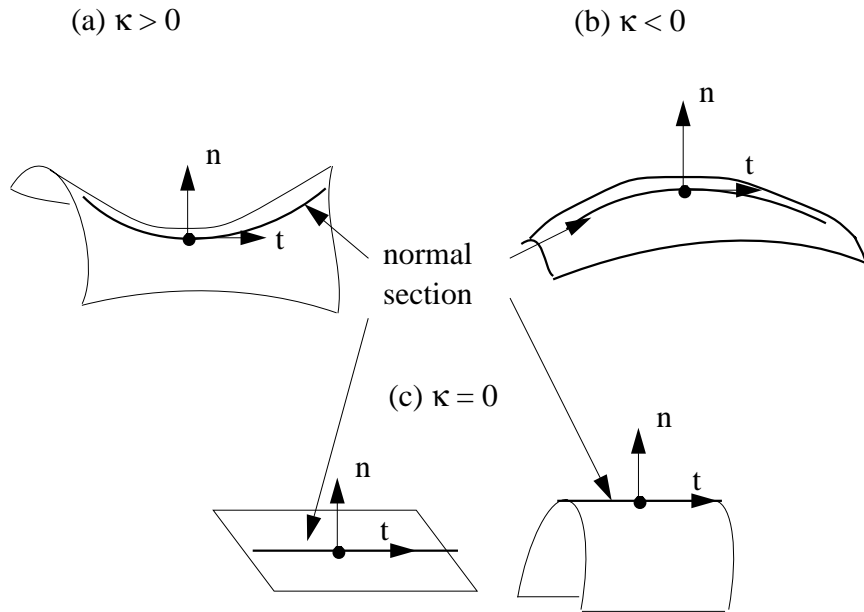


Figure 4.10: Example of normal sections with (a) positive normal curvature and (b) negative normal curvature.

directions. The principal directions are orthogonal to each other and form the basis of the tangent plane of the point. κ_1 , κ_2 , \hat{e}_1 , and \hat{e}_2 completely characterize the curvatures of normal sections at a point. Along any normal section, the curvature of a point can be classified into three categories: positive, negative and zero. Only surface points with negative curvature (convex normal sections) generate occluding contour edges in a 2D projection of the 3D object. However, the curvature at a surface point depends on which normal section is taken. Since it is possible for a point to have $\kappa_1 > 0$ and $\kappa_2 < 0$, some viewing directions in the point's tangent plane would generate occluding contours ($\kappa(\hat{v}) < 0$) while others would not ($\kappa(\hat{v}) \geq 0$).

Estimating Curvature from a Triangulated Surface Model

Using curvature information, we can determine which points on our 3D surface model are potential contour generators. Determining the curvature of the surface points of the model is tricky. The problem is that we have a triangulated (sampled) model of a surface: much shape information has been lost. The surface model is also not likely to be perfect—the surface will invariably be contaminated by noise. Since curvature is a second-order differential property, it is very computationally sensitive to noise and the effects of discrete sampling (e.g., aliasing).

Several solutions for computing the surface curvature from discrete data have been

proposed in the literature. Besl and Jain [5] presented a formulation for computing curvature from range images. Their formulation relies on the regular grid sampling of the depth (as is available directly from range images) so is not directly applicable to our problem. Chen and Schmitt [18] proposed a solution for computing curvature at points of a triangulated model. Their method involves fitting circles to triples of points to approximate normal sections and then use a least squares fit to Equation 4.7 to solve for the principal curvatures and directions. Unfortunately, the best fit circle for three haphazardly selected points on a surface can give wildly inaccurate estimates of normal curvature. In addition, there is a singularity for collinear triples which makes fitting circles to these points unreliable.

A more stable and natural method is the one proposed by Koenderink [76]. His idea is to fit a quadric surface in the neighborhood of each point and then use the algebraic representation of the surface to derive the principal curvatures and directions. This is a natural approach for estimating principal curvatures since, fundamentally, the principal curvatures and directions define a locally quadratic approximation of the surface shape. A variation of Koenderink's approach was used by Shi et al. [125] to measure surface curvature in tomographic medical data.

We also use a variation of Koenderink's approach to compute the principal curvatures and directions for each vertex on our triangulated surface model. While fitting a quadric surface seems simple enough, there are some subtleties that may interest the reader. The description of the quadric fitting and curvature estimation is presented in Appendix C. The main point is that we can easily compute the principal curvatures, κ_1 and κ_2 , and the principal directions, \hat{e}_1 and \hat{e}_2 , from the local quadric fit.

Given κ_1 and κ_2 , we can quickly classify each point into one of three categories:

1. $(\kappa_1 \geq 0) \wedge (\kappa_2 \geq 0)$: This point is not a contour generator, and we can eliminate it from consideration for our purposes.
2. $(\kappa_1 \geq 0) \wedge (\kappa_2 < 0)$: This point is either a cylindrical point (i.e., $\kappa_1 = 0$) or a saddle point and generates contours from some tangent viewing directions—those with negative normal curvature.
3. $(\kappa_1 < 0) \wedge (\kappa_2 < 0)$: This point is an elliptic point and generates contours for all tangent viewing directions.

Figure 4.11 shows examples of each of these three surface classes and the set of viewing directions from which the point generates an occluding contour (i.e., $\kappa(\hat{v}) < 0$).

Thus, we can classify all points on our model surface as belonging to one of the above three classes. We use this information to predict the visibility of contour edges in images of the object. The details of the visibility computation will be described in the next chapter on 3D-2D localization.

One point worth noting is the effect of corners and very high curvature points. These points are fundamentally different to occluding contours but also share some similarities. They are given a separate class: convex edgels.

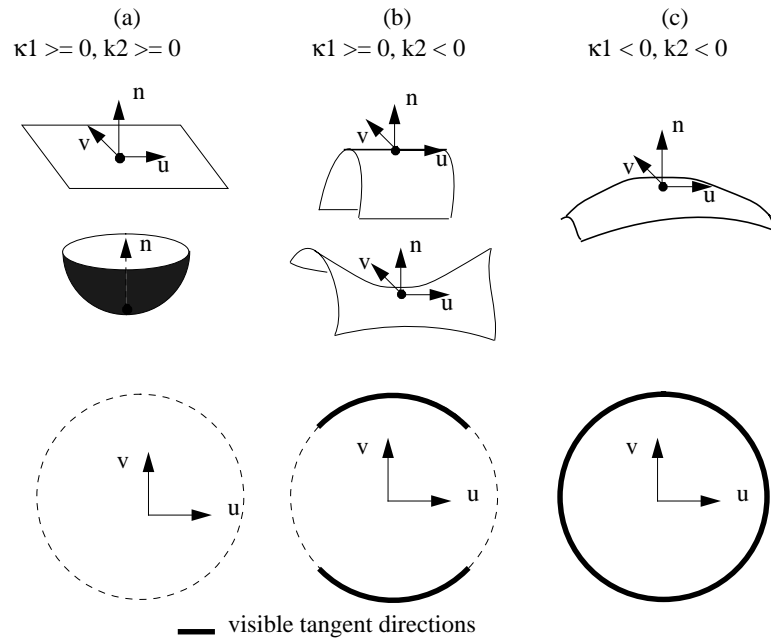


Figure 4.11: Classes of surfaces based on curvature. The third row shows a tangent plane for each class on which the dark shaded regions indicate viewing directions from which a contour is visible at the point in question.

Convex Edgels

High-curvature points (e.g., corners) are a hybrid of the rigid surface and occluding-contour edgels. From some viewing directions, high curvature (corner) points generate occluding contours. In this sense, the convex edgel is like an occluding-contour edgel. From other directions, they may generate intensity discontinuities because of the surface normal discontinuity across the edgel. In this sense, the convex edgel is like a rigid surface edgel.

For the curvature analysis presented in this section, we need not distinguish high curvature points since our method for acquiring rigid edgel models (described in Section 2.4) will usually detect this type of edgel as rigid. However, as we will see in the next chapter, the visibility constraints for convex edgels demands treatment separate from rigid surface edgels and occluding-contour edgels.

4.6 Object Modeling for 3D-2D Localization: Results

Here we present some experimental results of our implementation of the 3D edgel modeling algorithm described in this chapter.

As discussed above, we make use of a 3D surface model of the object constructed using the method described in Chapter 2. Thus, we are bound by the same constraints of the modeling system described there: the objects must be small enough to be imaged by the range finder and to be mountable on the Puma. We assume, as before, that the objects are rigid and opaque.

For our 3D edgel modeling experiments, we selected 7 objects to model using our system. We use the toy boxcar, rubber duck, ceramic mug, and toy car which were used in the experiments of Chapter 2. We also model 3 other simpler (planar) objects: a stop sign, a sign with a T on it (T-sign), and a bulls-eye like target.

For each object, we first built the 3D surface model following the methods of Chapter 2. We then acquired intensity image views of the objects, again using our calibrated image acquisition system. We manually determined the number of intensity image views for each object to 1) maximally cover the viewable surface of the object, and 2) provide a sufficient amount of overlap between views for the consensus-edgel algorithm to extract rigid surface edgels. The number of views required is related to the geometric complexity of the object: varying from 21 for the three planar objects to 54 for the toy car.

The views were acquired by varying the joint angles θ_y and θ_x of the robot's end effector as in Section 2.5 (see Figure 2.12 and Section 2.5 for a review of these details). Generally, we would vary θ_y from -180 degrees to 160 in increments of 20 degrees and would vary θ_x from anywhere from -30 degrees to +30 degrees in 20 degree increments as well.

In addition to varying the pose of the object, we also varied the illumination in order to reduce the dependence of our models on any single light source condition. We used three different illumination configurations for this purpose. The illumination configuration was switched after every image in the sequence.

The acquired intensity images contained 256×240 pixels. Each image was processed as described in Section 4.2 to produce a set of smoothed 2D edgel chains. The 2D edgel chains were then projected into 3D object coordinates using the calibrated position and 3D surface model of the object. The edgels were then resampled in 3D coordinates at a resolution of 1 mm. The resulting 3D edgel sets were then provided to the consensus-edgel algorithm to extract the significant 3D edgel generators from the observed data.

The results of the model acquisition for the test objects are shown in Figures 4.12- 4.18. Each of these figures show:

- an intensity image of the object
- an example from the set of observed intensity edge images
- the complete set of 3D edgels used as input to the consensus-surface algorithm
- a view of the 3D rigid edgels extracted from the data
- three views of the full edgel model, including 3D rigid edgels and occluding contour edgels extracted from the 3D surface model (the views are displayed using hidden edgel removal for clarity)

Object	Images	Edgels In	Edgels Out	Time (seconds)	θ_{quorum}	δ_d (mm)	θ_n (degrees)
stop	21	22k	914	10	11	1.5	25
T-sign	21	26k	970	14	8	1.5	25
target	21	18k	602	9	11	2.5	25
boxcar	33	39k	1537	48	7	3	45
mug	36	39k	1510	240	8	2	25
car	54	40k	1387	134	6	1	36
duck	49	21k	185	46	12	2	45

Table 4.1: Statistics of the edgel modeling experiments for each object.

The relevant statistics of the modeling experiments for each object are presented in Table 4.1. These statistics include the number of input images, the number of edgels input to the consensus-edgel algorithm, the number of edgels in the resulting model, the execution time on an SGI Indy 5 (a 124 MIPS/49.0 MFLOPS machine), and the parameters for our consensus-edgel algorithm (the quorum limit θ_{quorum} , the maximum distance, δ_d , between similar points and the maximum angle, θ_n between tangent vectors of similar edgels).

The results demonstrate that we can create fairly accurate models of the edgel generators of an object given many sample views of the object and a 3D surface model of the object. In particular, the consensus-edgel algorithm is able to extract the significant rigid edgels from a large set of rather noisy edgel observations.

4.7 Object Modeling for 3D-2D Localization: Summary

In this chapter, we have described our methods for automatically constructing a model for use in localizing a 3D object in 2D intensity images—3D-2D localization. For this localization task, we have chosen to match model edgels with image edgels using a 3D model representation rather than a view-based (2D) approach.

In order to build a 3D model of the edgel generators of the object, we make use of the 3D surface modeling and calibrated view alignment described in Chapter 2. Knowing the pose of the object and its shape allows us to convert 2D observations into the object’s 3D coordinate system, while eliminating background edgels from consideration. We presented the consensus edgel algorithm which extracts the stable rigid edgel generators from the sample views of the object. To account for occluding-contour edgels, we proposed a method for computing and analyzing the curvature at all points on our 3D surface model. Knowing the curvature of a point, we can classify it as a contour generator or not. The principal curvatures and directions of a point makes it possible to predict the viewing directions from which a contour generator will generate a contour.

We have postponed discussion of the visibility computation for our edgel model. At best, from our sampled data, we can collect a set of viewing directions from which each model edgel was detected. Visibility conditions of an edgel cannot be reliably or accurately

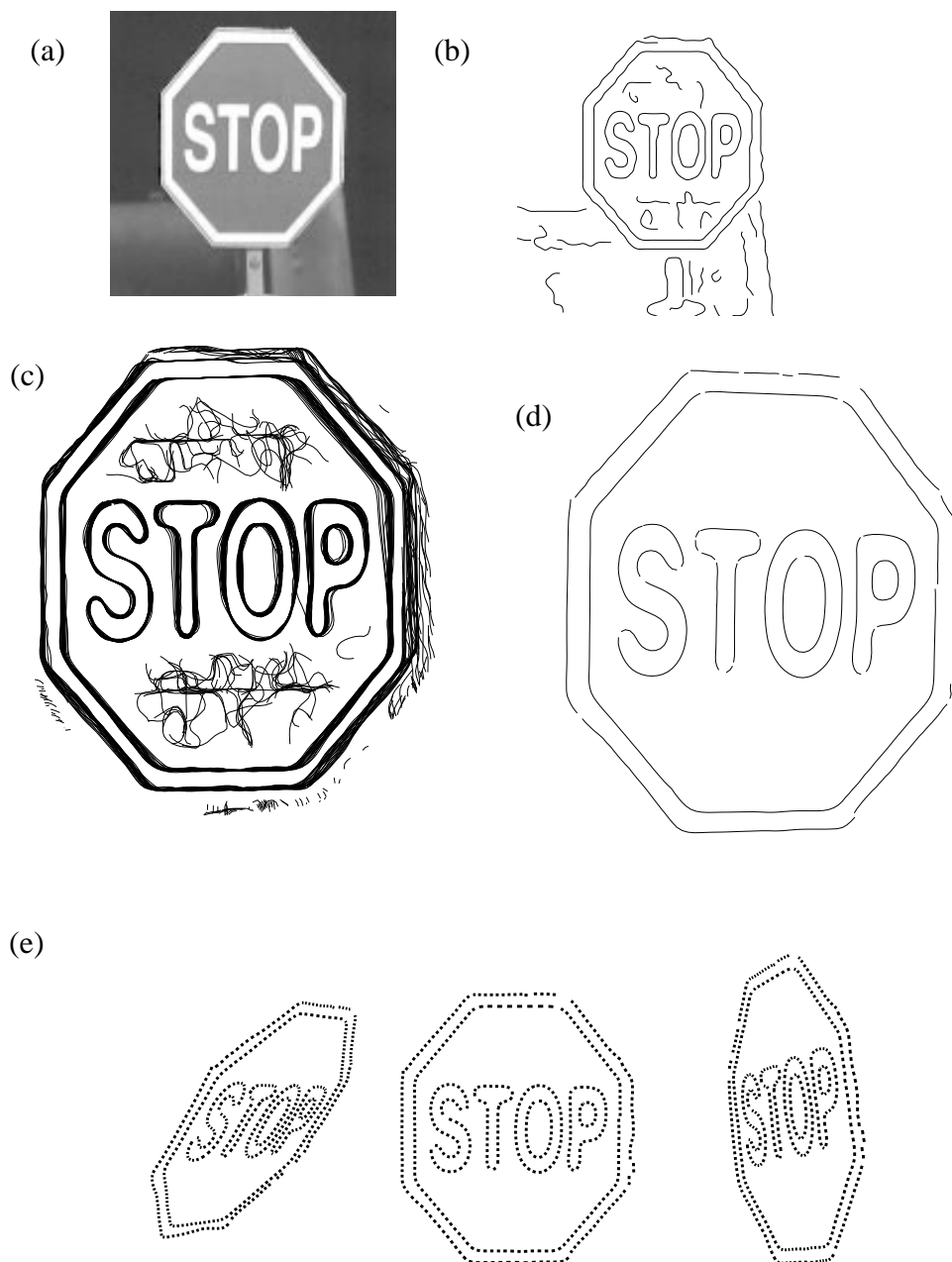


Figure 4.12: Results from modeling the 3D edgel generators of the stop sign. (a) An intensity image of the stop sign, (b) an example from the set of observed intensity edge images, (c) the complete set of mapped 3D edgels used as input to the consensus-surface algorithm, (d) the rigid surface edgels extracted by the consensus-surface algorithm, (e) three views of the resulting 3D edgel model (including occluding contour edgels and rigid surface edgels).

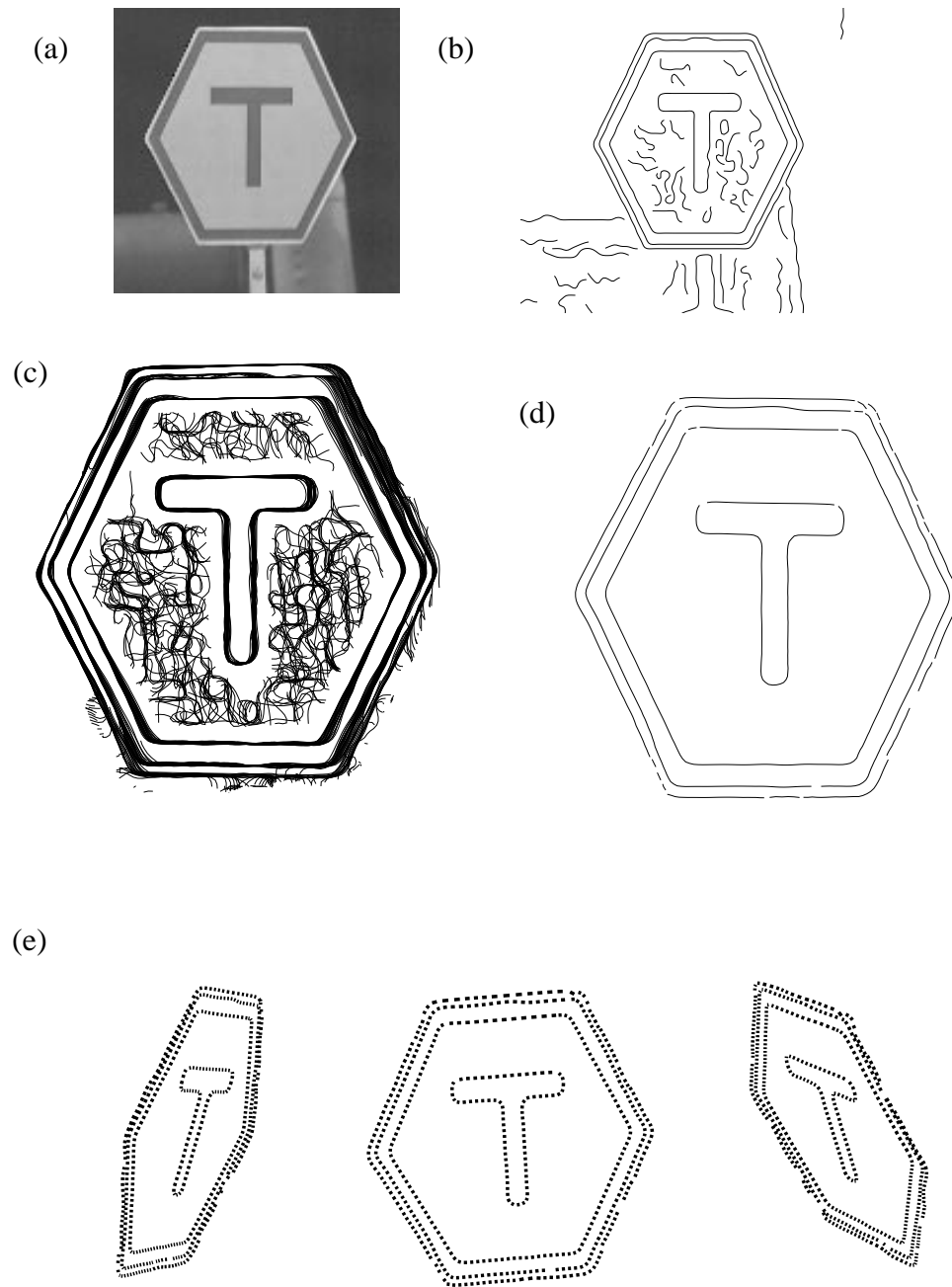


Figure 4.13: Results from modeling the 3D edge generators of the T-sign. (a) An intensity image of the T-sign, (b) an example from the set of observed intensity edge images, (c) the complete set of mapped 3D edgels used as input to the consensus-surface algorithm, (d) the rigid surface edgels extracted by the consensus-surface algorithm, (e) three views of the resulting 3D edgel model (including occluding contour edgels and rigid surface edgels).

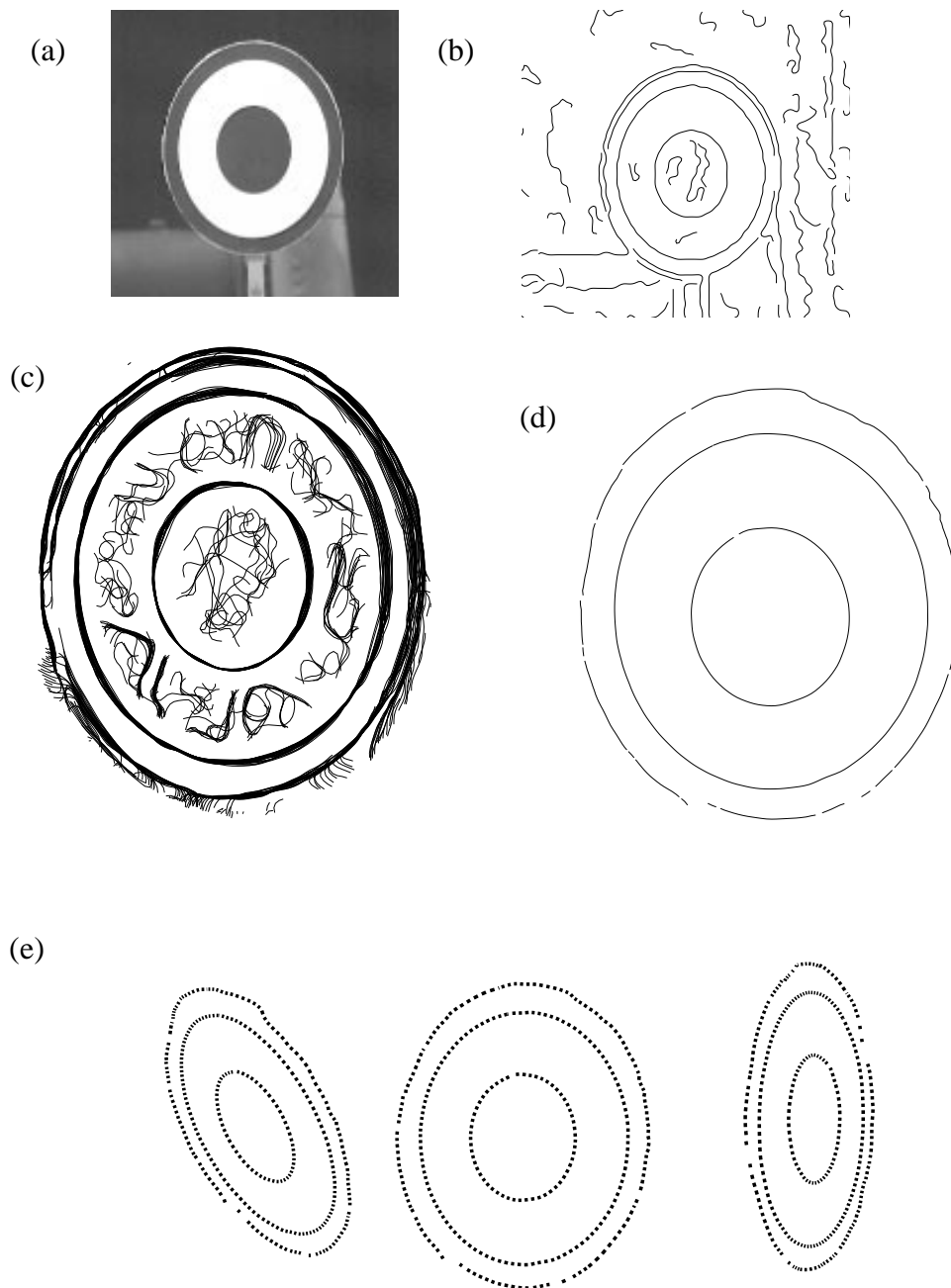


Figure 4.14: Results from modeling the 3D edgel generators of the bulls-eye. (a) An intensity image of the bulls-eye, (b) an example from the set of observed intensity edge images, (c) the complete set of mapped 3D edgels used as input to the consensus-surface algorithm, (d) the rigid surface edgels extracted by the consensus-surface algorithm, (e) three views of the resulting 3D edgel model (including occluding contour edgels and rigid surface edgels).

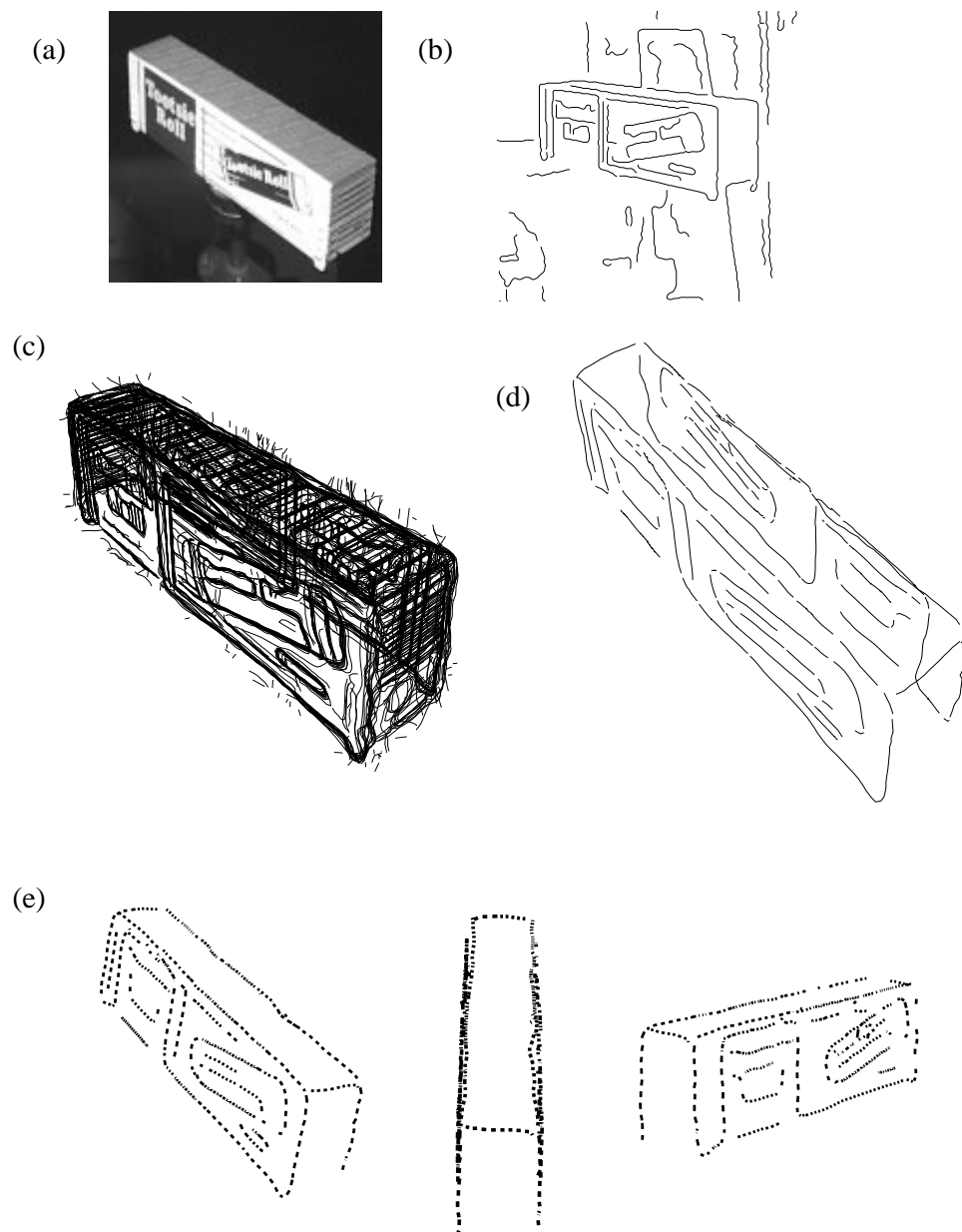


Figure 4.15: Results from modeling the 3D edge generators of the boxcar. (a) An intensity image of the boxcar, (b) an example from the set of observed intensity edge images, (c) the complete set of mapped 3D edges used as input to the consensus-surface algorithm, (d) the rigid surface edges extracted by the consensus-surface algorithm, (e) three views of the resulting 3D edgel model (including occluding contour edges and rigid surface edges).

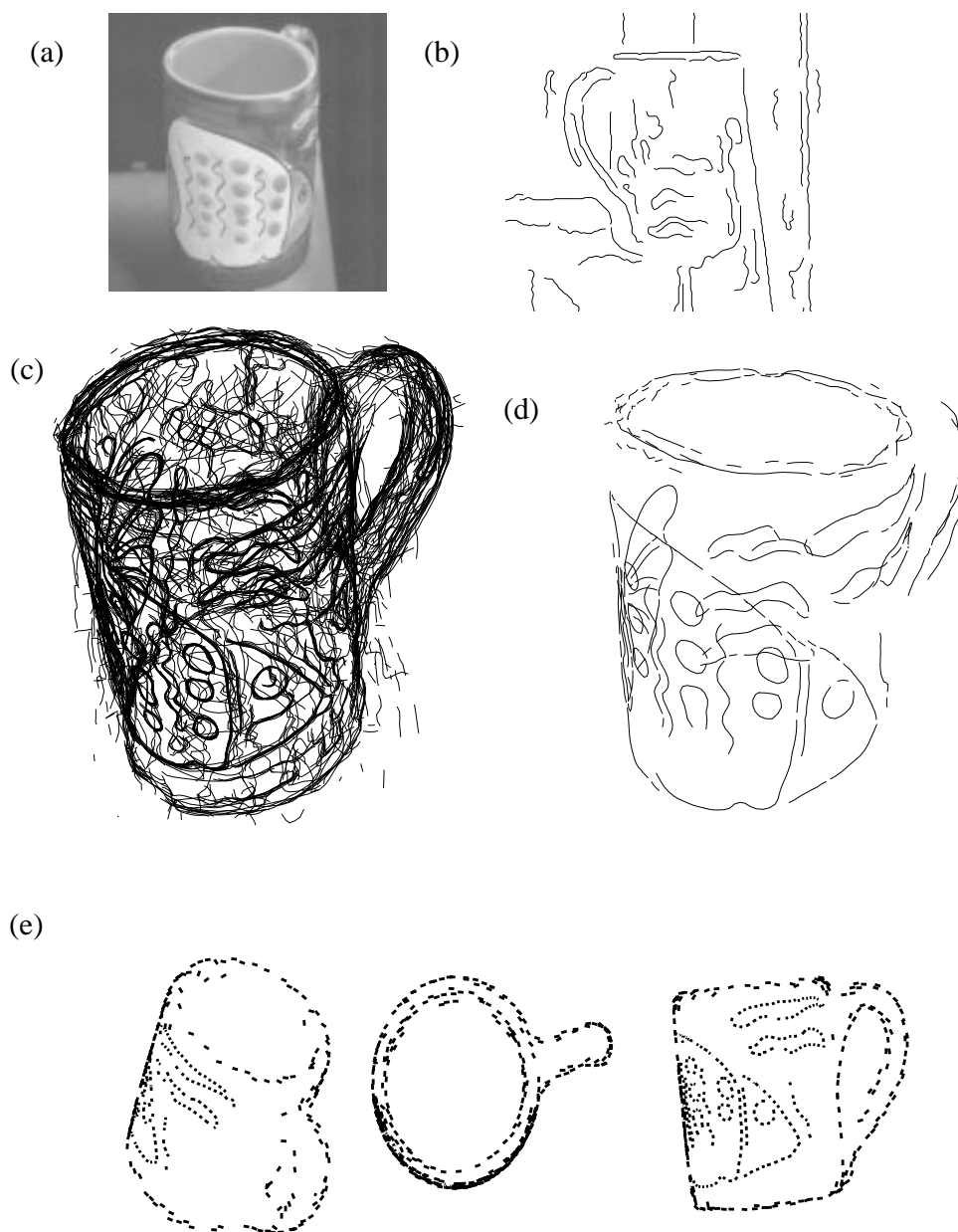


Figure 4.16: Results from modeling the 3D edgel generators of the mug. (a) An intensity image of the mug, (b) an example from the set of observed intensity edge images, (c) the complete set of mapped 3D edgels used as input to the consensus-surface algorithm, (d) the rigid surface edgels extracted by the consensus-surface algorithm, (e) three views of the resulting 3D edgel model (including occluding contour edgels and rigid surface edgels).

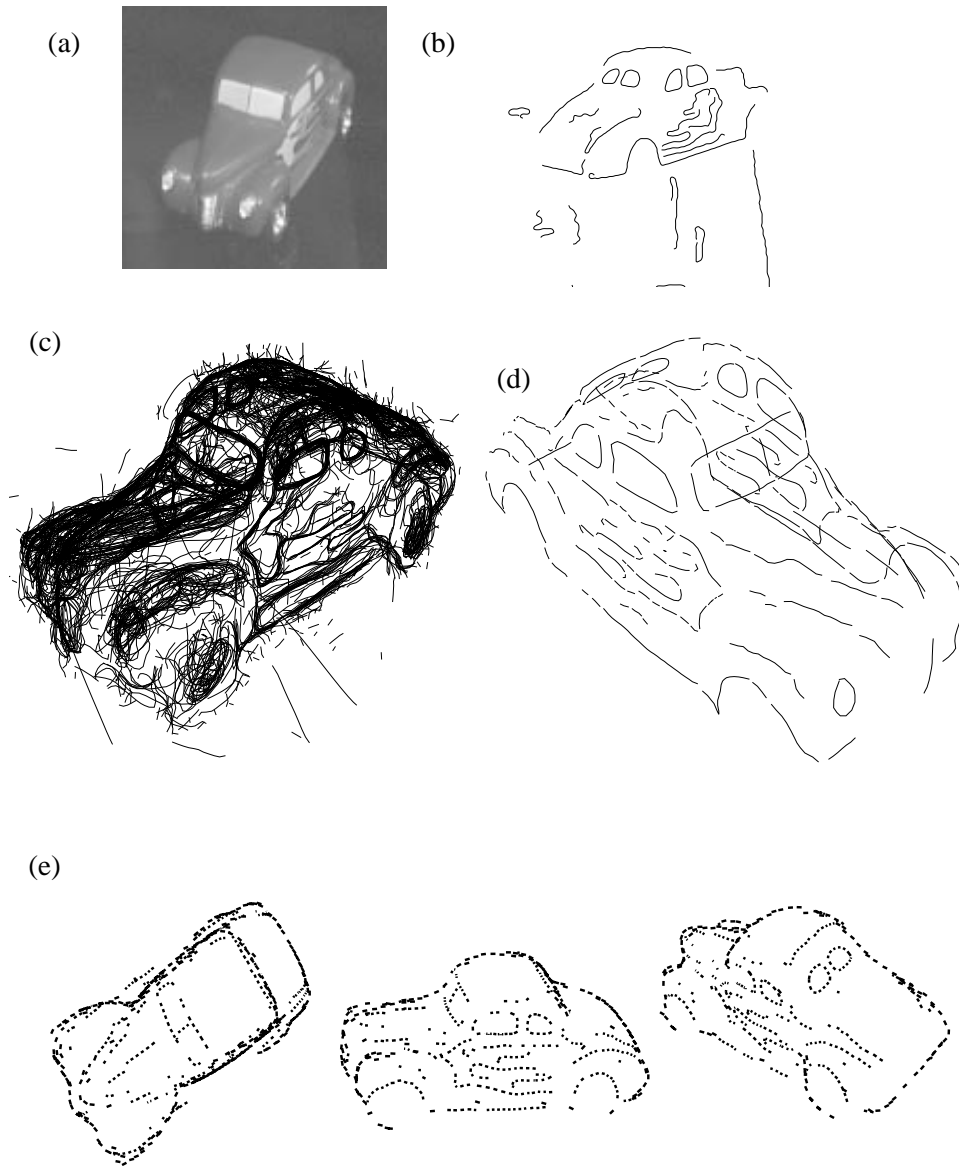


Figure 4.17: Results from modeling the 3D edgel generators of the car. (a) An intensity image of the car, (b) an example from the set of observed intensity edge images, (c) the complete set of mapped 3D edgels used as input to the consensus-surface algorithm, (d) the rigid surface edgels extracted by the consensus-surface algorithm, (e) three views of the resulting 3D edgel model (including occluding contour edgels and rigid surface edgels).

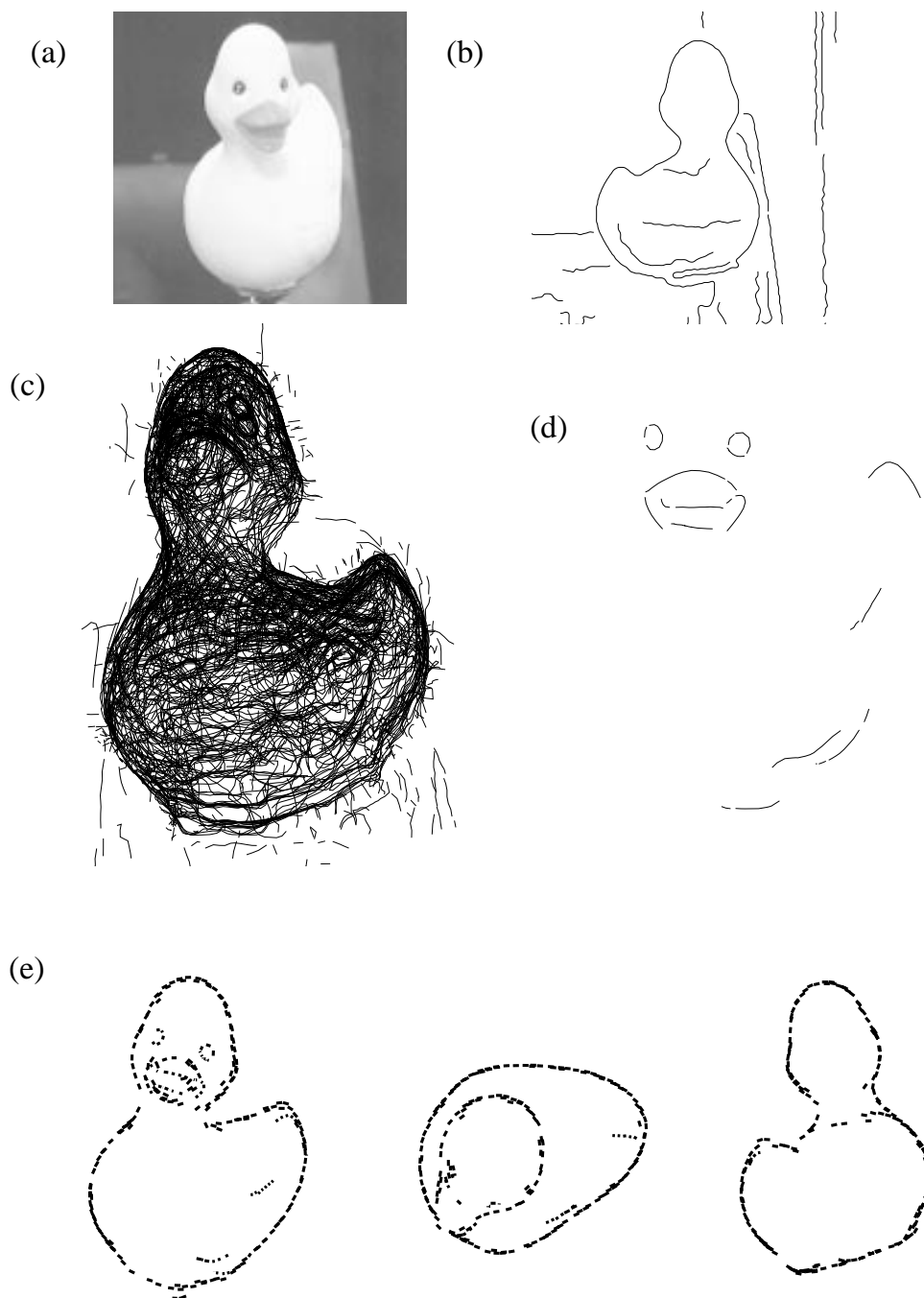


Figure 4.18: Results from modeling the 3D edgel generators of the duck. (a) An intensity image of the duck, (b) an example from the set of observed intensity edge images, (c) the complete set of mapped 3D edgels used as input to the consensus-surface algorithm, (d) the rigid surface edgels extracted by the consensus-surface algorithm, (e) three views of the resulting 3D edgel model (including occluding contour edgels and rigid surface edgels).

inferred from a set of discrete observations. As before we turn to 3D geometry for a solution. We can utilize the 3D surface geometry to infer visibility conditions for any point on the object, which includes all of our edgels. Global visibility (i.e., self occlusion) can be handled again as in Section 3.2 using the visibility lookup table approach to predict self occlusion. The details of the visibility computations for our edgel model will be described in the next chapter on 3D-2D localization.

Our results demonstrate that our consensus-edgel algorithm is able to extract the significant edgel generators from a large number of observations, much of which is noise and occluding boundaries. The results also demonstrates that the model acquisition can be achieve despite inaccuracies of observed edge location due to alignment/calibration errors and the typical noise and randomness of intensity edge locations which is magnified after reprojection.

The next chapter details our 3D-2D localization algorithm and will clarify how the 3D edgel model is utilized for localization.

Chapter 5

3D-2D Object Localization

The goal of this chapter and one of the principal objectives of this thesis is to localize 3D objects in 2D intensity images, which we refer to as 3D-2D localization. The discussion of 3D-2D localization began in Chapter 4 by motivating our choice of model and image representations to solve this localization task.

The object model is represented as a collection of 3D edgel generators—points on the object surface which often create edges when visible in intensity images. Using the edgel generators we can predict the appearance of object edgels in an image and then match them with intensity edgels in the input image. Using intensity edgels as the feature for matching provides some degree of invariance to changes in lighting and viewpoint. Edgels (points with tangent directions) are very simple and, thus, very general for representing shapes. The 3D edgel representation of the object was chosen for its succinctness and generality (with respect to camera models). Edgel generators provide an efficient method for predicting an object's appearance in images for purposes of matching. Chapter 4 detailed our method for automatically acquiring an object's 3D edgel generators from real images.

In this chapter, we focus on how to use a 3D edgel model to precisely find the location of the object in an intensity image given a rough initial estimate of its pose. 3D-2D localization shares much in common with the problem of 3D-3D localization which was described in Chapter 3. The requirements for 3D-2D localization are indeed the same as for 3D-3D localization. Applications of localization require it to be an efficient and robust operation. As will be shown, the similarities are much deeper. In the next section, we will overview the problems and our approach for 3D-2D localization.

5.1 Problems and Approach

Chapter 3 dealt with problems and issues of localizing 3D surfaces in range images, matching 3D surface points to 3D image points. Many of the problems we face with 3D-2D localization are similar to those encountered in the 3D-3D localization problem. We will make use of the methods and techniques of Chapter 3 when applicable.

As in Chapter 3, we regard as axiomatic that localization is an optimization problem (i.e., we can evaluate any pose estimate, and the true pose has the optimal value). The primary problem is how to evaluate a pose candidate. For 3D-2D localization, using intensity edgels as the primitive feature for matching the model to the image allows us to evaluate the pose by measuring the distance between (edgel) points on the model and (edgel) points in the image.

Since our model primitives (edgels) are essentially 3D points on the object's surface, we are able to take advantage of much of the work on 3D-3D localization of Chapter 3. The basic approach to localization remains the same. We must predict the visibility of features, establish correspondences between model and image features, and use the correspondences to refine the pose estimate. More importantly, the similarities make many of the techniques for 3D-3D localization directly applicable for the 3D-2D problem.

The first problem is to determine which edgels of the object are visible from a particular viewpoint. As described in Chapter 4, we have three distinct types of edgels: rigid edgels, occluding-contour edgels, and convex edgels. There is no general way to infer the visibility of edgel points simply from their appearance in sample image views¹; geometric shape information is necessary, which, fortunately, is available. As in Chapter 4, before building the edgel model we first build a 3D surface model of the object using the techniques of Chapter 2. Here, we utilize the surface model for determining visibility requirements for our various edgel points. The representation and computation of self-occlusion conditions are identical to that used in the 3D-3D localization case.

Once we have predicted the visible edgels of the model given the pose, we must compute correspondences between the visible model edgels and image edgels in order to refine the pose estimate. Like in the 3D case (Chapter 3), we also rely on efficient nearest-neighbor to compute correspondences. However, this time we must search in 2D image space.

Correspondences based on nearest-neighbor search in 2D are more likely to be incorrect than in the 3D-3D case—especially with large initial pose errors. This is because the density of edgels in the image is higher than in the 3D-3D case in which the data (visible surfaces of the 3D scene) is a 2D manifold in 3D space—a sparsely populated space. For localization to work, improvements over simple nearest-neighbor correspondence is necessary. We show how to improve correspondences while maintaining efficiency by using additional edgel attributes in the nearest-neighbor search.

Pose estimation in the 3D-2D case is—on the surface—much more complicated than the 3D-3D case. In the 3D-2D case, we are matching 2D points to the 2D projection of 3D points. In general, assuming a perspective camera model, the 2D projection introduces a non-linearity to the pose estimation problem that we must deal with. We show that the optimal way of refining a pose estimate in the 3D-2D case is to formulate it as a 3D-3D problem. Our formulation allows us to use much of the 3D-3D localization machinery for the 3D-2D problem.

¹At best, we can say that an edgel was visible in the set of views from which it was observed, however this set will usually be too sparse to specify its full geometric range of visibility. Photometric visibility is another issue entirely and is discussed in Chapter 7.

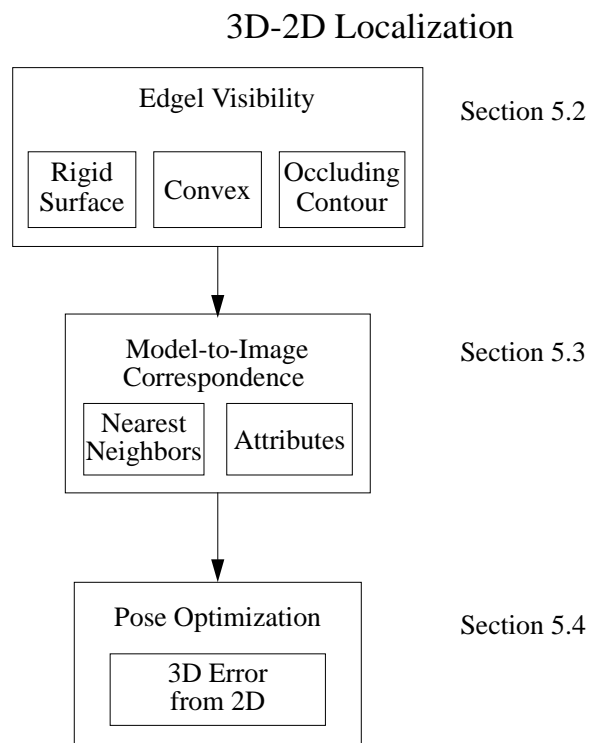


Figure 5.1: Organization of this chapter.

While the basic formulation of localization is for localizing an object in a *single* image, there is no fundamental limit to the number of images we may use. We show how 3D-2D localization can straightforwardly be extended to use multiple images simultaneously which avoids a significant problem of stereo vision—that the scene points in one view may not correspond to scene points in another view.

Figure 5.1 shows a diagram of the main technical sections of the thesis. We begin by discussing efficient approximations for the various edgel types. As in Chapter 3, we discuss a method for nearest neighbor correspondences and an extension to include additional attributes which are crucial for 3D-2D localization: edgel normals and reflectance ratio. We then show how a 3D error formulation in the 3D-2D problem makes our pose optimization problem equivalent to the 3D-3D problem of Chapter 3.

5.2 Edgel Visibility

In this section, we describe our method for efficiently predicting the visibility of edgels given the pose of the object.²

Our first task when localizing a 3D object in a 2D image is to determine which parts (edgels) of the object are visible from the current viewpoint. As stated in Section 3.2, achieving an exact solution for point visibility on a 3D surface requires expensive techniques such as ray-tracing or z-buffering [40, 141]. Again, such techniques are too expensive to consider for localization tasks. We desire an efficient approximation of visibility which is preferably a local computation. Such a solution for surface point visibility was presented in Section 3.2.

As described Chapter 4, we will make use of our 3D surface model to determine the visibility conditions. Since many of the problems of computing 3D surface visibility also are relevant to 3D edgel visibility—an edgel is really a point on the object surface—we will make use of many of the methods and representations developed in Section 3.2.

The chapter on 3D edgel modeling differentiates three classes of edgels:

- **Rigid surface edgels:** the result of reflectance/color discontinuities (e.g., surface marks) on the surface of the object. The surface is locally smooth in this case.
- **Occluding-contours edgels:** the result of boundaries observed at points on a smooth surface where there is a transition from visible surface points to occluded surface points from a particular viewing direction (e.g., the side of a cylinder). An intensity edge is created only if the detected intensity of the background is sufficiently different from the intensity of the surface at that point.
- **Convex edgels:** the result of a discontinuity of surface normals (e.g., the edge or corner of a cube). This is a hybrid of the rigid surface and occluding-contour edgels—high curvature (corner) points which generate occluding-contours from some viewing directions but are rigidly attached to the surface and generate edgels from other viewing directions that are not occluding boundaries.

Figure 5.2 shows examples of the above three classes of edgel generators. Clearly, the visibility conditions will differ for these three types of edgels.

All three of these types of edgels may be subject to self-occlusion or not. If so the point's visibility information is simply annotated with a visibility LUT as described in Section 3.2.2. In general, this visibility LUT is only consulted when an edgel point is otherwise determined to be visible. In the following, we will only describe the visibility computations specific to each edgel type. The self-occlusion LUT test is assumed to be understood. We now describe the visibility constraints and computations for each of these edgel types.

²The method for predicting visibility in this chapter is purely geometric. For completely accurate prediction of edgel visibility, we would need photometric constraints as well; however, photometric prediction would require precise knowledge of the environment in addition to the object model.

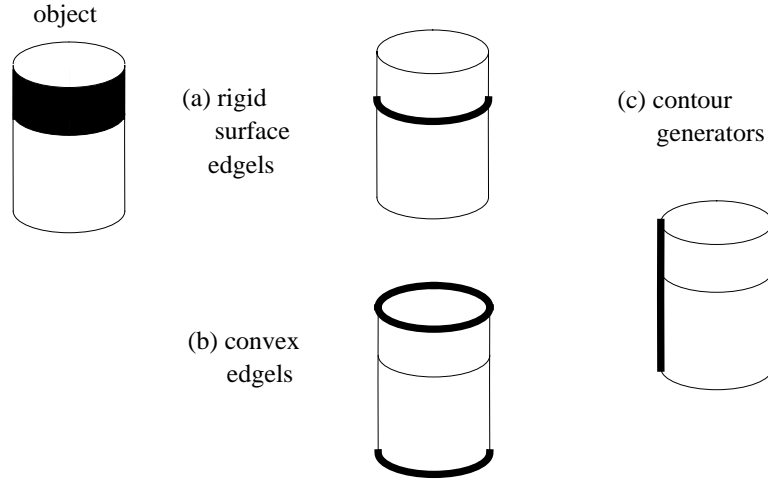


Figure 5.2: Examples of three types of edgel generators: (a) rigid surface marking, (b) convex edges, (c) occluding contours.

5.2.1 Rigid Surface Edgel Visibility

The first and simplest case is that of rigid surface edgels. The necessary condition for the surface edgel to be visible is that the surface point be visible. Fortunately, we have the 3D surface model at our disposal (thanks to the work described in Chapter 2). Given the edgel point, we can determine the triangular surface patch of the model on which it lies. We can then equate the visibility of the edgel to the visibility of the surface patch. From Section 3.2, we have the visibility definition of Equation 3.1:

$$\text{visible}_{\text{surface}}(\mathbf{x}) = \begin{cases} \text{true} & \hat{\mathbf{n}}_i \cdot \hat{\mathbf{v}} > \cos \theta \\ \text{false} & \text{otherwise} \end{cases} \quad (5.1)$$

where $\hat{\mathbf{n}}_i$ is the normal direction of the triangle τ_i , which is the surface triangle on which the edgel point \mathbf{x} lies. $\hat{\mathbf{v}}$ is the viewing direction to the point \mathbf{x} of the edgel. θ (similar to Equation 3.1) is an angle near 90 degrees which is the maximum orientation angle of the surface such that a rigid edgel on the surface will be detected. As in Chapter 3, θ is chosen empirically.

Thus, for rigid surface edgels, we need to precompute the normal $\hat{\mathbf{n}}_i$ by finding the surface triangle τ_i on which the edgel point \mathbf{x} lies.³ For each rigid surface edgel, we need to store $\hat{\mathbf{n}}_i$ in the localization model along with the point and tangent $\langle \mathbf{x}, \hat{\mathbf{t}} \rangle$.

³Again, k-d trees [42] come in useful to make the search for τ_i efficient.

5.2.2 Convex Edge Visibility

The next edgel type—in order of complexity of the visibility constraints—is the convex or corner edgel. This is a point at the non-smooth junction between two smooth surfaces of the object. While this type of edgel is, in some sense, an occluding-contour edgel, the visibility constraints are slightly different than the occluding-contour case. Fortunately, the visibility constraints are simpler since corner edges are common in man-made objects.

The necessary condition for the visibility of a convex edgel is that one or both of the adjacent surfaces (to the left and right of the edgel) are visible. If only one of the adjacent surfaces is visible, the edgel would generate an occluding boundary edge between the background and the visible surface. If both surfaces are visible, the edgel is more like a rigid surface edgel since the two surfaces, which have different orientations with respect to the light sources and camera, will usually reflect different intensities—creating an intensity edgel.

For a convex edgel, we can examine the triangular patches on either side of the edgel and use the normals of these two surfaces for the visibility computation. First, we determine the closest surface triangle τ_c to the edgel point \mathbf{x} . This gives us a surface normal $\hat{\mathbf{n}}_c$ for the edgel. We also have a tangent direction $\hat{\mathbf{t}}$ for the edgel. We can determine the surface normals immediately to the left and right of the edgel by locally searching along the surface in the $\hat{\mathbf{n}}_c \times \hat{\mathbf{t}}$ and $-\hat{\mathbf{n}}_c \times \hat{\mathbf{t}}$ directions respectively.

This gives us two triangle patches τ_L and τ_R with surface normals $\hat{\mathbf{n}}_L$ and $\hat{\mathbf{n}}_R$. The visibility computation is then

$$\text{visible}_{\text{convex}}(\mathbf{x}) = \begin{cases} \text{true} & (\hat{\mathbf{n}}_L \cdot \hat{\mathbf{v}} > \cos \theta) \vee (\hat{\mathbf{n}}_R \cdot \hat{\mathbf{v}} > \cos \theta) \\ \text{false} & \text{otherwise} \end{cases} \quad (5.2)$$

where $\hat{\mathbf{v}}$ is the viewing direction for edgel point \mathbf{x} , $\hat{\mathbf{n}}_L$ and $\hat{\mathbf{n}}_R$ are the normals of the surfaces adjacent to the left and right of the edgel point \mathbf{x} , and θ is defined in Equation 5.1.

Thus, in addition to the edgel's point and tangent $\langle \mathbf{x}, \hat{\mathbf{t}} \rangle$, we also need to compute the adjacent surface normals $\hat{\mathbf{n}}_L$ and $\hat{\mathbf{n}}_R$ and store them with the localization model.

5.2.3 Occluding Contour Visibility

Finally, we must determine the visibility for occluding contour edgel points. Section 4.5 discussed the computation of surface curvature at each point on the surface model and how to classify these points as either occluding contour generators, convex edges or non-contour points. Having classified a surface point \mathbf{x} as an occluding-contour point with normal $\hat{\mathbf{n}}$, principal curvatures κ_1 and κ_2 , and principal directions $\hat{\mathbf{e}}_1$ and $\hat{\mathbf{e}}_2$, we need an efficient way to compute its visibility given viewing direction $\hat{\mathbf{v}}$.

In Chapter 4, we identified two classes of occluding-contour points based on their principal curvatures:

1. $(\kappa_1 < 0) \wedge (\kappa_2 < 0)$: an elliptic point, which generates contours for all tangent viewing directions

2. $(\kappa_1 \geq 0) \wedge (\kappa_2 < 0)$: either a cylindrical point (i.e., $\kappa_1 = 0$) or a saddle point, which generates contours from a subset of the tangent viewing directions—those with negative normal curvature

Let us first assume that we are able to sample the surface at infinite resolution (i.e., we have a continuous surface of points). The visibility predicate for elliptic points could then be defined simply as:

$$\text{visible}_{\text{elliptic}}(\mathbf{x}) = \begin{cases} \text{true} & \hat{\mathbf{n}} \cdot \hat{\mathbf{v}} = 0 \\ \text{false} & \text{otherwise} \end{cases} \quad (5.3)$$

where $\hat{\mathbf{n}}$ is the normal of the elliptic surface point \mathbf{x} , and $\hat{\mathbf{v}}$ is the viewing direction for point \mathbf{x} .

For saddle/cylindrical points, we require one more piece of info to make the decision. We need to know the normal curvature of the point in the direction $\hat{\mathbf{v}}$. Fortunately, Euler's formula gives us

$$\kappa(\hat{\mathbf{v}}) = \kappa_1(\hat{\mathbf{e}}_1 \cdot \hat{\mathbf{v}})^2 + \kappa_2(\hat{\mathbf{e}}_2 \cdot \hat{\mathbf{v}})^2 \quad (5.4)$$

and the visibility predicate takes the general form

$$\text{visible}_{\text{occluding}}(\mathbf{x}) = \begin{cases} \text{true} & (\hat{\mathbf{n}} \cdot \hat{\mathbf{v}} = 0) \wedge (\kappa(\hat{\mathbf{v}}) < 0) \\ \text{false} & \text{otherwise} \end{cases} \quad (5.5)$$

where $\kappa(\hat{\mathbf{v}})$ is the normal curvature for arbitrary surface point \mathbf{x} , and $\hat{\mathbf{n}}$ is the normal of the surface point \mathbf{x} . This is valid for both classes of occluding contour generators. For elliptic points, $\kappa(\hat{\mathbf{v}}) < 0$, by definition.

Unfortunately, the above test will not be very useful for us as we must use finite samplings of points from the model surface. The piecewise-planar approximation complicates our task quite a bit. In Section 4.5, we rationalized the approximation of contour edgels by point samples using the example of a piecewise-linear circle and its projected contours (see Figure 4.9). We return to that illustration to help us here. If we were to use the ideal visibility predicate as in Equation 5.5 for our sampled points, the contour would only be apparent when the point is precisely normal to the viewing direction (in practice, almost never). In order to make the contour continuously visible with respect to the viewing direction, we must relax the constraint that the viewing direction $\hat{\mathbf{v}}$ must be exactly perpendicular to the surface normal $\hat{\mathbf{n}}$ of \mathbf{x} . We then have a predicate of the form

$$\text{visible}_{\text{occluding}}(\mathbf{x}) = \begin{cases} \text{true} & (|\hat{\mathbf{n}} \cdot \hat{\mathbf{v}}| < \epsilon) \wedge (\kappa(\hat{\mathbf{v}}) < 0) \\ \text{false} & \text{otherwise} \end{cases} \quad (5.6)$$

where ϵ is some threshold near zero. Care must be taken when choosing ϵ so that we do not predict that two adjacent points of the same normal section are visible simultaneously. This can be accomplished by selecting ϵ based on the local geometry of the surface. Figure 5.3 shows an example normal section of a piecewise-planar surface. The viewing directions that should generate an occluding contour edgel at point \mathbf{x} span an arc of angle θ .

We can expand the point's effective normal (for purposes of the predicate $\text{visible}_{\text{occluding}}$) to include half of the angle spanned by the normals of the two adjacent points. This

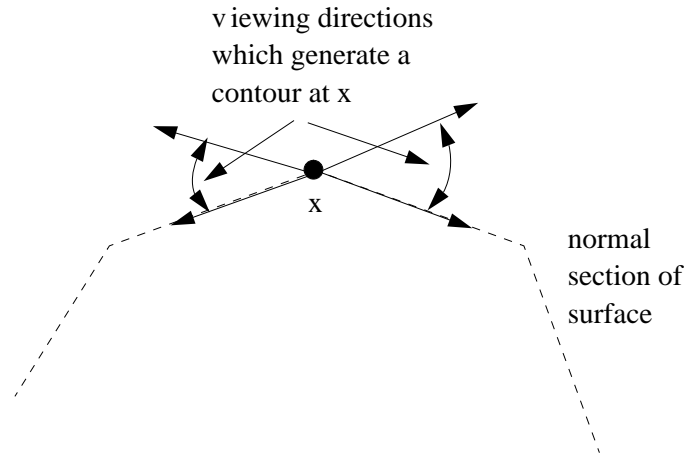


Figure 5.3: A normal section of a surface. The point x will be an occluding contour edgel for all viewing directions spanned by the indicated arcs.

effectively makes point x of the normal section visible when the viewing direction is in between the normals of x and the adjacent surface point on the normal section. If \hat{n}_a is the normal of the adjacent point on the normal section and \hat{n} is the normal for point x , then the angle between the two normals is

$$\alpha = \cos^{-1} \hat{n} \cdot \hat{n}_a$$

which gives the threshold

$$\epsilon = \cos \frac{\alpha}{2}.$$

Note that this assumes that the normal section is symmetric about the point x and that the threshold is for a specific normal section.

For elliptic points, we can compute the threshold ϵ along the normal sections for both of the principal directions—giving us ϵ_1 and ϵ_2 . At execution time, the threshold ϵ is computed using the same formula as the curvature $\kappa(\hat{v})$ is defined in Euler's formula (Equation 5.4)

$$\epsilon(\hat{v}) = \epsilon_1(\hat{e}_1 \cdot \hat{v})^2 + \epsilon_2(\hat{e}_2 \cdot \hat{v})^2. \quad (5.7)$$

This establishes a smooth transition between the two thresholds as the viewing direction varies between \hat{e}_1 and \hat{e}_2 . Thus, the threshold $\epsilon(\hat{v})$ is a smooth approximation of the surface sampling along the given viewing direction.

For cylindrical/saddle points, we can use the same equation to our advantage. In this case, if $\kappa(\hat{v}) \geq 0$, the contour point should not be visible. To enforce this using the visibility predicate of Equation 5.6, we need $\epsilon(\hat{v}) \leq 0$ whenever $\kappa(\hat{v}) \geq 0$. We can achieve this by first computing ϵ_2 (for the normal section along \hat{e}_2 , remembering $\kappa_2 < 0$) and then set

$\epsilon_1 = \epsilon_2 \frac{\kappa_1}{\kappa_2}$. This makes $\epsilon(\hat{\mathbf{v}}) = \frac{\epsilon_2}{\kappa_2} \kappa(\hat{\mathbf{v}})$ a scaled version of normal curvature which provides a smooth transition from the desired threshold for $\hat{\mathbf{v}} = \hat{\mathbf{e}}_2$ to a threshold of zero for the direction such that $\kappa(\hat{\mathbf{v}}) = 0$.

This allows us to test visibility for both elliptical and saddle/cylindrical points using a surprisingly simple rule

$$\text{visible}_{occluding}(\mathbf{x}) = \begin{cases} \text{true} & |\hat{\mathbf{n}} \cdot \hat{\mathbf{v}}| < \epsilon(\hat{\mathbf{v}}) \\ \text{false} & \text{otherwise} \end{cases} \quad (5.8)$$

which gives us the desired effect that when $\kappa(\hat{\mathbf{v}}) \geq 0$, then the point does not generate an occluding contour since $\epsilon(\hat{\mathbf{v}}) \leq 0$.

Our biggest assumption is that the points are uniformly and symmetrically sampled. Of course, this assumption cannot be met in practice. For example, consider the problem of uniformly sampling a sphere. The result for a surface that is sampled nearly uniformly is that occasionally multiple points of the same normal section will be visible simultaneously. However, this does not prove to be much of a problem for localization.

5.2.4 Edgel Visibility: Summary

We have described our solution for efficiently computing the visibility of edgels in our model for 3D-2D localization. Each computation requires at most a few dot products and a comparison. The visibility computation is also local—that is, independent of other edgel points and the surface points of the model. Thus, we may compute the visibility of one or all edgels. Global visibility (i.e., self occlusion) is assumed to be handled again as in Section 3.2 using the visibility lookup table approach to predict self occlusion. For this aspect, edgel visibility is equivalent to surface point visibility.

Off-line we must compute the normals and thresholds required to compute the visibility of each type of edgel. This information is stored with the localization model. The information required for each type of edgel is:

- Rigid surface edgels: the surface normal $\hat{\mathbf{n}}$ of edgel $\langle \mathbf{x}, \hat{\mathbf{t}} \rangle$
- Convex edgels: the adjacent surface normals $\hat{\mathbf{n}}_L$ and $\hat{\mathbf{n}}_R$ of edgel $\langle \mathbf{x}, \hat{\mathbf{t}} \rangle$
- Occluding-contour edgels: the surface normal $\hat{\mathbf{n}}$, the principal directions $\hat{\mathbf{e}}_1$ and $\hat{\mathbf{e}}_2$, and thresholds ϵ_1 and ϵ_2 for edgel $\langle \mathbf{x}, \hat{\mathbf{t}} \rangle$

While executing the visibility prediction for a given edgel point \mathbf{x} we must transform the viewing direction corresponding to the model edgel point \mathbf{x} into the model coordinate system. Then we may execute the following predicates for each edgel depending on its type:

- Rigid surface edgels: $\text{visible}_{surface}(\mathbf{x})$ of Equation 5.1
- Convex edgels: $\text{visible}_{convex}(\mathbf{x})$ of Equation 5.2

- Occluding-contour edgels: $\text{visible}_{occluding}(\mathbf{x})$ of Equation 5.8

These are all efficiently evaluated. For the occluding-contour edgels, we can save some time by quickly ruling out points where $\hat{\mathbf{n}} \cdot \hat{\mathbf{v}} \gg 0$.

Another option for predicting visible contour points might be to use an LUT much like the one used to detect self occlusion (Section 3.2). However, this is not a feasible option as the size of an LUT that achieves the same degree of accuracy would be excessively large. Any LUT approach would also suffer from occasionally predicting multiple contour edgels from the same normal section to be simultaneously visible.

Yet another option would be to model the smooth surface patches with algebraic equations [77, 46, 132]. Such a representation would be more precise than the piecewise-planar representation offered here; however, many more complicated issues are involved with algebraic surface representations. For example, surface patch segmentation, efficiency of contour prediction, and sampling the contour for localization. Making this efficient enough for localization applications would prove difficult.

5.3 Edgel Correspondence

We are given an initial pose estimate and a set of visible edgels of our model. In order to evaluate and, thus, refine the pose, we must be able to compute correspondences between the model edgels and edgels in the image. The image edgels are acquired using the method described in Section 4.2 (without the calibrated positioner). The intensity image is taken, the Canny edge operator and edgel linker is applied to the image, and the resulting edgel chains are smoothed to remove the aliasing and noise effects. The result is a set of smooth 2D edgel chains in image coordinates.

Since we know the rough pose of the object, we can use a local search to find the nearest-neighbor correspondences efficiently. As in Chapter 3, we do not need the absolute, correct correspondences in order to refine the pose. However, it is important that many of the model edgels are connected or related to the corresponding image edgels (i.e., the errors must be meaningful). If this is the case, the combined constraints of the related correspondences will act to pull the model toward the correct pose. Unrelated and random correspondences will not usually have any consistent trends to counteract the trend of the correct correspondences—assuming enough correct correspondences exist.

As a first attempt to find the correspondences, we will find the nearest neighbors in 2D image space. We first project the visible 3D model edgels into 2D image coordinates.⁴ The perspective projection of a 3D point \mathbf{x}_m in model coordinates is performed by the following sequence of transforms (repeated from Chapter 4):

$$\mathbf{x}_c = \mathbf{R}_{c \leftarrow m} \mathbf{x}_m \quad (5.9)$$

$$\mathbf{u} = \mathbf{R}_{u \leftarrow c} \mathbf{x}_c \quad (5.10)$$

⁴Without loss of generality, the projection equations will be presented as perspective projections. Other projections such as orthographic, parallel and central projection will work as well.

$$\mathbf{U} = \begin{bmatrix} \frac{u}{w} \\ \frac{v}{w} \end{bmatrix} \quad (5.11)$$

where \mathbf{x}_m and \mathbf{x}_c are the positions in model and camera coordinates respectively, $\mathbf{u} = [u \ v \ w]^T$ are the image projection coordinates, and $\mathbf{U} = [U \ V]^T$ are the 2D image pixel coordinates. $\mathbf{R}_{c \leftarrow m}$ is a rigid transformation that transforms model coordinates \mathbf{x}_m to (Euclidean) camera-centered coordinates \mathbf{x}_c . The camera-centered coordinate frame is defined such that $[0 \ 0 \ 0]^T$ is the center of projection and $[0 \ 0 \ 1]^T$ is the camera's focal axis. $\mathbf{R}_{u \leftarrow c}$ transforms the Euclidean camera coordinates \mathbf{x}_c to (possibly non-Euclidean) 3D projection coordinates \mathbf{u} . $\mathbf{R}_{u \leftarrow c}$ accounts for any scaling factors (such as aspect ratio) and translation of the image center to non-zero image coordinates. The image projection coordinates are specified so that the final transformation is a purely perspective projection.

Using the 2D coordinates of each edgel, we can then search for the nearest edgel in the 2D image using the dissimilarity measure

$$\Delta(\mathbf{x}, \mathbf{y}) = \|\mathbf{x} - \mathbf{y}\| \quad (5.12)$$

where \mathbf{x} and \mathbf{y} are the image coordinates of two points being compared. The nearest-neighbor search is again efficiently implemented using the k-d tree [42] data structure as used in Section 3.3.

Unfortunately, the straightforward approach to correspondences in 2D edgel images rarely provides sufficiently accurate correspondences for localization. The reason is that the density of 2D edgels in a 2D intensity image is likely to be so high that the nearest image edgel chain will often be unrelated to the actual edgel of the model. In the case of 3D-3D localization, the points of a range image occupy a 2D manifold in 3D space. Thus, in that domain, nearest-neighbor correspondences are likely to be related to the same object surface despite errors in the pose estimate.

For robust 3D-2D localization, we must do better. One way to improve nearest-neighbor correspondences is to enforce additional constraints on the search. In Section 3.3, we showed that we could integrate additional constraints into the nearest-neighbor search by adding attributes to each image-point entry in the k-d tree. We will consider both geometric and photometric attributes for this purpose.

5.3.1 Attributes for Correspondence: Geometric

For edgel correspondences, the most obvious geometric attribute to use is the normal (or equivalently the tangent) of the edgel in the image. The 2D normal direction can easily be computed from the model edgel $\langle \mathbf{x}, \hat{\mathbf{t}} \rangle$ by projecting the tangent direction $\hat{\mathbf{t}}$ to image coordinates. The normals of the image edgels are computed from the tangent direction along the edgel chains. The edgel chain smoothing described in the paper by Wheeler and Ikeuchi [147] and used in Section 4.2 proves useful for accurate estimation of the edgel normals.

There are a couple of problems with using the edgel normal as an attribute. First, 2D edgels do not have a unique coordinate system. It is an arbitrary decision as to which

direction the normal (or tangent) is chosen (i.e., \hat{n} or $-\hat{n}$ are equally correct normals). Edgel chains have no distinguishable inside or outside as do 3D surfaces as in Section 4.3. Thus, we must represent every image edgel twice—once for \hat{n} and once for $-\hat{n}$ —in the k-d tree to ensure that we find the closest edgel with respect to both proximity and normal similarity.

Another problem with normals is how to parameterize orientations for efficient k-d tree search. One might first choose to parameterize the 2D normal by its orientation angle. Unfortunately, there are additional ambiguities when using angles to represent an attribute for nearest-neighbor search in k-d trees. There are any number of ways to specify the same angle (e.g., 180 degrees is the same as -180 degrees). The orientation angle folds back on itself as it completes a circle. If we want to compare two angles using an Euclidean metric, we require that

$$\Delta(\alpha, \beta) = | \alpha - \beta |$$

behaves linearly for the nearest-neighbor search using a k-d tree. For example, if we compare a model value of 180 degrees with an image value of -170 degrees, we require a distance of 10 degrees rather than 350 degrees. The only way to make this happen is if we store an edgel multiple times for each equivalent value of the angle. In this example we would need to store the image edgel using -170 degrees and 190 degrees. This effectively doubles the number of entries in the k-d tree again. Add to that the expense of computing the orientation angle using relatively expensive trigonometric functions for each model edgel, then other alternatives are worth consideration.

We can follow the approach in Section 3.3 which represented the surface normal attribute simply as 3D unit normal vectors. In the 2D case, the dissimilarity metric is the same as Equation 3.8

$$\Delta(\hat{n}_1, \hat{n}_2) = \|\hat{n}_1 - \hat{n}_2\| \quad (5.13)$$

except that \hat{n}_1 and \hat{n}_2 are 2D vectors rather than 3D vectors. This equation has the same properties as Equation 3.8 since any 3D rotation is equivalent to a 2D rotation in a specific plane. Thus, from the analysis in Section 3.3.2, we may assume that Equation 5.13 is roughly linear over its range which is [0..90] degrees in this case.⁵ Thus, we represent each image edgel by two entries in the k-d tree

$$\langle U, V, w n_U, w n_V \rangle \quad \text{and} \quad \langle U, V, -w n_U, -w n_V \rangle$$

where the 2D edgel normal is $\mathbf{n} = [n_U \ n_V]^T$ and w is the weighting factor for normals as described in Section 3.3.2. For more details, the reader is referred back to Section 3.3 where this issue is discussed at greater length.

There are other possible geometric attributes that can be used to describe/disambiguate an edgel. One potentially useful geometric attribute is the curvature of the edge chain at each edgel. Unfortunately, the computed curvatures of points in an intensity edge chain are noisy even after applying the smoothing operators to the edgel chain. In addition,

⁵Since each edge is represented at two opposite orientations, the largest angular distance will be 90 degrees; if the orientation of an edgel was unique the range would increase to 180 degrees.

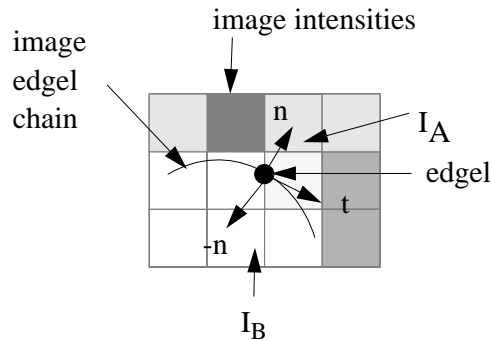


Figure 5.4: Using the tangent direction of an edgel to locate pixels to sample the left and right intensities, I_L and I_R , for computing the reflectance ratio.

computing the curvature of projected model edgels can suffer from inaccuracy making the dissimilarity metric very volatile. Thus, curvature is not utilized in the experiments described in this thesis.

5.3.2 Attributes for Edgel Correspondence: Photometric

In addition to geometric attributes, it is also possible to use photometric attributes of the edgel. The most obvious photometric attributes of an edge are the intensities on either side of the edgel. As discussed in Section 4.1, the detected intensities of points/regions on the object are quite variable and depend on many external factors. While the intensities themselves may be difficult to predict, there is a useful measure involving these intensities called the reflectance ratio which Nayar and Bolle [100] showed to be invariant to light source conditions and orientation (except for cases of shadowing and specular reflection). They showed that the ratio of intensities of two adjacent surface patches is invariant if the surface normals of the two patches are nearly the same. The reflectance ratio α is defined to be

$$\alpha = \frac{I_L - I_R}{I_L + I_R}$$

where I_L and I_R are the respective intensities of the left and right side of an edgel or surface patch boundary. Figure 5.4 shows an example of how we can locate the two intensities for computing the reflectance ratio, α , for a given edgel. The use of reflectance ratios assumes that the surface patches are connected, that the surface is locally smooth, and that the patches have similar reflectance properties. This is approximately true for any adjacent patches on a smooth surface if we sample points on the patch that are relatively close. In our application, we have a class of edgels, rigid surface edgels, which fits these assumptions. We can compute α for each edgel point when building our model, and

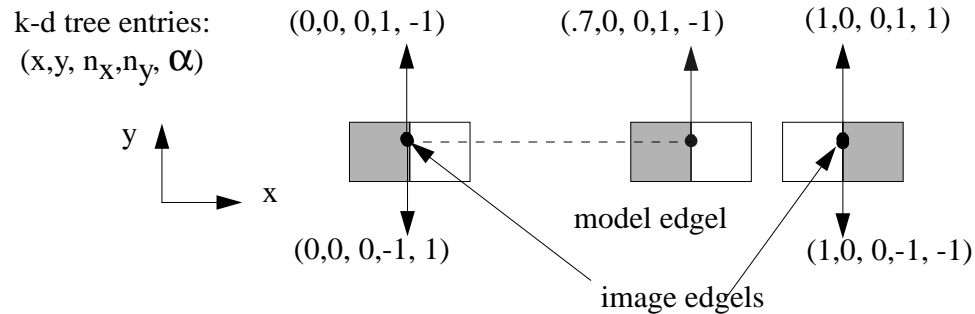


Figure 5.5: Example of correspondence search using reflectance ratios. The model edgel, though closer to the rightmost edgel will prefer the leftmost edgel since they share the same reflectance ratio with respect to the same normal direction. Note the two k-d tree entries for each of the image edgels.

average the observations when computing the consensus edgel for each rigid surface edgel as described in Section 4.4.

We now have five dimensions—image position, normal and reflectance ratio—for the k-d tree entries when looking for correspondences to a rigid surface edgel. We still need to store each entry twice to account for the fact that we do not know which direction the model edgel may be oriented. We simply add another entry to the k-d tree with the normal and α negated—giving us two entries for each image edgel:

$$\langle U, V, w n_U, w n_V, w_\alpha \alpha \rangle \quad \text{and} \quad \langle U, V, -w n_U, -w n_V, -w_\alpha \alpha \rangle$$

where w_α is the respective weighting factor for comparing reflectance ratios with image coordinates. Not only does the reflectance ratio give us one more attribute to improve correspondence accuracy, but it also solves a previous problem, namely orientation ambiguity. The choice of left or right when computing the reflectance ratio forces us to choose one tangent direction (and normal direction) or the other. For example, Figure 5.5 shows a model edgel projected into a 2D image containing two edgels with similar orientations. The k-d tree entries are labeled next to each edgel. From Figure 5.5, we can see that the reflectance ratio rules out the correspondence to the nearest edgel in 2D image coordinates, since the reflectance ratio for that point has the wrong sign. In this way the correspondence search can skip over nearby edgels that have similar normals but different reflectance ratios, which will be a common occurrence.

As mentioned above, the reflectance ratio is only suitable for rigid surface edgels. This requires us to build a second k-d tree, just for the rigid-surface-edgel class. When we are searching for the correspondence to a rigid surface edgel, we use the k-d tree which includes the reflectance ratio attribute, otherwise we use the k-d tree that includes only image coordinates and edgel normals.

Continuing along the line of photometric attribute, it may be possible to define other attributes based on color. A desirable attribute would be an invariant or pseudo-invariant that is applicable to occluding contours and convex edgels. One possibility involving color is hue. Hue is essentially the dominant wavelength of the light [40, 2]. Hue is potentially useful as it is invariant to intensity changes in the light source (assuming the intensity is from diffuse reflection or has zero saturation specular reflection) and orientation changes of the object with respect to the camera. Thus, we could acquire the hue on the object side of an occluding contour or convex edgel and have a useful attribute for these edgel classes. Unfortunately, there are problems with using hue as an attribute for nearest-neighbor search. Hue is a single-dimensional attribute which folds onto itself just like orientation does. Hue also suffers from the significant disadvantage that the colors white/grey/black (i.e., zero saturation) cannot be represented. These problems are equivalent to representing orientation of normal vectors using an angle, but then wanting to represent the point $[0\ 0]^T$ which of course has no well-defined angle. Just as the solution in the orientation case is to use normal vectors; the solution to the hue problem may be to use chromaticity (normalized color, a 2D quantity).

Conceptually, chromaticity is a two dimensional slice of 3D color space (e.g., RGB space) where intensity is normalized [2]. By taking a constant intensity slice of the color space, we get a 2D space in which the color (hue) changes with the orientation of the chromaticity vector and the saturation increases as the chromaticity vector moves radially away from the center. Under a known light source color (e.g., white light or natural light), chromaticity may be sufficiently invariant (again, assuming diffuse reflection) to use as an attribute for correspondence search. For this thesis, we have not attempted to work with color information.

We have described how correspondences between 3D model edgels and 2D image edgels are computed given the object's pose estimate. Now we face the problem of refining the object's pose using these correspondences as a guide.

5.4 Pose Optimization

The pose optimization problem that we face in this chapter is very similar to the the 3D-3D pose optimization problem of Chapter 3. We have a rough pose estimate and many correspondences between model points and image points. Most of these correspondences will be incorrect initially. In the 3D-2D case, many model edgels will be predicted that will not be present in the image due to various lighting conditions⁶ or occlusion. In addition, it is common to detect spurious/background edgels in and around the object of interest. In the sense of correspondence accuracy, we will have many more mistakes to deal with in the 3D-2D case than in the 3D-3D case. Thus, for 3D-2D localization, robust estimation is even more a necessity than for 3D-3D localization.

⁶Our method predicts the visibility of stable image edgels of an object over the light source conditions used during the modeling stage. In our discussion of future work in Chapter 7, we discuss what would be necessary to incorporate photometric constraints for edgel visibility prediction.

Section 3.4.2 laid the groundwork for how we make the pose optimization robust to incorrect correspondences. We will use the same framework here. We will consider minimizing a robust M-estimator which has the form

$$E(\mathbf{p}) = \sum_{i \in V(\mathbf{p})} \rho(z_i(\mathbf{p})) \quad (5.14)$$

where z_i is the error of the i th point (edgel) in the model and $\rho(z)$ is one of the robust M-estimator described in Section 3.4.2. $V(\mathbf{p})$ is the set of visible model edgels at pose \mathbf{p} with respect to the known camera parameters. The pose vector \mathbf{p} is defined as in Chapter 3 to be

$$\mathbf{p} = [\mathbf{q}^T \mathbf{t}^T]^T$$

where \mathbf{q} is a quaternion representing the rotation and \mathbf{t} is the 3D translation vector.

The first difference between 3D-3D and 3D-2D estimation is the form of the error z_i . In the 3D-3D case, z_i was simply the 3D distance between the corresponding points. In the 3D-2D case, we have a correspondence between a 2D image point and a 3D model point. The most obvious and common approach to measuring this error is to project the 3D model into the image coordinates and minimize the 2D image distance between the points.

The transformation of the 3D model point \mathbf{x}_m to 2D image coordinates was described in Section 5.3. However, we now must account for the pose of the object \mathbf{p} , which is defined. Adding the pose transformation into the list of transformations described in Section 5.3, we have

$$\mathbf{x}_c = \mathbf{R}(\mathbf{q})\mathbf{x}_m + \mathbf{t} \quad (5.15)$$

$$\mathbf{u} = \mathbf{R}_{u \leftarrow c} \mathbf{x}_c \quad (5.16)$$

$$\mathbf{U} = \begin{bmatrix} \frac{u}{w} \\ \frac{v}{w} \end{bmatrix} \quad (5.17)$$

where the 3×3 rotation matrix $\mathbf{R}(\mathbf{q})$ and translation vector \mathbf{t} replace the 4×4 homogeneous transform $\mathbf{R}_{c \leftarrow m}$ from model to camera coordinates from Equation 5.9.

The error of model point \mathbf{x}_i is then the squared⁷ 2D image distance

$$z_i = \|\mathbf{U}_i - \mathbf{y}_i\|^2 \quad (5.18)$$

where \mathbf{y}_i is the corresponding image edgel to model edgel \mathbf{x}_i , and \mathbf{U}_i are the image coordinates of \mathbf{x}_i .

Perspective projection is really what makes the 3D-2D case more difficult than the 3D-3D case. Even in the noise and error free case, no closed form solution exists for the even least-squares minimization (i.e., minimizing E with $\rho(z) = z$). Iterative techniques are required to solve this problem.

To facilitate further analysis, we now assume that the aspect ratio is unity, the focal length is unity, the image center is exactly at image coordinates $[0 \ 0]^T$, and the camera

⁷Using the squared distance rather than the distance, simplifies the subsequent algebraic manipulations as in Section 3.4.3.

coordinate system is the same as the projection coordinate system. This can be done without loss of generality. The projection equations are simplified to

$$\mathbf{u} = \mathbf{R}(\mathbf{q})\mathbf{x}_m + \mathbf{t} \quad (5.19)$$

$$\mathbf{U} = \begin{bmatrix} \frac{u}{w} \\ \frac{v}{w} \end{bmatrix}. \quad (5.20)$$

As in the 3D-3D case, we must use an iterative technique to minimize $E(\mathbf{p})$ (Equation 5.14). We can use gradient-descent search (or some variant of hill-climbing search) as in Chapter 3. In order to perform this search, we must be able to evaluate the gradient of $E(\mathbf{p})$ which has the form (repeated for the reader's convenience)

$$\frac{\partial E}{\partial \mathbf{p}} = \sum_i \psi(z_i) \frac{\partial z_i}{\partial \mathbf{p}} \quad (5.21)$$

where $\psi(z) = \frac{d\rho(z)}{dz}$ as described in Section 3.4.2.

In the next section, we examine the effect of following this gradient more carefully. What we find is that the formulation that minimizes the image error (Equation 5.18) is not optimal. We suggest an improvement which makes the formulation equivalent to 3D-3D pose optimization.

5.4.1 3D-2D via 3D-3D

We can think of the gradient $\frac{\partial z_i}{\partial \mathbf{p}}$ from Equation 5.21 as a correction vector. The summation of Equation 5.21 adds up several of these local correction vectors weighted by $\psi(z_i)$. We make an interesting discovery when we derive the form of the individual corrections. We first use the chain rule to break the correction vector into two components

$$\frac{\partial z_i}{\partial \mathbf{p}} = \frac{\partial z_i}{\partial \mathbf{u}_i} \frac{\partial \mathbf{u}_i}{\partial \mathbf{p}}. \quad (5.22)$$

The first component, $\frac{\partial z_i}{\partial \mathbf{u}_i}$, tells us how we must move \mathbf{u}_i , the camera-centered coordinates of \mathbf{x}_i , to reduce z_i and the second component, $\frac{\partial \mathbf{u}_i}{\partial \mathbf{p}}$, is the Jacobian of the camera coordinates with respect to the pose and is identical to the correction vector of Equation 3.32 in Section 3.4.3. If we look closer at $\frac{\partial z_i}{\partial \mathbf{u}_i}$, the camera-centered correction of the point, we have

$$\frac{\partial z_i}{\partial \mathbf{u}_i} = 2(\mathbf{U}_i - \mathbf{y}_i)^T \frac{\partial \mathbf{U}_i}{\partial \mathbf{u}_i} \quad (5.23)$$

$$= 2(\mathbf{U}_i - \mathbf{y}_i)^T \begin{bmatrix} \frac{1}{w_i} & 0 & -\frac{u_i}{w_i^2} \\ 0 & \frac{1}{w_i} & -\frac{v_i}{w_i^2} \end{bmatrix} \quad (5.24)$$

If we substitute $\Delta \mathbf{U}_i = \mathbf{U}_i - \mathbf{y}_i$, we get

$$\frac{\partial z_i}{\partial \mathbf{u}_i} = 2\Delta \mathbf{U}_i^T \begin{bmatrix} \frac{1}{w_i} & 0 & -\frac{u_i}{w_i^2} \\ 0 & \frac{1}{w_i} & -\frac{v_i}{w_i^2} \end{bmatrix} \quad (5.25)$$

$$= 2 \left[\frac{\Delta U_i}{w_i} \quad \frac{\Delta V_i}{w_i} \quad \frac{-u_i \Delta U_i - v_i \Delta V_i}{w_i^2} \right]. \quad (5.26)$$

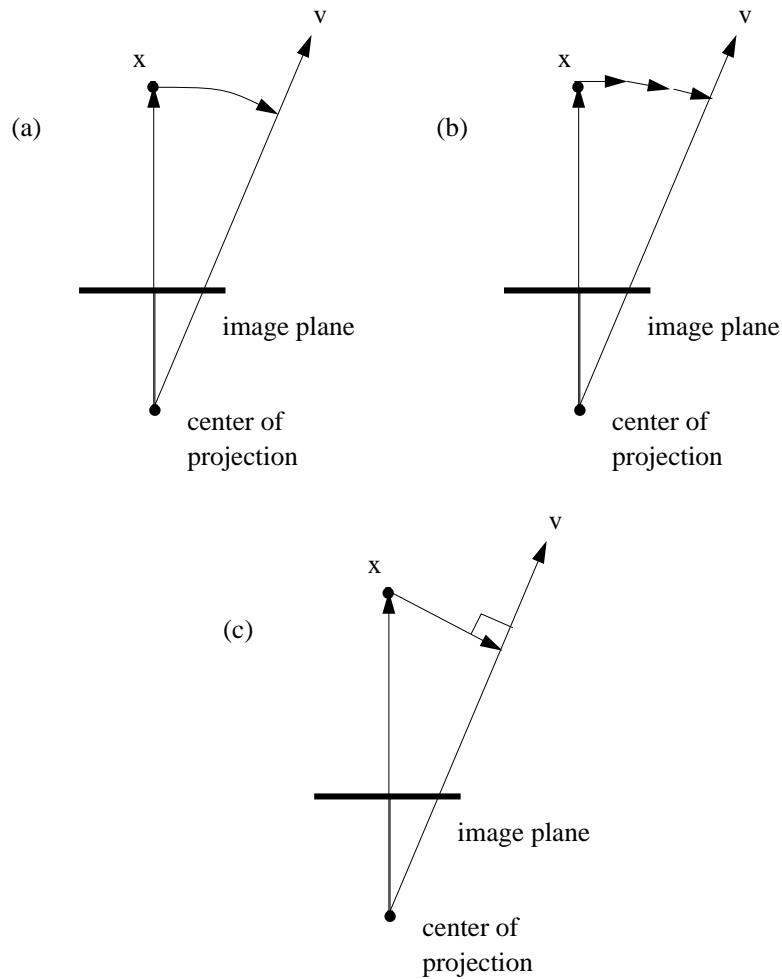


Figure 5.6: Gradient-descent minimization path to align a 3d point x with the line of sight \hat{v} (a) infinitesimal steps, (b) discrete steps, (c) shortest path.

The interesting thing to note about this equation is that $\mathbf{u}_i \cdot \frac{\partial z_i}{\partial \mathbf{u}_i} = 0$; thus, $\frac{\partial z_i}{\partial \mathbf{u}_i}$ is perpendicular to the vector \mathbf{u}_i . This fact is intuitively justified as motion along the viewing direction of \mathbf{u}_i does not reduce the error, z_i , in the 2D image space.

If we were to follow the gradient correction at infinitesimal steps, the path of the point would trace out an arc of radius u_i —not a straight line. Since infinitesimal steps are not possible in practice, the path traced out will usually be more inefficient. Examples of these paths are shown in Figure 5.6 (a) and (b) respectively. If we wanted to choose a correction vector to most quickly take us to the viewing direction of the matched edge point, we would choose a vector perpendicular to the 3D viewing direction of image point y_i (see Figure 5.6 (c)). If \hat{v} is the viewing direction to point y_i , we can determine the closest point

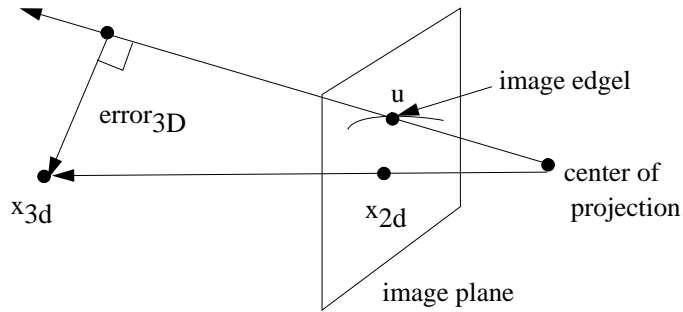


Figure 5.7: An example of the 3D error vector between the 3D point \mathbf{x}_{3D} and the line of sight of edgel \mathbf{u} . This is opposed to the 2D error vector between \mathbf{u} and the 2D projection, \mathbf{x}_{2D} , of \mathbf{x}_{3D} .

on that line of sight to point \mathbf{u}_i as

$$\mathbf{y}_i^c = (\mathbf{u}_i \cdot \hat{\mathbf{v}})\hat{\mathbf{v}}. \quad (5.27)$$

We can use this formula to define a new error measure z_i that uses \mathbf{y}_i^c rather than \mathbf{y}_i

$$z_i = \|\mathbf{u}_i - \mathbf{y}_i^c\|^2.$$

This error computation is now in 3D rather than 2D. Figure 5.7 shows an example of the 3D correction vector.

We can derive $\frac{\partial z_i}{\partial \mathbf{u}_i}$ using this formula giving

$$\frac{\partial z_i}{\partial \mathbf{u}_i} = 2(\mathbf{u}_i - \mathbf{y}_i^c)^T \left(I - \frac{\partial \mathbf{y}_i^c}{\partial \mathbf{u}_i} \right). \quad (5.28)$$

where

$$\frac{\partial \mathbf{y}_i^c}{\partial \mathbf{u}_i} = \frac{\partial (\mathbf{u}_i \cdot \hat{\mathbf{v}})\hat{\mathbf{v}}}{\partial \mathbf{u}_i} \quad (5.29)$$

$$= \frac{\partial (\hat{\mathbf{v}}^T \mathbf{u}_i)\hat{\mathbf{v}}}{\partial \mathbf{u}_i} \quad (5.30)$$

$$= \hat{\mathbf{v}}\hat{\mathbf{v}}^T. \quad (5.31)$$

Since—by construction of \mathbf{y}_i^c — $\hat{\mathbf{v}} \cdot (\mathbf{u}_i - \mathbf{y}_i^c) = 0$, then we have

$$\frac{\partial z_i}{\partial \mathbf{u}_i} = 2(\mathbf{u}_i - \mathbf{y}_i^c)^T I \quad (5.32)$$

$$= 2(\mathbf{u}_i - \mathbf{y}_i^c) \quad (5.33)$$

which is the desired correction from Equation 5.27 (shown in Figure 5.6 (c)).

Perhaps the biggest benefit of this formulation is that the equations for computing the gradient make our 3D-2D problem equivalent to the 3D-3D problem (after correspondences are determined). We only need to compute the 3D point of correspondence, \mathbf{y}_i^c , using Equation 5.27. This can easily be computed from the edgel position and camera parameters. The gradient of E then takes the same form as Equation 3.32, substituting \mathbf{y}_i^c for \mathbf{y}_i . Thus, we can apply Algorithm *3D-3D Localization* as described in Chapter 3 after replacing the visibility and correspondence search components to use those required for the 3D-2D case.

For 3D-2D localization, it makes sense to prefer 3D error measures over image errors. Using a purely 2D error metric would favor parts of the object that are closer to the camera. A 3D metric puts all points on an equal field. Haralick et al. [58] similarly utilized 3D errors for 3D-2D pose estimation.

Now that the form of the optimization function and its gradient are established, we can put it to use in an algorithm to perform 3D-2D localization.

5.5 Putting It Together: 3D-2D Localization

We have described the principal components of our 3D-2D localization algorithm: edgel visibility, model-edgel-to-image-edgel correspondence, and robust pose optimization via 3D error minimization. Here, we put everything together to present a pseudocode description of our complete 3D-2D localization algorithm:

Algorithm *3D-2D Localization*

Input: initial pose \mathbf{p}

Input: image edgel set

Input: 3D edgel model

Output: final pose \mathbf{p}

1. create k-d tree for rigid surface edgel matching
2. create k-d tree for convex and occluding-contour edgel matching
3. **repeat**
4. compute the set of visible model points: $V(\mathbf{p})$
5. $E_0 \leftarrow E(\mathbf{p})$
6. $d\mathbf{p} \leftarrow -\nabla E(\mathbf{p})$
7. $\lambda \leftarrow \arg \min_{\lambda} E(\mathbf{p} + \lambda d\mathbf{p})$
8. $\mathbf{p} \leftarrow \mathbf{p} + \lambda d\mathbf{p}$
9. **until** $E_0 - E(\mathbf{p}) < \epsilon$ **return** \mathbf{p}

The above algorithm is more or less identical to Algorithm *3D-3D Localization*.

In practice we use all the performance enhancements (e.g., conjugate gradient, golden-ratio bracketing for line minimization, etc.) as described in Section 3.5. Differences include the methods for computing edgel visibility $V(\mathbf{p})$ and correspondence and slight differences in computing the optimization function $E(\mathbf{p})$ and its gradient $\nabla E(\mathbf{p})$.

As we show in Section 5.7, this algorithm has a reasonable convergence time and produces accurate results.

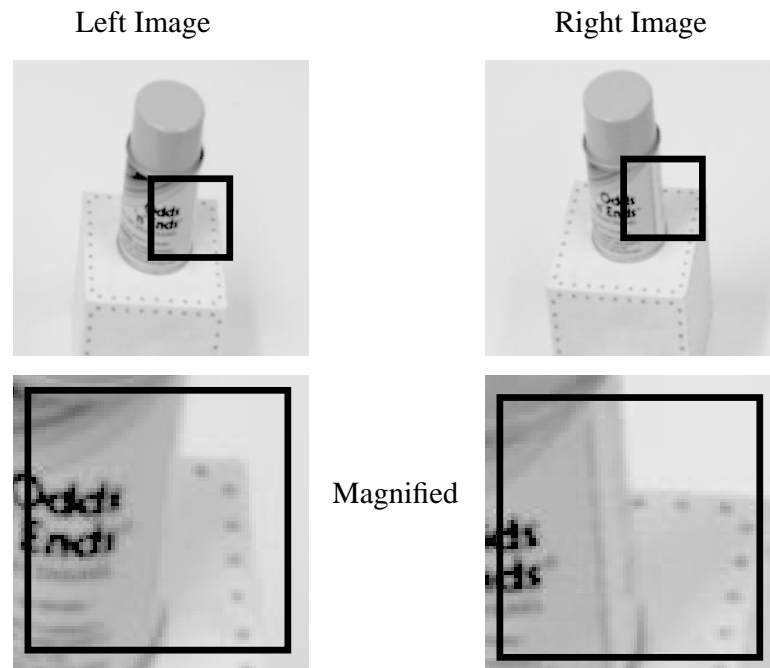


Figure 5.8: The stereo correspondence problem: several points are not visible in both views. Note especially the magnified regions of the two stereo images.

5.6 Multi-Image Localization

We now take a small diversion to discuss extending Algorithm *3D-2D Localization* to utilize multiple images to localize an object. Usually, when one thinks of using multiple images, one thinks of the traditional mode for stereo vision. The traditional mode for stereo vision [53, 101, 74] has been to use two or more cameras to compute depth at each pixel in the image. One well known problem with this approach is that there will invariably be points that are visible in one image while not visible in one or more of the other images. Figure 5.8 shows an example of this problem. There is no solution to this problem; at best, the obscured pixels can be identified and labelled as such.

We propose another mode for stereo/multi-camera systems that does not suffer from this problem. If we are able to calibrate two or more cameras to use the same coordinate system, then we can localize our 3D model in any of the images. The minimization we perform is simply matching image observations to our predicted model appearance for the specific image. Minimizing the error function for one image is no different than minimizing the function E over several images simultaneously. For example, extending Equation 5.14

to handle observations from multiple images is straightforward:

$$E(\mathbf{p}) = \sum_{j \in I} \sum_{i \in V_j(\mathbf{p})} \rho(z_{i,j}(\mathbf{p})) \quad (5.34)$$

where I is the set of images and $V_j(\mathbf{p})$ is the set of visible model edgels at pose \mathbf{p} in image j . $z_{i,j}(\mathbf{p})$ now depends on image j in addition to model edgel i . The only required modification to Algorithm *3D-3D Localization* is to iterate the summations for Equations 5.34 and 3.32 over the set of images. The only practical requirement is that we have the cameras calibrated with respect to the same world coordinate system. This is usually the case for stereo vision systems designed to compute depth maps.

This method of using multiple cameras for localization allows us to apply multiple constraints simultaneously. One advantage is that model edgels which are not detected in a given image (say, because of the lighting configuration or occlusion) may be detected in other images. Also, correct correspondences are likely to be consistent across images allowing implicit triangulation to occur. The algorithm would implicitly triangulate points to force convergence of the correctly matched points on the model. The accuracy of localization will be improved over single image localization since the implicit effect of triangulation is to reduce the uncertainty of the object's depth in the image. Incorrect correspondences (those matched to spurious edgels or background, or those that are occluded/undetected) are unlikely to be consistent across images. Thus, localization will be more robust when given multiple images as from a stereo system.

Localization with multiple cameras under this approach does not require depth map computation. However, a very promising direction would be to utilize 3D data info in addition to edgel info in an effort to make localization more robust. This is described in Chapter 7.

5.7 3D-2D Localization Results

In this section, we present experiments to evaluate the performance of our 3D-2D localization algorithm. We first present results which give a qualitative evaluation of the smoothness of the objective function E of Equation 5.14 with respect to the various M-estimator functions $\rho(z)$ described in Section 3.4.2. We then present quantitative results demonstrating the convergence of our algorithm with respect to these M-estimators. Examples of using our 3D-2D localization algorithm to track objects through a sequence of images are presented next. We conclude by presenting results and comparison of convergence and accuracy using single versus multiple images with our 3D-2D localization algorithm.

5.7.1 Qualitative Analysis of the Objective Function

As in Section 3.6.2 with regards to 3D-3D localization, we must determine if whether the objective function E is smooth enough for a local gradient-descent search to be effective.

To inspect the shape of $E(\mathbf{p})$, we computed the values of $E(\mathbf{q})$ over several range images containing known objects in known positions. Here, we show some plots of $E(\mathbf{q})$ for a range image of the toy car. For an example of the type of intensity image and edge data used for this analysis see Figure 5.17 (used for an experiment in the next section). The correct pose of the car was obtained via the automatic calibration system. As in the 3D-3D case, barring significant partial-occlusion or missing data, we would expect the correct pose estimate to be a local minima of any of the robust estimator functions described previously. Again, this is indeed the case.

In this section, we only consider the Lorentzian and Gaussian weight functions. In Section 3.6, the Threshold function was found to be inadequate, and the Huber and Tukey functions provided qualitatively similar performance to that of the Lorentzian; thus, we now focus on the Lorentzian and Gaussian. For both of these functions, we plotted the value of E along various lines in pose space which cross the desired pose. The plot in Figure 5.9 shows the values of E for each function $\rho(z)$ along a pure translation through the correct pose (at point $x = 0$). The axis dimensions of the plot is in millimeters and the range of the plot is 60 mm. The toy car is approximately 190 mm long. Figure 5.10 shows the value of E for each function $\rho(z)$ along a pure rotation through the correct pose (at point 0). The axis dimensions of the plot is in degrees and the range of the plot is 70 degrees. Finally, Figure 5.11 shows the value of E for each function $\rho(z)$ along a rotation and translation through the correct pose (at point 0). The axis dimensions of the plot is in combined degrees and millimeters and the range of the plot is 70 degrees and 60 mm.

One can see that the E is relatively smooth out to about 15 degrees and 10 millimeters. As in the graphs of E for the 3D-3D case in Section 3.6.2, E is smoother when using the Lorentzian or other down-weighting functions than with a Gaussian. Even at a coarse view, as in Figure 5.10, E has noticeable local minima for the Gaussian case both far away and near the global minimum.

5.7.2 3D-2D Localization Convergence Results

We now present quantitative results demonstrating the convergence of our 3D-2D localization algorithm using the 3D edgel models constructed in Section 4.6.

We performed experiments on images of each of the objects constructed in Section 4.6: the bulls-eye, the stop sign, the T-sign, the mug, the boxcar, the car, and the duck. For each experiment, we took an intensity image of our object in a known position—using the robotic positioner or by manually estimating the object’s precise position. Each image contains 256×240 pixels and is processed to produce a set of smoothed intensity edgels.

The test images are shown in Figures 5.12- 5.18. These figures show the intensity image, the smoothed Canny edgels, an overlay example of an initial (incorrect) pose estimate as used in the experiments, and the overlay of the object model on the intensity image at the estimated position.

As in Section 3.6.3, each experiment consists of 100 trials of the 3D-2D localization algorithm from a randomly generated initial pose estimate. The initial pose estimates were

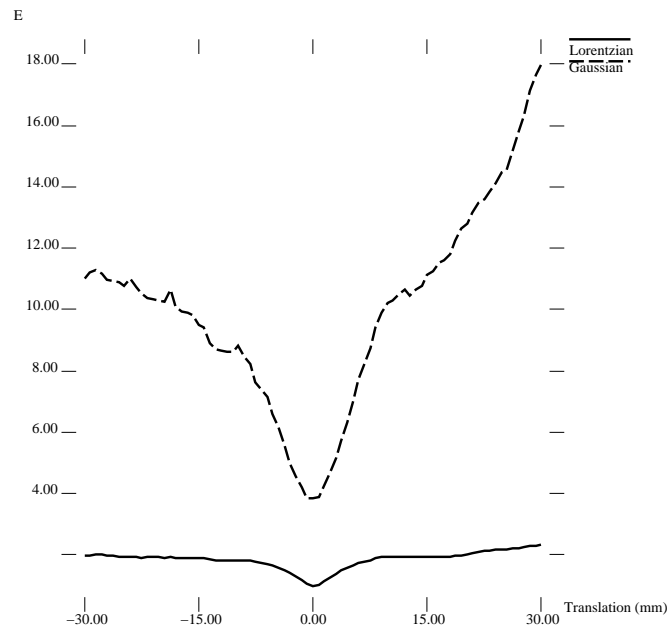


Figure 5.9: The variation of E along a line of translation in pose space for the Gaussian and Lorentzian weight functions. The true pose is at $x = 0$. The x -axis represents translation in millimeters. The rough range of the graph is $[-30, 30]$ millimeters (about half the length of the dog).

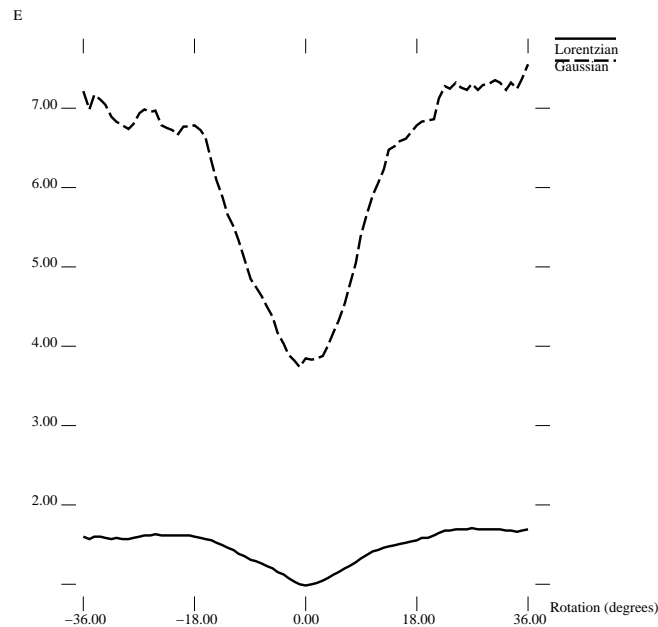


Figure 5.10: The variation of E along a line of pure rotation in pose space for the Gaussian and Lorentzian weight functions. The true pose is at $x = 0$. The x -axis represents rotation in degrees. The rough range of the graph is $[-35, 35]$ degrees.

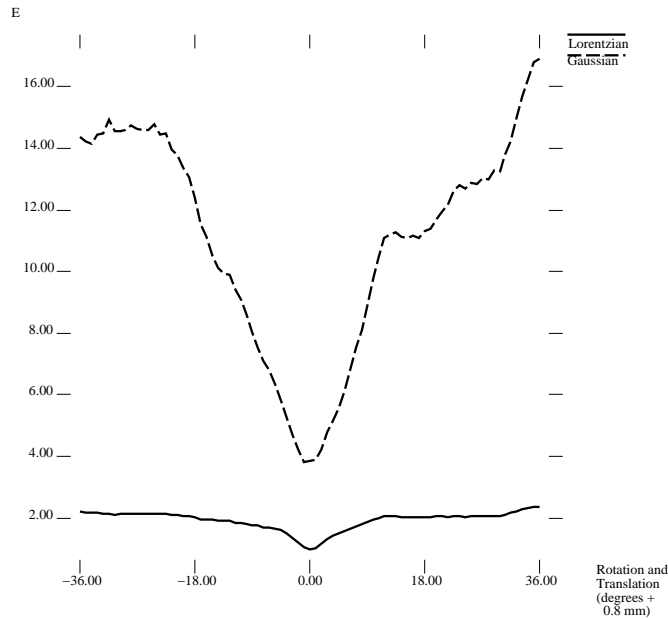


Figure 5.11: The variation of E along a line of translation and rotation in pose space for the Gaussian and Lorentzian weight functions. The true pose is at $x = 0$. The x -axis represents simultaneous rotation and translation. The rough range of the graph is $[-30, 30]$ millimeters and $[-35, 35]$ degrees.

generated by perturbing each pose by a random translation vector and a random rotation. Each trial was performed with the same magnitude of initial pose error: 10 millimeters in translation and 15 degrees of rotation. As before, the initial errors are not uniformly distributed between 0 and 10 millimeters of translation, and 0 and 15 degrees of rotation, but are exactly 10 millimeters and 15 degrees, respectively.

The size of the perturbation is reduced from those used in the 3D-3D localization tests since local minima are more of a problem in typical intensity edge images. From the plots of E in Section 5.7.1, we can see that the effective ranges which we may be able to localize an object in an intensity image is much smaller (by about half) than that of the 3D-3D case. As one can see from the examples of initial pose estimates, a 15 degree and 10 mm error is non-trivial.

For each image, we performed the convergence experiment on two versions of our 3D-2D localization algorithm: using the Gaussian and Lorentzian weight functions. See Section 3.4.2 and Figure 3.11 for a review of these functions. In Section 3.6, the Threshold function was found to be inadequate, and the Huber and Tukey functions provided qualitatively similar; thus, we see no real benefit for considering them here.

To account for large initial pose errors it is important that the errors z are normalized accordingly so that the robust estimators do not immediately discount correct correspondences. The errors are normalized by a progressively decreasing normalization factor σ (i.e., use $z' = \frac{z}{\sigma}$). This is effectively the standard deviation which controls the width of the M-estimator weight-functions (e.g., a 3σ threshold). In these experiments, we begin with

Object	% Correct	
	Lorentzian	Gaussian
stop sign	97	94
T-sign	78	64
bullseye	43	16
duck	73	65
mug	54	52
boxcar	37	28
car	30	27

Table 5.1: Results of the convergence experiments for our 3D-2D localization algorithm using the Lorentzian and Gaussian weight functions. The initial errors were of uniform magnitudes: 15 degrees of rotation and 10 mm of translation.

$\sigma = 20$ mm and reduce it to 15 mm, 10 mm and 5 mm as the algorithm progresses.

We manually verified the results of each trial and determined the number of correct trials—those that correctly align the model with the image—for each experiment. The results are listed in Table 5.1.

From these results we see that the Lorentzian weight function has slightly better convergence properties than a pure least-squared error objective function (corresponding to the Gaussian). For each convergence trial, our localization algorithm typically performed 10 to 15 conjugate-gradient steps and 70 to 90 function evaluations for each trial (approximately 7 seconds on a SPARC 20 workstation).

Again, there is nothing special about the images used for these tests (i.e., they weren't hand chosen, but rather randomly selected from a large set of sample images). They were taken with a plain black background which would suggest that the localization task would be trivial. In order to make it more realistic, the edge detection parameters were modified to produce noisier edgel images than would normally be used. This produced many spurious random edgels around the object where otherwise there might only be black background. It also created spurious edgels on the object which can also foul up the localization algorithm by creating more local minima around the correct pose.

The duck example provides a good example of the effectiveness of our occluding contour representation for localization. The stop sign is probably the easiest case, but if not for the use of reflectance ratios for the correspondence search, it would not be reliably localized in that image. The bulls-eye result is a bit disappointing, but the symmetry of the circles makes for quite a number of near-miss local minima where the orientation of the bulls-eye plane is noticeably incorrect. The poorer performance of the localization of the car and boxcar is possibly because these objects are significantly longer than the other objects; thus, a rotation will produce larger errors in positions of points of the objects than of more compact object.

In these experiments, the standard deviation of the translation errors in depth were consistently 5 to 7 mm across the various. This is a largely unavoidable problem for

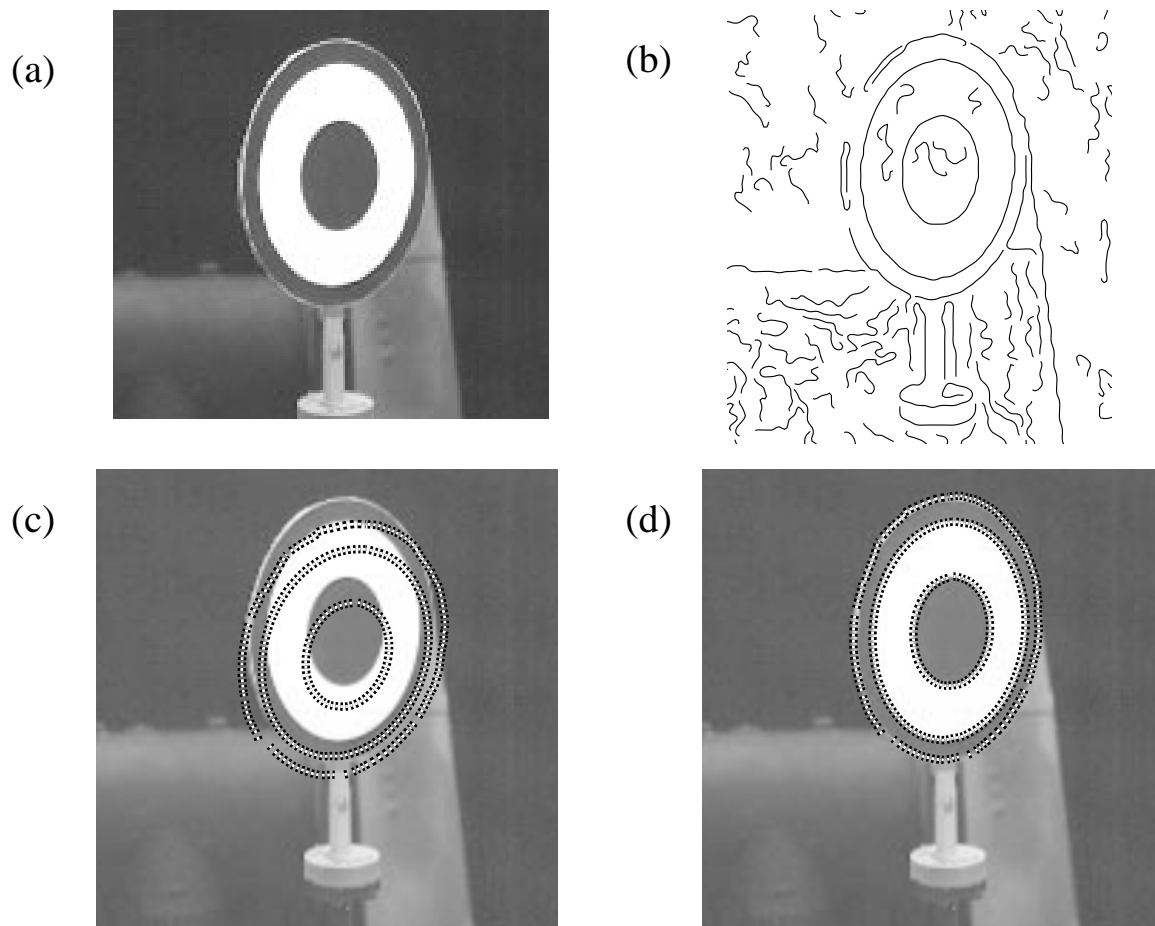


Figure 5.12: The bulls-eye convergence test data: (a) the intensity image, (b) the Canny edge image, (c) a typical initial starting point for the convergence tests (10 mm translation error and 15 degrees rotation error), and (d) an overlay of the bulls-eye model at the estimated location.

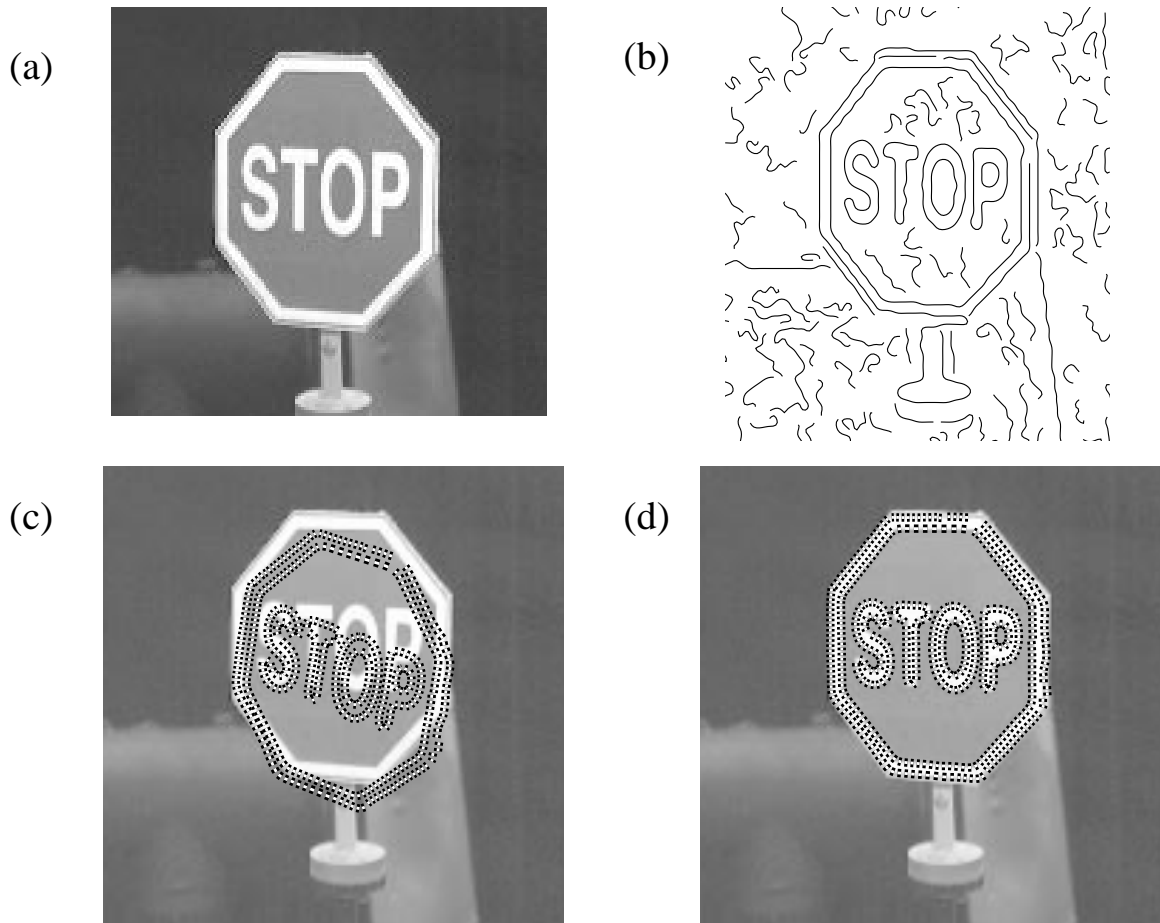


Figure 5.13: The stop sign convergence test data: (a) the intensity image, (b) the Canny edge image, (c) a typical initial starting point for the convergence tests (10 mm translation error and 15 degrees rotation error), and (d) an overlay of the stop sign model at the estimated location.

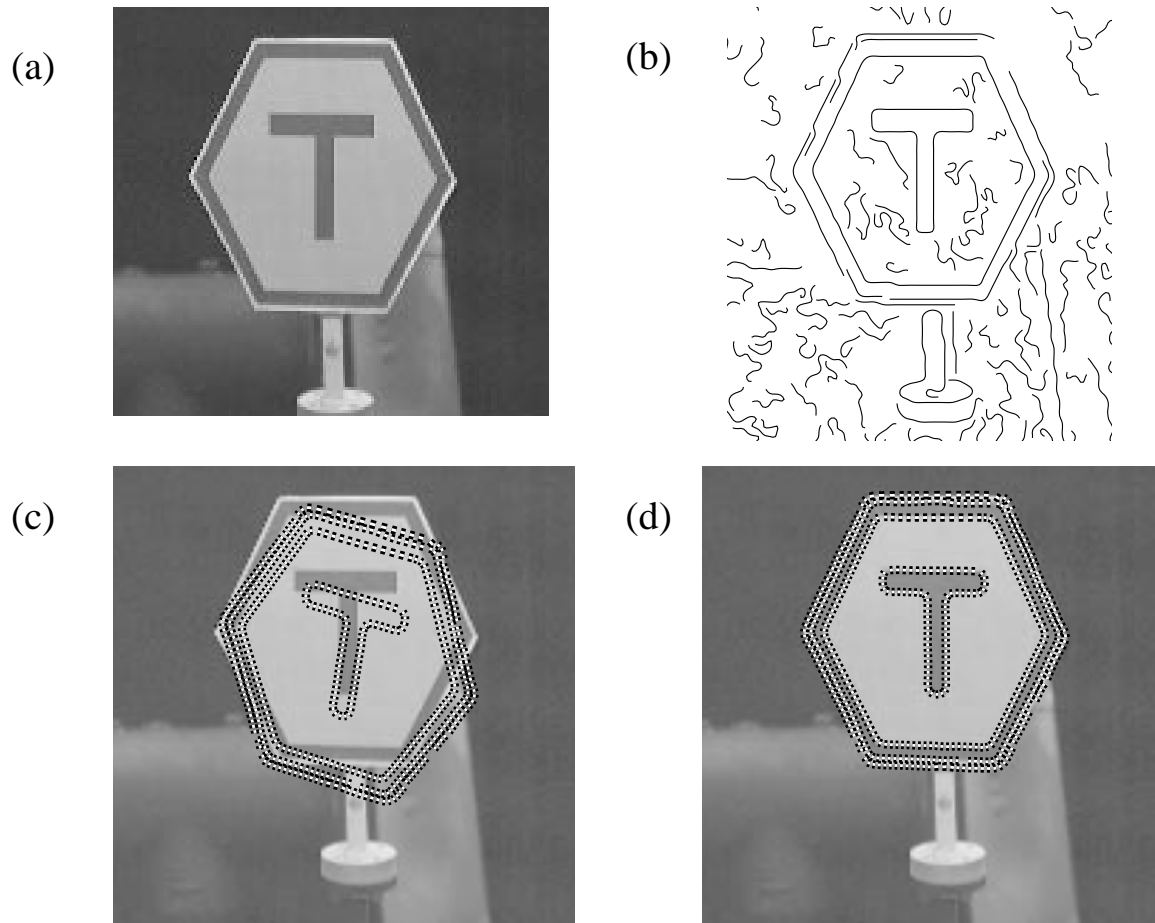


Figure 5.14: The T-sign convergence test data: (a) the intensity image, (b) the Canny edge image, (c) a typical initial starting point for the convergence tests (10 mm translation error and 15 degrees rotation error), and (d) an overlay of the T-sign model at the estimated location.

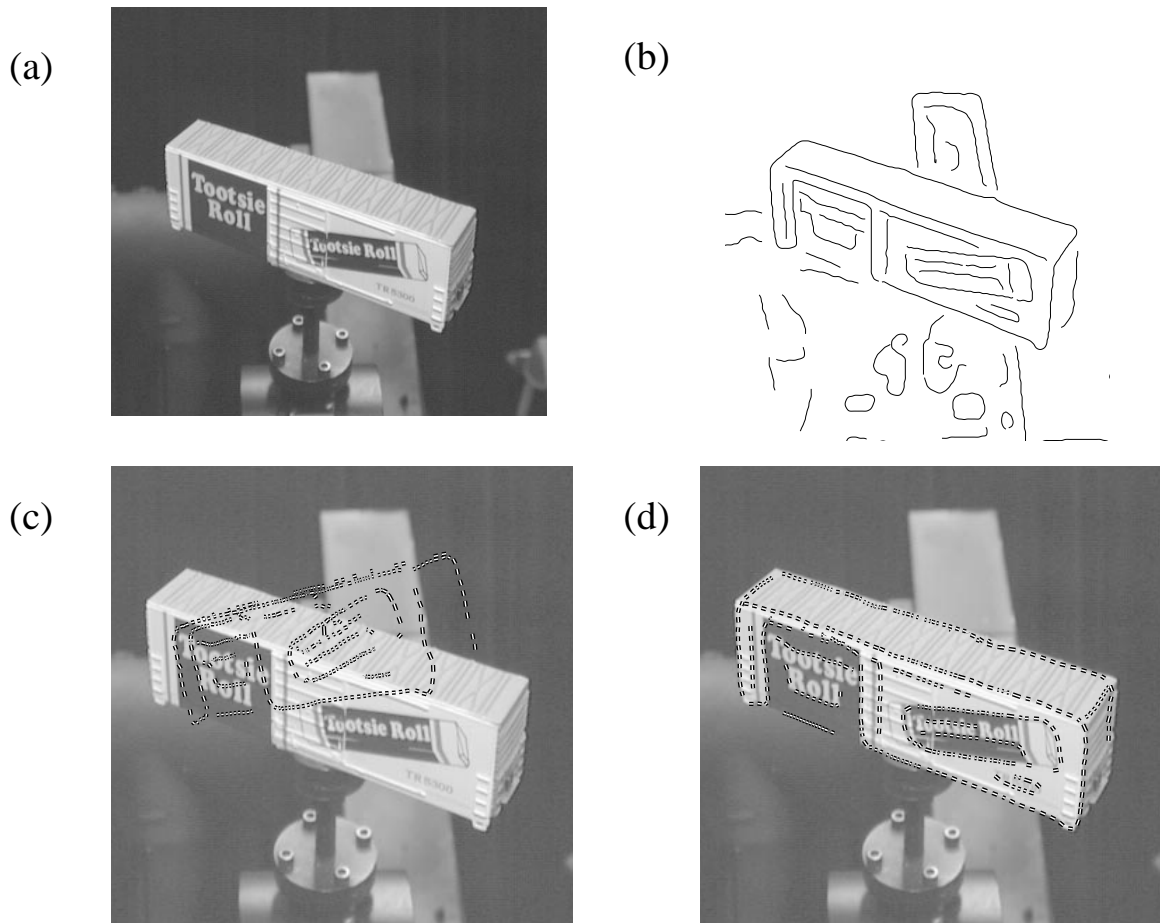


Figure 5.15: The boxcar convergence test data: (a) the intensity image, (b) the Canny edge image, (c) a typical initial starting point for the convergence tests (10 mm translation error and 15 degrees rotation error), and (d) an overlay of the boxcar model at the estimated location.

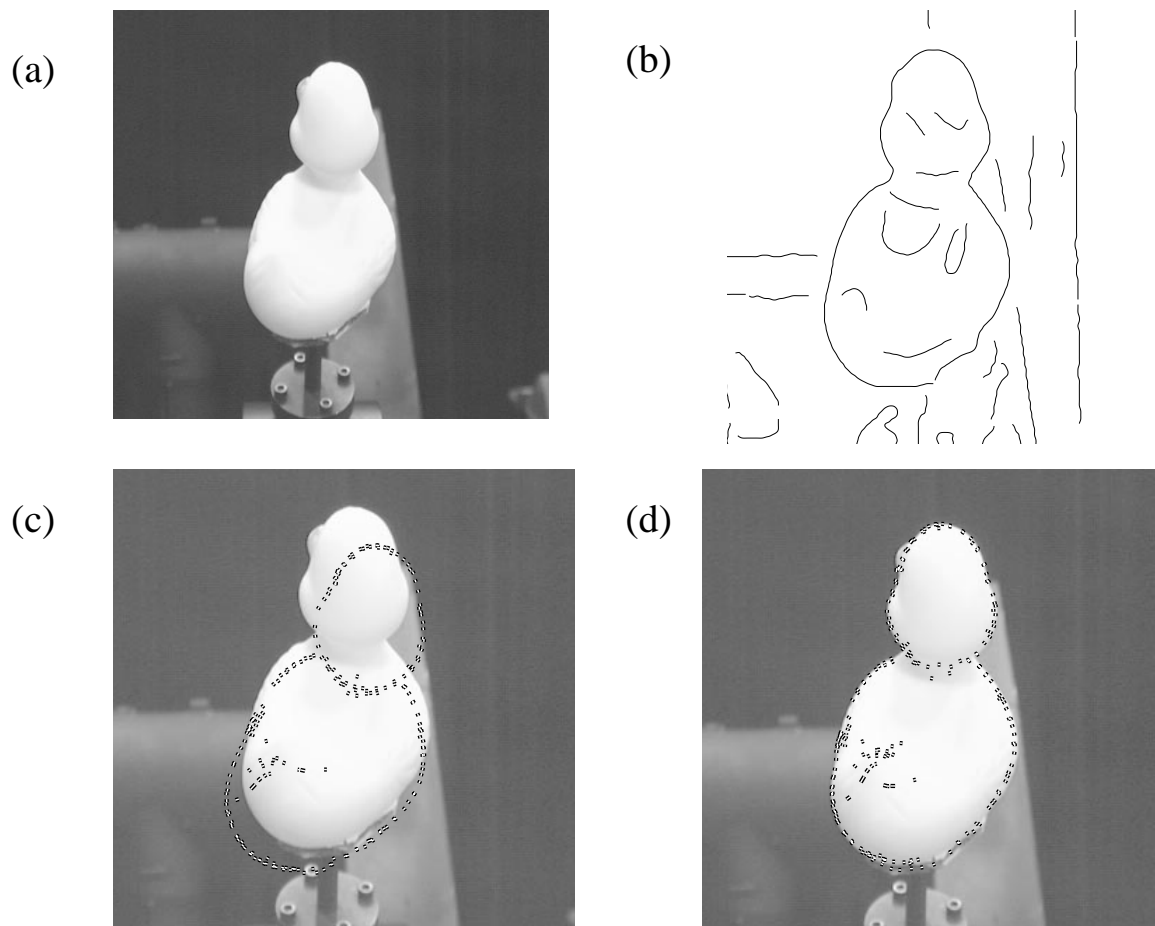


Figure 5.16: The rubber duck convergence test data: (a) the intensity image, (b) the Canny edge image, (c) a typical initial starting point for the convergence tests (10 mm translation error and 15 degrees rotation error), and (d) an overlay of the duck model at the estimated location.

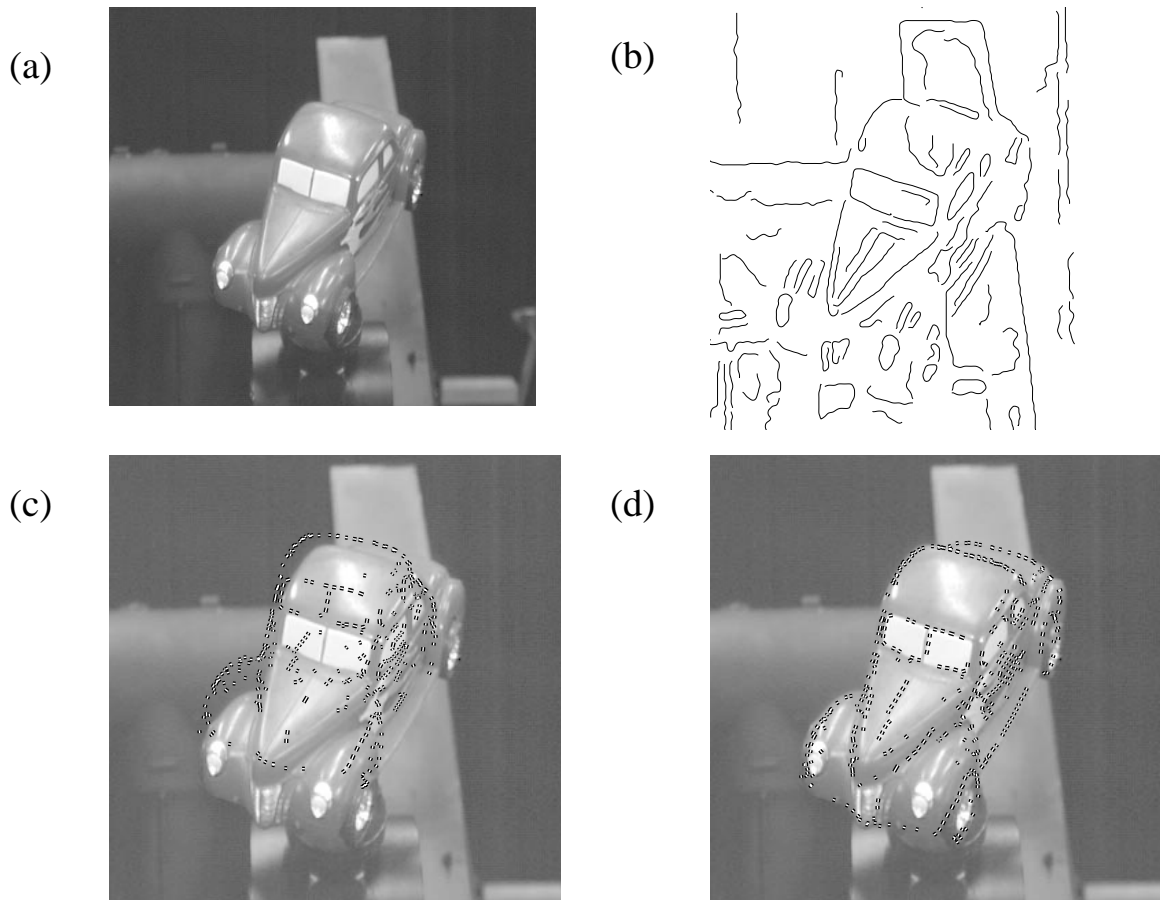


Figure 5.17: The toy car convergence test data: (a) the intensity image, (b) the Canny edge image, (c) a typical initial starting point for the convergence tests (10 mm translation error and 15 degrees rotation error), and (d) an overlay of the car model at the estimated location.

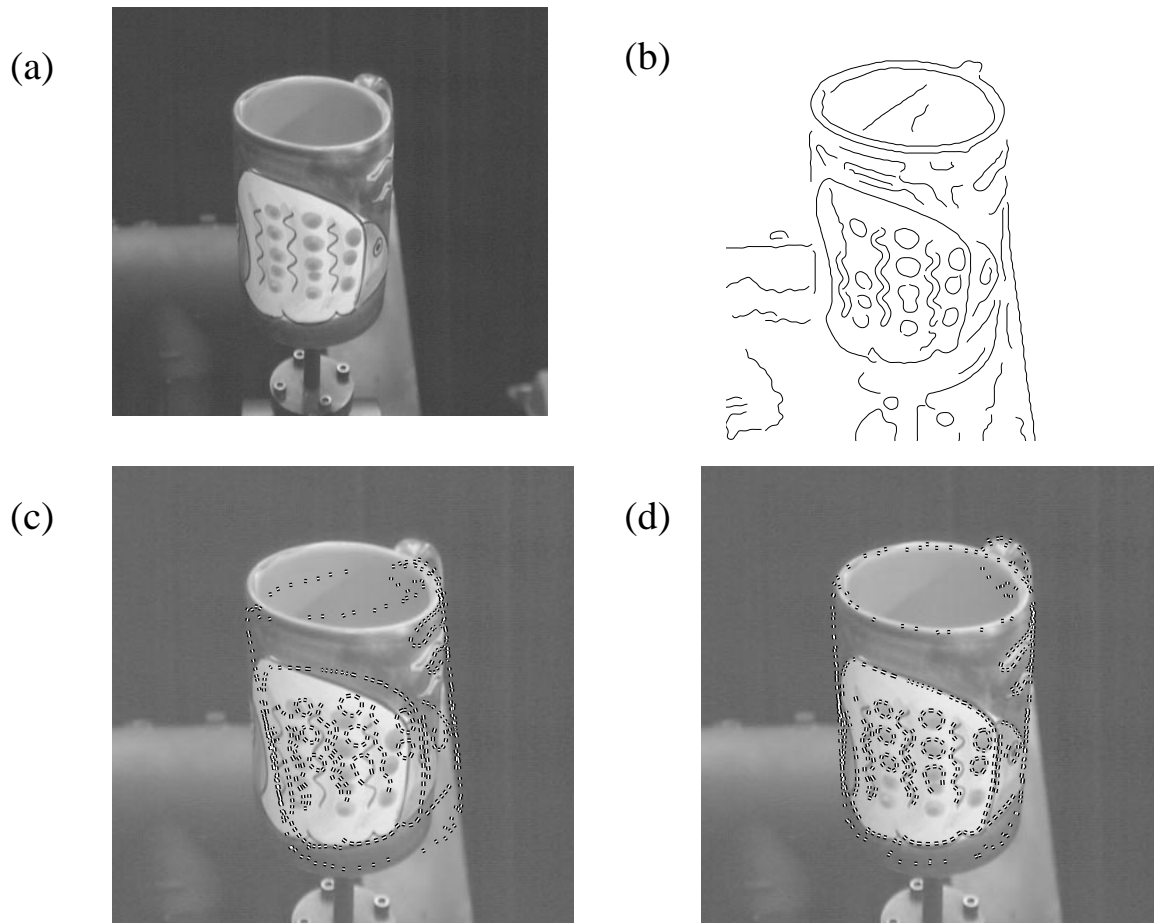


Figure 5.18: The ceramic mug convergence test data: (a) the intensity image, (b) the Canny edge image, (c) a typical initial starting point for the convergence tests (10 mm translation error and 15 degrees rotation error), and (d) an overlay of the mug model at the estimated location.

localizing objects in single intensity images. We address this more in Section 5.7.4.

These results demonstrate that our 3D-2D localization algorithm is effective at localizing a wide variety of 3D objects in relatively noisy input images.

5.7.3 Tracking Experiment

One important application of localization is object tracking in image sequences. In fact, tracking can be defined as a special case of localization as described here. It is a special case since it is fundamentally the same problem with slightly more information: that the position of the object in the previous image(s) is known. If we take the most simple-minded use of this extra information, we simply look for the object at the last place we saw it. More information can be derived from knowledge of the immediate past—such as the velocity and acceleration of the object [44]—and used to improve the initial guess.

We performed a simple experiment to test our algorithms performance on tracking an object through a sequence of images. We took 10 images of the car at 5 degree pure rotation increments. The simple minded approach—using the last known pose as the next starting point for the localization search—was used here. Our algorithm was able to successfully track the object through the 9 images (we assumed the pose of image 0 was known as our starting point). This experiment was successfully repeated after dropping every other image in the sequence—creating intervals of 10 degrees. The step-by-step results of this sequence are shown in Figure 5.19. While this tracking task may seem simple, there is a fair amount of random edges around the car in the images and the last step in the sequence undergoes a large aspect change—moving from one side of the car being visible to the other side of the car being visible in one step. The aspect change is handled cleanly. This is a noteworthy benefit of using a 3D object model.

Localization for these cases was very efficient due to the small initial errors—usually accomplished in 2 to 5 gradient search steps and 10 to 25 function evaluations. The overhead for loading the image and computing the Canny edge image was greater than the actual localization time.

Also of note is that the lighting used for this experiment was different from the lighting used to build the car model in Section 4.6. This demonstrates some effective invariance of our models to light source changes.

5.7.4 Multi-Image Localization

Section 5.6 described a simple extension of our algorithm to utilize additional images from cameras which are calibrated with respect to the same coordinate system as in a stereo vision system. To test this idea, we utilized stereo images of our objects taken from a calibrated stereo jig. Each camera was calibrated with respect to a single world coordinate system thus we are able to place our model in the world coordinate system and predict it's appearance in each image simultaneously.

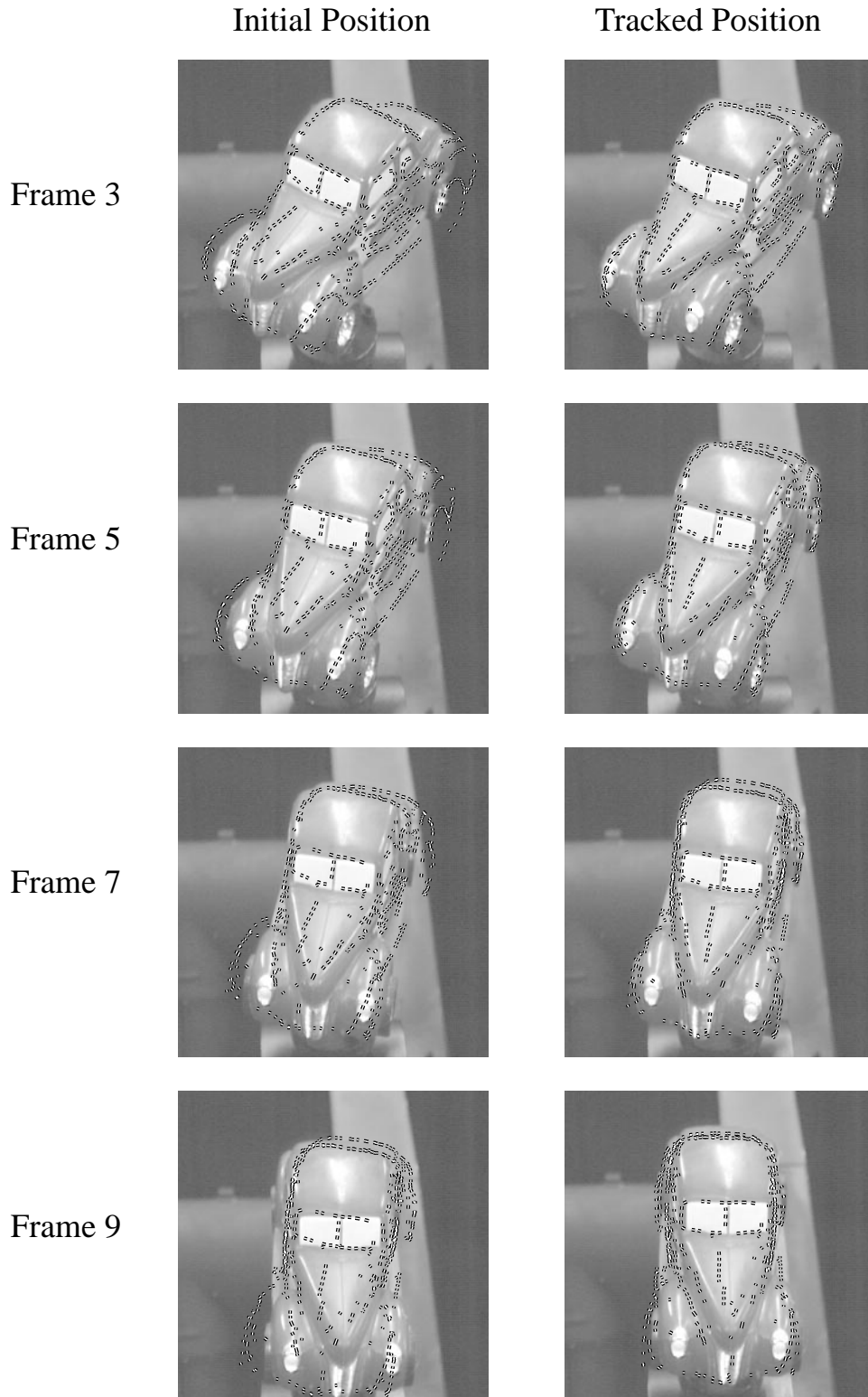


Figure 5.19: Tracking the car through 5 images at 10 degree intervals. In this example the car was tracked through frames 3, 5, 7 and 9 with the initial starting point at the car's position in frame 1. The left images in each pair show the initial guess from the previous tracking result, and the right images show the localized result.

Object	Single Image		Two Images	
	% Correct	Std Dev. in Depth (mm)	% Correct	Std Dev. in Depth (mm)
stop sign	85	6	100	1.1
paint can	77	5.8	87	3.4

Table 5.2: Results of the single versus multi-image convergence tests. All these experiments used our 3D-2D localization algorithm with the Lorentzian weight function. The initial errors were of uniform magnitudes: 15 degrees of rotation and 10 mm of translation.

A serious problem with single image recognition and localization is the uncertainty in depth. In the experiments of Section 5.7.2, the pose estimates from our algorithm would have large standard deviations in the translation estimate almost all of which are in the depth direction (along the viewing direction to the object). The straightforward approach to reducing uncertainty in depth is to triangulate as is done in stereo vision systems as well as light-striping range finders such as the one used in Chapters 2 and 3. In addition to reducing the uncertainty in depth, one would hope that the added constraints of more images would also increase the convergence of a localization algorithm.

We performed tests to determine the impact of adding a second image as input to our 3D-2D localization algorithm on convergence percentage and depth uncertainty.

For each experiment, we took two intensity images of the object using a stereo jig.⁸ We manually determined the precise position of the object. Then we performed two sets of 100 trials: one using a single image and another using both images simultaneously. Each trial was performed as in Section 5.7.2—perturb the known pose by a random translation of magnitude 10 mm and a random rotation of 15 degrees, and then localize the object. We performed the experiment on two objects: the stop sign and a paint can. Figures 5.20 and 5.21 shows the pair of intensity images of the respective object with an overlay of the respective model at one of the initial perturbed poses, and with an overlay of the respective model at the estimated pose.

Table 5.2 presents the results of these experiments. As these results show, the convergence percentage is significantly increased (by over 10%) and the standard deviation in the depth estimate is significantly decreased (by roughly 40% for the paint can and 80% for the stop sign).

5.8 3D-2D Localization: Summary

We have described our method for localizing a 3D object model in a 2D intensity image of the object. The model is described as a collection of 3D edgel generators which are matched to edgels derived from the intensity image. We have shown an efficient, local computation for predicting the visibility of 3D edgels in the image given the pose. The visible edgels are then used to create correspondences between the model and the image. Useful correspondences

⁸We do not use the stereo images to compute depth, we only use the jig to provide two intensity images from cameras which are calibrated with respect to the same coordinate system.

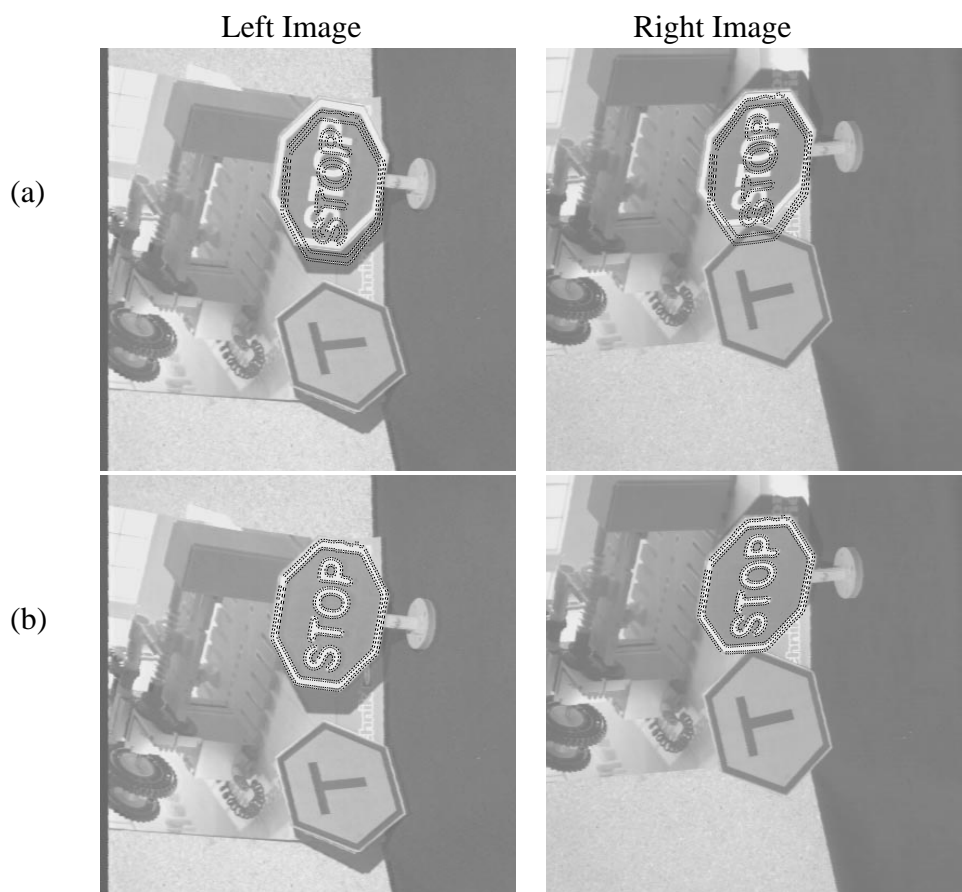


Figure 5.20: The stereo pair of intensity images of the stop sign with (a) an overlay of the stop sign at one of the initial perturbed poses, and (b) an overlay of the stop-sign model at the estimated pose.

are efficiently found—despite significant pose errors and high densities of edgels in the intensity image—by extending nearest-neighbor search concept to include edgel attributes such as edgel normals and reflectance ratios. Using these correspondences, we define an error measure for the the pose by measuring a 3D distance rather than a 2D image distance as is commonly done. The error is formulated as the perpendicular distance between the 3D edgel and the line of sight of the image edgel—in other words, the shortest motion of the 3D edgel to align it with the image edgel. This formulation of the pose error leads to an identical set of equations for computing the optimization function and its gradient as in the 3D-3D case of Chapter 3. Thus, the pose can be refined using much the same minimization algorithm as Algorithm 3D-3D Localization of Chapter 3.

We also showed how Algorithm 3D-2D Localization can be applied to solving for pose from multiple images without computing depth. This mode of using multiple images does

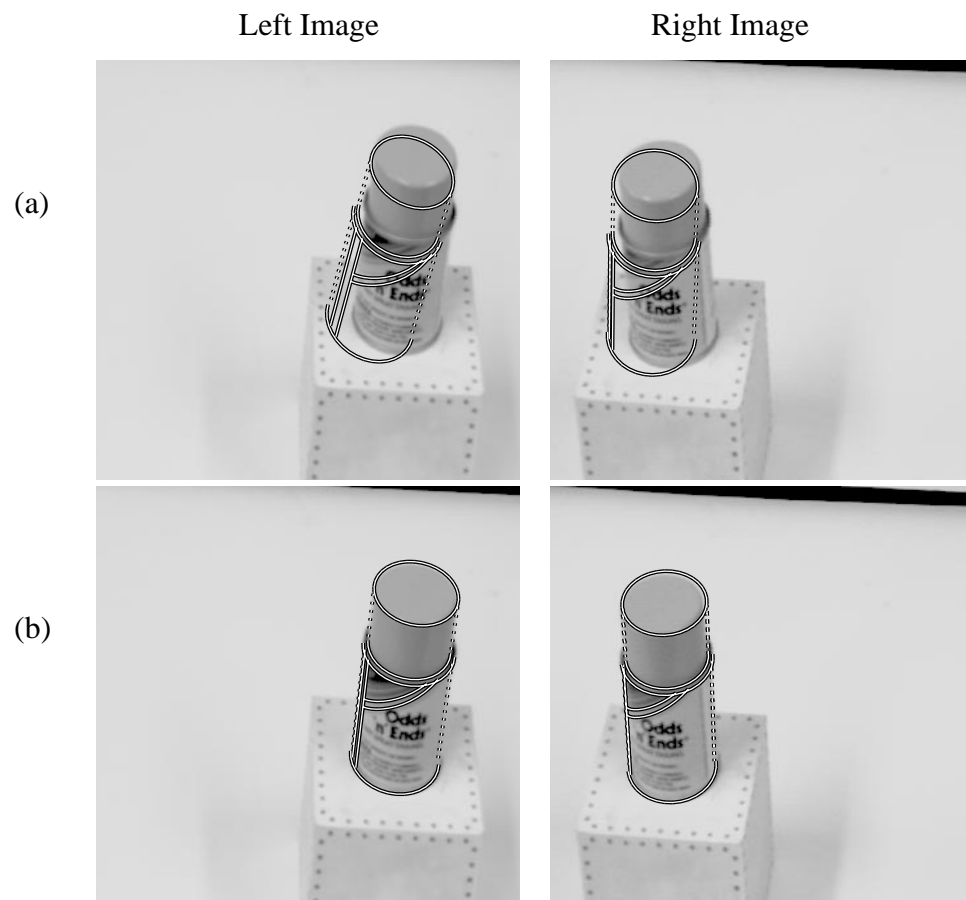


Figure 5.21: The stereo pair of intensity images of the paint can with (b) an overlay of the paint can at one of the initial perturbed poses, and (a) an overlay of the paint can model at the estimated pose.

not suffer from the ill-posed problem of finding point-wise correspondence from images at different views. By applying the constraints of multiple images of an object, localization will be more robust and accurate.

Our results demonstrate that a wide variety of objects can be localized despite large initial errors and noisy image data. Multi-image localization was shown to provide substantial improvements in resulting pose (with respect to depth uncertainty) and convergence accuracy.

This concludes our chapter on 3D-2D object localization. We will now discuss the work of others that is related to the work in this thesis.

Chapter 6

Related Work

In this section, we will provide an overview of related research on the problems of modeling and localization. The structure of this chapter will follow the structure of the technical part of the thesis—beginning with a review of the work on 3D object modeling, followed by reviews of 3D-3D localization, object modeling for 3D-2D localization, and 3D-2D localization. Finally, we will review some of the important work on object recognition and how it relates to the work here.

6.1 3D Object Modeling

In this section, we discuss the previous work related to the work on modeling 3D surfaces from real image data which was presented in Chapter 2. We begin by reviewing three methods which are most closely related to our work and follow that by a brief discussion of other related work. The first three works are similar to our algorithm in that they all make use of implicit surfaces and the marching-cubes algorithm [83] to merge the range-image data from several views into a surface model. The main differences between these algorithms are their methods for computing the signed distance from each voxel to the closest surface.

Hoppe et al. [65] were the first to propose constructing 3D surface models by applying the marching-cubes algorithm [83] to a discrete, implicit-surface function generated from a set of range images. Their algorithm computes the signed distance function from the points of the range images rather than from triangulated surfaces generated from the images. Their reliance on points, the lowest-level data provided by range images, is idealistic (as described in Section 2.2, range images provide points not surfaces). Using points rather than surfaces suffers from some practical problems. The main problem is that a surface is necessary to measure the signed distance correctly—points are insufficient. For example, consider computing the distance to the surface from a position lying between two neighboring point samples of the surface: the result should be zero, however, the distance to the nearest point will be non-zero. Hoppe et al. realized this and, to compensate, created an algorithm to locally infer surfaces at a point from the neighboring points in the input data (points from

all views combined). Fundamentally, this appears to be similar to the idea of consensus surfaces; however, their algorithm does not attempt to test whether there is sufficient evidence of a surface at the point in question. Instead, for each point, they estimate the tangent plane with respect to the best fit plane of the local neighborhood of points. The tangent plane gives a normal vector with an arbitrary sign (i.e., pointing out or in). To ensure that the estimated normals consistently point outward from the surface, a constraint-propagation method is employed. The signed distance is then defined as the distance from a given point to the tangent plane of the closest point in the set. The signed-distance function is evaluated for each voxel in the volume grid and the marching-cubes algorithm is applied to the volume grid to generate the desired triangulated surface mesh.

Hoppe's [65] method suffers from several problems which limit its applicability for many practical modeling problems. First, tangent-plane estimation from clouds of points is not likely to give the desired results for many configurations of points, especially in regions of high curvature; the tangent plane will also be corrupted by irregular sampling of a surface at any local region of the surface. Second, the algorithm does not compensate for noise or extraneous point data—the data is assumed to be part of the object and noise is assumed to be negligible. Thus, the algorithm would fail to produce useful results for the kind of input data as was used in our experiments in Chapter 2. The third problem is inefficiency of the algorithm. Estimating the tangent plane at each point and enforcing normal-direction consistency for all points makes their algorithm impractical for problems containing large numbers of data points as in our experiments described in Chapter 2.

Curless and Levoy [28] followed Hoppe's general scheme with a few significant departures. First, they triangulated the range-image data so that they use triangulated surfaces rather than points. Second, they do not perform a simple search for the closest point from a voxel's center to determine the signed distance. Instead, for each voxel, they take a weighted average of the signed distances from the voxel center to range-image points whose image rays intersect the voxel. This is accomplished by following the ray from the camera center to each range-image point and incrementing the sum of weighted, signed distances and the sum of weights for each voxel that the ray intersects using the signed-distance estimates from the voxel center to the given range-image point. This process is repeated for each point of each range image, and when completed, the weighted average of the signed distance can be computed for each voxel. To make this operation reasonably efficient, run-length encoding of the voxel grid is used and the voxels are only traversed around a specified range of distances from the observed surface. To accommodate for holes and missing data, empty (outside) and unseen (inside) voxels are marked with extremal values (of opposite sign) of the signed distance function. Surfaces will automatically be created between empty and unseen voxels during the isosurface extraction using the marching-cubes algorithm.

Curless and Levoy's signed distance integration scheme has two fundamental flaws for even perfect data. First, thin surfaces (i.e., the walls of the mug object from Section 2.5) may not be detected properly since their algorithm may integrate signed-distance estimates which correspond to surfaces with opposing normals. Figure 6.1 shows an example of a thin wall with two outward pointing surfaces. The graph of the signed distance contributions of each surface in the local area and their sum are shown as well. Since their sum is

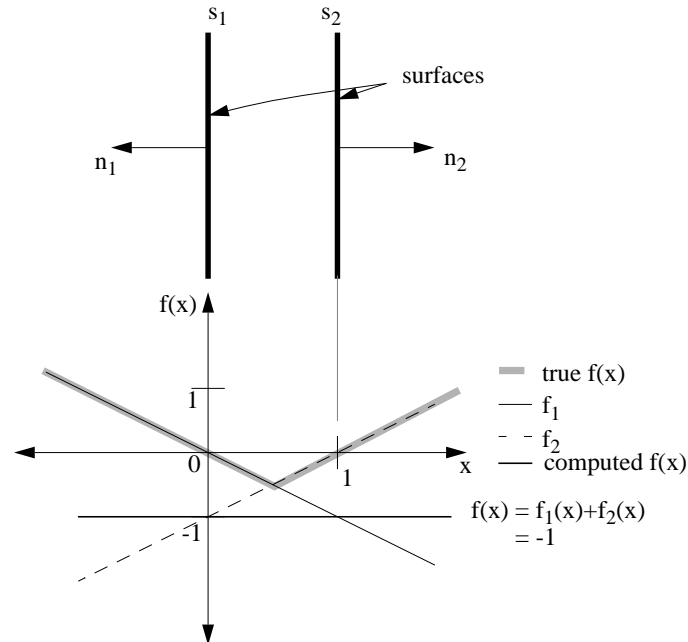


Figure 6.1: Illustration of the result of signed distance integration in the neighborhood of thin object parts. The object is a thin plate of width 1 unit with left side at $x = 0$. The graphs show the contribution of the signed distance to each surface as x varies. Their sum is -1 for all x —no zero contour exists. The true signed-distance function (in grey) shows the proper zero crossings for both surfaces of the object.

constant locally there is no zero contour created and no surface will be generated by the marching-cubes algorithm.

The second flaw in Curless and Levoy's integration scheme is that the signed-distance averages are biased. The magnitude of the averages will always be larger than the magnitude of the observed distance—even for perfect data. The bias is due to the fact that their integration method potentially uses more than one ray through each voxel corresponding to different range-image points. Only one such ray will be an unbiased estimate of the distance to the surface—the ray which is perpendicular to the surface. If a ray is not perpendicular to the closest surface point, the distance along the ray will necessarily be larger than the true distance to the surface. Figure 6.2 shows an example of 3 image rays, v_1, v_2 , and v_3 , which pass through a voxel. Only along v_2 (which is perpendicular to the surface) is an unbiased estimate of the signed distance available. Even more problematic is that the estimates used in the average may be estimates for the distance to some surface other than the closest surface. Figure 6.3 shows an example of 3 image rays, v_1, v_2 , and v_3 , which pass through a voxel. v_1 and v_2 are not perpendicular to the surface but at least intersect near the surface point closest to the voxel. v_3 is perpendicular to the object surface but not to the closest point on the surface. Thus, the signed distance estimates resulting from their integration method will be biased, resulting in inaccurate zero-crossing interpolation as described in Section 2.4.2.

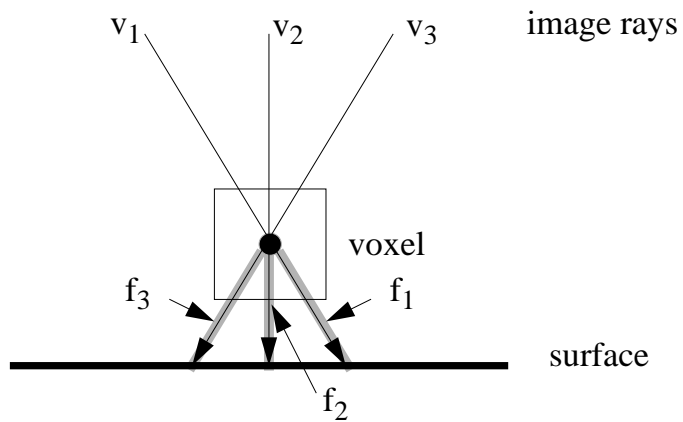


Figure 6.2: Illustration of estimating the distance to the surface along rays passing through a voxel. Of the three rays shown, only v_2 , which is perpendicular to the surface, provides an unbiased estimate.

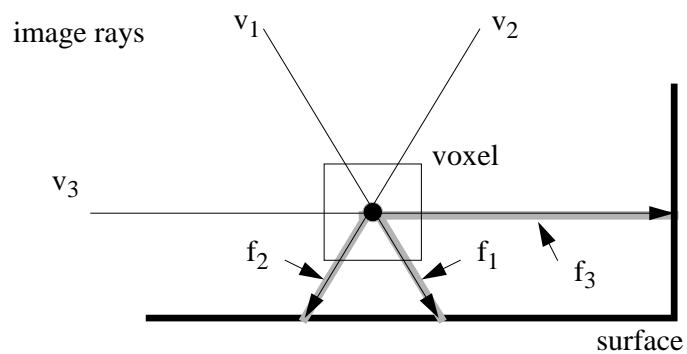


Figure 6.3: Illustration of estimating the distance to the surface along rays passing through a voxel. Of the three rays shown, only v_1 and v_2 are reasonably desirable for estimating the distance from the surface the given voxel.

Another drawback of Curless and Levoy's method is that it is still sensitive to noisy data and extraneous data. Though their averaging scheme may smooth some of the noise, the effects of large errors in the data cannot be overcome. Curless and Levoy's method is naturally incremental which is an advantage over our approach and Hoppe's approach. As for efficiency, it is unclear whether the use of octrees, as in our scheme, is more or less efficient than their run-length encoding scheme.

The method most similar to our work is that of Hilton et al. [64]. As in our work and Curless and Levoy's work, Hilton et al. generate a volumetric implicit-surface representation from a number of triangle sets (representing the observed surfaces of each range image). Similarly to our algorithm, Hilton's method uses a nearest-neighbor search to find the surface points from each view which are closest to a given voxel's center. For each view, the signed distance and surface normal of the closest surface point is added to a list. Basically, they then take the weighted average of all of these signed distances and use the average as the value of the implicit surface for the particular voxel. Their algorithm is slightly more complicated; heuristics are used to remove some of the undesirable points from this list. First, they do not use points which lie on the boundary of a view's triangle set unless all closest points (over all views) are also boundary points. Second, they use only those points in the list up to the point (if any) which has a normal direction opposite that of the closest point of the whole list.

The biggest problem with Hilton et al.'s method is that it assumes that there will be no large errors in the data as there is no provision for discounting or removing outliers. Even with perfect data, simple cases can easily be constructed which can result in arbitrarily large errors in their estimate. This can be done because their algorithm does not establish that the sample observations belong to the same surface. Their heuristics eliminate many incorrect points from being used to estimate the signed distance, however, the heuristics are not sufficient to eliminate many other incorrect points which could result in arbitrarily large errors in the signed distance function. The problem is that there is no guarantee that the signed distances, which they use to compute the weighted average, have any relation to each other (i.e., the signed distances used to compute the average will often be for different parts of an object surface). This is the point of our consensus-surface approach.

There have been several other approaches for creating surfaces from a number of range images. We now discuss some of these methods.

Soucy and Laurendre [129] and Turk and Levoy [138] presented methods for piecing together sets of triangulated surfaces. Soucy and Laurendre [129] presented a computationally intensive method which computed the Venn diagram for each pair of views ($O(2^n)$) and projected each overlapping pair to a 2D canonic view over which the views could be retriangulated and mapped back to three dimensions. Turk and Levoy's [138] "Zipper" algorithm merged pairs of triangle sets by eroding the overlapping regions and merging the sets along their remaining boundaries. Both methods perform poorly if the surfaces are slightly misaligned or if there is significant noise in the data. Typically, the resulting surfaces would have noticeable seams along the edges at which they were pieced together.

Boissanat [9] proposed an algorithm for computing the Delaunay triangulation of a set of 3D points. Rutishauser et al. [115] utilizes Boissanat's method to iteratively grow a mesh

from many triangle sets. Rutishauser et al.'s method extends the initial mesh by searching for a point nearby the boundary edge of the initial mesh and adding the triangle created by the edge and the point only if the new triangle does not overlap the current mesh. This is iteratively applied until the mesh cannot be extended anymore.

Higuchi, Delingette, Hebert and Ikeuchi [63] presented the simplex angle image (SAI) for representing 3D objects as attributes (simplex angles which are related to surface curvature) spread among the nodes of a tessellated sphere. Using their method, a sphere was mapped to the surface of the object by allowing the points on the sphere to deform to fit the range data for each view. Once fit, the simplex angle for each node on the tessellated sphere is computed. Through the SAI representation, each view could be matched via searching the space of 2D rotations of the sphere and merged by simply averaging their respective simplex angles. Shum [126] extended this work to improve the robustness by applying principal components analysis with missing data technique for simultaneously estimating the view rotation parameters and SAI parameters given several views of the object mapped to tessellated spheres.

Chen and Medioni [20] presented a similar method for fitting a mesh to sets of aligned range data. Their method involved inflating a balloon from within the object surface until it fit the extremities of the surface. Both the balloon and SAI methods are limited to modeling objects of spherical topology (genus 0) and have difficulty to accurately fit the high-curvature regions of the data while smoothing other noise in the data.

Chen and Medioni [19] presented techniques for registering and merging range images of an object. To merge the data, the range-data points were mapped to either a cylindrical or spherical coordinate system and overlapping values were averaged. Obviously, this produces a rather crude model (especially in areas of high curvature where the effects of discrete sampling will be quite noticeable) and the topology of objects which can be modeled is limited to those with a spherical topology.

Chien, Sim and Aggarwal [22] developed an algorithm for merging multiple range image views into an occupancy grid, represented using octrees. This built upon their previous work of constructing the 3D shape from intensity image silhouettes of the object [21]. The algorithm marked as empty those octants/voxels which were outside the silhouette of the object from each view. With a sufficient number of views, a reasonable approximation to the occupancy grid of the convex regions of the object could be obtained. The principal limitations of this method is its inability to eliminate voxels inside concavities of the object and the requirement for cleanly detecting silhouettes. Several other approaches have been presented for creating 3D models from occluding contours from intensity images, most notably those by Szeliski and Weiss [131], Seales and Faugeras [120], and Kutulakos, Seales and Dyer [80]. These techniques match the occluding contours over several views and infer 3D surface meshes from the correspondences.

There have also been several efforts in constructing higher-level symbolic model representations from range images. Bhanu's approach [8] utilizes multiple range image views of the object to build a 3-D planar surface description of the object. Parvin and Medioni [103] presented a technique for matching and merging range-image views using a boundary representation—a collection of quadric surface patches. Shum, Ikeuchi, and Reddy [127]

improved on this work by introducing the use of principal components analysis with missing data to simultaneously estimate the transformation between each view and the planar patch parameters of all observed patches. The variety of objects that can be modeled using the previous two techniques is limited by their simple shape representations. In addition, the reliability of the two techniques greatly depends on the quality of range-image segmentation [5] (into planar or quadric patches) and the ability to match (or track) these patches between views.

The above methods may only scratch the surface of proposed techniques for merging 3D image data to create surface models. In addition to these techniques, there are a number of techniques for computing shape from motion sequences; these include methods of [82, 135, 130, 124, 106] among others. Generally speaking, these techniques are limited to finding sparse shape (i.e., sparse sets of 3D points) from intensity images. Many of the above researchers have applied Boissanat's triangulation algorithm [9] to generate rather crude 3D shapes from the 3D points recovered in their experiments. Generally, the point sets available from such current techniques are much too sparse for application to 3D-3D localization, let alone accurate 3D object modeling.

6.2 3D-3D Object Localization

Many researchers have developed techniques to compute the location of the object given the correspondences between model and image features (pose estimation) or given a rough estimate of the object's location (localization or pose refinement). In this section, we will discuss the previous work on pose estimation and localization which is relevant to our work on 3D-3D localization.

The earliest research related to our 3D-3D localization work is the original work to solve the 3D-3D pose-estimation problem. As described in Section 3.4.1, the closed-form solution for the optimal pose given a set of point correspondences (assuming Gaussian noise) was first introduced by Sanso [116] in the photogrammetry field and then later in the computer-vision community by Faugeras and Hebert [36], Horn [66], and Arun et al. [1]. The first three solutions are essentially the same—making use of the quaternion to directly solve for rotation. Arun et al.'s [1] solution obtains the 3×3 rotation matrix directly using singular value decomposition. These results form the basis for much of the subsequent work on 3D-3D pose estimation and pose refinement in the computer-vision community.

The most closely related work to our 3D-3D localization work is that focusing on shape registration and tracking of 3D objects in 3D data.

Besl and McKay [6] presented the first general method for registering two sets of rigid, free-form data (e.g., triangles or point sets). Their method, the iterative closest-point (ICP) algorithm, iteratively computes nearest-neighbor correspondences between points on the model surface and points in the image data. They then compute the optimal, least-squares solution of the pose with respect to these correspondences and update the pose to this solution. The process is repeated until convergence to a solution is achieved. The main weaknesses of this method is its susceptibility to outliers: even a small number of missing

data will corrupt ICP's solution. As demonstrated by the results of Chapter 3, ICP has a much narrower convergence range when compared to our 3D-3D localization (even after applying outlier thresholding). This is due to ICP's reliance on the closed-form solution for pose which is used for each pose improvement step. When the pose error is large, the optimal pose with respect to the available correspondences is not always an improvement with respect to the object's true pose.

We are not the first to propose robust solutions to the pose-estimation or localization problems. Typically, computer-vision algorithms are made robust by outlier thresholding: removing samples with especially large errors from the set of data used for estimation. While this is a reasonable and easily justified operation for some cases, more often it is a source of problems—resulting in errors due to improper or unjustified threshold selection.

A relevant example of the use of outlier thresholding is the work by Zhang [151]. Zhang presented an improvement in the ICP algorithm to reduce the outlier sensitivity of ICP. He proposed a method for dynamic threshold selection to remove outliers. His improvement does little to extend the convergence range of ICP as demonstrated in the results of Section 3.6¹. However, his method for outlier thresholding does reduce the outlier sensitivity of ICP when the initial pose error is small enough. With Zhang's enhancement, ICP is applicable when portions of the model are not observed in the image data (i.e., in cases of partial occlusion of the object or partially overlapping data sets).

As described in Section 3.4.2, there are a number of other methods for robust estimation [67]. These have been applied to a limited number of computer-vision problems. Haralick et al. [58] proposed and analyzed the use of M-estimators for robust pose estimation. They performed experiments to test the convergence ability of their algorithm with respect to the number of outliers and the level of noise in the data. In their work, they dealt with the pose-estimation problem and not the pose-refinement/localization problem; that is they considered the problem of finding the pose given a fixed set of correspondences between two sets of points. Their algorithm used iteratively reweighted least-squares estimation; down-weighting M-estimators (such as those described in Section 3.4.2) were used as the weight functions. In their experiments, they demonstrated that the pose estimate could be accurately achieved despite high noise levels as long as a sufficiently large (e.g., 40) set of point correspondences were available. In an earlier paper, Haralick and Joo [57] show that their algorithm for 3D-2D pose estimation (using iteratively reweighted least squares as described above) reliably converged to the correct solution in spite of up to 30% of the correspondences being incorrect. In [58], Haralick et al. did not discuss their 3D-3D pose-estimation algorithm's sensitivity to outliers. We believe that this is due to the fact that the closed-form, weighted-least-squares solution—necessary for their algorithm as in ICP—is not valid when facing even a small number of outliers despite down-weighting.

Perhaps the first (explicitly) robust computer-vision algorithm was the random sample consensus (RANSAC) method of Fischler and Bolles [38]. The specific problem they addressed with RANSAC was the 3D-2D location determination problem for finding the

¹The outlier thresholding method used in our experiments was not exactly the same as described by Zhang [151]. In our experiments, the threshold was gradually lowered as the iterations proceeded which is roughly equivalent to his method.

pose of a set of 3D points with respect to a perspective projection of the points. Essentially, the location determination problem is the general object recognition problem where objects are collections of 3D points. The basic idea of RANSAC is to use the smallest possible subset of the observed data points to get an initial estimate of the model's pose parameters. The initial estimate of the parameters is then used to look for other data points whose error with respect to the transformed model points is small enough. These data points are termed the consensus set (in much the same way we use the concept of consensus surfaces and edgels in Chapters 2 and 4). If the consensus set is large enough, the solution is refined by re-estimating (using least-squares estimation) the parameters using all the data in the consensus set. This idea is much different than trying to directly estimate the parameters using all the observed data.

The RANSAC algorithm is applicable to other regression (model fitting) problems as well. A simple example of RANSAC is fitting a line to a set of observed point data when many of the observed points do not belong to the desired line. Instead of performing least-squares line fitting to all the data, RANSAC first chooses two data points (using random selection), computes the line parameters, and finds the consensus set of points which lie near the computed line. If the consensus set is large enough, RANSAC would then perform least-squares line fitting on the consensus set; otherwise, RANSAC would select another pair of points and repeat the process.

For fitting a line to a set of points, RANSAC works quite well: one only needs two observations which belong to the line to make the initial estimate. For general pose estimation, the combinatorics are much less favorable: many combinations of correspondences will need to be tested before a correct combination may be found. RANSAC is fundamentally the same algorithm as Huttenlocher and Ullman's [70] alignment algorithm for object recognition which will be described later in Section 6.5. Without going into detail, the difference between the two is the amount of prior knowledge used to determine the initial correspondences. RANSAC uses random selection, while the alignment algorithm searches serially through the set of possible correspondences (using depth-first search) and applies prior constraints to limit the number of combinations of correspondences which must be evaluated.

Meer, Mintz and Rosenfeld [96] provide a review of robust statistical methods and their application to several computer-vision regression problems. They also describe in detail the least-median-of-squares method (LMedS) and its application to image filtering. Another application of the LMedS technique is Kumar and Hanson's [79] work on 3D-2D pose estimation based on line-segment correspondences. While the LMedS algorithm can handle up to 50% outliers in the data, it is very computationally expensive because, fundamentally, it must test every combination of correspondences. The practical implementation of LMedS leads to an algorithm which is very similar to the RANSAC algorithm. For object localization, we would like to avoid the expensive combinatoric search as performed by robust algorithms such as RANSAC and LMedS.

6.3 Object Modeling for 3D-2D Localization

As mentioned in Chapter 4, the representation of 3D objects for recognition and localization in 2D images is a topic of great debate: 3D representations versus 2D (view-based) representations.

While there is no work of which we are aware that automatically creates 3D edgel models, as demonstrated in Chapter 4, the closest related work is the semi-automatic approach of Clemens [25]. Most work on 3D-2D recognition/localization using 3D edge models derives these edgel models from (manually generated) CAD models.

In contrast, most view-based approaches easily utilize real images to construct their models. There is a great deal of recent research on view-based approaches. Thus, we will mostly discuss view-based approaches to recognition and localization including the following approaches:

- Interpolating view-based: work by Ullman and Basri [139], Wells [142], Shashua [124], and Chen and Stockman [17].
- Pure view-based: work by Breuel [13], Murase and Nayar [99], and Huttenlocher, Lilien and Olson [69].
- Characteristic views: work by Connell and Brady [26], Gros [54], and Pope [110]

6.3.1 Interpolating View-based Representations

Ullman and Basri [139] made the interesting observation that under orthographic projection a view of a set of rigid 3D points can be constructed from a linear combination of two or more (appropriately chosen) orthographic views (LCV) of those 3D points. The requirement is that the correspondence between the points in the two original views is known. For general rotation in 3D space, 3 nearby views are necessary to span the space of views. Using this idea, it is possible to represent the space of 2D orthographic views as a set of samples over the viewing sphere. The correspondences between points in every pair of neighboring views must be determined. They also showed that occluding contours can be roughly approximated by adding 2 more views. To account for translation of the object in the image, another view is required: making a total of 6 views for smooth objects with arbitrary rotation and translation. They demonstrated LCV using a few examples of linear combinations of edge images of cars. One serious problem with the LCV approach is that it is restricted to orthography which is not a realistic model for many real world cameras.

Wells [142] presented methods for probabilistic object localization which utilized LCV models of the objects. As in our work, Wells used image edgels as the primary feature for matching. Models were represented using the LCV method with correspondences between edgels of multiple views of the object. He made one improvement over Ullman and Basri's method; for each view, Wells used a mean-edge image rather than a single edge image of the object. The mean-edge image is an average of several views of the object with varied illumination. Thus, only stable edgels (edgels apparent under several light source

conditions) are included in the model. For LCV, manual correspondences were made between the edgels of pairs of neighboring images. Chen and Stockman [17] also used the LCV model representation for localizing 3D objects in 2D images.

Shashua [124] presented two interesting extensions of the LCV idea of Ullman and Basri [139]. First, he proposed a method for computing projective structure from a pair of images. The notable improvement is that the reprojection of points is valid for both orthographic and central projection (generalization of perspective). Shashua's method for projective structure from two images requires the computation of the epipoles for both images and must be given 8 point correspondences between the two images. With 8 point correspondences from a novel view to one of the original views, the epipoles and two reference planes can be computed and used to compute two planar projections of each point. Combining these two projections with the original image projection and the cross-ratio of the point (computed from the original pair of images), we can reproject any point from the original views into the new view. The projection of the point in the new image is then determined by solving for the ray which produces the same cross-ratio.

Computing projective structure and reprojecting novel views depends on accurately computing the epipoles and reference planes so that the cross-ratio can be accurately determined. In general, the point locations in each image will have some error, and each level of computation will accumulate some error and result in rather inaccurate estimates for the reprojected views. Shashua does not consider occluding contour boundaries as in [139], and it would be particularly difficult using the cross-ratio to define the projective structure due to the noise sensitivity of the cross-ratio.

Shashua's second extension to LCV was to demonstrate that illumination factors could be modeled via an LCV method using three or more images of an object taken under varying illumination. The basic idea is that if one has a set of images of an object (assumed to have Lambertian reflectance) at a given position under various light sources, that any image of the object in the same position is a linear combination of the original views. Thus, the model can be compared to the image while accounting for the illumination conditions of the image. Shashua's insight into photometric alignment is interesting, as compensation for illumination variations would provide much greater reliability for a verification operation.

It remains to be seen if the photometric alignment method can be extended to a more general framework; otherwise, it may only be of theoretical interest. It suffers from the requirement that several images (one for each different illumination condition) must be stored in the model and that only a small variety of lighting variations can be practically accommodated. The restriction to convex, Lambertian surfaces greatly reduces the generality of the method. We believe that a 3D model-based approach has more potential in the long run. In other words, a model of the surface reflectance parameters can be built using the techniques of Sato and Ikeuchi [118] and this model can be used to more accurately and generally predict the image intensities. This is discussed in more detail in Section 7.2.

Shashua also proposed a method for automatically computing full correspondences using optical flow combined with geometric alignment. The correspondence problem is a long-standing problem in stereo vision and shape-from-motion. His method is based on a combination of affine structure from two views and optical flow constraints. For accurate

optical flow, the motion between views must be extremely small. Shashua proposes to bootstrap the correspondence by taking views in between the model views. This will not always be successful as features disappear and appear between views and errors will accumulate as the matching progresses across views. Because of the aperture problem, many edges will just not be trackable between images—this is an unfortunate fact. In his thesis, Wells [142] reported that he experimented with Shashua's correspondence algorithm to construct LCV models for testing his system; however, Wells used manually selected correspondences for his experimental work.

Computing the full correspondence of points between two views is a very difficult problem. This is not a practical requirement using present techniques and is not possible in general. Correspondences do not exist across aspect changes [77, 12] for example, and correspondences of occluding contours between two views is not always justified except possibly at high curvature points. The aperture problem, a common problem of stereo vision [53, 101, 74], is a problem here as well as it limits the number of correspondences which may be determined in practice. How many views will be necessary in practice? This is a difficult question. The answer depends on the number of free parameters to be considered. In general, one should expect a very large number of samples to model a single object for only 2 degrees of freedom. A related question, how close together must the views be to make the correspondences and so that new views are accurately interpolated from a local set of views? In stereo, a related problem for stereo vision is the choice of width for the baseline [101]: the wider baselines provide better measures of geometry but less accurate correspondences.

Another issue related to the interpolating view-based approximations [139, 142, 124] is how to sample objects over the viewing sphere such that neighboring views are connected. It is a simple case to vary 1 degree of freedom and determine the neighborhood relation between views; this can be done by taking a continuous image sequence while the camera or object moves. However, extending this to two dimensions is non-trivial and will usually require some calibrated positioning device or user input to organize the mesh of images. Extending the idea to more than two degrees of freedom would be nearly impossible.

A problem of both LCV and projective-structure methods is that rigid 3D transformations are only a small subset of the linear operations. It is much more likely for an alignment search using LCV or projective structure to produce a non-rigid transformation than a rigid transformation.

6.3.2 Pure View-based Representations

Another class of view-based approaches is in some sense the simplest approach: the pure view-based approaches. The model of an object is simply a set of views of the object. Recognition is then reduced to 2D-2D matching of image features or correlation of pixel intensities between a model and input image. We will discuss the pure view-based work by Breuel [13], Murase and Nayar [99], Huttenlocher, Lilien and Olson [69] as well as the related neural-network techniques for pattern matching [97, 108, 114].

Breuel [13] argues that 3D models are not necessary and that interpolating view-based approaches (e.g., LCV)² are unnecessary as well. He argues that the view space of a 3D object is a 2D manifold and that under bounded-error assumption, a sufficient number of views can be sampled to cover this manifold within the error tolerance. If one agrees with his assertion, then all recognition reduces to 2D-2D recognition and a simple algorithm such as RAST [13] may solve the problem. Unfortunately, Breuel's argument is only valid if orthographic projection is assumed.

Murase and Nayar [99] introduced the eigenspace representation for image sets. Using their method, the object is represented by a large number of intensity images. Eigenspace analysis is used to reduce the images to points in a low-dimensional subspace (the principal components of the eigenspace). Image matching can then be efficiently performed in the subspace.

Huttenlocher, Lilien and Olson [69] used the eigenspace method to represent binary edgel images of the object. The binary edgels are more stable than intensities with respect to illumination variations. They cleverly showed that the correlation in the subspace is approximately the same as a Hausdorff distance [68] which makes it robust to partial occlusion as well.

Another group of pure view-based techniques is the use of artificial neural networks to solve pattern matching problems [97, 108, 114]. The networks learn a functional mapping between images and the object/view identification—similar to image correlation and pattern recognition.

The neural network and eigenspace techniques are essentially an efficient form of image correlation and suffer from the problems encountered when using correlation for pattern matching. Unlike pure correlation, both groups of techniques can be used to generalize over several views, however, generalization can also negatively effect performance. Localization and verification is not possible in this framework since there is no real concept of a model, just images of the object. However, these methods show promise for solving the indexing problem.

Related to Breuel's approach [13] is 2D-2D recognition (i.e., the object is two dimensional). Grimson [49] extended the interpretation-tree constraints of [52] to use circular arc features in addition to linear intensity edges. This system recognized 2D objects using 2D intensity edges extracted from grey-level images. To build the models for his system, Grimson used the edge features extracted from a single image of the object in isolation—these features completely define the model for recognition purposes.

6.3.3 Characteristic-view Representations

The final view-based approach which we will discuss is the characteristic-view approach. The general idea of the characteristic-view approach is to represent a 3D object by a small

²While LCV is not strictly a 3D technique, the 3D information is implicit in the correspondences between the 2D views. This is a subtle but important difference between the methods of Breuel [13] and Ullman and Basri [139]. If the model is only a 2D sample view (as in Breuel's case), recognition is strictly 2D-2D.

set of models of similar views. The model is in some sense a characteristic view (or average view) of the set of views it represents. Connell and Brady [26], Gros [54], and Pope [110] have proposed various methods to automatically reduce many sample images to a small set of characteristic-view models which can then be used to recognize the object.

Connell and Brady [26] represent an object's edge contours from a given view as symbolic graph relating the various parts and regions of the contour. Attributes of parts/regions of the graph are represented by symbols attached to the graph. Models are created by merging similar graph structures. Similarity between two graphs is basically measured by the number of common nodes between the two.

Gros [54] uses a low-level definition of similarity between two views and uses a bottom-up, best-first, clustering algorithm to group the example views into a small set of characteristic views. Gros' image similarity metric is based on the percentage of image features which are matched between the two images. The matching of features (line segments) between images is performed via a combination of alignment search and Hough transforms over the space of similarity transforms. Given the estimated transform the matches are then improved by estimating a projective transform which best aligns the current matches. For each characteristic view, a model is created as the average of the matches over all images in the given cluster. As can be imagined, inconsistencies must be detected as the pair-wise matchings are not always transitively related. In addition, many features may appear and disappear between images.

Pope [110] presented an approach which lies somewhere between the purely symbolic approach of Connell and Brady [26] and the low-level approach of Gros [54]. Pope represents views as an attributed graph of several types of features (including line segments, arcs, junctions and ribbons). Each feature and their relation are quantified by attributes as probabilistic distributions such as the distribution of position variation, probability of detection, or probability of specific attribute values. As in Gros' method [54], Pope uses similarity transforms to map views into the same coordinate system for creating an aspect model. Pope uses a minimum-description-length measure to cluster views into an aspect model. The clustering algorithm adds each image to the cluster which will make best increase the quality measure which is specified to favor simplicity and accuracy of the resulting models. For recognition, a Bayesian probability measure is used to specify the relative quality of a matching between model and image features. A probabilistic alignment scheme is used to iteratively update the pose estimate (2D similarity transform) for the model.

The characteristic-view approach is more directed towards the indexing problem and, thus, it is best suited for that problem. Localization techniques such as those presented in this thesis can be applied once the object is indexed and a few matches to higher-level features (such as those used by Pope [110] and Gros [54]) are available. Characteristic-view models constructed using the previous techniques may or may not be very representative of any of the given views; the characteristic view may over-generalize the sample views such that the original views are not accurately represented. Gros' use of line segments as the primitive feature greatly restricts the reliability and class of objects which can be modeled using his method. Curved objects cannot be reliably modeled using such a representation

since the linear segmentation of a curve will differ between any pair of images. While Pope's features can represent a wide variety of shapes, the accuracy and stability of the representation can be a problem. Detection of these features can be unreliable as well, such method's rely on redundancy of representation. There is no real mapping between the model coordinate system and the object, localization and tracking is not possible. In fact, the general definition of characteristic views as purely similar views makes it is possible for non-neighboring views to be clustered together in a model.

6.3.4 3D Representations

The only effort towards building 3D edge models from real images is the work by Clemens [25]. He developed an interface for manually building polyhedral object models from multiple views of the object. The user labels the extracted edges and vertices from each image to establish the correspondences. The 3D positions of the features are computed by solving the system of simultaneous equations. This method is in some sense a hybrid between our modeling approach and the LCV approach. With LCV, the 3D information is implicitly encoded in the correspondences.

While the view-based approaches of Ullman and Basri [139], Breuel [13] and Shashua [124] offer an interesting alternative, they have fundamental problems and practical limitations which makes it premature to dismiss 3D model representations. 3D information is often desirable, if not necessary, for interacting and measuring the real world. Working with 3D models, transformations are simply and naturally constrained to be rigid transformations. 3D models can also be easily applied to any type of camera model and, possibly, any type of illumination condition (assuming the illumination is known or can be estimated). View-based methods do not interact well with perspective projection. This is because these methods invariably assume that the view-space is two dimensional. While this assumption is perfectly reasonable for orthographic projection, it does not work with perspective projection. Once the view space increases beyond two dimensions, the number of images needed to model an object grows by an order of magnitude. This is all without considering the other potential image variations on the dimension of the view space. 3D models are naturally concise; for view-based methods, storage requirements can quickly exhaust resources.

The pluses of view-based methods include fast 2D-2D matching/recognition and their conceptual simplicity (e.g., a model is a collection of images). The lack of reliance on camera calibration is also a benefit of view-based methods.

Our work in Section 3.2 and 5.2 showed that the object's geometry is necessary to accurately approximate and predict the visibility constraints for points on an object. In the view-based approaches described previously, visibility is simply defined as what is detectable the current view—the feature may or may not have been detected depending on lighting, shadows and any other number of factors.

The requirement for calibration is one detraction for using 3D representations, however, much of the work on affine/projective structure from weakly calibrated views (i.e.,

epipoles are computed/known) [34, 60, 124, 112] can be applied towards Euclidean camera calibration with a little work and some additional assumptions [31].

6.4 3D-2D Object Localization

As in the 3D-3D case, several researchers have developed techniques to compute the location of the object given the correspondences between model and image features (pose estimation) or given a rough estimate of the object's location (localization or pose refinement). In this section, we will discuss the previous work on pose estimation, tracking and localization which is relevant to our work on 3D-2D localization. A good starting point for this discussion is the problem of 3D-2D pose estimation.

The problem of finding the pose of a 3D object from a 2D projection was solved as early as 1841 by Grunert [55] who solved the 3-point perspective problem. The 3-point perspective problem is the simplest form of 3D-2D pose estimation and involves finding the pose of 3 model points when matched to 3, perspective projections of the points³. Grunert's solution was later refined and new solutions were proposed independently throughout the 1900's. Haralick et al. [59] presented a historical overview and quantitative comparison of the major solutions to the 3-point perspective problem. The solution of Finsterwalder [37] was found to give the best accuracy.

The first solution of the 3D-2D pose-estimation problem that was presented in the computer-vision community was by Fischler and Bolles [38]. Other solutions have been proposed by Horn [66], Faugeras and Toscani [35], Phong et al. [105] and Haralick et al. [58]. Many of these solutions use more than 3 points and perform an iterative least-squares estimation of the pose rather than a closed form as in the solutions to the 3-point perspective problem. Shakunaga [123] and Dhome et al. [32] presented closed-form solutions to enumerate the poses from 3D line-segment to 2D line-segment matches.

Haralick et al. [57, 58] investigated the use of robust weight functions with weighted least-squares estimation for point-based, 3D-2D pose estimation. They analyzed the convergence of their pose-estimation algorithm with respect to various levels of noise and outliers. Haralick and Joo [57] show that their algorithm for 3D-2D pose estimation reliably converged to the correct solution in spite of up to 30% of the correspondences being incorrect. As in our 3D-2D localization algorithm, Haralick et al. also used the 3D interpretation of errors rather than 2D image errors.

Gennery [44] and Lowe [81] have presented approaches to localization/tracking of 3D polyhedral models in intensity images. Gennery [44] presented an algorithm for tracking 3D objects in 2D image sequences. He uses a 3D polyhedron as the object model. On each iteration of the pose refinement step, the visible edges of the polyhedron are projected into the image. Points along each edge are sampled and matched to local intensity edgels in the image. The pose update rule uses a variant of Kalman filtering to iteratively estimate the 6 rigid body degrees of freedom along with 7 velocity components (3 translational and 4

³Three points are the minimal number of points needed to determine a finite number of poses for 3D-2D pose estimation. In general, 4 solutions exist for the 3 point case.

rotational). Gennery also proposed (but did not demonstrate) the integration of images from multiple cameras in the tracking scheme as we have shown for our localization algorithm in Section 5.6.

Lowe [85, 86, 87, 89, 84, 90] has presented techniques for recognizing, localizing and tracking 3D objects in intensity images. His methods model objects as collections of line segments and arcs. His tracking and localization work uses best first search of model to image matches using prior probability models to order the search. At each step of the search, he computes least-squares fitting of the matched model segments to the image segments. Lowe's method minimizes the least-squared error using a technique based on Newton-Raphson root-finding (linearization) and Levenberg-Marquardt minimization to iteratively compute the model parameters with respect to the image error of the projected model. His technique attempts to achieve robustness via correspondence search as in RANSAC [38] rather than using statistical methods such as robust M-estimators as in [58]. The search can escape from local minima by backtracking; however, incorrect correspondences made early in the search will be costly to recover from. In addition, the representation of objects as collections of arcs and line segments limits the variety of objects to which his method may be applied. Chen and Stockman [17] present a hybrid of Lowe's pose-estimation algorithm [81] (using Newton's method and Levenberg-Marquardt minimization) and LCV model representation [139]. They demonstrate reasonable convergence results for small initial pose errors for some simple shapes and images containing no background edges.

Wells [142] presented two view-based methods for probabilistic object localization⁴ of 3D objects in 2D intensity images. Wells first presented the MAP (maximum a posteriori) model matching approach which formulated the objective function as a function over both pose and correspondence space. He showed that the search of correspondence space could be equivalently performed as a search through pose space using nearest neighbors to determine the best correspondences with respect to pose. Wells then went on to show a localization algorithm which did not utilize correspondences at all. Instead, the error of a model edgel is a sum of a non-linear function over all possible correspondences (all edgels in the image). Interestingly, Wells showed that in its simplest form, minimizing the objective function is similar to maximum-likelihood estimation assuming Gaussian distributed errors with uniformly distributed background noise. This is closely related to robust M-estimation using the Tukey or Sigmoid weight functions as described in Section 3.4.2. Wells also presented a first attempt at multi-resolution localization, using low-resolution models and smoothed image data for coarse scale localization. Wells' method is prone to more local minima than our 3D-2D localization algorithm since the model features will simply be pulled towards the nearest image edgel. To avoid this, we utilize attributed correspondence to efficiently improve the quality of match. As it is presented, Wells' method is also likely to be very expensive to compute since it compares all image edgels to each model edgel when evaluating the objective function. This limitation could possibly be removed by performing some cutoff of the evaluation with respect to distance from the model edgel.

⁴Wells' [142] work, though presented in the context of solving the recognition problem, is more appropriately classified as localization since the indexing contribution was not a major focus of the work. Initial alignments were provided using standard techniques of alignment search [70].

Few approaches have explicitly used the occluding contours of smooth surfaces to localize an object. Wells [142] and Chen and Stockman [17] have applied Ullman and Basri's LCV approach [139]. Lowe [81] has approximated smooth objects as polyhedra with some success. Another approach to modeling occluding contours is that of Ponce and Kriegman [77] who represent the surface of the object using an algebraic polynomial, and then analytically solve for occluding contours. Ponce and Kriegman algebraically solve for the contours using implicit surface equations and constraints for perspective projection of contours. The problem is that these algebraic equations can become very large even for simple shapes. They formulate localization as finding the root of a set of simultaneous algebraic equations relating the shape of the object, its pose, constraints on contour generation, and the detected edgel points in the image. This formulation requires that all contour points in the image be identified as belonging to the object's occluding boundary—a very impractical assumption. Localization based on their method is impractical in all except trivial cases. Algebraic representations of occluding contours are also difficult to build. In practice, objects will have to be modelled using several algebraic surface pieces. Inferring the algebraic representation from a triangulated surface is an extremely difficult problem—fundamentally the same as range image surface segmentation, for which no completely satisfactory solution exists. Even if segmentation were solved, the boundaries between surfaces and greatly complicates the solution of the algebraic surfaces.

Even fewer approaches have attempted to use intensities for 3D-2D localization (not considering pure view-based or correlation methods). Viola [140] accomplishes this using mutual information to align 3D objects in 2D intensity images. For 3D-2D localization, Viola exploits the implicit functional relationship between surface normals and intensity. This is achieved by maximizing mutual information which minimizes the joint entropy (randomness) of two functions. The method, as presented, is only applicable for Lambertian surfaces with (mostly) uniform surface properties. To minimize the joint entropy, a stochastic gradient-descent algorithm is employed. Since random samples are used to estimate distributions, the algorithm can be made efficient by using small numbers of samples. In addition, randomization allows the search to escape from local minima which are many since the gradient information will be very noisy and often uninformative (i.e., pointing in the wrong direction, since the gradient is evaluated locally based on incorrect model to pixel correspondences). Viola's algorithm takes on the order of 1000 iterations to converge.

Our work on 3D-2D localization is unique in many respects. First it uses a general representation of edgel generators in three dimensions—allowing smooth appearance prediction of object edges over arbitrary views and camera models. The point-based representation can efficiently accommodate a wide variety of shapes at arbitrary resolution and accuracy. Our use of attributed correspondence makes gives our method wider convergence ranges than other methods. Our work is the only one we are aware of that addresses the visibility issue for iterative localization methods. Previous work uses simple visibility bitmaps or aspects over the 2D view sphere (assuming orthography) [47, 85, 86, 148], uses brute-force z-buffering [140], or assumes a simple geometric form of the objects [44]. Our method is specifically designed to be robust to outliers. It makes use of the robust M-estimation machinery used in our 3D-3D localization algorithm via the straightforward interpretation

of errors in three dimensions rather than as image errors.

6.5 Object Recognition

Now we will briefly describe some of the important work on object recognition which motivates much of the work in this thesis.

Presently, the most prominent recognition paradigm is the interpretation tree (IT) search made famous by Grimson and Lozano-Perez [52]. The idea of IT search is to explore the combinations of matches between image features and model features. These combinations effectively form a tree of labelings where each path from a leaf to the root represents an interpretation. The basic algorithm, searching all paths, is exponential in the number of image features. Several researchers [47, 11, 36, 85, 39] have observed that at a certain level in the IT, the pose of the object can be computed. The idea is to first find a sufficient set of matches to determine the pose and then to use the rigidity constraint to efficiently determine the other correspondences. The result is a recognition algorithm that is polynomial in the number of image features. Its simplest form is the best known as *alignment* [38, 70].

The alignment algorithm searches for minimal sets of matches between image and object features to align a 3D object to a 2D image. It is essentially solving a linear system of n unknowns (the pose) using n equations (the constraints from the correspondences). Since there is uncertainty and noise in the measurements, the estimate of the n unknowns will be noisy as well. Thus, some form of pose refinement/localization is necessary to complete the search to enable accurate verification of the result.

Several other researchers independently developed IT/Alignment algorithms. The general goal of these algorithms is to minimize search by applying prior knowledge to prune and order the search. If the first few selected matches are correct, IT/Alignment algorithms can be very efficient. Goad's approach [47] was a precursor for many as it performed alignment with bounds on search for subsequent levels based on knowledge of the pose at a given stage of the search. He also introduced concept of detectability for ordering the search. The 3DPO system of Bolles and Horaud [11] started with the most obvious possible match and grows the matches by searching for feature matches that will add the most information to the current interpretation, thereby reducing the degrees of freedom in the interpretation. Similarly, Faugeras and Hebert [36] used the rigidity constraint to select subsequent matches in the IT—performing recognition and localization simultaneously. Grimson and Lozano-Perez [52] explored the use of geometric constraints to prune the search. Ikeuchi [71] presented a technique for precompiling the order of comparisons of an interpretation tree. Flynn and Jain [39] used heuristic knowledge of the model database to order and prune the tree for efficient search.

Using probabilistic evidence (perceptual grouping) to order the IT search was introduced by Lowe [85]. Camps, Haralick and Shapiro [15] took the approach of using probabilistic evidence to cutoff or prune the IT. IT search is a conservative approach since it considers all possibilities. This is both a strength and weakness; it is robust at the expense of efficiency.

One of the oldest object recognition paradigms frames the labeling problem in terms of constraint satisfaction networks (CSN). Typically, each node in the CSN represents an image feature and its label represents its matching model feature. An energy function that accounts for the model constraints is specified over the CSN such that the best labeling of the image features produces the minimum energy value. Optimization techniques are then applied to solve for the minimum energy state of the CSN. Bhanu [8] used relaxation labeling to determine the labeling of image regions to model regions that is most consistent with the 3D model. Bolle, Califano, and Kjeldsen [10] described a paradigm for recognition which uses networks of constraints between each level of representation from extracted image features to object hypotheses. Cooper [27] modeled object and image primitives in a Markov random field (MRF) and used optimization to find good interpretations of the scene. Wells [142] formulated the object recognition problem as a maximum a posteriori (MAP) estimation problem over the correspondence and pose spaces. Ben-Arie [3] used relaxation techniques with statistical constraints on interpretations. Wheeler and Ikeuchi [148] introduced a recognition approach based on the ideas of alignment and probabilistic constraint satisfaction. Constraint satisfaction search ventures that the labeling metric can correctly distinguish the correct from incorrect labelings—sacrificing robustness for efficiency.

Image feature formation depends on the sensor (quantization, digitization, and noise), the scene environment (lighting and background), the feature-extraction algorithm (biases and thresholds), as well as the object (geometry and photometric properties)—a complete model should account for these effects. Ikeuchi and Kanade [72] were the first to recognize this problem. They utilized a model of the sensor (in addition to the geometric object model) to compute the detectability of features for recognition and the reliability (predicted variance) of feature values with respect to the sensor. Sato et al. [117] developed a system to recognize objects using specular reflections as the basic feature. The use of specular features necessitated the use of a sensor simulator to predict the appearance of specular features. Camps et al. [15] also recognized this problem and devised an analytical model of the feature formation process. Camps samples the predicted features to compute statistics on feature attributes and relations. These statistics are used to define a probabilistic match cost function. The cost function is used to prune the combinatorial search for the least cost interpretation of the image features. The three previously described algorithms [72, 15, 117] all assume that the object features are segmented from background features—this is a very limiting assumption. Wheeler and Ikeuchi [148] used a ray-tracing simulation of the entire sensing process to derive recognition constraints from a CAD model of the object. One finding of that work was the need to increase accuracy of constraints by eliminating the approximations of the CAD model and sensor simulator. The approximations can be eliminated using the techniques described in this thesis as described in Section 7.2.

Verification remains one of the main roadblocks to accurate recognition. Typically, the approaches described previously use a simple form of verification: a threshold on the percentage of matched features. This statistic will often fail to answer the verification question correctly. Grimson and Huttenlocher [50] studied the verification problem with respect to 2D-2D recognition of point sets. They presented a formula for the optimal

threshold on the percentage of matches. This threshold is a function of model size and image clutter and the image noise. Grimson, Huttenlocher and Alter [51] later analyzed the error bounds on 3D points after minimal alignment in 2D images. They showed that the uncertainty regions for the reprojections of other object points can be quite large, making accurate verification extremely difficult. This is the main motivation for utilizing a localization search for recognition. In general, the alignment of a model in an image will be inaccurate using any of the efficient strategies for indexing. Breuel [13] makes interesting observations with respect to verification and suggests a second-order verification metric to account for spatial of missing data such as by occlusion, shadows, or undetected edges. This idea was applied by Wheeler and Ikeuchi [148] in a 3D-3D recognition system with much improved results over the simple first-order statistic.

This ends our discussion of related work. In the next section, we offer our conclusions, the contributions of this thesis, and present some ideas for future research which will build on our work.

Chapter 7

Conclusions

In this thesis, we have presented new algorithms for:

- 3D object modeling: automatically constructing 3D surface models of an object from a set of range images of the object
- 3D-3D localization: localizing a 3D object in a range image of the object given a rough estimate of its pose in the image
- 3D edgel modeling: automatically constructing a model of edgel generators on the object surface from a set of intensity images of the object and a surface model of the object
- 3D-2D localization: localizing a 3D object in an intensity image of the object given a rough estimate of its pose in the image

Our experimental results demonstrate that our modeling algorithms can extract clean models from rather noisy data, and that these models can be efficiently and effectively used for localization tasks. Our 3D-3D localization results show that our algorithm has much better convergence ability than Besl and McKay's ICP [6] for rather large initial pose errors. Our 3D-2D localization results show that we can indeed localize a wide variety of objects using a collection of edgel generators as the basic model representation. The results show that occluding contours of objects be effectively and efficiently utilized for 3D-2D localization within the edgel generator framework.

We would like to highlight some of the conclusions which we can take away from this thesis.

Consensus Works

For both modeling and localization, consensus is the key to make sense of the noisy data available from real sensors. When modeling objects from many images containing even small amounts of spurious data, one must take care when adding a feature (surface point or

edgel) to the model. In particular, features observed only once or relatively few times are often spurious. Model building algorithms must utilize redundancy from many views in order to avoid the pitfalls inherent in real data.

In localization, consensus is also the reason for our algorithms ability to convergence from large pose errors in noisy images. In general, if there is a significant initial error in the pose estimate, none of the local correspondences will be correct. However, many of the correspondences may be connected to the correct edge or surface and these correspondences tend to dominate the objective function and force the model to move towards the true pose. Once the pose estimate is close, the effect of consensus is great and convergence is quickly achieved.

Dynamic Correspondences for Robust M-estimation

The principal reason for our algorithm's convergence ability is that the objective function E specifies a relatively large and smooth basin of attraction in pose space. The size and smoothness of the basin of attraction is principally due to the use of smooth down-weighting M-estimators (e.g., Lorentzian or Tukey weight functions). Our use of dynamic correspondences in minimizing the objective function ensures that we remain in this basin of attraction as the search proceeds. Dynamic correspondences ensures that we are minimizing the desired objective function. While more expensive than the ICP algorithm in terms of objective function evaluations, the convergence rate in terms of gradient steps taken is comparable to ICP. Dynamic correspondences also implies dynamic weights. Large steps are likely to greatly effect the weights of each observation, the result of large (greedy) steps is often getting stuck in local minima. Dynamic correspondences can be likened to closely hugging the wall while following a dark corridor, while ICP [6] is more like taking a large step while blindfolded and peeking at one's feet.

Point-Based Models

Representing the object models for 3D-3D and 3D-2D localization as a collection of points provides many benefits. First, it keeps the algorithms simple and efficient. We can straightforwardly control the resolution of the models (by adding or dropping points) without adversely changing their general appearance. This proves useful when applying randomization strategies to improve these algorithms. In addition to being simple, the point representation is rather general, allowing us to model arbitrary (rigid) surface shapes in 3D and arbitrary configurations of edgel generators of all types.

Using 3D for 2D

For both edgel modeling and 3D-2D localization, the use of 3D information and representations makes things easier. When creating 2D models, the use of a 3D surface model provides the following advantages:

- Simplifies the foreground/background problem when creating models
- Allows us to map features to a unique coordinate system for merging observed edgels from multiple views.
- Gives us a way to predict the appearance of occluding contours.

For 2D localization, interpreting errors as 3D errors using known camera parameters simplifies the pose estimation problem and allows us to use the same optimization engine as used for 3D localization.

7.1 Contributions

We now list the main contributions of this thesis:

- Robust 3D surface model construction with the consensus-surface algorithm: We have demonstrated an algorithm can construct extremely accurate surface models from rather noisy input data.
- Robust 3D-3D and 3D-2D object localization by performing M-estimation using dynamic correspondences: We have demonstrated that our algorithm has superior convergence properties to the recognized state of the art (ICP) with reasonable efficiency. These properties are largely due to the use of robust M-estimators for our objective function. We have shown that the potential exists for even wider convergence and more efficient performance through the use of randomization. The localization searches in the 3D-3D and 3D-2D domains are unified by minimizing the 3D error rather than 2D image error. The 3D error for 3D-2D localization was shown to be optimal with respect to estimating a pose in three dimensions.
- Robust 3D edgel model construction with the consensus-edgel algorithm: We have demonstrated a method for extracting salient 3D edgel generators from large numbers of intensity image views which contain a large number of spurious edgels.
- Treatment of occluding contours in 3D-2D localization: We have presented and demonstrated a new approach to predicting the appearance of and utilizing occluding contours of an object for localization.

7.2 Future Work and Discussion

We conclude with a discussion of open problems and future improvements which we are interested in pursuing and would like to see pursued.

3D-3D + 3D-2D

While we demonstrated strong results for 3D-2D localization with multiple (stereo) images, the next step is to combine the two modalities—range/depth images and intensity images—to get the best of both worlds. 3D-2D object localization can help improve 3D-3D localization and vice versa. In the depth image from stereo domain, the accuracy of the depth data may be rather low. However it will usually be good enough to get a rough localization estimate in depth. Once close enough, 3D-2D localization can provide a much finer resolution of the pose than would be available from 3D-3D localization alone.

Learning Recognition Models

The localization and modeling algorithms of this thesis have great potential for advances in object recognition. Having the ability to track and locate objects in 3D makes it possible correlate detected image features or attributes to specific locations on the 3D object. With this capability, it is possible to use acquire/learn recognition constraints from real image data (possibly requiring an operator to initialize the object pose before tracking it through a sequence of views).

Uncalibrated Model Acquisition

The first step in making the modeling systems described here of general use will be to eliminate the requirement of calibration. Shape from motion, motion estimation, and registration algorithms (such as the 3D-3D and 3D-2D localization algorithms described here) are becoming mature. At the very least, a reliable semi-automatic procedure for view alignment is within sight. By combining sensor modalities (such as the depth and intensity idea described above), the accuracy of the alignments between views will improve. Applying batch estimation techniques such as Shum, Ikeuchi and Reddy's [127] robust algorithm for simultaneously estimating the motions of all views may soon make it feasible to automatically align a large set of views accurately.

Edgel Likelihoods

An improvement of the 3D-2D localization algorithm would be to incorporate edgel visibility likelihoods. For the implementation and experiments described in this thesis, the number of views used (e.g., 40-60) were insufficient to really make any useful estimate of edgel likelihoods.

Photometric Visibility

The thesis focused on geometric visibility constraints. Eventually, however, this may be extended to include photometric constraints as well. Techniques such as Sato and Ikeuchi's [118] algorithm for automatically modeling the reflectance properties of objects from real

images may soon be useful for predicting the likelihood of edgel or surface visibility based on photometric information of the object and some knowledge of the illumination in the scene.

Localization and Local Minima

Finally, perhaps the most important area of future work is to reduce the effect of local minima on localization and recognition in general.

All localization searches are susceptible to local minima. The shape of the optimization function for localization searches is determined by the object shape and image data. For example, the worst case object for any localization program would be a porcupine like object. The spikes present a problem when the rotation error is greater than the angle between spikes. Each of these rotations creates a local minima since the optimization function is smaller when the model and image spikes line up (even if it is not the global minima) than when the model spikes lie between the image spikes.

Similarly, the image may contain extraneous data that happens to lie in front of (i.e., partially occluding the object) or nearby the object being localized. The model may possibly be closer to the extraneous object, thus creating a local minima from which the local search cannot escape to reach the global minima.

For the first problem, difficult object shapes, the local minima are predictable and it is possible to add higher level info to deal with this when localizing the object.

The second problem, dealing with extraneous data, is more difficult but is slightly alleviated by adding attributes (such as surface normals as described in Sections 3.3 and 5.3) to the correspondence search. When tracking objects with small velocities, it is unlikely to become a problem until such point that the object is so severely occluded (i.e., more than half occluded) that there is insufficient correct correspondences to localize the object.

Unfortunately, these kind of solutions will only help so much; localization searches will still find themselves stuck in local minima more often than we would like. We believe that the key to avoiding local minima must to first be able to detect when you are in a local minimum—an incorrect pose. Once you can detect this situation, a strategy may be available to deal with it. This leads right back to the verification problem—the heart of the recognition problem.

One potential solution which could utilize a verification capability is a simulated-annealing search [43, 62, 111, 140]. Simulated annealing uses random perturbations of the search direction to escape local minima—often making non-optimal local decisions to improve its chances at finding a better global solution. Viola [140] made use of just such a technique for localizing 3D objects in 2D images by maximizing mutual information. Simulated annealing often requires many iterations to converge, however if combined with an efficient hill-climbing (gradient-descent) method which can detect when it is stuck, the randomness may be efficiently harnessed.

Scale Space Recognition/Localization

One other idea which may prove useful in reducing the effect of local minima is to apply the ideas of scale space [149, 150] to object localization. The idea would be to have the localization model change continuously with respect to scale, from coarse to fine, as the search proceeds. This would have the potential of smoothing away many of the local minima which are near the global minimum. Wells [143] presented a first-order approximation towards this idea with a multi-level localization recognition model. It will be critical to use real images to acquire a scale-space localization model because it is likely that the changes in the model with respect to scale will be difficult to otherwise model or predict.

:

Appendix A

Camera and Robot Calibration

In this appendix, we overview the method for calibrating the camera with respect to our robotic positioner. Our experimental image acquisition setup comprises:

- a CCD camera
- an OGIS light-stripping projector
- a Unimation PUMA robot

The setup is pictured in Figure A.1 which shows the configuration of the CCD camera, robot end effector and the light-stripe projector. The light-stripping projector projects a set of stripes on the scene. Each stripe has a distinct pattern (e.g., a binary code). The CCD camera is used to acquire images of the scene as the pattern is projected. Each pattern corresponds to a different plane/stripe of the projected light. With knowledge of the relative positions of the camera and projector, the image location and projected-light plane determine the position of the point in the scene with respect to the camera.

Objects are mounted on the end effector of the robot in front of the camera. In this work, we control two rotation axes of the robot when acquiring data as shown in Figure 2.12 of Section 2.5. To determine the motion of the robot with respect to the camera, it is sufficient to determine the location and direction for each of these rotation axes with respect to the camera.

We have three calibration tasks:

- calibrating the CCD camera: internal parameters such as focal length, image center and scaling
- range sensor calibration: position of light-stripping projector with respect to the camera
- hand-eye calibration: position of the robot's end effector with respect to the camera

The first two calibration tasks are accomplished in one step with the light-stripping range finder. A calibration cube, pictured in Figure A.2, is used to calibrate a 3D world coordinate system with the CCD camera and the light-stripping projector. The world coordinate

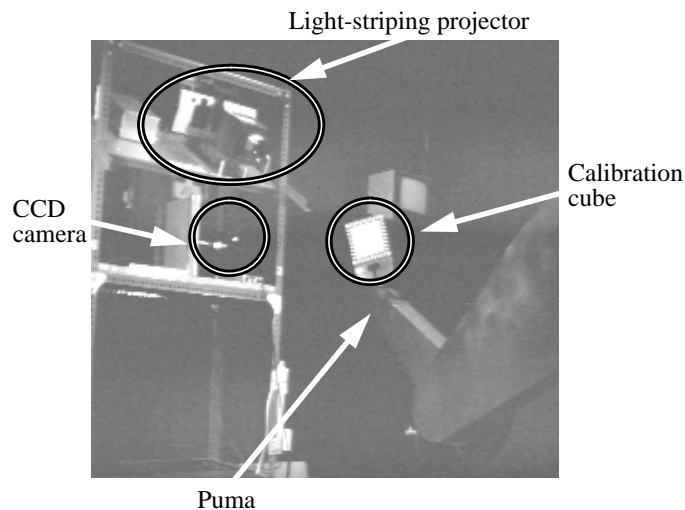


Figure A.1: An image of the experimental setup including the CCD camera, light-stripping projector, and Puma robot.

system is defined with respect to the cube. The cube is mounted on the robot in the “home” position. The light pattern is projected onto the cube. The human operator then proceeds to click on the 12 (white) corner points (4 on each visible face) of the cube. For each face, the 4 corner points are used to automatically detect the 10 white marks along the edge each face. These markings are connected to form a grid, creating 100 points on each face of the cube. We now know the 3D world coordinate of each point and the 2D image coordinate of each point. These can then be used with a camera calibration method, such as Tsai’s [136] or Faugeras and Toscani’s [35] method to determine the internal camera parameters and the projection matrix from camera coordinates to world coordinates. In addition, we also know the pattern of the the projected light stripes at each point. The (world-coordinate) plane equation for each stripe can be computed using least-squares techniques. Using the camera projection matrix and stripe plane equations, we can compute the 3D world coordinates of any scene point given the image position and light-stripe slice identification.

The calibration cube is also useful for estimating the rotation axes of the Puma robot. We can rotate the robot’s end effector by a fixed angle and determine the motion of the cube in world coordinates. With small enough angular step of the end effector, we can use our 3D-3D localization algorithm, presented in Chapter 3, to compute the precise pose of the cube in the new image following rotation of the cube. This process can be repeated for any number of steps. The result is that we have a sequence of angular steps of known angles and a set of poses of the cube at these end-effector positions. We can then perform a least-squares estimate of the rotation axis direction and location.

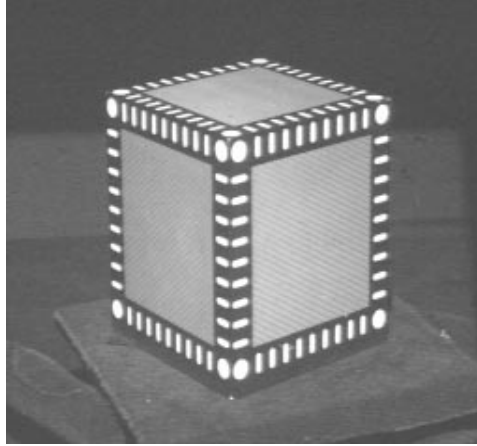


Figure A.2: The calibration cube used for range sensor and camera calibration.

Estimation of the rotation axis is accomplished by first solving for the rotation component of the rotation axis: the axis direction. We can compute the axis direction by solving for the quaternion \mathbf{q} that maximizes the following objective function:

$$f_a(\mathbf{q}) = \sum_i (\mathbf{R}(\mathbf{q})\hat{\mathbf{n}}_i) \cdot \hat{\mathbf{n}}_{i+1}$$

where $\mathbf{R}(\mathbf{q})$ is the 3×3 rotation matrix corresponding to the quaternion \mathbf{q} (see Appendix B for more details on the quaternion representation) and $\hat{\mathbf{n}}_i$ is the world-coordinate normal vector of a face of the cube in view i . The principal term in $f_a()$ is maximized when the rotated normal vector of the current view matches exactly the normal vector from the next view. The optimal quaternion \mathbf{q} is an estimate of the axis direction and angle of a single-step rotation of the end effector. The axis direction vector can easily be extracted from the quaternion by normalizing the vector component of the quaternion (again, see Appendix B).

Using the direction of the end-effector's rotation axis, we can then compute the location \mathbf{t} of the rotation axis. This is achieved by minimizing the function:

$$f_t(\mathbf{t}) = \sum_i (\mathbf{R}(\mathbf{q})(\mathbf{x}_i - \mathbf{t}) + \mathbf{t} - \mathbf{x}_{i+1})^2$$

where \mathbf{x}_i is the position of a specific point on the cube (not lying on or near the rotation axis) in the i th view. The least-squares solution of the location \mathbf{t} is a 3D line. We can choose any point on this line as the location of the rotation axis. One choice is to set \mathbf{t} to the point on the line which is closest to the origin of our world coordinate system.

Each rotation axis can be calibrated similarly. The axis direction and location and the angle of rotation of the end effector is sufficient to determine the motion of the robot in

world coordinates. Rotations of multiple robot axes can be straightforwardly composed to determine the motion in world coordinates.

Typically, we can accurately estimate the rotation axis using anywhere from 45 to 90 views of the cube taken at rotational increments of 4 to 8 degrees. Finer rotational sampling is possible to improve the accuracy of the rotation-axis estimate. For best results, it is important that the samples cover as large a rotational range as possible.

Appendix B

Quaternions and Rotation

In this Appendix, we review the use of quaternions to represent rotation and present the derivation of the gradient of the 3×3 rotation matrix \mathbf{R} with respect to the quaternion parameters. We begin with a general overview of quaternions and their utility for motion- and pose- estimation problems in computer vision.

B.1 Why Quaternions?

A common problem in computer vision is solving for rigid-body motions or poses consisting of a rotation and translation in 3D space. For example, given a set of points \mathbf{x}_i and correspondences \mathbf{p}_i , it is often of interest to compute the 3x3 rotation matrix \mathbf{R} and 3-vector translation \mathbf{t} such that

$$\mathbf{R}\mathbf{x}_i + \mathbf{t} = \mathbf{p}_i. \tag{B.1}$$

Although this system of equations is essentially linear, a number of problems arise when formulating solutions that account for the non-linear constraints on the components of \mathbf{R} . The constraints arise from using nine values of rotation matrix \mathbf{R} to represent three independent variables of 3D rotation. The rotation matrix is constrained to be orthogonal which is satisfied when $\mathbf{R}^T\mathbf{R} = \mathbf{I}$ (i.e., the rows and columns are orthonormal). Also, the rotation must not be a reflection; this is satisfied when the determinant is 1 (i.e., $|\mathbf{R}| = 1$).

A number of techniques have been developed to deal with this added complexity. One of the most convenient is the quaternions representation. We will describe quaternions in some detail in what follows, but first we provide the reader a list of some of the advantages and mathematical niceties of the quaternion representation of rotation.

- Maintaining the constraints (orthogonal with unit determinant) of rotation is made simple with quaternions by standard vector normalization.
- Quaternions can be composed/multiplied in a straightforward manner to accumulate the effects of composed rotations.

- The inverse of a quaternion (specifying the inverse rotation) is obtained by simply negating 3 components of the quaternion vector.
- The rotation between two rotations can be computed by multiplying one quaternion with the inverse of the other.
- One can easily transform a quaternion into an axis-and-angle representation. Using this and the previous item, one can compute a rotational distance metric between two rotations—the angle of rotation between them.
- Quaternions can be easily transformed to a 3x3 rotation matrix for efficient computation when rotating vectors.
- It has been shown by Sanso [116], Faugeras and Hebert [36] and Horn[66] that with the quaternion representation, the rotation can be solved for in closed form when correspondences between three-dimensional point sets are available.

We would like to add to this list that the quaternion representation of rotation has some advantageous differential properties (to be described later). These differential properties combined with the properties of quaternions described above make quaternions particularly well suited to requirements of iterative gradient- or Jacobian-based search for rotation and translation. In this section, we derive a simple form for the gradient and Jacobian of rotation with respect to quaternions. The form of the Jacobian leads to a straightforward analysis of the problem presented by scale when solving for rotation and translation, and leads to simple steps to ensure scale invariant performance of search algorithms.

B.2 Quaternions

In this section, we will define the quaternion and its essential properties for representing and algebraically manipulating rotations. For further details on quaternions the reader is referred to [56, 36, 66, 94]. The quaternion \mathbf{q} is a four vector $[u, v, w, s]^T$ which is often considered as a three-vector $\mathbf{u} = [u, v, w]^T$ and a scalar s . We will often refer to \mathbf{q} as $[\mathbf{u}, s]^T$ for notational simplicity. The dot product and vector norm for quaternions is defined as usual

$$\begin{aligned}\mathbf{q}_1 \cdot \mathbf{q}_2 &= \mathbf{u}_1 \cdot \mathbf{u}_2 + s_1 s_2 \\ |\mathbf{q}| &= (\mathbf{q} \cdot \mathbf{q})^{-\frac{1}{2}}.\end{aligned}$$

Multiplication is defined over quaternions as

$$\mathbf{q}_1 \mathbf{q}_2 = [[s_1 \mathbf{u}_2 + s_2 \mathbf{u}_1 + \mathbf{u}_1 \times \mathbf{u}_2], s_1 s_2 - \mathbf{u}_1 \cdot \mathbf{u}_2]^T. \quad (\text{B.2})$$

The complex conjugate of a quaternion is defined by negating the vector component and is denoted $\bar{\mathbf{q}} = [-\mathbf{u}, s]^T$. The complex conjugate of a unit quaternion, $|\mathbf{q}| = 1$, is the inverse of the quaternion with respect to multiplication, i.e.,

$$\mathbf{q}\bar{\mathbf{q}} = \mathbf{q}_I$$

where $\mathbf{q}_I = [0, 0, 0, 1]^T$ (we will refer to this often). From Equation B.2, one can see that $\mathbf{q}\mathbf{q}_I = \mathbf{q}_I\mathbf{q} = \mathbf{q}$ which is why we refer to \mathbf{q}_I as the identity quaternion.

A unit quaternion \mathbf{q} can be used to perform a rigid rotation of a vector $\mathbf{x} = [x, y, z]^T$ by two quaternion multiplications

$$\mathbf{x}' = \mathbf{q} \begin{bmatrix} x \\ y \\ z \\ 0 \end{bmatrix} \bar{\mathbf{q}},$$

where the scalar component of \mathbf{x} is simply set to zero. Observe that quaternion multiplication is not commutative; this is consistent with the fact that general three-dimensional rotations do not commute; however, quaternion multiplication is associative and distributive.

Working from this definition of quaternion rotation, one can derive a formula for the corresponding orthogonal (Euclidean) 3x3 rotation matrix from a unit quaternion

$$\mathbf{R}_u(\mathbf{q}) = \begin{bmatrix} s^2 + u^2 - v^2 - w^2 & 2(uv - sw) & 2(uw + sv) \\ 2(uv + sw) & s^2 - u^2 + v^2 - w^2 & 2(vw - su) \\ 2(uw - sv) & 2(vw + su) & s^2 - u^2 - v^2 + w^2 \end{bmatrix}.$$

We use the subscript u in \mathbf{R}_u to denote that this is the rotation matrix when given a unit quaternion. Given an arbitrary quaternion, \mathbf{R}_u would no longer be unitary but rather a scaled rotation matrix. The reader can verify that for the identity quaternion (defined above) $\mathbf{R}(\mathbf{q}_I) = \mathbf{I}$, the 3x3 identity matrix.

Finally, we define the relationship between quaternions and the axis-and-angle representation. A unit quaternion \mathbf{q} can be straightforwardly interpreted to specify a rotation of angle θ around the unit vector $\hat{\omega}$ using the relations

$$\begin{aligned} \mathbf{u} &= \sin \frac{\theta}{2} \hat{\omega} \\ s &= \cos \frac{\theta}{2}. \end{aligned}$$

This relationship can be derived (see [66]) from Rodrigues' formula for axis-and-angle rotation

$$\mathbf{x}' = \cos \theta \mathbf{x} + \sin \theta (\hat{\omega} \times \mathbf{x}) + (1 - \cos \theta)(\hat{\omega} \cdot \mathbf{x})\hat{\omega} \tag{B.3}$$

where \mathbf{x} is the vector being rotated.

The next section will examine some differential properties of quaternions with respect to rotation.

B.3 The Jacobian of Rotation With Respect to Quaternions

In this section, we explore a special case which greatly simplifies the form of the Jacobian of rotation with respect to quaternions. This form of the Jacobian was introduced in Equation 3.29 of Section 3.4.3.

The rigid transformation of Equation B.1 is now a function of \mathbf{q} instead of the nine elements of \mathbf{R}

$$\mathbf{x}' = \mathbf{R}(\mathbf{q})\mathbf{x}_i + \mathbf{t}, \quad (\text{B.4})$$

and the derivatives with respect to \mathbf{q} (which is all that we are interested in at the moment) are only a function of the rotation term.

We begin by eliminating the restriction to unit quaternions in our analysis. We can enforce the constraint that the rotation matrix is orthogonal without requiring \mathbf{q} to be a unit vector by dividing the matrix by the squared length of the quaternion

$$\mathbf{R}(\mathbf{q}) = \frac{1}{\mathbf{q} \cdot \mathbf{q}} \mathbf{R}_u(\mathbf{q}). \quad (\text{B.5})$$

This constraint is necessary in general to ensure the Jacobian and gradient accurately reflect the differential properties of a change in the quaternion parameters. As one might guess, the addition of this constraint greatly complicates the form of the Jacobian; however, as we will see shortly, this constraint actually slightly simplifies the Jacobian when evaluated at the identity quaternion, \mathbf{q}_I .

If we are computing the Jacobian of

$$\mathbf{x}' = f(\mathbf{q}, \mathbf{x}) = \mathbf{R}(\mathbf{q})\mathbf{x}$$

with respect to \mathbf{q} , things are greatly simplified if we know $\mathbf{q} = \mathbf{q}_I$. Setting things up to make sure we evaluate all derivatives at \mathbf{q}_I is quite painless. Say that quaternion specifying the current rotation of the data is \mathbf{q}_c . We can easily change coordinate systems so that our current quaternion is \mathbf{q}_I by simply premultiplying all of the model points by $\mathbf{R}(\mathbf{q}_c)$. That is, replace \mathbf{x} with $\mathbf{x}_c = \mathbf{R}(\mathbf{q}_c)\mathbf{x}$.

By premultiplying the data with the current rotation, we will now solve for a rotation that composes with our current rotation position instead of attempting to solve for the corrections of our current rotation parameters. The premultiplication should not increase the number of computations for most applications since $\mathbf{R}(\mathbf{q}_c)\mathbf{x}$ must be computed anyway to compute error terms. After estimating this rotation, we can easily compute the quaternion of the complete rotation by quaternion multiplication (i.e., $\mathbf{q}' = \mathbf{q} \mathbf{q}_c$).

Fundamentally, we have not changed the problem since

$$f(\mathbf{q}_I, \mathbf{x}_c) = f(\mathbf{q}_c, \mathbf{x}),$$

and we can still represent the same set of rotations. However, the form for the Jacobian is much simpler when evaluated at \mathbf{q}_I as we will see.

We now derive the Jacobian matrix $\frac{\partial(f(\mathbf{q}, \mathbf{x}))}{\partial \mathbf{q}}$ at \mathbf{q}_I

$$\left. \frac{\partial f}{\partial \mathbf{q}} \right|_{\mathbf{q}_I} = \left. \frac{\partial \mathbf{R}}{\partial \mathbf{q}} \right|_{\mathbf{q}_I} \mathbf{x}.$$

Using $z(\mathbf{q}) = \frac{1}{\mathbf{q} \cdot \mathbf{q}}$ and Equations B.5, this can be broken up as follows

$$\frac{\partial \mathbf{R}}{\partial \mathbf{q}} \Big|_{\mathbf{q}_I} = z(\mathbf{q}_I) \frac{\partial \mathbf{R}_u}{\partial \mathbf{q}} \Big|_{\mathbf{q}_I} + \frac{\partial z}{\partial \mathbf{q}} \Big|_{\mathbf{q}_I} \mathbf{R}_u(\mathbf{q}_I) \quad (\text{B.6})$$

$$= \frac{\partial \mathbf{R}_u}{\partial \mathbf{q}} \Big|_{\mathbf{q}_I} + \frac{\partial z}{\partial \mathbf{q}} \Big|_{\mathbf{q}_I} \mathbf{I}, \quad (\text{B.7})$$

using $\mathbf{R}(\mathbf{q}_I) = \mathbf{I}$ and $z(\mathbf{q}_I) = 1$.

The first term can be computed by realizing that only the components in $\mathbf{R}_u(\mathbf{q})$ with a factor of s in it will have a value in the derivative evaluated at \mathbf{q}_I

$$\begin{aligned} \frac{\partial \mathbf{R}_u}{\partial \mathbf{q}} \Big|_{\mathbf{q}_I} &= \left[\begin{array}{cccc} \frac{\partial \mathbf{R}_u}{\partial u} \Big|_{\mathbf{q}_I} & \frac{\partial \mathbf{R}_u}{\partial v} \Big|_{\mathbf{q}_I} & \frac{\partial \mathbf{R}_u}{\partial w} \Big|_{\mathbf{q}_I} & \frac{\partial \mathbf{R}_u}{\partial s} \Big|_{\mathbf{q}_I} \end{array} \right] \\ &= \left[\begin{array}{ccc} \left[\begin{array}{ccc} 0 & 0 & 0 \\ 0 & 0 & -2 \\ 0 & 2 & 0 \end{array} \right] & \left[\begin{array}{ccc} 0 & 0 & 2 \\ 0 & 0 & 0 \\ -2 & 0 & 0 \end{array} \right] & \left[\begin{array}{ccc} 0 & -2 & 0 \\ 2 & 0 & 0 \\ 0 & 0 & 0 \end{array} \right] & \left[\begin{array}{ccc} 2 & 0 & 0 \\ 0 & 2 & 0 \\ 0 & 0 & 2 \end{array} \right] \end{array} \right]. \end{aligned}$$

The second term is easily found to be

$$\frac{\partial z}{\partial \mathbf{q}} \Big|_{\mathbf{q}_I} \mathbf{I} = -2z(\mathbf{q}_I) \mathbf{q}_I \mathbf{I} = -2\mathbf{q}_I \mathbf{I} = [0, 0, 0, -2] \mathbf{I}.$$

Summing up the terms from Equation B.7, we see that the term $\frac{\partial \mathbf{R}}{\partial s} \Big|_{\mathbf{q}_I}$ disappears (which is not true at other points in general). The normalization factor $z(\mathbf{q})$ effectively cancels out any gain in f from increasing or decreasing the s component at $\mathbf{q} = \mathbf{q}_I$; thus, the gradient of normalized rotation accurately reflects the effect of changes in the parameters. Since the Jacobian evaluated at \mathbf{q}_I is nonzero only in the u , v and w components, we only have three rotation parameters to estimate.

We can now return to the original gradient equation and multiply through to get

$$\begin{aligned} \frac{\partial f}{\partial \mathbf{q}} \Big|_{\mathbf{q}_I} &= \frac{\partial \mathbf{R}}{\partial \mathbf{q}} \Big|_{\mathbf{q}_I} \mathbf{x} \\ &= \begin{bmatrix} 0 & 2z & -2y & 0 \\ -2z & 0 & 2x & 0 \\ 2y & -2x & 0 & 0 \end{bmatrix} \end{aligned}$$

where $\mathbf{x} = [x, y, z]^T$. Ignoring the last column of the Jacobian, the result will be familiar to most readers as -2 times the skew-symmetric matrix of \mathbf{x} . For example, the cross product of two vectors can be expressed as a matrix-vector multiplication

$$\mathbf{x} \times \mathbf{a} = C(\mathbf{x})\mathbf{a} = \begin{bmatrix} 0 & -z & y \\ z & 0 & -x \\ -y & x & 0 \end{bmatrix} \mathbf{a},$$

where we refer to $C(\mathbf{x})$ as the skew-symmetric matrix of \mathbf{x} . Notice that, by the skew-symmetry of $C(\mathbf{x})$, $C^T = -C$. Thus, we have a very simple form for the Jacobian of our function at \mathbf{q}_I

$$\left. \frac{\partial f}{\partial \mathbf{q}} \right|_{\mathbf{q}_I} = \left. \frac{\partial \mathbf{R}}{\partial \mathbf{q}} \right|_{\mathbf{q}_I} \mathbf{x} = 2C(\mathbf{x})^T. \quad (\text{B.8})$$

The above derivation enables us to trivially and efficiently compute the gradient/Jacobian of any rotation with respect to quaternion parameters. The computation of these entities at quaternions other than \mathbf{q}_I requires many more operations and involves a term for the s component as well.

Starting the search at \mathbf{q}_I has some other advantages for gradient-based searches of rotation. Consider performing a line minimization in the (negative) gradient direction. Remember the gradient direction with respect to \mathbf{q} will have no s component and will be of the form

$$d\mathbf{q} = - \left. \frac{\partial f}{\partial \mathbf{q}} \right|_{\mathbf{q}_I} = [du, dv, dw, 0]^T.$$

and each step of the each successive rotation in this direction will be of the form

$$\mathbf{q}' = \mathbf{q}_I + \lambda d\mathbf{q} = [\lambda du, 1]^T \quad (\text{B.9})$$

where $d\mathbf{u} = [du, dv, dw]$. Remember that \mathbf{q}' does not need to be normalized (we did that in Equation B.5). This means that the rotation axis of our corresponding line search is constant while the angle

$$\theta = 2 \cos^{-1} \left(\frac{1}{\lambda^2 + 1} \right) \quad (\text{B.10})$$

increases with λ (assume $|d\mathbf{q}| = 1$). If the gradient is evaluated at $\mathbf{q} \neq \mathbf{q}_I$, we get a gradient with $s \neq 0$ and our steps in the search are now of the form

$$\mathbf{q}(\lambda) = \mathbf{q}_c + \lambda d\mathbf{q} = [\mathbf{u}_c + \lambda d\mathbf{u}, s_c + \lambda ds]^T. \quad (\text{B.11})$$

It is interesting to note that searching across an arbitrary line in the 4D quaternion space is equivalent to searching along θ while rotating around a fixed rotation axis.

Also note that θ is not a linear function of λ Equations B.10. It is very close to a linear relationship for small angles and reasonably so for $\theta \leq 90^\circ$. Beyond this linear region the search may run into trouble. The gradient search can compensate for this by linearly increasing the value of θ directly, but this should rarely be necessary.

As we have shown above, the quaternions possess some advantageous differential properties which make it amenable to gradient- and Jacobian-based iterative search. Since they are easily composable, we can maintain a single rotation estimate while simplifying the analysis by premultiplying our data with the current rotation estimate. The Jacobian can be computed very efficiently, and line searches in quaternion space effectively equate to linearly increasing the rotation angle (for all practical purposes) about a fixed rotation axis.

Appendix C

Principal Curvatures from Triangulated Surfaces

In Section 4.5, we described the general approach that we use to estimate the principal curvatures and directions at points on a triangulated surface. Our approach is based on Koenderink's [76] proposal to fit a quadric surface in the neighborhood of each point and then use the algebraic representation of the surface to derive the principal curvatures and directions. In this appendix, we present the derivation of our solution.

C.0.1 Fitting Quadrics to Triangles

We begin by fitting a quadric equation to the vertex of interest \mathbf{x}_0 and its neighbor vertices \mathbf{x}_i where $i = 1, \dots, n$. The general form of a quadric is

$$f(x, y, z) = Ax^2 + By^2 + Cz^2 + Dxy + Exz + Fyz + Gx + Hy + Iz + J = 0. \quad (\text{C.1})$$

This has 10 degrees of freedom and admits surfaces such as spheres, ellipsoids, planes, and cones among others. This form of the quadric is too general for our purposes. Some of these surface types, such as cones, are of no interest to us for computing curvature. Also, we need at least 10 points in the neighborhood of a given point to perform the fit. Fortunately, we can reduce the number of degrees of freedom of the quadric while still representing the surface types of interest to us. This is accomplished by reorienting the coordinate system with respect to the surface (eliminating several degrees of freedom).

We choose a coordinate frame centered at \mathbf{x}_0 whose z direction is equivalent to the estimated surface normal $\hat{\mathbf{n}}_0$ of point \mathbf{x}_0 .¹ The x and y directions can be arbitrarily chosen with the constraint that the coordinate system is orthogonal and right-handed. We then transform each point \mathbf{x}_i to this new coordinate system

$$\mathbf{x}'_i = \mathbf{R}(\mathbf{x}_i - \mathbf{x}_0)$$

¹We do not know the surface normal precisely but can estimate it by averaging the normals of the neighboring triangles; the accuracy of the surface normal at this stage is not crucial.

where \mathbf{R} is the rotation from the model coordinate system to the point's local coordinate system.

This change of coordinate system allows us to use a simpler equation for the quadric

$$f(x, y, z) = Ax^2 + By^2 + Cxy + Dx + Ey + F + z = 0 \quad (\text{C.2})$$

which has six parameters and eliminates the undesired quadric surfaces that were possible with Equation C.1. Since each point adds one equation to a linear system of six variables, we can solve for these quadric parameters given six or more points in the local neighborhood of \mathbf{x}_0 .

If more than six points are available, the system becomes over-determined and we can use the pseudo-inverse to find the least-squares solution. If \mathbf{x}_0 has fewer than six neighbors, we simply create new points by interpolating new points on the neighboring triangles.

C.0.2 From Quadrics to Curvature

From the fitted quadric surface, we would like to infer the principal curvatures and their directions to characterize the curvature at the given surface point. From differential geometry [102], the curvature of a point can be defined as

$$\kappa(\hat{\mathbf{v}}) = -\hat{\mathbf{v}} \cdot \nabla_{\hat{\mathbf{v}}} \left(\frac{\mathbf{n}}{\|\mathbf{n}\|} \right)$$

where $\nabla_{\hat{\mathbf{v}}}$ specifies the directional derivative with respect to direction $\hat{\mathbf{v}}$, and \mathbf{n} is the (non-unit) normal direction of the surface. If we expand this equation, we can simplify it a bit if we assume that all $\hat{\mathbf{v}}$'s will be tangent vectors. If $\hat{\mathbf{v}} \cdot \mathbf{n} = 0$, then

$$\kappa(\hat{\mathbf{v}}) = -\hat{\mathbf{v}} \cdot \nabla_{\hat{\mathbf{v}}} \left(\frac{\mathbf{n}}{\|\mathbf{n}\|} \right) \quad (\text{C.3})$$

$$= -\frac{1}{\|\mathbf{n}\|} \hat{\mathbf{v}} \cdot \nabla_{\hat{\mathbf{v}}}(\mathbf{n}) - (\hat{\mathbf{v}} \cdot \mathbf{n}) \nabla_{\hat{\mathbf{v}}} \left(\frac{1}{\|\mathbf{n}\|} \right) \quad (\text{C.4})$$

$$= -\frac{1}{\|\mathbf{n}\|} \hat{\mathbf{v}} \cdot \nabla_{\hat{\mathbf{v}}}(\mathbf{n}). \quad (\text{C.5})$$

From our quadric surface approximation, the normal, \mathbf{n} , of our quadric-surface approximation is the gradient direction at the given point:

$$\mathbf{n}(x, y, z) = \nabla f(x, y, z) \quad (\text{C.6})$$

$$= 2 \begin{bmatrix} 2A & C & 0 & D \\ C & 2B & 0 & E \\ 0 & 0 & 0 & 1 \end{bmatrix} \begin{bmatrix} x \\ y \\ z \\ 1 \end{bmatrix}. \quad (\text{C.7})$$

Note, that \mathbf{n} is generally not a unit vector. The directional derivative of \mathbf{n} in direction $\hat{\mathbf{v}}$ is then conveniently found to be

$$\nabla_{\hat{\mathbf{v}}}\mathbf{n}(x, y, z) = \hat{\mathbf{v}} \cdot \nabla\mathbf{n}(x, y, z) \quad (\text{C.8})$$

$$= \begin{bmatrix} 2A & C & 0 \\ C & 2B & 0 \\ 0 & 0 & 0 \end{bmatrix} \hat{\mathbf{v}}. \quad (\text{C.9})$$

Using this, we can solve for the curvature

$$\kappa(\hat{\mathbf{v}}) = -\frac{1}{\|\mathbf{n}\|} \hat{\mathbf{v}} \cdot \nabla_{\hat{\mathbf{v}}}(\mathbf{n}) \quad (\text{C.10})$$

$$= -\frac{2}{\|\mathbf{n}\|} \hat{\mathbf{v}}^T \begin{bmatrix} A & \frac{C}{2} & 0 \\ \frac{C}{2} & B & 0 \\ 0 & 0 & 0 \end{bmatrix} \hat{\mathbf{v}} \quad (\text{C.11})$$

$$= -\frac{2}{\|\mathbf{n}\|} \hat{\mathbf{v}}^T \begin{bmatrix} A & \frac{C}{2} \\ \frac{C}{2} & B \end{bmatrix} \hat{\mathbf{v}} \quad (\text{C.12})$$

$$= -\frac{2}{\|\mathbf{n}\|} \hat{\mathbf{v}}^T \mathbf{M} \hat{\mathbf{v}}. \quad (\text{C.13})$$

This form of $\kappa(\hat{\mathbf{v}})$ makes the principal curvatures readily computable from the eigenvalues of the symmetric, 2×2 matrix \mathbf{M} . The eigenvalues are the solution of the characteristic equation

$$(A - \lambda)(B - \lambda) - \frac{C^2}{4} = 0.$$

Using

$$\gamma = \sqrt{A^2 + B^2 + C^2 - 2AB},$$

the eigenvalues are found to be

$$\lambda_1 = \frac{A + B + \gamma}{2} \quad (\text{C.14})$$

$$\lambda_2 = \frac{A + B - \gamma}{2}. \quad (\text{C.15})$$

The principal curvatures differ from the eigenvalues by only the scale of the (non-unit) normal vector \mathbf{n} ; in other words,

$$\kappa = \frac{-2\lambda}{\|\mathbf{n}\|} \quad (\text{C.16})$$

$$= \frac{-2\lambda}{\sqrt{D^2 + E^2 + 1}}. \quad (\text{C.17})$$

Thus, we have a closed form of the principal curvatures with respect to our quadric surface parameters. From the eigenvalues, we can then compute the eigenvectors of \mathbf{M} , from which we can compute the principal directions. The 2D eigenvectors are extended to 3D by

computing the z component such that \hat{e}_1 and \hat{e}_2 are orthogonal to $\mathbf{n}(0, 0, 0) = [D \ E \ 1]^T$. The closed form solution for the eigenvectors of \mathbf{M} may be derived by solving for the non-trivial (i.e., $\mathbf{x} \neq 0$) solutions of \mathbf{x} in

$$\begin{bmatrix} A - \lambda & \frac{C}{2} \\ \frac{C}{2} & B - \lambda \end{bmatrix} \mathbf{x} = 0 \quad (\text{C.18})$$

for each eigenvalue λ_1 and λ_2 . The details are omitted here. Technically, only one eigenvector needs to be computed since one principal direction and the normal uniquely determines the other principal direction. Thus, we have a closed form for the principal curvatures and directions from the quadric parameters.

Bibliography

- [1] K.S. Arun, T.S. Huang, and S.D. Blostein.
Least-squares fitting of two 3-d point sets.
IEEE Transactions on Pattern Analysis and Machine Intelligence, 9(5):698–700,
1987.
- [2] Dana Ballard and Christopher M. Brown.
Computer Vision.
Prentice Hall, Englewood Cliffs, New Jersey, 1982.
- [3] Jezekiel Ben-Arie.
The probabilistic peaking effect of viewed angles and distances with application to
3-d object recognition.
IEEE Transactions on Pattern Analysis and Machine Intelligence, 12(8):760–774,
1990.
- [4] Paul J. Besl and Ramesh C. Jain.
Three-dimensional object recognition.
ACM Computing Surveys, 17(1):75–145, 1985.
- [5] Paul J. Besl and Ramesh C. Jain.
Segmentation through variable-order surface fitting.
IEEE Transactions on Pattern Analysis and Machine Intelligence, 10(2):167–192,
1988.
- [6] Paul J. Besl and Neil D. McKay.
A method for registration of 3-d shapes.
IEEE Transactions on Pattern Analysis and Machine Intelligence, 14(2):239–256,
1992.
- [7] Gordon S. Beveridge and Robert S. Schechter.
Optimization: Theory and Practice.
McGraw-Hill, 1970.
- [8] Bir Bhanu.
Representation and shape matching of 3-d objects.
IEEE Transactions on Pattern Analysis and Machine Intelligence, 6(3):340–351,
1984.
- [9] Jean-Daniel Boissonat.
Geometric structures for three-dimensional shape representation.

- ACM Transactions on Graphics*, 3(4):266–286, 1984.
- [10] Ruud M. Bolle, Andrea Califano, and Rick Kjeldsen.
A complete and extendable approach to visual recognition.
IEEE Transactions on Pattern Analysis and Machine Intelligence, 14(5), 1992.
- [11] Robert C. Bolles and Patrice Horaud.
3DPO: A three-dimensional part orientation system.
International Journal of Robotics Research, 5(3):3–26, 1986.
- [12] Kevin Bowyer, Olivier Faugeras, Joe Mundy, Narendra Ahuja, Charles Dyer, Alex Pentland, Ramesh Jain, and Katsushi Ikeuchi.
Workshop panel report: Why aspect graphs are not (yet) practical for computer vision.
Computer Vision, Graphics and Image Processing: Image Understanding, 55(2):212–218, 1992.
- [13] Thomas M. Breuel.
Fast recognition using adaptive subdivisions of transformation space.
In *Proceedings of IEEE Conference on Computer Vision and Pattern Recognition*, pages 445–451, 1992.
- [14] Thomas M. Breuel.
Geometric aspects of visual object recognition.
PhD thesis, Massachusetts Institute of Technology, 1992.
- [15] Octavia I. Camps, Linda G. Shapiro, and Robert M. Haralick.
PREMIO: An overview.
In *IEEE Workshop on Directions in Automated CAD-Based Vision*, pages 11–21, 1991.
- [16] J. Canny.
A computational approach to edge detection.
IEEE Transactions on Pattern Analysis and Machine Intelligence, 8(6):679–698, November 1986.
- [17] J. L. Chen and G. C. Stockman.
Determining pose of 3d objects with curved surfaces.
IEEE Transactions on Pattern Analysis and Machine Intelligence, 18(1):52–57, January 1996.
- [18] Xin Chen and F. Schmitt.
Intrinsic surface properties from surface triangulation.
In *Proceedings of the European Conference on Computer Vision*, pages 739–43. Springer-Verlag, 1992.
- [19] Yang Chen and Gerard Medioni.
Object modelling by registration of multiple range images.
Image and Vision Computing, 10(3):145–155, 1992.
- [20] Yang Chen and Gerard Medioni.

- Fitting a surface to 3-d points using an inflating balloon model.
In *Second CAD-Based Vision Workshop*, pages 266–273, 1994.
- [21] C.H. Chien, Y. B. Sim, and J.K. Aggarwal.
Volume/surface octrees for the representation of 3-d objects.
Computer Vision, Graphics and Image Processing: Image Understanding, (36):100–113, 1986.
- [22] C.H. Chien, Y. B. Sim, and J.K. Aggarwal.
Generation of volume/surface octree from range data.
In *Proceedings of IEEE Conference on Computer Vision and Pattern Recognition*, pages 254–260. IEEE, 1988.
- [23] Roland T. Chin and Charles R. Dyer.
Model-based recognition in robot vision.
ACM Computing Surveys, 18(1):67–108, 1986.
- [24] Paul B. Chou and Christopher M. Brown.
The theory and practice of Bayesian image labeling.
International Journal of Computer Vision, 4:185–210, 1990.
- [25] David T. Clemens.
Region-Based Feature Interpretation for Recognizing 3D Models in 2D Images.
PhD thesis, Massachusetts Institute of Technology, 1991.
- [26] J. H. Connell and M. Brady.
Generating and generalizing models of visual objects.
Artificial Intelligence, 31:159–183, 1987.
- [27] Paul Cooper.
Parallel Object Recognition from Structure (The Tinkertoy Project).
PhD thesis, Department of Computer Science, University of Rochester, 1989.
- [28] Brian Curless and Marc Levoy.
A volumetric method for building complex models from range images.
In *Proceedings of SIGGRAPH*. ACM, 1996.
- [29] Herve Delingette, Martial Hebert, and Katsushi Ikeuchi.
Shape representation and image segmentation using deformable surfaces.
Image and Vision Computing, 10(3):132–144, 1992.
- [30] R. Deriche.
Using Canny’s criteria to derive a recursively implemented optimal edge detector.
International Journal of Computer Vision, 1(2):167–187, 1987.
- [31] F. Devernay and O. D. Faugeras.
From projective to euclidean reconstruction.
In *Proceedings of IEEE Conference on Computer Vision and Pattern Recognition*, pages 264–9. IEEE, 1996.
- [32] Michel Dhome, Marc Richetin, Jean-Thierry Lapreste, and Gerard Rives.
Determination of the attitude of 3-d objects from a single perspective view.

- IEEE Transactions on Pattern Analysis and Machine Intelligence*, 11(12):1265–1278, 1989.
- [33] S. Edelman.
On learning to recognize 3-d objects from examples.
IEEE Transactions on Pattern Analysis and Machine Intelligence, 15(8):833–837,
August 1993.
- [34] O. D. Faugeras.
What can be seen in three dimensions with an uncalibrated stereo rig?
In *Proceedings of the European Conference on Computer Vision*, pages 563–78.
Springer-Verlag, 1992.
- [35] O. D. Faugeras and G. Toscani.
Camera calibration for 3d computer vision.
In *Proceedings of the International Workshop on Industrial Applications of Machine
Vision and Machine Intelligence*, pages 240–247. IEEE, 1987.
- [36] O.D. Faugeras and Martial Hebert.
The representation, recognition, and locating of 3-d objects.
International Journal of Robotics Research, 5(3):27–52, 1986.
- [37] S. Finsterwalder and W. Scheufele.
Das Ruckwartseinschneiden im Raum.
Verlag Herbert Wichmann, Berlin, Germany, 1937.
- [38] M.A. Fischler and R.C. Bolles.
Random sample consensus: A paradigm for model fitting with applications to image
analysis and automated cartography.
Communications of the ACM, 24(6), 1981.
- [39] Patrick J. Flynn and Anil K. Jain.
BONSAI: 3-d object recognition using constrained search.
IEEE Transactions on Pattern Analysis and Machine Intelligence, 13(10):1066–
1075, 1991.
- [40] James D. Foley, Andries van Dam, Steven K. Feiner, and John F. Hughes.
Computer Graphics: Principles and Practice.
Addison Wesley, New York, 1990.
- [41] Jerome H. Friedman, Jon Bentley, and Raphael Finkel.
An algorithm for finding best matches in logarithmic expected time.
ACM Transactions on Mathematical Software, 3(3):209–226, 1977.
- [42] J.H. Friedman, J.L. Bentley, and R.A. Finkel.
An algorithm for finding best matches in logarithmic expected time.
ACM Transactions on Mathematical Software, 3(3):209–226, 1977.
- [43] Stuart Geman and Donald Geman.
Stochastic relaxation, Gibbs distributions, and the Bayesian restoration of images.

- In Martin A. Fischler and Oscar Firschein, editors, *Readings in Computer Vision: Issues, Problems, Principles, and Paradigms*, pages 564–584. Morgan Kaufmann, 1987.
- [44] Donald B. Gennery.
Visual tracking of known three-dimensional objects.
International Journal of Computer Vision, 7(3):243–270, 1992.
- [45] Peter J. Giblin and Richard S. Weiss.
Epipolar fields on surfaces.
In *Proceedings of the European Conference on Computer Vision*, pages 15–23. Springer-Verlag, 1994.
- [46] R. Glachet, M. Dhome, and J.T. Lapreste.
Finding the pose of an object of revolution.
In *Proceedings of the European Conference on Computer Vision*. Springer-Verlag, 1992.
- [47] Chris Goad.
Special purpose automatic programming for 3-d model-based vision.
In *Proceedings ARPA Image Understanding Workshop*, 1983.
- [48] W. Eric L. Grimson.
On the recognition of parameterized objects.
Technical Report A.I. Memo No. 985, Massachusetts Institute of Technology, 1987.
- [49] W. Eric L. Grimson.
On the recognition of curved objects.
IEEE Transactions on Pattern Analysis and Machine Intelligence, 11(6):632–643, 1989.
- [50] W. Eric L. Grimson and Daniel P. Huttenlocher.
On the verification of hypothesized matches in model-based recognition.
IEEE Transactions on Pattern Analysis and Machine Intelligence, 13(12):1201–1213, 1991.
- [51] W. Eric L. Grimson, Daniel P. Huttenlocher, and T.D. Alter.
Recognizing 3d objects from 2d images: An error analysis.
Technical Report 1362, Massachusetts Institute of Technology, 1992.
- [52] W. Eric L. Grimson and Tomas Lozano-Perez.
Localizing overlapping parts by searching the interpretation tree.
IEEE Transactions on Pattern Analysis and Machine Intelligence, 9(4):469–482, 1987.
- [53] W.E.L. Grimson.
Computational experiments with a feature based stereo algorithm.
IEEE Transactions on Pattern Analysis and Machine Intelligence, 7(1):17–34, January 1985.
- [54] Patrick Gros.

- Matching and clustering: Two steps towards automatic object modelling in computer vision.
International Journal of Robotics Research, 14(6):633–642, 1995.
- [55] J. A. Grunert.
Das pothenotische problem in erweiterte gestalt nebst uber seine anwendungen in der geodasie.
Grunerts Archiv fur Mathematik und Physik, 1:238–248, 1841.
- [56] William R. Hamilton.
Elements of Quaternions.
New York Chelsea Pub. Co., 1969.
- [57] R. M. Haralick and H. Joo.
2d-3d pose estimation.
In *Proceedings of the International Conference on Pattern Recognition*, pages 385–391, 1988.
- [58] Robert M. Haralick, Hyonam Joo, Chung-Nan Lee, Xinhua Zhuang, Vinay G. Vaidya, and Man Bae Kim.
Pose estimation from corresponding point data.
IEEE Transactions on Systems, Man, and Cybernetics, 19(6):1426–1446, 1989.
- [59] Robert M. Haralick, Chung-Nan Lee, Karsten Ottenberg, and Michael Nolle.
Review and analysis of solutions of the three point perspective pose estimation problem.
International Journal of Computer Vision, 13(3):331–356, 1994.
- [60] R.I. Hartley, R. Gupta, and T. Chang.
Stereo from uncalibrated cameras.
In *Proceedings of IEEE Conference on Computer Vision and Pattern Recognition*, pages 761–764. IEEE, 1992.
- [61] Richard I. Hartley.
In defense of the 8-point algorithm.
In *Proceedings of the International Conference on Computer Vision*, pages 1064–1070, 1995.
- [62] John Hertz, Anders Krogh, and Richard G. Palmer.
Introduction to the Theory of Neural Computation.
Addison Wesley, 1991.
- [63] K. Higuchi, H. Delingette, M. Hebert, and K. Ikeuchi.
Merging multiple views using a spherical representation.
In *Second CAD-Based Vision Workshop*, pages 124–131, 1994.
- [64] A. Hilton, A.J. Stoddart, J. Illingworth, and T. Winder.
Reliable surface reconstruction from multiple range images.
In *Proceedings of the European Conference on Computer Vision*, pages 117–126.
Springer-Verlag, 1996.

- [65] H. Hoppe, T. DeRose, T. Duchamp, J.A. McDonald, and W. Stuetzle.
Surface reconstruction from unorganized points.
Computer Graphics, 26(2):71–78, 1992.
- [66] B.K.P. Horn.
Closed-form solution of absolute orientation using unit quaternions.
Journal of the Optical Society of America, 4(4):629–642, 1987.
- [67] Peter J. Huber.
Robust Statistics.
John Wiley and Sons, New York, New York, 1981.
- [68] Daniel P. Huttenlocher, Gregory A. Klanderman, and William J. Rucklidge.
Comparing images using the hausdorff distance.
IEEE Transactions on Pattern Analysis and Machine Intelligence, 15(9):850–863,
1993.
- [69] Daniel P. Huttenlocher, Ryan H. Lilien, and Clark F. Olson.
Object recognition using subspace methods.
In *Proceedings of the European Conference on Computer Vision*, pages 536–545.
Springer-Verlag, 1996.
- [70] Daniel P. Huttenlocher and Shimon Ullman.
Recognizing solid objects by alignment with an image.
International Journal of Computer Vision, 5(2):195–212, 1990.
- [71] Katsushi Ikeuchi.
Generating an interpretation tree from a cad model for 3d-object recognition in
bin-picking tasks.
International Journal of Computer Vision, 1(2):145–165, 1987.
- [72] Katsushi Ikeuchi and Takeo Kanade.
Automatic generation of object recognition programs.
Proc. IEEE Special Issue Comput. Vision, 76:1016–1035, 1988.
- [73] Andrew E. Johnson.
Control of mesh resolution for 3-d object recognition.
Technical Report CMU-RI-TR-96- TBD, Carnegie Mellon University, 1996.
- [74] S.B. Kang, J. Webb, L. Zitnick, and T. Kanade.
A multibaseline stereo system with active illumination and real-time image acquisition.
In *Proceedings of the International Conference on Computer Vision*, pages 88–93,
1995.
- [75] Michael Kass, Andrew Witkin, and Demetri Terzopoulos.
Snakes: Active contour models.
International Journal of Computer Vision, 2(1):322–331, 1987.
- [76] Jan J. Koenderink.
Solid Shape.

- The MIT Press, Cambridge, Massachusetts, 1990.
- [77] David J. Kriegman and Jean Ponce.
Computing exact aspect graphs of curved objects: Solids of revolution.
International Journal of Computer Vision, 5(2):119–135, 1990.
- [78] John Krumm.
Space/frequency shape inference and segmentation of textured 3d surfaces.
PhD thesis, Carnegie Mellon University, 1993.
- [79] Rakesh Kumar and Allen Hanson.
Robust methods for estimating pose and a sensitivity analysis.
Computer Vision, Graphics and Image Processing: Image Understanding,
60(3):313–42, 1994.
- [80] Kiriakos Kutulakos, W. Brent Seales, and Charles R. Dyer.
Building global object models by purposive viewpoint control.
In *Second CAD-Based Vision Workshop*, pages 169–181, 1994.
- [81] Xun Li and David G. Lowe.
Model-guided grouping for 3-d motion tracking.
Technical Report 91-22, Computer Science Department, University of British
Columbia, 1991.
- [82] H. C. Longuet-Higgins.
A computer algorithm for reconstructing a scene from two projections.
Nature, 293:133–135, 1981.
- [83] W.E. Lorensen and H. E. Cline.
Marching cubes: a high resolution 3d surface construction algorithm.
In *Proceedings of SIGGRAPH*, pages 163–169. ACM, 1987.
- [84] David Lowe.
Fitting parameterized three-dimensional models to images.
IEEE Transactions on Pattern Analysis and Machine Intelligence, 13(5):441–450,
1991.
- [85] David G. Lowe.
Perceptual Organization and Visual Recognition.
Kluwer Academic Publishers, 1985.
- [86] David G. Lowe.
Three-dimensional object recognition from single two-dimensional images.
Artificial Intelligence, 1(31):355–395, 1987.
- [87] David G. Lowe.
The viewpoint consistency constraint.
International Journal of Computer Vision, 1(2):57–72, 1987.
- [88] David G. Lowe.
Organization of smooth image curves at multiple scales.
International Journal of Computer Vision, 3:119–130, 1989.

- [89] David G. Lowe.
Integrated treatment of matching and measurement errors for robust model-based motion tracking.
In *Proceedings of IEEE Conference on Computer Vision and Pattern Recognition*, pages 436–440, 1990.
- [90] David G. Lowe.
Robust model-based motion tracking through the integration of search and estimation.
International Journal of Computer Vision, 8(2):113–122, 1992.
- [91] B. D. Lucas and T. Kanade.
Optical navigation by the method of differences.
In *International Joint Conference on AI*, pages 981–984, 1985.
- [92] Larry H. Matthies.
Dynamic Stereo Vision.
PhD thesis, Carnegie Mellon University, 1989.
- [93] Bruce Maxwell.
Segmentation of Multiple Physical Hypotheses of Image Formation.
PhD thesis, Carnegie Mellon University, 1996.
- [94] J. Michael McCarthy.
An Introduction to Theoretical Kinematics.
The MIT Press, Cambridge, Massachusetts, 1990.
- [95] D. J. R. Meagher.
The octree encoding method for efficient solid modeling.
PhD thesis, Rensselaer Polytechnic Institute, 1980.
- [96] Peter Meer, Doron Mintz, and Azriel Rosenfeld.
Robust regression methods for computer vision: a review.
International Journal of Computer Vision, 6(1):59–70, 1991.
- [97] B. Mel.
Seemore: A view-based approach to 3-d object recognition using multiple visual cues.
In *ICPR96*, page A81.13, 1996.
- [98] Hans Moravec.
Towards automatic visual obstacle avoidance.
In *International Joint Conference on AI*, page 584, 1977.
- [99] Hiroshi Murase and Shree K. Nayar.
Visual learning and recognition of 3-d objects from appearance.
International Journal of Computer Vision, 14(1):5–24, 1995.
- [100] Shree K. Nayar and Ruud M. Bolle.
Reflectance based object recognition.
International Journal of Computer Vision, 17(3):219–40, 1996.

- [101] Masatoshi Okutomi and Takeo Kanade.
A multiple-baseline stereo.
IEEE Transactions on Pattern Analysis and Machine Intelligence, 15(4):353–63,
1993.
- [102] Barrett O’Neill.
Elementary Differential Geometry.
Academic Press, Inc., New York, 1966.
- [103] B. Parvin and G. Medioni.
B-rep from unregistered multiple range images.
In *Proceedings of IEEE Conference on Computer Vision and Pattern Recognition*,
pages 1602–1607, 1992.
- [104] Alex Pentland and Stan Sclaroff.
Closed-form solutions for physically based shape modeling and recognition.
IEEE Transactions on Pattern Analysis and Machine Intelligence, 13(7):715–729,
1991.
- [105] Thai Quynh Phong, R. Horaud, A. Yassine, and Pham Dinh Tao.
Object pose from 2-d to 3-d point and line correspondences.
International Journal of Computer Vision, 15(3):225–243, 1995.
- [106] Conrad J. Poelman and Takeo Kanade.
A paraperspective factorization method for shape and motion recovery.
In *Proceedings of Third European Conference on Computer Vision*, pages 97–108.
Springer-Verlag, 1994.
- [107] T. Poggio and S. Edelman.
A network that learns to recognize 3d objects.
Nature, 343:263–266, 1990.
- [108] Tomaso Poggio.
A theory of how the brain might work.
Technical Report A.I. Memo No. 1253, Massachusetts Institute of Technology Arti-
ficial Intelligence Laboratory, 1990.
- [109] Arthur R. Pope.
Model-based object recognition a survey of recent research.
Technical Report 94-04, Computer Science Department, University of British
Columbia, 1994.
- [110] Arthur R. Pope.
*Learning to Recognize Objects in Images: Acquiring and Using Probabilistic Models
of Appearance*.
PhD thesis, Computer Science Department, University of British Columbia, 1995.
- [111] William Press, Brian Flannery, Saul Teukolsky, and William Vetterling.
Numerical Recipes in C: The Art of Scientific Computing.
Cambridge University Press, 1991.

- [112] C. Rothwell, G. Csurka, and O. D. Faugeras.
A comparison of projective reconstruction methods for pairs of views.
In *Proceedings of the International Conference on Computer Vision*, pages 932–7.
IEEE, 1995.
- [113] C. A. Rothwell, A. Zisserman, J.L. Mundy, and D.A. Forsyth.
Efficient model library access by projectively invariant indexing functions.
In *Proceedings of IEEE Conference on Computer Vision and Pattern Recognition*,
pages 109–114, 1992.
- [114] H.A. Rowley, S. Baluja, and T. Kanade.
Neural network-based face detection.
In *CVPR96*, pages 203–208, 1996.
- [115] M. Rutishauser, M. Stricker, and M. Trobina.
Merging range images of arbitrarily shaped objects.
In *Proceedings of IEEE Conference on Computer Vision and Pattern Recognition*,
pages 573–580, 1994.
- [116] F. Sanso.
An exact solution of the roto-translation problem.
Photogrammetria, 29:203–216, 1973.
- [117] Kosuke Sato, Katsushi Ikeuchi, and Takeo Kanade.
Model based recognition of specular objects using sensor models.
Computer Vision, Graphics and Image Processing: Image Understanding,
55(2):155–169, 1992.
- [118] Yoichi Sato and Katsushi Ikeuchi.
Reflectance analysis for 3d computer graphics model generation.
Graphical Models and Image Processing, page to appear, 1996.
- [119] William J. Schroeder and Jonathon A. Zarge.
Decimation of triangle meshes.
In *Proceedings of SIGGRAPH*, pages 65–68. ACM, 1992.
- [120] W. Brent Seales and Olivier Faugeras.
Building three-dimensional cad/cam models from image sequences.
In *Second CAD-Based Vision Workshop*, pages 116–123, 1994.
- [121] Steven A. Shafer.
Automation and calibration for robot vision systems.
Technical Report CMU-CS-88-147, Carnegie Mellon University, 1988.
- [122] Takeshi Shakunaga.
Pose estimation of jointed structures.
In *Proceedings of IEEE Conference on Computer Vision and Pattern Recognition*,
pages 566–572, 1991.
- [123] Takeshi Shakunaga.
Robust line-based pose enumeration from a single image.

- In *Proceedings of the International Conference on Computer Vision*, pages 545–550. IEEE, 1993.
- [124] Amnon Shashua.
Projective structure from uncalibrated images: Structure from motion and recognition.
IEEE Transactions on Pattern Analysis and Machine Intelligence, 16(8):778–790, 1994.
- [125] Pengcheng Shi, Glynn Robinson, and James Duncan.
Myocardial motion and function assessment using 4d images.
In *IEEE Conference on Visualization in Biomedical Computing*, 1994.
- [126] Heung-Yeung Shum.
An Integral Approach to Object Modeling.
PhD thesis, Carnegie Mellon University, 1996.
- [127] Heung-Yeung Shum, Katsushi Ikeuchi, and Raj Reddy.
Principal component analysis with missing data and its application to polyhedral object modeling.
IEEE Transactions on Pattern Analysis and Machine Intelligence, 17(9), 1995.
- [128] Fred Solomon and Katsushi Ikeuchi.
An illumination planner for convex and concave lambertian polyhedral objects.
In *IEEE Workshop on Physics-Based Modeling in Computer Vision*, 1995.
- [129] Marc Soucy and Denis Laurendeau.
Multi-resolution surface modeling from multiple range views.
In *Proceedings of IEEE Conference on Computer Vision and Pattern Recognition*, pages 348–353, 1992.
- [130] Richard Szeliski and Sing Bing Kang.
Recovering 3d shape and motion from image streams using nonlinear least squares.
In *Proceedings of IEEE Conference on Computer Vision and Pattern Recognition*, pages 752–3. IEEE, 1993.
- [131] Richard Szeliski and Richard Weiss.
Robust shape recovery from occluding contours using a linear smoother.
In *Proceedings of IEEE Conference on Computer Vision and Pattern Recognition*, pages 666–667. IEEE, 1993.
- [132] Gabriel Taubin.
Estimation of planar curves, surfaces, and nonplanar space curves defined by implicit equations with applications to edge and range image segmentation.
IEEE Transactions on Pattern Analysis and Machine Intelligence, 13(11):1115–1138, 1991.
- [133] Demetri Terzopoulos and Dimitri Metaxas.
Dynamic 3d models with local and global deformations: Deformable superquadrics.
IEEE Transactions on Pattern Analysis and Machine Intelligence, 13(7):703–714, 1991.

- [134] Demetri Terzopoulos, Andrew Witkin, and Michael Kass.
Constraints on deformable models: Recovering 3d shape and nonrigid motion.
Artificial Intelligence, 36:91–123, 1988.
- [135] Carlo Tomasi.
Shape and motion from image streams : a factorization method.
PhD thesis, Carnegie Mellon University, 1991.
- [136] R. Y. Tsai.
A versatile camera calibration technique for high-accuracy 3d machine vision metrology using off the shelf tv cameras and lenses.
IEEE Journal of Robotics and Automation, 3(4):323–344, 1987.
- [137] J. W. Tukey.
Exploratory Data Analysis.
Addison-Wesley, 1976.
- [138] Greg Turk and Marc Levoy.
Zipped polygon meshes from range images.
In *Proceedings of SIGGRAPH*, pages 311–318. ACM, 1994.
- [139] Shimon Ullman and Ronen Basri.
Recognition by linear combinations of models.
IEEE Transactions on Pattern Analysis and Machine Intelligence, 13(10), 1991.
- [140] Paul A. Viola.
Alignment by Maximization of Mutual Information.
PhD thesis, Massachusetts Institute of Technology, 1995.
- [141] Alan Watt.
3D Computer Graphics.
Addison Wesley, New York, 1992.
- [142] William M. Wells.
Statistical Object Recognition.
PhD thesis, Massachusetts Institute of Technology, 1992.
- [143] William M. Wells.
Statistical object recognition with the expectation-maximization algorithm in range-derived features.
In *DARPA IUS Workshop*, pages 839–850, 1993.
- [144] Mark D. Wheeler and Katsushi Ikeuchi.
Towards a vision algorithm compiler for recognition of partially occluded 3-d objects.
Technical Report CMU-CS-92-185, Carnegie Mellon University, 1992.
- [145] Mark D. Wheeler and Katsushi Ikeuchi.
Sensor modeling, markov random fields, and robust localization for recognizing partially occluded objects.
In *DARPA IUS Workshop*, 1993.

- [146] Mark D. Wheeler and Katsushi Ikeuchi.
Sensor modeling, probabilistic hypothesis generation, and robust localization for object recognition.
In *Second CAD-Based Vision Workshop*, pages 46–53, 1994.
- [147] Mark D. Wheeler and Katsushi Ikeuchi.
Iterative smoothed residuals: a low-pass filter for smoothing with controlled shrinkage.
IEEE Transactions on Pattern Analysis and Machine Intelligence, 18(3):334–337, 1995.
- [148] Mark D. Wheeler and Katsushi Ikeuchi.
Sensor modeling, probabilistic hypothesis generation, and robust localization for object recognition.
IEEE Transactions on Pattern Analysis and Machine Intelligence, 17(3):252–265, 1995.
- [149] Andrew Witkin.
Scale-space filtering.
In *International Joint Conference on AI*, pages 1019–1022, 1983.
- [150] Andrew Witkin, Demetri Terzopoulos, and Michael Kass.
Signal matching through scale space.
In *National Conference on Artificial Intelligence*, pages 714–719, 1986.
- [151] Zhengyou Zhang.
Iterative point matching for registration of free-form curves and surfaces.
International Journal of Computer Vision, 13(2):119–152, 1994.